

HIGH PRECISION COSMOLOGY WITH THE COSMIC BACKGROUND RADIATION

by

Marzieh Farhang

A thesis submitted in conformity with the requirements
for the degree of Doctor of Philosophy
Graduate Department of Astronomy and Astrophysics
University of Toronto

Copyright © 2013 by Marzieh Farhang

Abstract

High Precision Cosmology with the Cosmic Background Radiation

Marzieh Farhang

Doctor of Philosophy

Graduate Department of Astronomy and Astrophysics

University of Toronto

2013

In this thesis we investigate the two cosmic epochs of inflation and recombination, through their imprints on the temperature and polarization anisotropies of the cosmic microwave background radiation.

To probe the early universe we develop a map-based maximum-likelihood estimator to measure the amplitude of inflation-induced gravity waves, parametrized by r , from the cosmic microwave background (CMB) polarization maps. Being optimal by construction, the estimator avoids E - B mixing, a possible source of contamination in the tiny B -mode detection, the target of many current and near future CMB experiments. We explore the leakage from the E - to the B -mode of polarization by using this estimator to study the linear response of the B -mode signal at different scales to variations in the E -mode power. Similarly, for various observational cases, we probe the dependence of r measurement on the signal from different scales of E and B polarization. The estimator is used to make forecasts for Spider-like and Planck-like experimental specifications and to investigate the sky-coverage optimization of the Spider-like case. We compare the forecast errors on r to the results from a similar multipole-based estimator which, by ignoring the mode-mixing, sets a lower limit on the achievable error on r . We find that an experiment with Spider-like specifications with $f_{\text{sky}} \sim 0.02$ – 0.2 could place a $2\sigma_r \approx 0.014$ bound ($\sim 95\%$ CL), which rises to 0.02 with an ℓ -dependent foreground residual left over from an assumed efficient component separation. For the Planck-like survey, a Galaxy-masked ($f_{\text{sky}} = 0.75$) sky would give $2\sigma_r \approx 0.015$, rising to ≈ 0.05 with the foreground residuals. We also use a novel information-based framework to compare how different generations of CMB experiments reveal information about the early universe, through their measurements of r .

We also probe the epoch of recombination by investigating possible fluctuations in the free

electron fraction X_e around the fiducial model of the standard recombination scenario. Though theoretically well studied, the detailed assumptions in the recombination history, based on standard atomic physics, have never been directly tested. However, for our CMB-based cosmological inferences to be reliable, the recombination scenario needs to be observationally verified. We approach this problem in a model-independent way and construct rank-ordered parameter eigen-modes with the highest power to probe X_e . We study various properties of these modes, including their convergence, fiducial model-dependence, dataset dependence, and the eigen-modes response to marginalization over different standard parameters. We demonstrate that, if enough modes are included, the eigen-modes form a practically complete set of basis function for expanding different physically motivated X_e perturbations. We also develop an information-based criterion to truncate the eigen-mode hierarchy, which can be used in similar hierarchical model selections as well. We show how our measurements of cosmic parameters will be affected if possible deviations in the recombination history are ignored. The method is applied to simulations of Planck+ACTPol and a cosmic variance limited survey with differing simulated recombination histories and the recovered X_e trajectories are constructed. We also apply the method to the best currently available CMB datasets, WMAP9+ACT/SPT. The first constructed eigen-mode turns out to be a direct measure of the damping envelope. Its current measurement with SPT slightly indicates a damping tail anomaly, while ACT data agree well with the standard scenario. High resolution Planck data will resolve this tension with high significance.

To my family, in the background and foreground.

Acknowledgements

It is now time to play backward and remember all those to whom you believe the minimum you owe is a thank you message. For me, however, here does not seem like the best place: many of them will probably never know how grateful I feel for them. Thus, I keep it short, as a reminder to myself.

I would like to thank you, all my science companions, through my BSc days at Sharif University of Technology, my officemates in my MSc at Sharif and my PhD at University of Toronto, the most helpful, smart and knowledgable collaborators of CITA, my math and physics teachers at Sharif, like whom I never met, to teach so devotedly and deeply, and my advisors, whose broad knowledge and deep insight were the best research guides.

I feel so lucky to have met you, my beyond-physics friends. You made my days richer and happier in many ways, whether it was for long walks together, or in camps, in the mountains, or parties.

My dearest parents, how can I ever thank you?! If I were to choose my parents, I believe I couldn't make such a perfect choice.

Salman, I am not sure if I would have done physics if it was not because of all our fun math and physics discussions. Should I thank you for that or ... ?!

Mohammad, thanks for filling my PhD life with love and happiness! Continue the good job! You are the best!

Maryam, the sweetest little flower! Thanks for stretching my limits in the last 9 months of my PhD!

And, before and after everything, and in the midst of everything, All praise goes to Allah, the Lord of the worlds.

Contents

1	Introduction	1
1.1	The Cosmic History	1
1.1.1	The Epoch of Inflation	2
1.1.2	The Epoch of Recombination and CMB Formation	3
	The last scattering surface	3
	CMB anisotropies	3
	CMB polarization	4
1.2	CMB As A Probe of the Cosmic History	4
1.2.1	Probing Inflation	4
1.2.2	Probing the Recombination History	5
1.3	CMB Surveys	6
1.4	This work	7
2	Gravitational Wave Detectability with the CMB	9
2.1	Chapter Overview	9
2.2	Introduction	10
2.2.1	Inflation and Its Observables	10
2.2.2	Observations	12
2.3	Bayesian CMB Analysis of Bandpowers and Cosmic Parameters	13
	Pixel Maps and E - B Maps	15
	Maps to Parameters with Map-based Likelihoods	16
	Bandpower estimation	17
	Pseudo- $C_{X\ell}$ cf. Map-based Methods	18
2.3.1	The Downward Flow of Shannon Entropy from Maps to Theory Subspaces	19
2.3.2	2σ Calculation	20
2.4	Constrained Correlations and Linear Response In Pixel-Pair and Parameter Space	21
2.4.1	Linear Response of $C_{BB\ell}$ to $C_{EE\ell}$: Power Leakage	24

2.4.2	Linear Response of r to $\mathcal{C}_{BB\ell}$ and $\mathcal{C}_{EE\ell}$	24
2.5	Simulation Methods and Computational Results	26
2.5.1	Calculation of Ensemble-Averaged Posteriors on Parameter Grids	26
2.5.2	Residual Foreground-Subtraction “Noise”	29
2.5.3	Correlations of r with Other Cosmic Parameters	31
2.5.4	Results in r - τ Space	35
2.5.5	Results in r - n_s Space	39
2.5.6	Results in r - n_t Space	39
2.5.7	Breaking r up into $r_{X\beta}$ -Shape Parameters: A Tensor Consistency Check	40
2.5.8	Breaking f_{sky} into Many Fields	41
2.6	Summary and Conclusions	41
2.6.1	Leakage Levels and Leakage Avoidance	41
2.6.2	Computational Feasibility of Exact Likelihoods	43
2.6.3	Matrix Estimation from Monte Carlo Noise and Signal Simulations and Relation to Master/XFaster	43
2.6.4	The CBIpol Approach as a Guide for Small Deep-sky Analyses	44
2.6.5	Exact 2D Likelihood Computation	45
2.6.6	The Inflation and Tensor Consistency Checks	45
2.6.7	Relation to Planck	46
2.6.8	Relation to Spider	46
2.6.9	History and Forecasts of r Constraints	47
2.6.10	The 1D Shannon Entropy of r	48
3	Eigen-analyses of recombination histories	49
3.1	Chapter Overview	49
3.2	Introduction	50
3.3	Methodology	53
3.3.1	The standard recombination scenario	53
3.3.2	Choice of perturbation parametrization	55
	Alternative parametrizations	56
3.3.3	Basis functions and their different characteristics	58
3.3.4	Constructing the eigenmodes	60
3.4	Perturbation eigenmodes for Recombination	62
3.4.1	XeM construction	62
3.4.2	eXeM construction	66
3.4.3	From eXeMs to XeMs	68

3.4.4	Perturbations to helium recombination	70
3.4.5	Impact of the eigenmodes on differential visibility and CMB power spectra	72
3.4.6	Criteria for truncating the eigenmode hierarchy	72
3.4.7	Perturbation reconstruction: eigenmodes as a complete basis	75
	Standard recombination corrections	78
	Dark matter annihilation scenario	79
3.5	Measuring the amplitudes of perturbation eigenmodes for simulated data	80
3.5.1	Case 1: The standard recombination scenario	81
3.5.2	Case 2: A perturbed recombination scenario	87
3.5.3	Trajectories	90
3.5.4	Beyond small perturbations	92
3.6	conclusion and discussion	93
3.7	Appendix	96
3.7.1	Localized basis functions	96
3.7.2	Non-localized basis function	97
3.7.3	Eigenmodes with fixed and varying background cosmology	97
3.7.4	Fiducial model and dataset dependence	100
4	recombination history from damping tail	104
4.1	Chapter Overview	104
4.2	Introduction	105
4.3	Eigenmodes for Perturbations to the High- z Ionization History	107
4.3.1	Eigenmode construction	107
4.3.2	Datasets and their eigenmodes	108
4.3.3	The Damping Physics of the Low Order Recombination Modes	109
4.4	Constraints from circa 2011 ACT, SPT and WMAP7 data	111
4.5	The impact of electron number conservation on the posterior	115
4.6	Discussion	118
4.7	Appendix: Fisher Analysis	122
5	Outlook	124
5.1	Summary	124
5.2	Future Prospects	126
	Bibliography	128

List of Tables

2.1	Specifications of Spider-like, Planck-like and CMBPol (mid-cost) experiments for simulations.	28
2.2	Parameters of our assumed foreground model, adopted from Baumann et al. (2009). 30	
2.3	σ_r from the full likelihood computed on a 2D r - τ grid (bottom) cf. 1D, 2D and 6D Fisher determinations $[F^{-1}]^{rr}$ using pixel-space matrices (middle) and the simplified ℓ -space sums, with $r_{\text{fid}} = 0.12$. This demonstrates that the use of reduced parameter spaces gives robust results, independent of cap sizes, here for $f_{\text{sky}} = 1, 0.07, 0.007$	32
3.1	The forecasted standard deviations of the first six XeMs ($\sigma = 0$) from the Fisher analysis for different observational cases.	63
3.2	The forecasted standard deviations of the first six eXeMs from the Fisher analysis constructed by marginalization over different number of standard cosmic parameters and for different observational cases. In all cases, $\ell_{\text{max}} = 3500$	67
3.3	The coefficients of projection of the six most constrained eXeMs on the first eight XeMs.	67
3.4	The projection of the modifications to recombination history on the first six XeMs. Note the different values of σ used for the two cases.	79
3.5	The standard deviations of the first five XeMs from chains produced by CosmoMC, marginalized over the main six standard parameters (for the CVL case with $\ell_{\text{max}} = 3500$).	81
3.6	Y_p and its measured error from simulations for a CVL and a Planck-ACTPol-like experiment (abbreviated as Pl-Apol), with XeMs and eXeMs taken into account as perturbation eigenmodes, compared to the case with no eigenmodes.	84
4.1	The constraints on cosmological parameters with different sets of parameters used, as measured by SPT+WMAP7. μ_1 and μ_2 refer to the amplitudes of the first and second modes.	113

4.2	The constraints on cosmological parameters with different sets of parameters used, as measured by ACT+WMAP7. μ_1 and μ_2 refer to the amplitudes of the first and second modes.	114
4.3	The constraints on the first two modes (μ_1 and μ_2), as measured by SPT12+WMAP7 and ACT12+WMAP7.	114

List of Figures

2.1	SPIDER Forecast	14
2.2	The filters $W_{X\ell, X'\ell'}$, $X, X' \in \{EE, BB\}$, show how the mode $\mathcal{C}_{X\ell}$ linearly responds to a small change in the mode $\mathcal{C}_{X'\ell'}$. The leakage responses shown here are for an $\ell' = 100$ stimulus, for a Spider-like experiment with $f_{\text{sky}} = 7\%$ at $N_{\text{side}} = 64$ (left) and $f_{\text{sky}} = 0.7\%$ at $N_{\text{side}} = 128$ (right). Note the different scales for the y -axis. The corner box of the right panel magnifies $W_{EE\ell, BB100}$ for $f_{\text{sky}} = 0.7\%$, whose details are not clear in the main plot.	21
2.3	Beam and pixel window functions for different resolutions are compared to the polarization power spectra for the best fit WMAP7-only parameters for the Λ CDM + lensing + SZ + tensor model, with the addition of a tensor component of strength $r_{\text{fid}} = 0.12$. B -mode (GW) shows just the gravity wave-induced contribution and B -mode (GW+lens) includes the lensing contribution as well.	22

2.4	Window functions $W_{r,X\ell}$ for $X \in \{EE, BB\}$ for different sky cuts show that, as expected, all-sky experiments are nicely sensitive to the reionization BB bump, but smaller sky experiments are not, although they pick up well the $\ell \sim 50 - 100$ region. We have used $r = 0.12$ for the fiducial model. The rapid declines to high ℓ are more due to the onset of experimental noise than to the onset of the lensing-induced B “noise”. Residual foreground noise has not been included in these plots. Note that even a coverage with f_{sky} only 0.007 can punch out a robust detection from 50 to 150 in ℓ . The coverage with $f_{\text{sky}} = 0.07$, although loses out a bit (relatively) at 150, its detection would come from a wider stretch in $\ln \ell$, out to $\ell \sim 20$ before falling off. Only at $f_{\text{sky}} > 0.25$ does one begin to pick up the reionization bump. The curious drop in the all-sky $N_{\text{side}} = 16$ red line at the top is due to the Spider-like noise for higher ℓ being heavily enhanced because all of the sky is covered in the same amount of observing time. To illustrate the role of this, a CMBPol-like experiment with C_N decreased by ~ 1000 is plotted, with $N_{\text{side}} = 16$ (dashed straight line) and $N_{\text{side}} = 64$ (triple-dot-dashed line). The reason all three are offset from one another is because the normalizing σ_r^2 depends upon the amount the filter captures of the total r signal.	25
2.5	Uncertainty in measuring r for different sky coverages with Spider-like (top) and Planck-like (bottom) experiments, with and without foregrounds (squares and triangles respectively), for the fiducial model $r_{\text{fid}} = 0.12$. The solid lines are the results of ℓ -space analysis (ignoring foregrounds). The analysis has been performed with different resolutions for different f_{sky} , ranging from $N_{\text{side}} = 32$ for full sky to $N_{\text{side}} = 128$ for the smallest sky coverage. The f_{sky} refers to the sky coverage before applying the Galactic cut so for full sky f_{sky} is effectively ~ 0.75 . The dashed line is the $2\sigma_r$ if the full sky needs to be effectively considered as a combination of several smaller patches with the individual observed sky fraction being f_{sky} and the total area of all patches equal to the Galaxy-masked full sky.	33
2.6	Similar to figure 2.5 with $r_{\text{fid}} = 0.001$	34
2.7	The curves show $2\sigma_r$ as a function of r_{fid} obtained from the Fisher matrix in ℓ and pixel-space for $f_{\text{sky}} = 0.007$ (top) and 0.07 (bottom). The choices for the curves are meant to unravel the impact of the cosmic variance, lensing, instrument noise and mode mixing on σ_r . The symbols show errors from the full likelihood calculated on a gridded 2D parameter space, and agree nicely for both pixel-space (squares) and ℓ -space (diamonds).	36

2.8	1σ and 2σ r -τ contours with and without foregrounds for a Spider-like experiment with different sky cuts and for a Planck-like Galaxy-masked experiment with effective $f_{\text{sky}} \sim 0.75$. In the two right panels the contours for the combined Spider-like and Planck-like experiments are also plotted. The black plus signs denote the input $r_{\text{fid}} = 0.12$ and $\tau_{\text{fid}} = 0.09$. Expending Spider-like observing time on large sky coverage would not improve much the Planck forecasted τ error, but would decrease the combined r error, suggesting the deep small-sky option is better.	36
2.9	r - n_s contours for a Spider-like ($f_{\text{sky}} \sim 0.08$)+WMAP7 experiment, contrasted with a Planck-like (Galaxy-masked $f_{\text{sky}} \sim 0.75$) experiment, assuming no foreground contamination, compared to the results for the combination of the two (the solid and dot-dashed blue curves). The $r - n_s$ correlation has been ignored, as discussed in § 2.5.3. We also explicitly verified this for the specific case of the Planck-like survey from post-processing the CosmoMC chains. The r constraints are calculated by the numerical methods used throughout the paper. For the case of Spider+WMAP7, we assumed an asymmetric Gaussian likelihood for n_s with the widths coming from the lower and upper $1\sigma_{n_s}$ as measured by WMAP7 (http://lambda.gsfc.nasa.gov/product/map/dr4/params/lcdm_sz_lens_tens_wmap7.cfm). For the n_s likelihood from the Planck-like case, CosmoMC chains (http://cosmologist.info/cosmomc/) were used to properly take into account the correlations of n_s with other cosmic parameters, which, unlike r , are non-negligible. Top has $r_{\text{fid}} = 0.12$ and bottom has 0.001; both have $n_{s,\text{fid}} = 0.98$. The plots indicate a possibly very rosy picture for constraining these two critical inflation parameters.	37
2.10	1σ and 2σ r - n_t contours for a Spider-like experiment with different sky cuts and for a Planck-like Galaxy-masked $f_{\text{sky}}=0.75$ experiment. The contours for a CMBPol-like experiment as well as those for the combined Planck-like and Spider-like experiments are plotted for comparison. The black line is the inflation consistency line and the black plus sign is the fiducial input, $r = 0.12$ and $n_t = -0.015$. Even with this CMBPol, inflation consistency is not that well tested.	38
2.11	1σ and 2σ contours in the r_{EE} - r_{BB} plane for a Spider-like experiment with different sky cuts and for a Planck-like experiment with $f_{\text{sky}}=0.75$. The black solid lines show the <i>tensor consistency</i> curves $r_{EE} = r_{BB}$ and the plus signs show the fiducial $r_{EE} = r_{BB} = 0.12$ input model. As expected, r_{BB} is better determined than r_{EE} and this tensor consistency is not well tested.	41

2.12	When one patch covering f_{sky} is broken up into four $f_{\text{sky}}/4$ cap-patches, but the noise and observing time remain constant, the (τ -marginalized) r -errors remain similar except at very small f_{sky} . We also show that factors of two changes in the noise swamp this effect. The calculations were done with $r_{\text{fid}} = 0.12$ in the pixel-space except for the highest sky coverages where the pixel and ℓ -space analysis are in excellent agreement. The effect of foreground contamination and Galaxy cut has not been taken into account here.	42
3.1	The cosmological ionization history (left), $X_e \equiv N_e/[N_p + N_{\text{HI}}]$, and differential visibility function (right) for the standard recombination scenario with $T_{\text{CMB}} = 2.726\text{K}$ (Fixsen, 2009) contrasted to a case with $T_{\text{CMB}} = 3\text{K}$. Here N_p and N_{HI} represent the number density of ionized and neutral hydrogen, while N_e denotes the number density of free electrons. The visibility function has been plotted in units of maximum visibility.	54
3.2	Localized perturbations in the X_e history, in the form of M_4 splines (left) and the derivatives of the C_ℓ 's with respect to the amplitude of each perturbation (TT power spectrum in the center, EE on the right).	57
3.3	Similar to Fig. 3.2 but for non-localized perturbations in the form of Chebyshev polynomials.	57
3.4	The six most constrained XeMs with $\delta u(z) = \delta \ln(X_e + \sigma)$ as the parameter, having four different values for σ , and with Gaussian bumps as the basis functions. The maximum and width (at 68% and 95% levels) of the Thomson visibility function have been marked in all figures.	61
3.5	The three most constrained XeMs for five different basis functions (with 160 parameters).	63
3.6	Testing the convergence of the eigenmodes. As examples, the second and the sixth most constrained XeMs are shown for cases with different number of parameters (40, 80, 160 and 320) and with M_4 splines as the basis functions. We see that the modes for 160 and 320 parameters are basically the same, indicating that these modes have already converged with 160 parameters.	64
3.7	The three most constrained eXeMs. The solid blue lines correspond to modes constructed after marginalization over six standard parameters while for the dashed red curves Y_p is marginalized over in addition.	67
3.8	The first three eXeMs with only Y_p being marginalized over (dashed blue curves). For comparison, the first three XeMs are also plotted (solid black curves). . . .	69

3.9	The best three eXeMs with the two inflationary parameters A_s and n_s being marginalized over, compared to the XeMs, where all standard cosmic parameters are held fixed in the construction process of perturbation eigenmodes.	70
3.10	The $\delta\text{vis} = (\text{vis} - \text{vis}_{\text{fid}})$, normalized to the maximum of the fiducial visibility, (left) and the relative changes in the TT and EE power spectra (middle and right) for the six most constrainable XeMs.	71
3.11	Various measures of entropy differences defined in the text are plotted against increasing eigenmode number, for (a) the XeM case and (b) the eXeM case. The Cosmic Variance Limited mode results have heavy lines or points, the Planck+ACTpol forecast has lighter lines and points, as indicated. They look quite similar. For this figure, the modes are determined by the densely-packed Gaussian bump expansion, but the triangular and spline expansions look similar, differences becoming notable only at higher n . The basic information on growing entropy is given by $S_n - S_1$, and the mean difference $S_{\leq n}/n - S_1$, with the latter bracketed by the two white-noise entropies. The criteria for threshold selection discussed in the text involve the injection entropy, $S_n - S_{\leq n}/n$ and $S_{n+1} - S_n$ (plotted with opposite sign for clarity). Thresholding at $\Delta S_t \sim 1/2$ selects the first mode or two, but mode-groups are also evident, suggesting modes should be added in blocks rather than singly as we eliminate bias, check convergence and demonstrate robustness.	76
3.12	The reconstruction of two physically motivated X_e perturbation scenarios on (different number of) XeMs generated with Gaussian bumps (top) and the relative difference in the temperature power spectrum between the reconstructed perturbations and the full corrections (bottom). Right: The perturbations come from deviation from physical corrections to the recombination process (CT2011). Here the perturbation parameter is $\delta \ln(X_e)$. Left: The perturbations are due to a model of dark matter annihilation. As the perturbation parameter we used $\delta \ln(X_e + 0.01)$ to better accommodate for the freeze-out perturbation. A case with $\delta u(z) = \delta \ln(X_e)$, i.e., $\sigma = 0$, is shown for comparison.	77
3.13	2D contours for the amplitudes of some of the best five XeMs, chosen as examples, as measured by a CVL experiment and with the standard recombination history. Here the six standard cosmic parameters were also allowed to vary. That is why the measured eigenmodes are correlated. The solid black lines mark the 1σ and 2σ contour levels.	81

3.14	2D contours for the amplitudes of some of the best six eXeMs, chosen as examples, as measured by a CVL experiment and with the standard recombination history. The six standard cosmic parameters were also allowed to vary in the simulations.	82
3.15	The contours at 1σ and 2σ levels for the standard parameters as measured by an ideal experiment in the presence of five (six) XeMs (eXeMs) compared to the case with no eigenmodes included. The input value of the parameters is shown by the black diamond.	83
3.16	The derivatives of the $C_\ell^{T,E}$'s with respect to some of the standard parameters.	84
3.17	Contours of some of standard parameters for CT2011 case, with eight XeMs in one case and 20 eXeMs in the other case included in the analysis, compared to a case where no perturbation eigenmodes (of any kind) has been included (the solid red curves). The simulations are performed for a CVL experiment. The input value of the parameters is shown by the black diamond.	85
3.18	Similar to Fig. 3.17 but for a Planck-ACTPol-like experiment. Here three eigenmodes were added for both the XeM and eXeM case.	86
3.19	Left: The $\delta X_e/X_e$ as measured by a CVL experiment by including eight XeMs (and six standard parameters) in the analysis. The colors show the density of trajectories going through each point in the z - $\delta X_e/X_e$ space, normalized to one at each z . The maximum and 1 and 2σ widths of the Thomson visibility function have been marked at the bottom of the plot. As this plot and the next ones indicate, the main recovery of X_e is the slope of the curve around this visibility peak. Middle and right: similar to the left figure, but for $\delta C_\ell^{TT,EE}/C_\ell^{TT,EE}$ trajectories.	88
3.20	Similar to Fig. 3.19 but with the first ten eXeMs.	89
3.21	Similar to Fig. 3.19 but with the first twenty eXeMs. As this figure demonstrates, including a higher number of modes does not necessarily lead to better X_e recovery. Here the recovered X_e becomes noisier compared to the case with only ten modes included, while the C_ℓ trajectories do not change significantly except for the diminished oscillations around the input model, as discussed in the text.	90
3.22	Similar to Fig. 3.19 but for a Planck-ACTPol-like experiment and with only three XeMs taken into account.	91
3.23	Similar to Fig. 3.20 but for a Planck-ACTPol-like experiment and with only three eXeMs taken into account.	91

3.24	The three most constrained XeMs for three different fiducial models. The default model corresponds to the SRS and the effect of gravitational lensing on the CMB anisotropies has been included. One model corresponds to a recombination history with a different CMB temperature and in the other model lensing is not included. For the case of the two different CMB temperatures, the major difference is the shift in the eigenmodes associated to the shift in the fiducial X_e and visibility functions (see Fig. 3.1).	101
3.25	The three most constrained XeMs with and without polarization and with $\ell_{\max} = 2000$ and 3500.	102
3.26	The three most constrained XeMs for a Planck-CTPol-like experiment compared to a CVL experiment.	102
4.1	The first two modes (constructed for SPT+WMAP7 data), normalized to have unit norm (left), the corresponding changes in the visibility functions (middle), and the resulting differential changes in the temperature power spectrum C_ℓ (right). The middle and right plots corresponds to perturbations with SNR=1. The visibility function is defined as $g(z) = de^{-\tau}/d\eta$, where η is the conformal time and τ is the optical depth to the last scattering surface. The visibility functions have been normalized to the maximum of the fiducial model's visibility, which occurs at $z_{\text{dec}} = 1088$. The width (at 68% and 95% levels) of the visibility function has been marked as error bars about z_{dec} in the figures.	109
4.2	Black lines: marginalized 1D-prior (dotted lines) and posterior probabilities (solid lines) with SPT+WMAP7 data for the first three modes, in an analysis where six standard parameters, three nuisance parameters and the first three X_e perturbation modes were used. Blue lines, left plot: the prior (dashed line) and posterior (solid line) distributions for μ_1 , similar to black lines, but with only one mode included in the analysis. Note that the solid black and blue curves coincide in the left plot.	115
4.3	Increase in the information content of the measured modes delivered by data relative to the volume of parameter space allowed by electron conservation, for different number of modes included in the analysis and various experimental cases. The modes in each case are constructed for the corresponding dataset. . .	117

- 4.4 The solid red line corresponds to the difference between the best-fit C_ℓ 's for the standard case and the case with the first mode included, measured by SPT+WMAP7. That is, the two cases have different background cosmology (as measured by data) as well as different values for μ_1 ($\mu_1 = 0$ and $\mu_1 = -0.77$). The dashed and dotted curves show the response to changes in Y_p , N_{eff} and the first mode. In these cases, the six standard parameters are fixed for all models, while $Y_p = 0.296$, $N_{\text{eff}} = 3.898$ and $\mu_1 = -0.77$ have been chosen for their corresponding curves. 119
- 4.5 The marginalized 68% and 95% n_s - $\Omega_b h^2$ contours for various sets of parameters being included in the analysis. The 6s contours represent the standard model with six parameters. Other cases each have one extra parameter, being Y_p , N_{eff} and μ_1 . Note that these extended models favor a slightly higher value of n_s compared to the standard case. 119
- 4.6 The relative X_e and differential visibility changes due to relative infinitesimal changes in Y_p and N_{eff} (with other parameters fixed). The first mode has been added in the background (the gray dotted lines) to aid visual comparison. It has been normalized to be comparable to Y_p changes. 120

Chapter 1

Introduction

1.1 The Cosmic History

According to the concordance model of cosmology, the universe started from an extremely hot and dense state, the *Big-Bang*. A pivotal building block of this standard model is the epoch of *inflation*, a period of accelerated expansion in the very early universe, around 10^{-35} sec after the Big-Bang. Inflation left behind a homogenous isotropic universe filled with particles of the standard model of particle physics. These particles were generated by the decay of the hypothesized inflaton field, through the so-called reheating process. Afterwards, through its expansion and cooling, the universe went through a long chain of physical processes of different energy scales.

Among these phenomena and of particular importance in observational cosmology, is the so-called *recombination* epoch. It refers to a period in the life of the young universe, at about the age of 380,000 years, when it was cool enough for the protons to capture electrons and form neutral hydrogen atoms. Helium was fully recombined earlier at the redshift of $z \sim 1800$ (and singly recombined at $z \sim 5000$). At around this point an important milestone in the cosmic history took place: with electrons now trapped in the Coulomb potential of nuclei, the photons, which formerly frequently Thomson-scattered off free electrons, decoupled from matter and freely travelled afterwards. These photons formed the Cosmic Microwave Background (CMB) radiation. With no further photon-baryon interactions, the transparent universe went through "dark ages", which only finished when the first luminous objects formed, probably after $z \sim 30$. The UV radiation of these objects also reionized the hydrogen in the intergalactic medium. However, the interaction of the photons with the now free electrons was much less frequent since the plasma had diluted due to the expansion.

The two epochs of inflation and recombination are the focus of this work. Inflation provides a unique opportunity to study physics at energy scales well beyond those achievable by man-

made accelerators. The recombination process, on the other hand, lays the framework for CMB formation. The detailed assumptions about that epoch impact our CMB-based cosmological inferences, including the measurements of some of the inflationary parameters. The following sections briefly review the periods of inflation and recombination, and how they are explored by CMB data.

1.1.1 The Epoch of Inflation

Inflation as an early phase of accelerated expansion was postulated to solve some of the problems of the otherwise successful standard model of cosmology, including its observed flatness, and homogeneity and isotropy beyond the causally connected scales. Moreover, inflation is thus far the unrivalled theory to seed cosmic structures. According to inflation, all structures in the universe grew gravitationally from small perturbations against a homogenous background distribution of matter, which, in turn, had arisen from scalar quantum fluctuations in the space-time metric during inflation. Inflation also generated tensor fluctuations in the space-time metric, commonly referred to as gravity waves. Vector perturbations, although probably generated in the early universe, decay in an expanding universe and thus are not considered observationally important in cosmology.

In the slow-roll models of inflation, the expansion is driven by the slow rolling, compared to the expansion rate of the universe, of a single scalar field, dubbed inflaton, ϕ , down a relatively flat potential field $V(\phi)$ and ends when this potential field becomes steep. Except for the smallness of the slow-roll parameters, $\epsilon \approx M_{\text{pl}}^2/2(V'/V)^2$ and $|\eta| \approx M_{\text{pl}}^2|V''/V|$, the potential field is, theoretically, quite arbitrary. Here, M_{pl} is the reduced Planck mass and the derivatives are with respect to the (homogenous) inflaton field. However, the uniquely predicted power spectra of fluctuations for an assumed potential field¹ should agree with observations. Generically, the power spectra $\mathcal{P}_{s,t}(k)$ of inflation-induced perturbations, predicted by most inflationary models to be near scale-invariant, are modeled by power laws around relevant scalar and tensor pivots, k_{sp} and k_{tp} . The main inflationary observables that parametrize these power laws include A_s and r for parametrizing the scalar amplitude and tensor-to-scalar ratio, and n_s and n_t for the spectral index of scalar and tensor perturbations:

$$\begin{aligned} \mathcal{P}_s(k) &\approx A_s(k_{\text{sp}}) (k/k_{\text{sp}})^{n_s(k_{\text{sp}})-1}, & \mathcal{P}_t(k) &\approx A_t(k_{\text{tp}}) (k/k_{\text{tp}})^{n_t(k_{\text{tp}})}. \\ r &\equiv r(k_{\text{tp}}) \equiv \mathcal{P}_t(k_{\text{tp}})/\mathcal{P}_s(k_{\text{tp}}). \end{aligned}$$

The running of the scalar spectral index, $dn_s/d\ln(k)$, where k is the perturbation wavenumber, is also sometimes introduced to characterize possible deviations from power-law spectrum. The

¹The distributions of perturbations predicted by most inflationary models are (close to) Gaussian, and can thus be well characterized by their power spectra.

primordial perturbations provide initial conditions for the observed anisotropies in the temperature and polarization of the CMB. These anisotropies, still in the linear regime, make CMB measurement a unique probe of the early universe and its initial conditions.

1.1.2 The Epoch of Recombination and CMB Formation

The last scattering surface

The combination of electrons and protons to form hydrogen atoms, at $z \sim 1100$, is called (hydrogen) recombination. Recombination, by transforming the universe from an ionized to a neutral plasma, is accompanied by the unavoidable decoupling of matter and radiation and thus the formation of CMB photons. The last scattering surface, i.e., when it is most likely that the CMB photons had their last scatter off the electrons, is described by the differential visibility function $g(z)$,

$$g(z) = -de^{-\tau}/d\kappa, \quad \tau = \int \sigma_{\text{T}} n_e c dt. \quad (1.1)$$

$g(z)dz$ determines the probability that a photon last scattered between redshifts of z and $z+dz$. Its peak defines the last scattering surface and its width shows how long the recombination process took. Here κ is the conformal time, $a d\kappa = c dt$, and τ is the optical depth to the last scattering surface, and c , n_e and σ_{T} are the speed of light, number density of free electrons and the Thomson scattering cross section, respectively.

CMB anisotropies

The cosmic background radiation is highly isotropic on all scales, as was detected by Penzias and Wilson in the mid 60s (Penzias and Wilson, 1965). However, as observed in early 90s by the COBE satellite (Smoot et al., 1992), it encompasses small anisotropies of the order of 10^{-5} , seeded by chiefly adiabatic perturbations during the epoch of inflation. The patterns of CMB spatial fluctuations, usually expressed by their power spectra in harmonic space, have been the subject of intense study in the last two decades and revealed immense amount of information about our universe.

The primary cosmological information revealed by primordial CMB anisotropies, generated by acoustic oscillations during recombination, is about the initial conditions of the fluctuations, as well as the matter and energy content of the universe, its curvature and also our distance to the last scattering surface. On the other hand, secondary anisotropies, generated during the journey of CMB photons from the last scattering surface toward the observer today, shed light on the conditions at the epoch of reionization (through the re-scattering of CMB photons off the newly freed electrons), on the large scale structure of the universe (through the Sunyaev–Zel’dovich effect), and on the characteristics of dark energy (through the late-time Integrated

Sachs-Wolf effect).

CMB polarization

The primary CMB polarization is produced at the last scattering surface when the quadrupole component of the anisotropic radiation field is Thomson-scattered by free electrons. For this to happen, the electron plasma should be dilute enough so that the anisotropies are no longer washed out by too frequent scatterings. On the other hand, the low free electron density reduces chances of scattering, the basic requirement for the generation of polarization. As a result, CMB polarization, which can only form toward the end of recombination, is relatively small.

An inevitable source of CMB quadrupole anisotropy is the gradient of the electron velocity field at the last scattering, generating polarization patterns which are out of phase with temperature anisotropies. In inflationary models of cosmology, the stochastic background of gravity waves also contributes to the quadrupole component of anisotropies and thus produces polarization. Polarization is also generated at late times on large scales by Thomson-scattering of CMB photons off free electrons during and after the epoch of reionization, so far as there are still adequate scatterings in the expanding universe.

The CMB polarization is described by the two Stokes parameters Q and U (with the circular V component theoretically vanishing). It is common to decompose the CMB polarization fields into two of their linear combinations, the curl-free E -mode and the gradient-free B -mode (more in chapter 2). The B -mode component on large scales can only be produced by inflation-induced gravity waves, while the E -mode has contributions from both scalar and tensor perturbations. As gravity waves, with a measurable, yet tiny amplitude, are definite predictions of most models of inflation, B -mode detection is regarded as the smoking gun for inflation. On small scales, however, contributions from lensed E -modes dwarf the primordial B -modes from gravity waves, requiring accurate separation techniques to extract the primordial signal. The lensing signal, on the other hand, is a great source to study the large scale structure of the universe.

1.2 CMB As A Probe of the Cosmic History

The analysis of the cosmic background radiation has been so far the most powerful tool in providing cosmologists with precise measurements of cosmic parameters. In the following we briefly review how the CMB carries traces of the epochs of inflation and recombination.

1.2.1 Probing Inflation

The main inflationary observables, A_s , n_s and $dn_s/d \ln k$ for scalar perturbations and r and n_t for tensor perturbations can be directly measured by CMB data at given proper pivots. A_s sets

the amplitude of temperature fluctuations, with small contribution from tensor perturbations. However, it is degenerate with τ , the optical depth of CMB to reionization, as the anisotropies are damped during the reionization epoch by a factor of $e^{-\tau}$ (in the power spectrum). Measurements of large scale CMB polarization, produced during the reionization epoch, break this degeneracy by independently estimating τ . The scalar spectral index determines the slope of the power spectrum. It is thus degenerate with parameters that modify the CMB damping tail, such as the primordial helium abundance Y_p and the effective number of relativistic species N_{eff} . The running of n_s is also most sensitive to small scale anisotropies, and similarly, modifications to the damping tail, primordial or secondary, significantly impact its measurement.

The current upper limit on the tensor-to-scalar ratio, r , comes from the amplitude of temperature fluctuations. However, due to the tininess of the signal compared to density perturbations, B -mode measurement is required to pin it down. The signal is contaminated by foreground radiation and the lensed E -mode signal. Extra care should be given to foreground separation which puts the most hindering challenge for B -mode detection. That is because, unlike the lensing signal, the much larger foreground radiation is not well characterized. Given the tininess of r , the tensor spectral index n_t , being about an order of magnitude smaller², will probably evade our measurements even with the proposed post-Planckian CMB satellites.

1.2.2 Probing the Recombination History

The recombination history is well studied and modeled based on the standard physics and is treated, for a given set of cosmological parameters, as a theoretical input in the standard CMB analysis. The analysis of high precision data is measurably sensitive to the details of this process. This explains the extensive effort made so far in the theoretical study of the recombination physics and the relevant atomic processes. However, observational verification of the details of the recombination scenario is needed for the CMB-based higher-precision cosmological inferences to be reliable. We put this model to test by searching for fluctuations around it, using the high- ℓ CMB anisotropies. Detection of possible deviations around the standard scenario would point to exotic physics at those early times, such as variations in the physical constants or energy injection from dark matter annihilation.

Any physical process that impacts the recombination history inevitably affects the CMB power spectrum, but not necessarily in a measurable way. The CMB spectrum is most sensitive to variations in the recombination history around the last scattering surface. For example, changes in the width or position of the visibility peak, leading to shifts in the position of CMB peaks and also its small scale damping, are among the best constrained observables. These,

² $n_t \approx -r/8$

however, are degenerate with other cosmic parameters with similar impacts on the CMB spectra, again justifying the extra care required in modeling the recombination history.

1.3 CMB Surveys

The cosmological information revealed by the CMB emerges from a broad range of angular scales, from arc minute to degree. After the discovery of CMB anisotropies in early 90s, many ground-based and balloon-borne experiments were designed and deployed to probe the anisotropies at different scales with increasing precision. BOOMERanG (de Bernardis et al., 2000a), MAXIMA (Hanany et al., 2000), Saskatoon (Netterfield, 1995), MAT/TOCO (Nolta et al., 2003) and other experiments determined our distance to the last scattering surface, which, when combined with the measurements of the Hubble parameter, revealed the flatness of our universe. These were followed by higher precision experiments (including ACBAR (Reichardt et al., 2009a), CBI (Sievers et al., 2007a), DASI (Halverson et al., 2002) and the WMAP satellite (Hinshaw et al., 2012)) which measured higher multipoles. With these experiments, cosmologists could make unprecedented measurements of the basic cosmic parameters and a new era in cosmology began.

The more recent ACT (Dunkley et al., 2011; Sievers et al., 2013) and SPT (Keisler et al., 2011; Hou et al., 2012) have measured the CMB temperature at very high multipoles (up to $\ell \sim 10000$). These small scales carry information about standard cosmic parameters, such as N_{eff} and Y_p , as well as being affected by possible extensions to the standard model, e.g., through dark matter annihilation or decay and cosmic strings.

The E -mode polarization of the CMB is also a powerful probe of cosmic parameters. It does not suffer from foreground contamination as much as temperature anisotropies do, and can therefore more tightly constrain cosmic parameters. Moreover, it helps break the degeneracy between some parameters measured by temperature anisotropies such as τ and A_s . The E -mode polarization of CMB was first detected by DASI experiment (Kovac et al., 2002), with its power spectrum first measured by CBI (Sievers et al., 2007a), followed by other experiments including BOOMERanG 2003 (Montroy et al., 2006), CAPMAP (Barkats et al., 2005) and WMAP (Page et al., 2007).

The large-scale B -mode signal is unique in constraining the amplitude of gravity waves by measuring r . The best constraint on the tensor spectral index will also be from B -mode measurements. However, it will not be very tight due to the short baseline of the primordial B -mode signal. The small scale B -mode measurements, on the other hand, will provide us with the stringent measurements of the sum of neutrino masses, by measuring the amplitude and shape of the lensing structure. Many ground-based and balloon-borne experiments are now

being developed with the goal to measure the B -mode on small and large scales. These include Spider (Fraisse et al., 2011), KECK (Sheehy et al., 2010), QUIET (QUIET Collaboration et al., 2012), ABS (Essinger-Hileman et al., 2010), BICEP (Chiang et al., 2010), EBEX (Reichborn-Kjennerud et al., 2010) and PIPER (Chuss et al., 2010). These experiments have different targets, e.g., broad vs deep observations, but all share the detection of the gravity-wave-induced B -modes. ACTPol (Niemack et al., 2010) and SPTPol (Austermann et al., 2012), on the other hand, mainly target the small-scale lensing sector of the B -mode. Planck, being broad and relatively deep, will be able to address both.

1.4 This work

This work concentrates on the two important cosmic epochs of inflation and recombination, and decoding the CMB signal at large (low- ℓ) and small (high- ℓ) scales respectively to study them. Getting most from the current and near future high precision CMB data calls for detailed and unbiased modeling of relevant cosmological scenarios as well as accurate handling of computational and numerical complications. In Chapter 2, we develop a map-based maximum likelihood estimator for optimal measurement of the amplitude of inflationary gravity waves from CMB polarization. This method bypasses E - B mixing, an important source of contamination to B -mode detection. We demonstrate its feasibility and power for the current generation of B -mode experiments and apply the method to investigate sky-coverage dependence of r measurement for various experimental setups. Throughout the analysis, in parallel, we study the effect of foregrounds on the results by considering a few percent residual foreground contamination after an assumed efficient foreground subtraction. We also compare the results to a simplified multipole-space maximum likelihood analysis, which, by ignoring the mode mixing, sets the lower limit on the obtainable error on r . We also introduce a Shannon information-based figure of merit to assess the performance of different experiments. Similar information-based criteria are used in the later sections of this work in different contexts.

In Chapters 3 and 4, we investigate the reliability of some of the observable theoretical details of the recombination history. We study perturbative fluctuations in the free electron fraction around the standard recombination scenario, using a model-independent approach. In chapter 3 the general framework is built up and various related theoretical and numerical issues are studied. The method is applied to Planck+ACTPol-like simulations, as well as to the extreme case of a full sky, noise-free survey. Chapter 4 concentrates on the application of the method to the best available CMB data to date and puts the tightest constraint, in a blind analysis, on deviations from the standard recombination history.

Chapter 5 is a summary of the main results of previous chapters and an outlook to further

extensions of the current work and future plans.

The main chapters of this work, chapters 2–4, consist of three papers, published in or submitted to the *Astrophysical Journal* (Farhang et al., 2011, 2012a,b). I was the lead author and writer in these papers, developing the required softwares, performing the analysis and presenting the results. I largely benefited from the scientific advice of my advisors, Prof. J. Richard Bond and Prof. C. Barth Netterfield, everywhere throughout this work, as well as their comments on issues as detailed as wordcrafting. Also, Prof. Bond was the main developer and writer of section 2.1 of Farhang et al. (2011), section 3.6 of Farhang et al. (2012a) and section 2.3 of Farhang et al. (2012b). He also significantly revised section 5 of Farhang et al. (2011). This work also improved a lot through lively interactions with former and current CITAzens, in particular our collaborators, Olivier Doré (in Farhang et al., 2011), Jens Chluba (in Farhang et al., 2012a,b) and Eric Switzer (in Farhang et al., 2012b).

Chapter 2

Primordial Gravitational Wave Detectability with Deep Small-Sky CMB Experiments

A version of this chapter has been submitted to the Astrophysical Journal as “Primordial Gravitational Wave Detectability with Deep Small-Sky CMB Experiments”, Farhang, M., Bond, J. R., Doré, O., Netterfield, C. B.

2.1 Chapter Overview

We use Bayesian estimation on direct T - Q - U CMB polarization maps to forecast errors on the tensor-to-scalar power ratio r , and hence on primordial gravitational waves, as a function of sky coverage f_{sky} . This map-based likelihood filters the information in the pixel-pixel space into the optimal combinations needed for r detection for cut skies, providing enhanced information over a first-step linear separation into a combination of E , B and mixed modes, and ignoring the latter. With current computational power and for typical resolutions appropriate for r detection, the large matrix inversions required are accurate and fast. Our simulations explore two classes of experiments, with differing bolometric detector numbers, sensitivities and observational strategies. One is motivated by a long duration balloon experiment like Spider, with pixel noise $\propto \sqrt{f_{\text{sky}}}$ for a specified observing period. This analysis also applies to ground-based array experiments. We find that, in the absence of systematic effects and foregrounds, an experiment with Spider-like noise concentrating on $f_{\text{sky}} \sim 0.02$ – 0.2 could place a $2\sigma_r \approx 0.014$ bound ($\sim 95\%$ CL), which rises to 0.02 with an ℓ -dependent foreground residual left over from an assumed efficient component separation. We contrast this with a Planck-like fixed instrumental noise as f_{sky} varies, which gives a Galaxy-masked ($f_{\text{sky}} = 0.75$) $2\sigma_r \approx 0.015$,

rising to ≈ 0.05 with the foreground residuals. Using as the figure of merit the (marginalized) 1D Shannon entropy of r , taken relative to the first 2003 WMAP CMB-only constraint, gives -2.7 bits from the 2012 WMAP9+ACT+SPT+LSS data, and forecasts of -6 bits from Spider (+ Planck); this compares with up to -11 bits for a CMBPol, COrE and PIXIE post-Planck satellites and -13 bits for a perfectly noiseless cosmic variance limited experiment. We thus confirm the wisdom of the current strategy for r detection of deeply probed patches covering the f_{sky} minimum-error trough with balloon and ground experiments.

2.2 Introduction

2.2.1 Inflation and Its Observables

Inflation, a period of accelerated expansion in the very early universe, is the most widely accepted scenario to solve the problems of the otherwise successful standard model of cosmology. In the simplest models the expansion is driven by an effective potential energy $V(\phi)$ of a single scalar field degree of freedom,

$$H^2 = \frac{1}{3M_{\text{P}}^2} \left(\frac{\dot{\phi}^2}{2} + V(\phi) \right)$$

$$\frac{\ddot{a}}{a} = -\frac{1}{3M_{\text{P}}^2} \left(\dot{\phi}^2 - V(\phi) \right).$$

The evolution of the scalar field is described by

$$\ddot{\phi} + 3H\dot{\phi} + V'(\phi) = 0.$$

An unavoidable consequence of inflation is the quantum generation of scalar and tensor zero-point fluctuations in the space-time metric. The former are curvature perturbations, with associated density fluctuations that can grow via gravitational instability to create the cosmic web, with its rich observational characterization. The latter are gravity waves that induce potentially observable signatures in the spatial structure of the Cosmic Microwave Background (CMB), in particular in its polarization, the focus of this paper. Whereas curl-free E -modes of polarization can be produced both by tensor and scalar perturbations, divergence-free modes of CMB polarization (B -modes) would be induced on large scales by primordial gravitational waves but not by scalar curvature fluctuations. At smaller scales, B modes are induced from primordial E modes through gravitational lensing distortions of the CMB polarization patterns, adding to the complexity of making a clean separation of the tensor-induced signal.

The primordial scalar and tensor power spectra (fluctuation variances per $\ln k$) and their ratio $r(k)$ are often approximated by power laws in the 3D comoving wavenumber k ,

$$\mathcal{P}_{\text{s}}(k) \approx A_{\text{s}}(k_{\text{sp}}) (k/k_{\text{sp}})^{n_{\text{s}}(k_{\text{sp}})-1},$$

$$\begin{aligned}
\mathcal{P}_t(k) &\approx A_t(k_{\text{tp}}) (k/k_{\text{tp}})^{n_t(k_{\text{tp}})} . \\
r(k) &\equiv \mathcal{P}_t(k)/\mathcal{P}_s(k) \approx r (k/k_{\text{tp}})^{n_t(k_{\text{tp}})-n_s(k_{\text{tp}})+1} , \\
r &\equiv r(k_{\text{tp}}) \equiv \mathcal{P}_t(k_{\text{tp}})/\mathcal{P}_s(k_{\text{tp}}) ,
\end{aligned}$$

where the normalization factors $A_s(k_{\text{sp}})$ and $A_t(k_{\text{tp}})$ are the amplitudes of the scalar and tensor power spectra at the pivots k_{sp} and k_{tp} respectively. The pivots k_{sp} and k_{tp} about which the expansions occur are usually chosen to be different for scalars and tensors to reflect where the optimal signal weights come from. The main target of many of the current and coming CMB polarization experiments is, firstly, a one-parameter uniform r . An advantage of this ratio over $\mathcal{P}_t(k_{\text{tp}})$ is that it removes a dominant near-degeneracy with the Thompson depth to Compton scattering τ . The trajectory $r(k)$ also measures the inflation acceleration history $\epsilon(a)$. Note that in $r(k)$, n_s is approximated by $n_s(k_{\text{tp}})$, i.e., at a different pivot, assuming small running of n_s with wavenumber. To the first order in the slow-roll parameter $\epsilon \equiv -d \ln H / d \ln a$, $r(k)$ can be directly related to V through the relation

$$\begin{aligned}
r(k) &\approx 16\epsilon, \quad (a \approx k/H) \\
V &\approx \frac{3\pi^2}{2} M_{\text{P}}^4 r \mathcal{P}_s \sim (10^{16} \text{GeV})^4 r / 0.008.
\end{aligned}$$

We have used $10^{10} A_s \approx 24.4^1$. Here $M_{\text{P}} = 1/\sqrt{8\pi G}$ is the reduced Planck mass, with c and \hbar set to unity. The relation $k \approx Ha$, of resolution k^{-1} to the dynamics encoded in the expansion and Hubble parameters, a and H , is only approximate of course, but very useful (e.g., Bond, 1996a).

There is no consensus on what pure theory will tell us about the best value for r , or even its likely range. However, if r drops below the benchmark $r \sim 0.01$ set by the GUT scale $\sim 10^{16}$ GeV, the consequences will be profound (Baumann et al., 2009). Experiments with Spider-like sensitivity could probe such a limit. In this paper, we explore the very small $r_{\text{fid}} < 0.01$ regime. To show what happens when there are detections, we often use $r_{\text{fid}} = 0.12$ as a fiducial high- r case for tests, a value which lies just below the 0.13 coming from the simplest $V = m^2 \phi^2 / 2$ chaotic inflation model.

We would of course like to learn as much as we can about the full $r(k)$, hence $\epsilon(a)$, from CMB data. In addition to the deviations of the slopes from scale invariance ($n_t = 0$ and $n_s - 1 = 0$), the slopes are expected to “run with k ” just as the power does, although they may be approximately constant over the observable CMB range. The first order variations in $\ln k$ define scalar and tensor “running” parameters, the first terms in polynomial expansions in higher order “running of running” parameters. In this paper $n_s(k)$ is not our target, nor are

¹http://lambda.gsfc.nasa.gov/product/map/dr4/params/lcdm_sz_lens_wmap7_bao_h0.cfm

high multipole CMB experiments which are necessary to get the long baseline needed to show whether n_s runs or not.

A consequence of the fall-off of the tensor-induced CMB signal beyond $\ell \sim 150$ is that only limited information can be obtained on $n_t(k)$ — enough to allow a number of broad bands for $r(k)$, but not enough for $n_t(k_{\text{tp}})$, let alone $n_t(k)$, to be determined with sufficient accuracy to test well the inflation consistency relation for gravity waves. In the limited 2-parameter tensor parameter space of r and uniform n_t , this consistency condition to the first order of the slow roll parameters is (e.g., Bond, 1996a)

$$n_t \approx -\frac{r}{8}, \quad (2.1)$$

so a convincing test would require an order of magnitude better determination of n_t than r .

Another complication in relating the experiments to inflation theory is that there is still observational room for subdominant scalar isocurvature perturbations in addition to the dominant curvature ones when multiple fields are dynamically important during or immediately after inflation; such fields are widely invoked for catalyzing the production of entropy at the end of inflation. Isocurvature perturbations with a nearly scale invariant primordial spectrum have significantly enhanced low- ℓ CMB power because of the isocurvature effect (Bond, 1996a), and that region, overlapping with the gravity wave-induced CMB power, is where the constraint on the overall isocurvature amplitude comes from (Sievers et al., 2007b; Larson et al., 2011).

2.2.2 Observations

All CMB polarization experiments are limited in sky coverage by instrumental or Galactic foreground constraints. Thus, even though the B -modes provide a unique r -signature and are orthogonal to the E -modes over the full sky, realistically mode-mixing must always be dealt with, even though it may be larger for smaller f_{sky} . Assessing the trade offs between shallow large-sky and deep small-sky observational strategies is the target of our investigation. Going for deep and small has the advantage that one can select the most foreground-free patches to target to decrease the high level of foreground subtraction. As well, the long waves which dominate foregrounds are naturally filtered. Ground-based or balloon-borne experiments using the deep and small-sky strategy include BICEP (Chiang et al., 2010) and BICEP2², QUIET³ (QUIET Collaboration et al., 2010), PolarBear⁴ (The Polarbear Collaboration et al., 2010), EBEX⁵ (Reichborn-Kjennerud et al., 2010), Spider⁶ (Fraisse et al., 2011), KECK (Sheehy et al.,

²<http://bicep.caltech.edu/public/>

³<http://quiet.uchicago.edu/>

⁴<http://bolo.berkeley.edu/polarbear/>

⁵<http://groups.physics.umn.edu/cosmology/ebex/>

⁶http://www.astro.caltech.edu/lgg/spider/spider_front.htm

2010), ABS⁷ (Essinger-Hileman et al., 2010), PIPER (Chuss et al., 2010). Planck (and WMAP) are (relatively) shallow and large-sky. Proposed next-generation satellite experiments such as CORE (The CORE Collaboration, 2011), PIXIE (Kogut et al., 2011) and LiteBIRD⁸ are deep and large-sky.

The current 2σ r -constraints come from the CMB-only data from ACT+SPT+WMAP9 (< 0.17) and with LSS added (< 0.12). Figure 2.1 gives a succinct summary of the current status of r measurements and what can be achieved with the Spider-like sensitivities we use as an example throughout the text, compared to a case of Spider with more realistic specifications as envisaged in Fraisse et al. (2011) (labeled as “Spider” in the plot), and for an even more ambitious campaign of subsequent flights of the Spider instrument, as proposed for SCIP. It also shows a CMBPol case. The various theoretical possibilities shown for r are swept through by these achievable (foreground-less) r -likelihood curves. The main purpose of this paper is to explain how these forecasted likelihoods are obtained.

In this paper, we first review the general Bayesian framework for determining parameters to introduce the notations we use. We cast the quest for r into an information-theoretic language in which the forecasted outcomes of different experiments can be contrasted by considering the differences in their reduced *a posteriori* Shannon entropies for r , $S_{\text{If}}(r|\text{expt})$. We discuss the two basic approaches for constraining cosmological observables, such as those associated with inflation, and the relation of these to E - B mixing: (1) the ℓ -space approach in which CMB maps are first compressed onto power spectrum parameters for TT - TE - EE and BB , which are then compressed onto cosmic parameters; and (2) direct parameter extraction of r from map likelihoods. Our primary target is r and not the B -mode spectrum, hence the optimal one-step estimation from maps is preferred, provided it is computationally feasible – which it is for Spider-like experiments. The leakage between the E and B modes and its impact on r is quantified in § 2.4. In § 4.4 we present details of the method we use to bypass explicit E - B demixing and apply it to simulated data for realistic instrumental and foreground-residual noise levels for Spider-like and Planck-like experiments as f_{sky} varies. We end with our conclusions from this study.

2.3 Bayesian CMB Analysis of Bandpowers and Cosmic Parameters

As has become conventional in CMB analysis, the framework envisaged to compress the information from Spider-like raw time-ordered data to constraints on cosmic parameters, in particular

⁷<http://www.princeton.edu/physics/research/cosmology-experiment/abs-experiment/>

⁸<http://cmbpol.kek.jp/litebird/index.html>

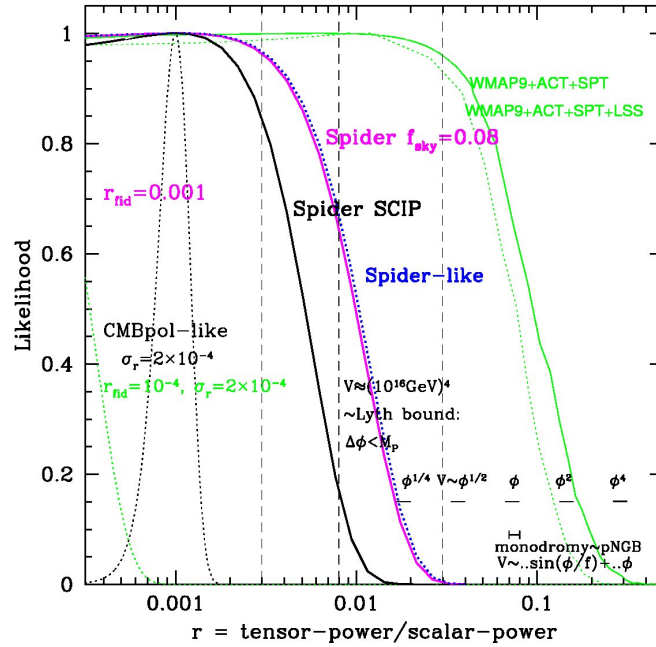


Figure 2.1: Forecasted r -likelihood values for the Spider-like specifications used in the paper observing 8% of the sky. The one labeled as Spider corresponds to the actual, more recent Spider proposal with two flights described in Fraisse et al. (2011) (see the footnotes of table 2.5.1). The SCIP envisages three subsequent flights of the Spider payload. This is contrasted with the current constraints from the ACT+SPT+WMAP9 data, and also combined with the measurements of LSS (Hinshaw et al., 2012). The marginalized 1D likelihood curves are based on the publicly available chains http://lambda.gsfc.nasa.gov/product/act/act_chainsv2_get.cfm binned into 50 bins, and Gaussian-fitted to plot the very small r region where not enough points were available. These are compared with a forecast for an idealized CMBPol all-sky experiment like PIXIE or CoRE with a $\sigma_r \sim 0.0002$ error. A model input of $r_{\text{fid}} = 0.001$ was assumed, which would give a solid CMBPol detection for it. A $r_{\text{fid}} = 0.0001$ case is also shown. Foregrounds and systematic errors were ignored in these plots; modifications resulting from errors in foreground subtractions are shown in other plots in the paper. A number of theoretical predictions are also shown, for power law inflation potentials with slope ranging from 0.25 up to 4. The width covers the range of 60 to 50 e-folds for inflation. The linear potential is contrasted with the similar range for a string-inspired mixed model called monodromy (McAllister et al., 2010) with a linear potential added to a sinusoidal pseudo-Nambu-Goldstone potential. A few target lines are also shown, one at 0.03 which many theories of the 80s and 90s were above, one at 0.008 corresponding to an inflation energy scale about the Grand Unification scale, which is near the Lyth bound (Lyth, 1997) as indicated. Supergravity-inspired theories can get values anywhere in the range from ~ 0.003 to ~ 0.3 (Kallosh & Linde, 2010). Thus small-patch experiments with Spider-like specs could explore much of the r -terrain of theoretical relevance.

our target r , is one of a long Bayesian chain of conditional probabilities (Bond, 1996a; Bond & Crittenden, 2001). It includes reducing noisy data to maps, maps to band-powers and then to cosmic parameters, or directly maps to parameters. Starting from pixel maps, we review the framework with polarization to introduce our notation. We also remark on how the associated conditional Shannon entropies decrease as the maps are reduced to a precious set of parameter bits.

Pixel Maps and E - B Maps

The map data vector Δ for CMB experiments is composed of a number of signals s as well as the map noise n . The noise encompasses true instrumental noise, experimental systematic effects, and possibly, may draw terms from the signal side that are unwanted residuals on the sky, e.g., from foreground subtraction uncertainty. Each signal has a frequency dependence and polarization components, labelled by 4 Stokes parameters $x = T, Q, U, V$ referred to a fixed polarization sky reference frame in real space. The map components for each x , each pixel $p = 1, \dots, N_{\text{pix}}$ and each frequency channel c are expressible as

$$\begin{aligned}\Delta_{cpx} &= \sum_J s_{Jcpx} + n_{cpx}, \quad x \in \{T, Q, U, V\}, \\ s_{Jcpx} &= \sum_{\ell m} \int_{\nu} \mathcal{F}_{cpx, J\nu\ell m} a_{J\nu\ell m},\end{aligned}\tag{2.2}$$

where the spherical harmonic signal amplitude for signal J is $a_{J\nu\ell m}$. The transformation from this natural multipole space for the signals to the pixel map space is encoded in $\mathcal{F}_{cpx, J\nu\ell m}$, which includes beam information, the frequency response function for the channels, and the mask, whether a sharp cookie cutter or a tapered one.

For Thompson scattering anisotropies, the V Stokes parameter associated with circular polarization vanishes, as it also does for most Galactic foregrounds contaminating the primary CMB signal, so we now drop it from our consideration. It would of course be of interest to show experimentally that there is indeed no circular polarization in the CMB data.

The $a_{J\nu\ell m}$ are the coefficients in the standard expansion of the CMB temperature and polarization fields in orthogonal mode functions. The mode functions are the spherical harmonics, spin-0 for T and spin-2 for polarization:

$$\begin{aligned}T_{J\nu}(\theta, \phi) &= \sum_{\ell=2}^{\infty} \sum_{m=-\ell}^{\ell} a_{J\nu T\ell m} Y_{\ell m}(\theta, \phi), \\ (Q \pm iU)_{J\nu}(\theta, \phi) &= \sum_{\ell=2}^{\infty} \sum_{m=-\ell}^{\ell} \pm 2a_{J\nu\ell m} [\pm 2Y_{\ell m}(\theta, \phi)].\end{aligned}$$

Further linear combinations of the spin-2 expansion coefficients define the E and B modes:

$$a_{J\nu E\ell m} = -\frac{1}{2}(2a_{J\nu\ell m} + -2a_{J\nu\ell m}),$$

$$a_{J\nu B\ell m} = -\frac{1}{2i}(2a_{J\nu\ell m} - 2a_{J\nu\ell m}).$$

The separation of CMB polarization into E and B -modes is useful because scalar perturbations only result in the E mode whereas tensor perturbations generate both (Kamionkowski et al. (1997), Zaldarriaga & Seljak (1997)). Nonlinear transport effects associated with the weak lensing of primary CMB fluctuations turn some scalar E-mode into scalar B-mode, mostly at higher ℓ s than the tensor component gives, so separation for r detection can be done. Note that this lensing source has non-Gaussian features which means the power spectra are not enough to characterize its signal.

Maps to Parameters with Map-based Likelihoods

Following the familiar Bayesian analysis techniques applied to CMB data (e.g., Bond, 1996a), we wish to construct the *a posteriori* probability distribution $P(\mathbf{q}|\Delta, \mathcal{T})$ of parameters $\mathbf{q} = (q_1, \dots, q_n)$, an update from the *a priori* probability $P(\mathbf{q}|\mathcal{T})$ on the theory space \mathcal{T} of the parameters that is driven by the likelihood of the data Δ given \mathbf{q} , $\mathcal{L}_\Delta(\mathbf{q}) \equiv P(\Delta|\mathbf{q}, \mathcal{T})$,

$$P(\mathbf{q}|\Delta, \mathcal{T}) = P(\Delta|\mathbf{q}, \mathcal{T})P(\mathbf{q}|\mathcal{T})/P(\Delta|\mathcal{T}).$$

The prior may include theoretical prejudice, information derived from other data, and, at the very least, the specific measure adopted for the parameters. The *evidence*, $P(\Delta|\mathcal{T})$, a single normalization, is also needed to ensure the posterior integrates to unity. Its determination is generally computationally intense if one integrates over all parameter space, but it may only be needed at late stages of reduction, e.g., over 2D and 1D reduced parameter spaces.

If the noise is Gaussian with a covariance matrix \mathbf{C}_n and the signals are also Gaussian with their own covariance \mathbf{C}_s about a zero mean, then

$$\ln \mathcal{L}_\Delta(\mathbf{q}) = -\frac{1}{2}\Delta^T \mathbf{C}_t^{-1} \Delta - \frac{1}{2} \ln \det \mathbf{C}_t - \frac{1}{2} N_{\text{pix}} \ln(2\pi), \quad (2.3)$$

where $\mathbf{C}_t = \mathbf{C}_n + \sum_{JJ'} \mathbf{C}_{s, JJ'}$, with

$$\begin{aligned} \mathbf{C}_{n, cxp, c'x'p'} &= \langle n_{cxp} n_{c'x'p'} \rangle \\ \mathbf{C}_{s, Jcxp, J'c'x'p'} &= \langle s_{Jcxp} s_{J'c'x'p'} \rangle. \end{aligned}$$

We have assumed no correlation between signal and noise.

The extra ingredient needed to determine the posterior $P(\mathbf{q}|\Delta, \mathcal{T})$ is the prior defining the measure on \mathbf{q} , $\mathcal{L}_{\text{prior}}(\mathbf{q}) \equiv \mathcal{P}(\mathbf{q}|\mathcal{T})$. The prior is most often taken to be uniform within some parameter region. Another simple possibility is a Gaussian prior with correlation matrix F_{prior}^{-1} about the mean $\bar{\mathbf{q}}$. In this work we usually assume the uniform prior, though sometimes for

small coverage experiments we shall use a Gaussian prior reflecting the WMAP determination of parameters.

In this paper we usually determine the full likelihood $\ln \mathcal{L}_t \equiv \ln(\mathcal{L}_\Delta + \mathcal{L}_{\text{prior}})$ on a suitably chosen grid in the parameter space. We can then search for the maximum likelihood \mathbf{q}_m and, with suitable marginalizations over other variables, get 2D significance contours and 1D Bayesian errors. It is customary to refer to methods which directly search for the maximum likelihood point as (map- or pixel-based) maximum likelihood estimators (MLE).

Bandpower estimation

For statistically isotropic signals there are generally six cross-spectra among the coefficients,

$$\begin{aligned} \langle a_{x\ell m} a_{x'\ell' m'}^* \rangle &= C_{X\ell} \delta_{\ell\ell'} \delta_{mm'}, \quad X = xx', \\ \text{for } x \in \{T, E, B\}, \quad X &\in \{TT, EE, BB, TE, TB, EB\}. \end{aligned}$$

Typically the EB and TB power vanish (theoretically anyway) and only four power spectra are needed to characterize the CMB temperature and polarization fields. However, EB and TB may be kept for systematics monitoring. For statistically homogeneous and isotropic 3D Gaussian initial conditions, the primary CMB T, Q, U are isotropic 2D Gaussian fields whose probability distribution depends only upon the power spectra $C_{X\ell}$, or, equivalently the X -power per $\ln(\ell + 1/2)$,

$$C_{X\ell} \equiv \frac{\ell(\ell + 1)}{2\pi} C_{X\ell}.$$

The goal of bandpower estimation is to radically-compress the map information onto ℓ -bandpower amplitudes $q_{X\beta}$, with templates of the form $C_{X\beta, X\ell}$. With sufficiently fine ℓ -space banding, this stage of compression can be relatively lossless, allowing the cosmic parameters to be derived accurately. The inter-band shape of these templates may be crafted to look like theoretically expected shapes, or could just be flat, which imposes no prior prejudice. Both approaches have been effectively used.

With cut-sky maps, bands are coupled even though they would not be for full sky observations with statistically homogeneous noise. The optimal method for estimating power spectra in the general case is the computationally expensive brute-force maximum likelihood analysis (e.g., Bond et al., 1998). This method iteratively corrects a quadratic expression for deviations of the various bandpowers q_β from their initial values until the maximum likelihood q_m^β is reached. The weight matrix $\mathbf{C}_t^{-1}(\mathbf{q})$ is adjusted at each step, until it settles into $\mathbf{C}_t^{-1}(\mathbf{q}_m)$. The weight enters in two ways, one is quadratically in the likelihood-curvature matrix (approximately the Fisher matrix) and the other is in the force that drives the relaxation of the parameters to q_m^β .

These map-based methods for bandpower estimation were used by Boomerang (de Bernardis et al., 2000b; Ruhl et al., 2003) and in all CBI papers. If bandpowers are linear in the cosmic parameter of interest, like r , then the parameter can be viewed as a single-template big-band bandpower. Even with the fully nonlinear $C_{X\ell}(q)$, the amplitudes δq can be iteratively solved for using linear derivative templates, and, with convergence, the result is the same as a full nonlinear treatment gives.

Pseudo- $C_{X\ell}$ cf. Map-based Methods

Several fast sub-optimal approximate methods have been developed to make the bandpower computation less computationally intense than in the map-based method, e.g., pseudo- C_ℓ estimators (Hansen & Górski, 2003; Chon et al., 2004), SPICE (Szapudi et al., 2001), MASTER (Hivon et al., 2002) and Xfaster (Contaldi et al., 2010; Rocha et al., 2010, 2011). Pseudo- C_ℓ 's are constructed by direct spherical harmonic transform of the cut-sky maps, or more generally, taper-weighted CMB maps. The all-sky bandpower centred on a specific ℓ_β , $q_{X\beta}$, is then related to the desired ℓ_β -band by an appropriate filtering which draws the pseudo- $C_{X\ell}$'s from a wide swath of ℓ 's determined by a mask-defined coupling matrix. In spite of this ℓ -space mixing, extensive testing has shown these methods to be accurate for temperature anisotropies for large pixel numbers where the matrix inversions of the iterated quadratic approach are prohibitively expensive computationally. They have also been applied effectively to polarization datasets such as Boomerang (Montroy et al., 2006; Piacentini et al., 2006).

The pseudo- $C_{X\ell}$'s for $X = EE, BB$ suffer from E - B mixing in addition to the ℓ -space mixing: the estimated $C_{BB\ell}$ receives contributions from both E and B -modes. The contamination coming from the E -mode can be removed from $C_{BB\ell}$ in the mean by having the estimators undergo a de-biasing step. However, there is still an extra contribution to the variance of estimators which is due to the dominance of the relatively large E signal mixed into the B measurement. This can limit the primordial gravitational wave detection to $r \approx 0.05$ for deep small sky surveys (covering about 1% of the sky) as shown by Challinor & Chon (2005). Lewis et al. (2002) show how to construct window functions that cleanly separate the E and B modes in harmonic space for azimuthally symmetric sky observations at the cost of some information loss due to the boundary of the patch. In another treatment of the E - B mixing problem, Bunn et al. (2003) show that the polarization maps can be optimally decomposed into three orthogonal components: pure E , pure B , and ambiguous modes. The ambiguous modes receive a non-restorable contribution from both E and B signals, and are dominated by E signal, thus should be removed in B -mode analysis. Based on this decomposition, a near-optimal *pure* pseudo- C_ℓ estimator was proposed (Smith, 2006) and developed (Smith & Zaldarriaga, 2007; Grain et al., 2009) which ensures no E - B mixing. Recently Bunn (2011) has given a more

efficient recipe for decomposing polarization data into E, B and ambiguous maps, although still along the lines of Bunn et al. (2003).

It is clear that if the full map-likelihood analysis can be done, then it should be done, since relevant information is not being thrown away. There are two drawbacks to this map-based approach. The first is that \mathbf{C}_t should saturate all contributions to signal and noise since we are in quest of a small, essentially perturbative, component associated with r whose values can be biased by the missing components. This could be challenging in the presence of complex filtering resulting from time-ordered data processing. Also the computational cost of the required large matrix manipulations is high compared to the suboptimal methods. The matrix size depends upon the fraction of sky covered and the resolution. For example, for an experiment covering 25% of the sky analyzed at a Healpix resolution of $N_{\text{side}} = 64$, the sizes are $35K \times 35K$ and we find the likelihood calculation takes about 5 minutes on a node with 16 Dual-Core Power 6 CPU's at 4.7 GHz (and theoretically capable of doing 600 GFLOPS/node). In practice, our matrices are usually smaller than this since the quest for r requires a relatively low resolution analysis. Also only a few other parameters that are correlated with r need to be carried along (see § 2.5.3). To include many more parameters standard Bayesian sampling algorithms such as MCMC and adaptive importance sampling (Wraith et al., 2009) can be used. If we need to cover small angular scales as well as large, the matrices become prohibitively large, and hybrid methods, with a map-based likelihood for large scales joined to an ℓ -space-based likelihood for small scales, are needed.

2.3.1 The Downward Flow of Shannon Entropy from Maps to Theory Subspaces

The Shannon entropy S_f of the final (posterior) probability distribution is an average of the log of the local phase space volume $\langle \ln p_f^{-1} \rangle_f$ over the posterior probability distribution p_f , and is considered to provide an estimate of the total information content in the final ensemble (see, e.g., MacKay, 2003),

$$S_f(\mathcal{T}|\mathcal{D}) = \langle \ln P(\mathbf{q}|\mathcal{D}, \mathcal{T})^{-1} \rangle_f = - \int d^N \mathbf{q} p_f \ln p_f.$$

where \mathcal{D} represents data (here CMB maps Δ). The initial entropy is similarly averaged over the initial ensemble $S_i \equiv \langle \ln P(\mathbf{q}|\mathcal{T})^{-1} \rangle_i$. For a uniform prior over a volume $V_{\mathbf{q},i}$ in \mathbf{q} -space, it is $S_i = \ln V_{\mathbf{q},i}$. The final entropy can be thought of as having a contribution from (the log of) an *effective* phase space volume, reduced relative to the initial one because of the measurement, plus a term related to the average χ^2 associated with the mean-squared deviations of \mathbf{q} . This term is usually just the number of degrees of freedom unless the model is a very poor representation of the information content of the data.

It should not seem curious to say that the information entropy decreases as a result of measurements, but it may seem curious to word it as: the average information content decreases. That is because the fully random initial state has more information, in that the variables can take on a wider range of values. We think the reduced post-experiment information content is of higher quality. What constitutes Quality in information is subjective of course.

The common figure of merit for error in parameter (here r) measurement is $2\sigma_r$. That is also what we primarily quote in this paper, determined as explained in § 2.3.2. However, a better figure of merit than $2\sigma_r$ is the change in 1D Shannon entropy which tells us the average amount by which the log of the allowed volume in the r parameter space shrinks in response to varying the experimental setups. It is 1D because we marginalize over all other $N - 1$ parameters, the cosmic ones of interest and any nuisance parameters deemed necessary for the analysis, such as those characterizing uncertainties in calibration, beams, bolometer T - Q - U leakage, and foreground uncertainties.

The 1D Shannon information entropy, $S_{1f}(r) = \langle \mathcal{S}_{1f}(r) \rangle_f + \ln P(\Delta|\mathcal{T})$, where the information action $\mathcal{S}_{1f}(r)_f = -\ln P(\Delta|r, \mathcal{T}) - \ln(r|\mathcal{T})$, is best calculated by numerical integration over the r -grid. The result is very simple if we truncate the ensemble-averaged expansion of $\mathcal{S}_{1f}(r)$ at quadratic order

$$S_{1f}(r) \approx \frac{1}{2} + \frac{1}{2} \ln(2\pi) + \ln(\sigma_r) = \frac{1}{2} + \ln V_r,$$

where V_r (defined by the equation) is the compressed phase space volume for r after the measurements.

Although we have used the natural log to make the entropy expressions familiar for physicists, in information theory one often uses the binary logarithm, $lb \equiv \log_2$. With natural logs the information is in *nats*, but with lb it is in *bits*. When expressing information differences in § 2.6 we translate to bits. Since a full bit represents a factor of 2 improvement in the error bar, $\Delta S_{1f}(r)$ may only be a fraction of a bit, trivial perhaps, but subtle too, given the mammoth information compression from raw data to this one targeted parameter degree of freedom.

2.3.2 2σ Calculation

We define σ_{95} through

$$\int_{\max(0, r_b - \sigma_{95})}^{r_b + \sigma_{95}} \mathcal{L}(r) dr = 0.954 \int_0^\infty \mathcal{L}(r) dr \quad (2.4)$$

where r_b is the best-fit value of r . The σ_{95} -limit is determined by numerically integrating the Gaussian-fitted 1D likelihood curve.

In most cases considered in this paper the likelihood curves turn out to be well approximated by Gaussians. Therefore, when there is a few σ detection (e.g. for $r = 0.12$) or when $r \sim 0$, to

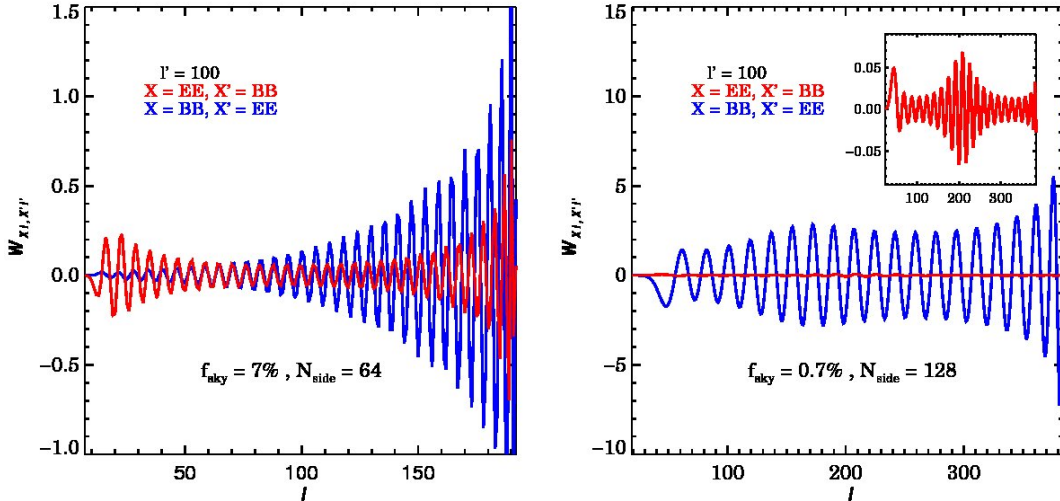


Figure 2.2: The filters $W_{X\ell, X'\ell'}$, $X, X' \in \{EE, BB\}$, show how the mode $\mathcal{C}_{X\ell}$ linearly responds to a small change in the mode $\mathcal{C}_{X'\ell'}$. The leakage responses shown here are for an $\ell' = 100$ stimulus, for a Spider-like experiment with $f_{\text{sky}} = 7\%$ at $N_{\text{side}} = 64$ (left) and $f_{\text{sky}} = 0.7\%$ at $N_{\text{side}} = 128$ (right). Note the different scales for the y -axis. The corner box of the right panel magnifies $W_{EE\ell, BB100}$ for $f_{\text{sky}} = 0.7\%$, whose details are not clear in the main plot.

a very good approximation we have $\sigma_{95} = 2\sigma$ where σ is the width of the Gaussian fit. Thus, throughout this paper we will use the common notation of 2σ which represents σ_{95} and has been calculated through eq. 2.4. The only exception to this way of determining 2σ is when it is being directly given by the inverse of the Fisher matrix, where σ represents the width of the likelihood function, under the assumption of its Gaussianity.

2.4 Constrained Correlations and Linear Response In Pixel-Pair and Parameter Space

Here we quantify the sensitivity of cosmic parameters to variations in different $\mathcal{C}_{X\ell}$ spectra. We find general forms for filters or “susceptibilities” which relate the linear response of a target variable to the stimulus of a driver variable (with the $\mathcal{C}_{X\ell}$ as a special case) through the CMB data. These filters can also be referred to as window functions to be consistent with the language used for bandpowers, in which the driver is the $\mathcal{C}_{X\ell}$ and the response is the bandpower. The window function attached to each bandpower “gathers in ℓ -space” from a given $\mathcal{C}_{X\ell}$ the bandpower. There is a long history of making such windows publicly available. They were used in likelihood evaluations in the 2000 release of the Boomerang “B98” results (Lange et al.,

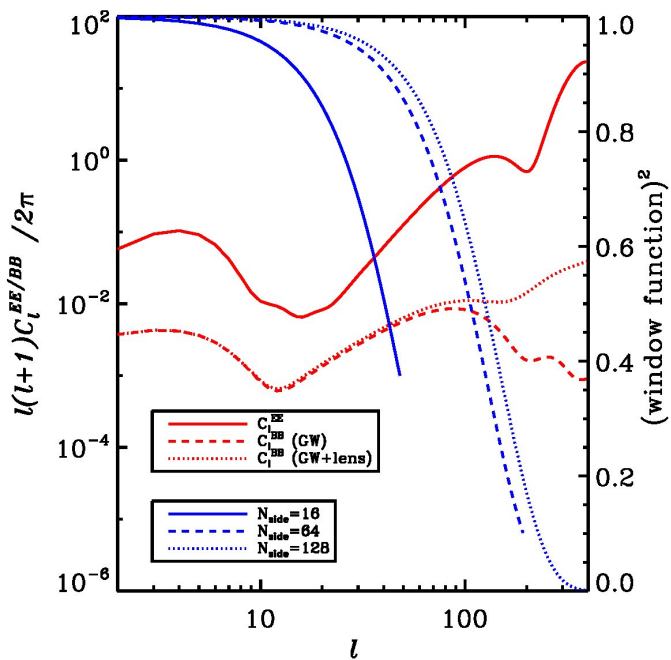


Figure 2.3: Beam and pixel window functions for different resolutions are compared to the polarization power spectra for the best fit WMAP7-only parameters for the Λ CDM + lensing + SZ + tensor model, with the addition of a tensor component of strength $r_{\text{fid}} = 0.12$. B -mode (GW) shows just the gravity wave-induced contribution and B -mode (GW+lens) includes the lensing contribution as well.

2001). Tegmark & de Oliveira-Costa (2001) used similar window functions in a quest for the best quadratic estimator.

In the following we use \mathbf{q}_S for the stimuli (or driver parameters) and \mathbf{q}_R for the response parameters. Assume that Δ is a realization of the CMB sky for $\mathbf{q}_R = \mathbf{q}_R^*$ and $\mathbf{q}_S = \mathbf{q}_S^*$. In the attempt to estimate the maximum likelihood parameters from Δ , if \mathbf{q}_S is displaced from its fiducial value by $\delta\mathbf{q}_S$, in response \mathbf{q}_R needs to be readjusted to achieve the (constrained) maximum likelihood. Here we search for this displacement $\delta\mathbf{q}_R$. We Taylor-expand the logarithm of the likelihood function (eq. 2.3) to the second order of $\delta\mathbf{q}_R$ around $\mathbf{q}_R = \mathbf{q}_R^*$, with the constraint that \mathbf{q}_S is fixed at $\mathbf{q}_S^* + \delta\mathbf{q}_S$. We solve for the $\delta\mathbf{q}_R$ that maximizes the likelihood (Bond et al., 1998)

$$\delta q_{R\alpha} = \frac{1}{2} \sum_{\beta \in R} [F^{-1}]_{\alpha\beta} \text{Tr} [\mathbf{C}_t^{-1} \mathbf{C}_{s,\beta} \mathbf{C}_t^{-1} (\langle \Delta \Delta^T \rangle - \mathbf{C}_t)]$$

where $\mathbf{C}_{s,\beta} = \partial \mathbf{C}_s / \partial q_\beta$ and the sum (over $\beta \in R$) only runs over the response parameters. We have approximated the curvature term by its ensemble average, i.e., by the Fisher matrix \mathbf{F} ,

$$F_{\alpha\beta} \equiv -\frac{1}{2} \left\langle \frac{\partial^2 \ln P(\mathbf{q}|\Delta, \mathcal{T})}{\partial q_\alpha \partial q_\beta} \right\rangle = \frac{1}{2} \text{Tr} (\mathbf{C}_t^{-1} \mathbf{C}_{s,\alpha} \mathbf{C}_t^{-1} \mathbf{C}_{s,\beta}), \quad (2.5)$$

assuming uniform prior distributions for the parameters. We have also replaced $\Delta \Delta^T$ by its ensemble average $\langle \Delta \Delta^T \rangle$ to remove the fluctuations in the response parameters due to cosmic variance. Inserting the first order approximation $\langle \Delta \Delta^T \rangle - \mathbf{C}_t = -\sum_{\mu \in S} \mathbf{C}_{s,\mu} \delta q_{S\mu}$ (with the sum $\mu \in S$ only over stimulus parameters) yields

$$\delta q_{R\alpha} = -\sum_{\mu} \delta q_{S\mu} \sum_{\beta} [F^{-1}]_{\alpha\beta} F_{\beta\mu}.$$

Note that we have reserved α and β for the response parameters and μ for the stimuli. One can equivalently write

$$\frac{\delta q_{R\alpha}}{q_{R\alpha}} = -\sum_{\mu \in S} W_{\alpha\mu} \frac{\delta q_{S\mu}}{q_{S\mu}}, \quad W_{\alpha\mu} = +\frac{q_{S\mu}}{q_{R\alpha}} \sum_{\beta \in R} [F^{-1}]_{\alpha\beta} F_{\beta\mu}.$$

One can consider the $\mathbf{q}_{R,S}$ to represent extended parameters of $\mathcal{C}_{X\ell}$'s as well. A case of special interest for us is when \mathbf{q}_S is the $\mathcal{C}_{X\ell}$ while \mathbf{q}_R is r or another subset of $\mathcal{C}_{X\ell}$'s. The explicit form of the filter for $\mathbf{q}_S = \mathcal{C}_{X\ell}$ would be

$$W_{\alpha, X\ell} = +\frac{\mathcal{C}_{X\ell}}{q_\alpha} \sum_{\beta} [F^{-1}]_{\alpha\beta} F_{\beta, X\ell}. \quad (2.6)$$

2.4.1 Linear Response of $C_{BB\ell}$ to $C_{EE\ell}$: Power Leakage

We can quantify the leakage of CMB power among different $C_{X\ell}$'s, which are already the stimulating drivers in eq. 2.6, by taking them to be the response variables as well,

$$W_{X\ell, X'\ell'} = \frac{C_{X'\ell'}}{C_{X\ell}} \sum_{X'', \ell''} [F^{-1}]_{X\ell, X''\ell''} F_{X''\ell'', X'\ell'}.$$

Here the $X\ell$ and $X''\ell''$ correspond to the parameters which are being measured, while the $X'\ell'$ only refer to constrained variables. The case of specific interest in this work is $X = BB, X' = EE$, that is the leakage of the larger E -mode into B -mode. We also consider $X = EE, X' = BB$ for comparison. One could investigate the $X = X'$ filters, which characterize the mask coupling, but we leave them out as they are not of direct relevance to our power leakage study.

We have verified numerically that for a full sky observation using the map-based methods gives uncorrelated modes $W_{EE\ell, BB\ell'} = W_{BB\ell, EE\ell'} = 0$. Figure 2.2 shows the cross filters for an $\ell = 100$ stimulus, i.e., $W_{EE\ell, BB100}$ and $W_{BB\ell, EE100}$, for $f_{\text{sky}} = 0.07$ (at $N_{\text{side}} = 64$, pixel size $\approx 56'$) and $f_{\text{sky}} = 0.007$ (at $N_{\text{side}} = 128$, pixel size $\approx 28'$). The observed patches are in the form of spherical caps. (Figure 2.3 shows the associated beam and pixel window functions along with the polarization power spectra.) We see that the mode correlation increases with decreasing f_{sky} for a fixed observation time. The high- ℓ rise in the filters is due to finite pixel sizes, hence is more pronounced at lower resolution. We also see that variations in the E -mode at most scales have a relatively larger impact on the small B signal compared to the impact of the B -mode on the E signal. The width of the oscillation $\Delta\ell \sim \theta_{\text{patch}}^{-1}$ is related to the cap size, narrowing as f_{sky} goes up. The leakage is larger for smaller r , hence must be well characterized for highly sensitive B -mode experiments.

2.4.2 Linear Response of r to $C_{BB\ell}$ and $C_{EE\ell}$

We now use these filters to quantify the linear response of r to uncertainty in the $C_{X\ell}$ through the following filter

$$W_{r, X\ell} = \frac{F_{r, X\ell} C_{X\ell}}{F_{rr} r}.$$

The filter for a Spider-like experiment with a fiducial $r = 0.12$ is shown in Figure 2.4, as f_{sky} varies (as does the pixel size). The red, purple, blue and green curves correspond to $f_{\text{sky}} = 0.75, 0.25, 0.07$ and 0.007 , calculated at $N_{\text{side}} = 16, N_{\text{side}} = 32, N_{\text{side}} = 64$ and $N_{\text{side}} = 128$ respectively. As expected, the figures show that the measured r is more sensitive to BB than to EE on most scales.

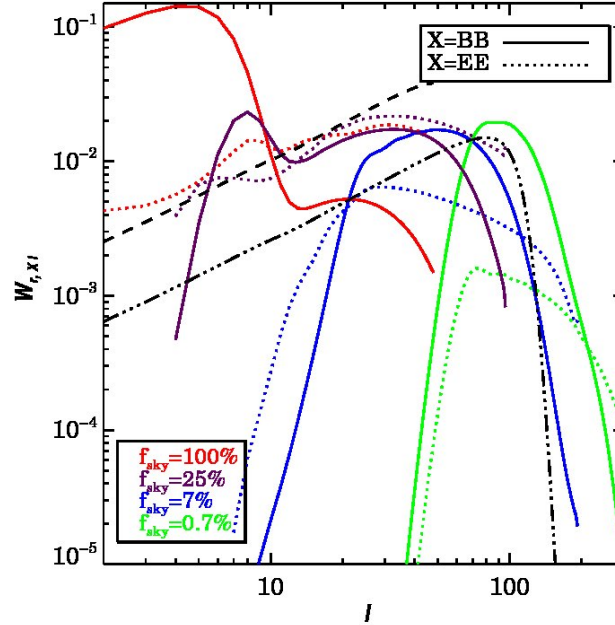


Figure 2.4: Window functions $W_{r,X\ell}$ for $X \in \{EE, BB\}$ for different sky cuts show that, as expected, all-sky experiments are nicely sensitive to the reionization BB bump, but smaller sky experiments are not, although they pick up well the $\ell \sim 50 - 100$ region. We have used $r = 0.12$ for the fiducial model. The rapid declines to high ℓ are more due to the onset of experimental noise than to the onset of the lensing-induced B “noise”. Residual foreground noise has not been included in these plots. Note that even a coverage with f_{sky} only 0.007 can punch out a robust detection from 50 to 150 in ℓ . The coverage with $f_{\text{sky}} = 0.07$, although loses out a bit (relatively) at 150, its detection would come from a wider stretch in $\ln \ell$, out to $\ell \sim 20$ before falling off. Only at $f_{\text{sky}} > 0.25$ does one begin to pick up the reionization bump. The curious drop in the all-sky $N_{\text{side}} = 16$ red line at the top is due to the Spider-like noise for higher ℓ being heavily enhanced because all of the sky is covered in the same amount of observing time. To illustrate the role of this, a CMBPol-like experiment with C_N decreased by ~ 1000 is plotted, with $N_{\text{side}} = 16$ (dashed straight line) and $N_{\text{side}} = 64$ (triple-dot-dashed line). The reason all three are offset from one another is because the normalizing σ_r^2 depends upon the amount the filter captures of the total r signal.

2.5 Simulation Methods and Computational Results

In this section we use the map-based T - Q - U likelihood procedure of § 2.3 to compute the posterior $P(\mathbf{q}|f_{\text{sky}}, \Delta, \mathcal{T})$ in parameter subspaces and, by marginalization, the 1D posterior $P(r|f_{\text{sky}}, \Delta, \mathcal{T})$ as a function of f_{sky} . We also make identical calculations to the T - Q - U pixel-based ones in ℓ -space using TT , TE , EE and BB , and assuming no mixing. We show that such a naive approach does quite well in predicting the errors: if properly handled, polarization-mode-mixing is not a significant error source in most cases. Of course for either method to be successful, all generalized noise sources need to be identified including instrumental leakage from T to Q and U .

2.5.1 Calculation of Ensemble-Averaged Posteriors on Parameter Grids

We calculate the posterior distribution on a gridded parameter space, a method mostly applicable to low dimensional parameter spaces. At each point of the parameter grid the $\mathcal{C}_{X\ell}$'s are calculated using the public code CAMB⁹. These are then multiplied by beam windows, $\mathcal{B}_\ell^2 = e^{-\ell(\ell+1)\sigma_b^2}$, assuming a Gaussian beam of width $\sigma_b = 0.425\theta_{\text{FWHM}}$, and by pixelization windows $W_{\text{pix},\ell}^2$, an isotropized approximation to finite pixel size effects. (Timestream digitization filters are also generally required, but are swamped by these two filters.) The product is used to construct the symmetric $3N_{\text{pix}} \times 3N_{\text{pix}}$ theoretical pixel-pixel signal covariance matrices, with 6 independent sub-matrices, $\mathbf{C}_{s,X}$, $X \in \{TT, TQ, TU, QQ, QU, UU\}$. We assume experimental noise is Gaussian and usually take it to be white. So $\mathbf{C}_{n,T} = \sigma_{n,T}^2 \mathbf{I}$ for the temperature block and $\mathbf{C}_{n,Q,U} = \sigma_{n,\text{pol}}^2 \mathbf{I}$ for the polarization block of the covariance matrix, where we usually have $\sigma_{n,\text{pol}} \sim \sqrt{2}\sigma_{n,T}$. Here the σ_n 's are effective noises per pixel, an amalgamation of the noises coming from different frequency channels. \mathbf{I} is the identity matrix. We neglect leakage from T to Q and U .

Since we are forecasting the uncertainties in r from different experimental setups, and not analyzing actual CMB maps, we can bypass creating a large ensemble of simulated CMB maps by replacing the observed correlation matrix $\mathbf{C}_{t,O} \equiv \Delta\Delta^T$ by its ensemble average:

$$\text{Tr}(\mathbf{C}_t^{-1}(\mathbf{q})\mathbf{C}_{t,O}) \rightarrow \text{Tr}(\mathbf{C}_t^{-1}(\mathbf{q})\bar{\mathbf{C}}_{t,O}).$$

Here $\bar{\mathbf{C}}_{t,O}$ is the ensemble-averaged ‘‘pixel-pair data’’, namely the covariance matrix of the input fiducial signal model together with the instrument noise, and $\mathbf{C}_t(\mathbf{q})$ is the signal pixel-pixel covariance matrix for the parameters \mathbf{q} plus the various noise contributions, instrumental and otherwise. An advantage of this approach is that the recovered values of the parameters are what the ensemble average of sky realizations would yield, and will not move hugely due

⁹<http://camb.info/>

to the chance strangeness of any one realization (as the real sky may provide for us). Note that while sample variance does not impact the location of the maximum likelihood in this ensemble-averaged approach, it is fully reflected in the width of the posterior distribution from which our uncertainties are derived.

We mask out the part of Galaxy falling in the observed patch (the P06 WMAP-mask in Page et al., 2007), assuming it to be too foreground-dominated for useful parameter extraction. We also project out modes larger than the fundamental mode of the observed patch since, due to time-domain filtering, information is not usually recoverable on such large scales. For instance, if the mask has the shape of a spherical cap extending from the north pole to $\theta = \theta_{\text{patch}}$, we add a very large noise to the modes with $2\ell + 1 < [2\pi/\varpi]$ where $[..]$ takes the integer part and $\varpi = 2 \sin(\theta_{\text{patch}}/2)$ is the flat 2D radius of the disk with an area equal to the solid angle of the cap. This makes the likelihood insensitive to any information at and beyond the patch scale. This large scale mode cut is especially important to include for larger values of f_{sky} , where the low ℓ modes contribute significantly to r measurement through the reionization bump. In real large sky experiments it will not be easy to draw such modes from maps.

Our simulations cover two observational cases: an all-sky experiment with Planck-like white noise levels, and a partial sky experiment with Spider-like white noise levels, each with two frequency channels, assuming other frequencies are used for subtracting foregrounds. We have also made the simplifying assumption that in each experiment, the FWHM of both channels is the same as the channel with the larger beam. This does not affect the results much due to the crude size of the pixelization and the absence of the gravitational wave signal at small scales. See Table 2.5.1 for other experimental assumptions.

For the Spider-like case we keep the flight time constant so that the observation gets deeper as f_{sky} decreases, while for the Planck-like experiment the pixel noise is assumed constant for different values of f_{sky} . The latter case, with small values of f_{sky} , is used to illustrate how well a strategy of only analyzing the lowest foreground sky could work, if, e.g., foreground removal turns out to be prohibitive over much of the sky. If foregrounds can be well removed from Planck, then full sky is appropriate.

We calculate the constraints on targeted cosmological parameters for different f_{sky} 's, assuming the observed patches are spherical caps from $\theta = 0$ to $\theta = \theta_{\text{patch}}$, corresponding to $\theta = \cos^{-1}(1 - 2f_{\text{sky}})$. We perform the analysis at different resolutions for different sky cuts to minimize the effect of pixelization for small f_{sky} on the one hand, and to keep the computational time reasonable for large f_{sky} on the other hand. We use $N_{\text{side}} = 32$, $N_{\text{side}} = 64$ and $N_{\text{side}} = 128$ for $f_{\text{sky}} > 0.25$, $0.007 < f_{\text{sky}} \leq 0.25$, and $f_{\text{sky}} \leq 0.007$, respectively. We checked the results for two neighbour resolutions at resolution switches. For the low f_{sky} switch, results are not sensitive to the change of resolution while for the switch at larger f_{sky} we are about 10% – 15%

Table 2.1: Specifications of Spider-like, Planck-like and CMBPol (mid-cost) experiments for simulations.

Experiment	Freq (GHz)	FWHM	num. of det.	ΔT^a		obs. time
				I	Q & U	
Spider-like ^b	96	50'	768	3.2	4.5	580 hr
Spider-like	150	32'	960	2.7	3.8	580 hr
Planck-like ^c	100	10'	8	3.8	6.1	2.5 yr
Planck-like	143	7'	8	2.4	4.6	2.5 yr
CMBPol (mid-cost) ^d	100	8'	–	0.18	0.26	–
CMBPol (mid-cost)	150	5'	–	0.19	0.27	–

^a nK, the instrument sensitivity divided by $\sqrt{\text{total observation time}}$.

^b These Spider-like specifications which are used as the default in this paper are different from the ones proposed in Fraisse et al. (2011) with two 20 day flights. The first flight uses three 90 and three 150 GHz receivers each with 288 and 512 detectors respectively. In the second flight, two 280 GHz receivers replace one 90 and one 150 GHz telescope, leaving the configuration of the flight identical to the first one. The detector sensitivity as proposed in Fraisse et al. (2011) is 150, 150 and 380 $\mu\text{K}_{\text{CMB}}\sqrt{\text{s}}$ at 90, 150 and 280 GHz, respectively. The performance of the default Spider-like experiment in this paper and the more recent proposal as in Fraisse et al. (2011) are very close (see Figure 2.1).

^c <http://www.rssd.esa.int/index.php?project=planck> ^d For a mid-cost full-sky CMBPol experiment based on table 13 of Baumann et al. (2009). We are using 100 and 150 GHz channels in our simulations. Adding more channels, in the unrealistic case of no foreground contamination we simulate, would not affect the limits on r , since with these low instrument noise levels, either lensing or cosmic variance, depending on how small r is, would be the dominant source of uncertainty.

pessimistic in the results by choosing the lower resolution, specifically for a Planck-like case (with small beam) and for a higher value of r , e.g., $r = 0.12$. In these cases, lensing starts to dominate at higher multipoles and choosing a high enough resolution for the analysis would improve the errors on r by resolving the primordial gravity waves at relatively high multipoles.

2.5.2 Residual Foreground-Subtraction “Noise”

No study of gravitational wave detectability by B -mode experiments can ignore the impact of polarized foreground emission. Component separation is a major industry in itself. Various techniques have been utilized with CMB data up to now - often involving template parameter marginalization of one sort or another. We have been lucky so far in that the foregrounds have been manageable for TT , TE and EE . The level of subtraction needed to unearth the very tiny gravity wave-induced B -signal is rather daunting, especially since the foregrounds are largest at the low ℓ . Thus, although we may wrestle the generalized noise from the detectors and from experimental systematics to levels allowing small r to be detectable, the foregrounds will need to be well addressed before any claim of primordial detection will be believable. Although we have learned much already about the TT foregrounds and, from WMAP, the synchrotron EE , we do not know the ℓ -shape or the amplitude of the polarization for dust.

In O’Dea et al. (2011, 2012), the polarization emission from thermal dust is based on a three-dimensional model of dust density and two-component Galactic magnetic field. It is assumed that the degree of polarization has a quadratic dependence on the magnetic field strength and its direction is perpendicular to the component of the local magnetic field in the plane of the sky, similar to the model assumed by WMAP in Page et al. (2007). In forecasting for proposed post-Planck satellite experiments, simple approximations for thermal dust and synchrotron emission have been made, (e.g., Baumann et al., 2009, and references therein). The dusty ℓ -structure in this model is similar to the O’Dea et al. (2011) form: $C_{X\ell} \sim \ell^{-0.5}$ for $X = EE, BB$. We follow this Baumann et al. (2009) approach here, but apply it to our pixel-based analysis.

We therefore assume that the maps are already foreground-subtracted, possibly with the wider Planck frequency coverage used in conjunction with the Spider maps, with the CMB-component having a residual uncertainty, which we incorporate in our analysis as an additional large-scale (inhomogeneous) noise component $C_N^{(\text{fg})}$. We assume the power spectrum of the foreground residuals has the same shape as the original foreground spectrum, but with only a few percent of the amplitude

$$C_{X\ell} \rightarrow C_{X\ell} + \sum_{\text{fg}=\text{S,D}} \epsilon_X^{(\text{fg})} C_{X\ell}^{(\text{fg})}, \quad X = EE, BB,$$

with the sum over synchrotron (S) and dust (D) emissions. The tunable removal-efficiency

Table 2.2: Parameters of our assumed foreground model, adopted from Baumann et al. (2009).

Parameters	Synchrotron	Dust
$A_{S,D}(\mu K^2)$	4.7×10^{-5}	1
ν_0	30	94
ℓ_0	350	10
α	-3	2.2
β^E	-2.6	-2.5
β^B	-2.6	-2.5

parameters $\epsilon^{(\text{fg})}$ are taken to be 5% in our plots. The shapes are

$$\begin{aligned}
C_{X\ell}^{(S)}(\nu) &= \frac{\ell(\ell+1)}{2\pi} A_S \left(\frac{\nu}{\nu_0}\right)^{2\alpha_S} \left(\frac{\ell}{\ell_0}\right)^{\beta_S} \\
C_{X\ell}^{(D)}(\nu) &= \frac{\ell(\ell+1)}{2\pi} p^2 A_D \left(\frac{\nu}{\nu_0}\right)^{2\alpha_D} \left(\frac{\ell}{\ell_0}\right)^{\beta_D} \\
&\times \left[\frac{e^{h\nu_0/kT} - 1}{e^{h\nu/kT} - 1} \right]^2.
\end{aligned}$$

The dust polarization fraction, p , is assumed to be around 5%. The values for the other parameters taken from Baumann et al. (2009) are listed in Table 2.5.2. They were chosen to give agreement with WMAP, DASI and IRAS observations (and the Planck sky model, which is based on these). Although this model provides only a rough guide to the impact that incomplete foreground subtraction will have on r -estimation, it does include the crucial large-scale dependence which differentiates it so much from the structure of the instrumental noise.

A natural question when considering deep small sky observations is how many patches there are on the sky with low foregrounds so the requisite cleaning is at a minimum. The Planck Sky Model for the polarized foreground emission (Leach et al., 2008; Delabrouille et al., 2012) is similar to the one we have adopted. Using a code developed by Miville-Deschênes, we have calculated for patches of radius R the pixel-averaged variance at pixel p , $\sigma_{\text{pol,fg}}^2(p, R) = \langle (P - \bar{P}(< R))^2 \rangle$ of the polarization intensity $P = \sqrt{Q^2 + U^2}$ about the patch-average \bar{P} arising from the synchrotron and dust foregrounds. We compare this with the $\sigma_{\text{pol,gw}}^2(p, R)$ we obtain for each patch in a single tensor-only primordial polarization realization (which is proportional to r^2). The patches are sorted in decreasing order of the “signal-to-noise” ratio $\sigma_{\text{pol,gw}}(p, R)/\sigma_{\text{pol,fg}}(p, R)$. The next pixel on the list is included in a patch list if it has no overlap with the patches in the previously-determined higher signal-to-noise list. A patch is considered to be r -clean if this polarization signal-to-noise exceeds unity, a rather strong criterion. At 100 GHz, we found

no “ $r=0.01$ ”-clean patches, seven “ $r=0.05$ ”-clean patches and ten “ $r=0.1$ ”-clean patches with $f_{\text{sky}} \gtrsim 0.007$ ($R = 10^\circ$). There are one “ $r=0.05$ ”-clean patch and two “ $r=0.1$ ”-clean patches for $f_{\text{sky}} \gtrsim 0.03$ ($R = 20^\circ$). At 150 GHz, we found no “ $r=0.05$ ”-clean patches and one “ $r=0.1$ ”-clean patch with $f_{\text{sky}} \gtrsim 0.007$ but no $r=0.1$ -clean patches for $f_{\text{sky}} \gtrsim 0.03$.

The non-overlapping criterion is quite severe. Another measure of r -cleanliness is to determine the fraction of sky with $\sigma_{\text{pol,gw}}(p, R)/\sigma_{\text{pol,fg}}(p, R)$ above unity. The r -clean fraction is clearly ~ 0 for those values of r and R with no corresponding clean patches (as stated above). Here only the non-zero values are reported. At 100 GHz, the “ $r=0.05$ ”-clean fraction is ~ 0.14 ($R = 10^\circ$) and the “ $r=0.1$ ”-clean fraction is ~ 0.24 ($R = 10^\circ$); For both values of r , there is no appreciable decrease in the sky fraction by increasing the patch sizes to $R = 20^\circ$. At 150 GHz, the “ $r=0.1$ ”-clean fraction is ~ 0.04 ($R = 10^\circ$). It should be noted that as these sky fractions do not necessarily correspond to contiguous regions, the sky fraction of interest for small-sky B-mode experiments is in principle smaller. The Planck Sky Model at the lower frequencies agrees with the (extrapolated) synchrotron emission from WMAP, but the higher frequency polarized dust emission really requires the better observations of the Planck mission.

2.5.3 Correlations of r with Other Cosmic Parameters

Either detecting r or placing a tight upper bound is crucial for progress in inflation studies. Correlations of r with other parameters q_α must be properly accounted for, since they are marginalized in the reduction to the 1D r -posterior. The relative importance of the various q_α is determined by calculating the posterior-averaged cross-correlations $\rho_{r\alpha} \equiv \langle \delta r \delta q_\alpha \rangle_{\text{f}}$, which depend upon the experimental configuration and its noise. Within the Gaussian approximation for the posterior distribution, the correlations can be estimated from the inverse components, $[F^{-1}]_{r\alpha}$, using the Fisher matrix equation (eq. 2.5). Lensing and instrumental noise are included in the generalized noise matrix. Here F is determined from numerical differentiation by taking small steps in the main parameters of the standard Λ CDM model ($\ln(\Omega_b h^2), \ln(\Omega_c h^2), H_0, n_s, \tau, r$) from the fiducial WMAP7 values¹⁰. The scalar amplitude A_s is treated as a normalization parameter here, so it is not included in the parameter list. We use two different fiducial values for r , 0.2 and 0.01, and three values of f_{sky} , 0.007, 0.07 and 0.75, for a Spider-like experiment. We use a Gaussian prior on all parameters q_α but r , with the mean and width given by the WMAP7 measurements. For these parameters we choose $(F_{\text{prior}})_{\alpha\beta} = \sigma_{\alpha, \text{WMAP7}}^{-2} \delta_{\alpha\beta}$, which gives a weaker prior than the true WMAP7 results would give. In the quadratic approximation to the posterior information action, the correlation of r

¹⁰http://lambda.gsfc.nasa.gov/product/map/dr4/params/lcdm_sz_lens_wmap7.cfm

Table 2.3: σ_r from the full likelihood computed on a 2D r - τ grid (bottom) cf. 1D, 2D and 6D Fisher determinations $[F^{-1}]^{rr}$ using pixel-space matrices (middle) and the simplified ℓ -space sums, with $r_{\text{fid}} = 0.12$. This demonstrates that the use of reduced parameter spaces gives robust results, independent of cap sizes, here for $f_{\text{sky}} = 1, 0.07, 0.007$.

method	param space	$N_{\text{side}} = 32$	$N_{\text{side}} = 64$	$N_{\text{side}} = 128$
		$f_{\text{sky}} = 1$	$f_{\text{sky}} = 0.07$	$f_{\text{sky}} = 0.007$
Fisher	1 param	0.022	0.018	0.037
ℓ -space	2 param	0.023	0.018	0.037
	6 param	0.025	0.020	0.037
Fisher	1 param	0.022	0.019	0.034
pixel-space	2 param	0.023	0.019	0.034
	6 param	0.025	0.020	0.035
grid-based	2 param	0.021	0.018	0.036

with other parameters is approximated by

$$\rho_{r\alpha} \approx \frac{[F_t^{-1}]_{r\alpha}}{\sqrt{[F_t^{-1}]_{rr}[F_t^{-1}]_{\alpha\alpha}}} \quad (2.7)$$

where $F_t = F + F_{\text{prior}}$ is the total Fisher matrix.

For the full sky case, we find the largest $\rho_{r\alpha}$ for τ and n_s , with $\rho_{r\tau}$ and ρ_{rn_s} both ≈ 0.25 . For smaller sky coverage, the degeneracy between r and τ disappears since the main constraints on τ come from the large scale polarization, which small cut-sky cases are not sensitive to. The dominant correlations of r are with the matter density parameters $\Omega_c h^2$ and $\Omega_b h^2$, at the 0.1–0.2 level, a consequence of the gravitational lensing-induced BB noise. Note that under the quadratic approximation the conditional uncertainty in r for given \bar{q}_α is $\langle \delta r^2 | \bar{q}^\alpha \rangle = \sigma_r^2 (1 - \rho_{r\alpha}^2)$, where σ_r is the fully marginalized error on r . As a result, even in the 25% case for $\rho_{r\alpha}$, the error diminishes only by 3% for fixed q_α relative to the full σ_r .

Thus we should be able to safely estimate the error on r with all or none of the basic cosmic parameters held fixed. We verified this explicitly by comparing the 2D uncertainties calculated from the full 2D r – τ -grid with the full 6D uncertainties calculated from the inverse Fisher matrix, in ℓ -space and in pixel space, in Table 2.5.3, for different f_{sky} and at different resolutions, defined here by the value of N_{side} . With all six parameters included, σ_r increases by only $\sim 10\%$ over the single τ -marginalized σ_r , which justifies our exploration using a heavily truncated parameter space to determine the errors on r .

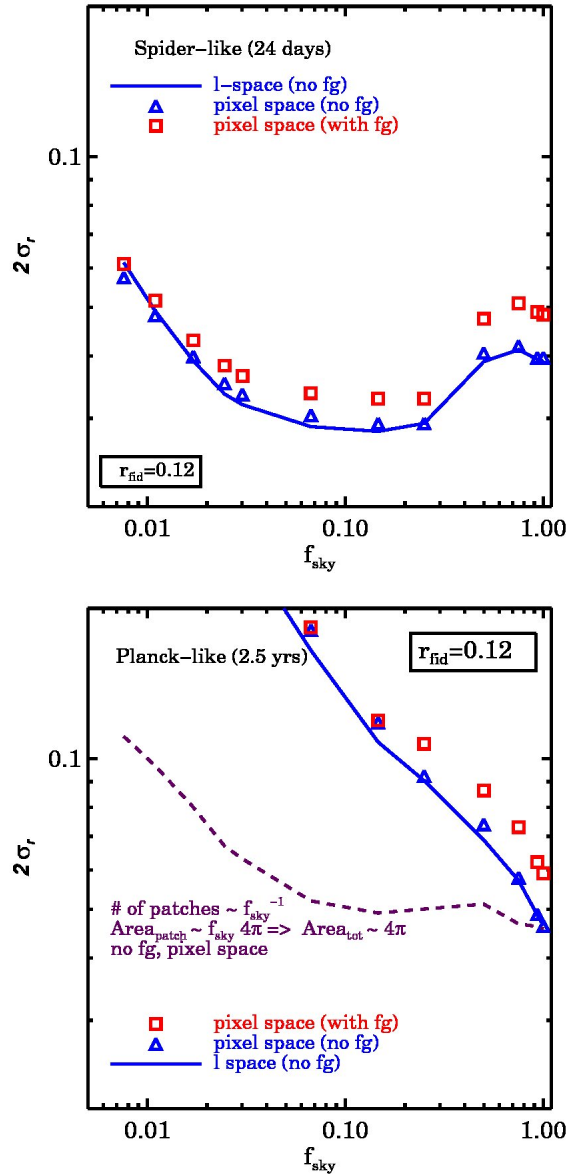


Figure 2.5: Uncertainty in measuring r for different sky coverages with Spider-like (top) and Planck-like (bottom) experiments, with and without foregrounds (squares and triangles respectively), for the fiducial model $r_{\text{fid}} = 0.12$. The solid lines are the results of l -space analysis (ignoring foregrounds). The analysis has been performed with different resolutions for different f_{sky} , ranging from $N_{\text{side}} = 32$ for full sky to $N_{\text{side}} = 128$ for the smallest sky coverage. The f_{sky} refers to the sky coverage before applying the Galactic cut so for full sky f_{sky} is effectively ~ 0.75 . The dashed line is the $2\sigma_r$ if the full sky needs to be effectively considered as a combination of several smaller patches with the individual observed sky fraction being f_{sky} and the total area of all patches equal to the Galaxy-masked full sky.

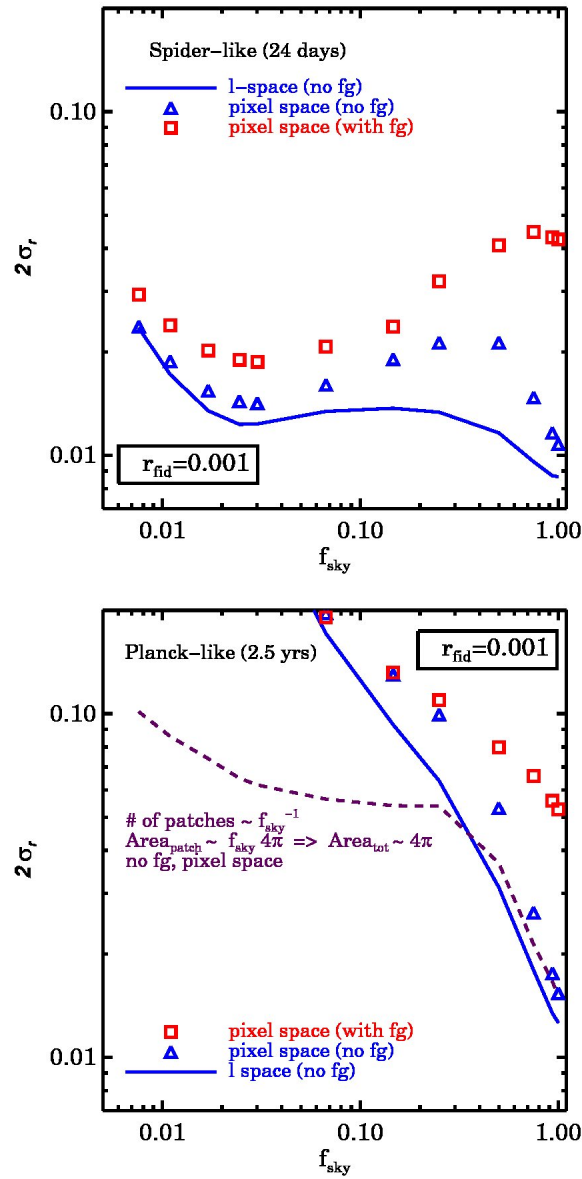


Figure 2.6: Similar to figure 2.5 with $r_{\text{fid}} = 0.001$.

2.5.4 Results in r - τ Space

In this section, we use τ as well as r to make our 2D parameter space since it has a direct impact on the BB reionization bump. We fix the overall \mathcal{C}_ℓ normalization for each parameter pair to the WMAP TT measurement at $\ell = 220$. This is equivalent to having A_s as an adjustable parameter. If not otherwise stated, lensing has been included in all of the following simulations with a fixed noise template, linearly scaled with A_s accordingly. Treating lensing in the noise covariance completely takes into account its effect on sample variance. It may be possible for it to be partly removed in the patch using delensing algorithms (see, e.g., Smith et al., 2008, and references therein), leading to a reduced variance in the same way that we are treating a foreground residual. However, treating lensing as a noise source is a good assumption for our purposes here.

The $2\sigma_r(f_{\text{sky}})$ plots in Figures 2.5 and 2.6 are our main results. Shown are two fiducial models with $r_{\text{fid}} = 0.12, 0.001$, both having $\tau_{\text{fid}} = 0.09$. The f_{sky} in the plots is the sky coverage before the Galaxy is masked. The Galaxy cut starts coming into the observed patch for $\theta_{\text{patch}} \sim 40^\circ$.

The results are compared to the expected error bars on r from a simplified ℓ -space analysis. Proper mode counting is a difficulty in the ℓ -space approximation for cut-skies. (This differs from the full pixel-pixel covariance matrix analysis in which all modes are naturally taken care of.) For the ℓ -space approximation, we have taken the mode number to be the naive $[f_{\text{sky}}(2\ell + 1)]$ where $[..]$ indicate the integer part. This imposes a low ℓ -cut on the modes by demanding $[f_{\text{sky}}(2\ell + 1)] \geq 1$ which overrides the ℓ -cut from the fundamental mode of the patch, $2\ell + 1 = [2\pi/2 \sin(\theta_{\text{patch}}/2)]$, up to $\theta \approx 30^\circ$.

This ℓ -space $\sigma_r(f_{\text{sky}})$ is a lower bound since it ignores the mode mixing on the cut sky. Still, in the absence of systematic errors and for the simplified noise assumed here, the errors we find are near the true (matrix) values, as Figure 2.5 confirms for $r_{\text{fid}} = 0.12$. A similar measurement with $r_{\text{fid}} = 0.2$ shows the same thing, though with a more-flattened curve for $\sigma_r(f_{\text{sky}})$ for the Spider-like case and with foregrounds playing a smaller role. $E - B$ mixing does not seem to be a serious impediment, at least down to $f_{\text{sky}} \approx 0.01$. For the Spider-like experiment, the error minimum is $2\sigma_r = 0.035$ for $r_{\text{fid}} = 0.12$, at $f_{\text{sky}} \approx 0.15$, but the trough is broad. For the low $r_{\text{fid}} = 0.001$, for which only an upper limit can be expected, Figure 2.6 shows the agreement in $\sigma_r(f_{\text{sky}})$ between ℓ -space and pixel-space is not quite as good. This is especially true for $f_{\text{sky}} \approx 0.25 - 0.5$ for which considerable observation time is expended on the $\ell \approx 12$ BB valley (see Figure 2.3) where there is little signal. The naive ℓ -space approximation underestimates this, but agreement with pixel-space is regained in runs with the reionization bump removed, by setting $\tau = 0$; for this case the monotonic rise in $\sigma_r(f_{\text{sky}})$ with increasing f_{sky} continues to

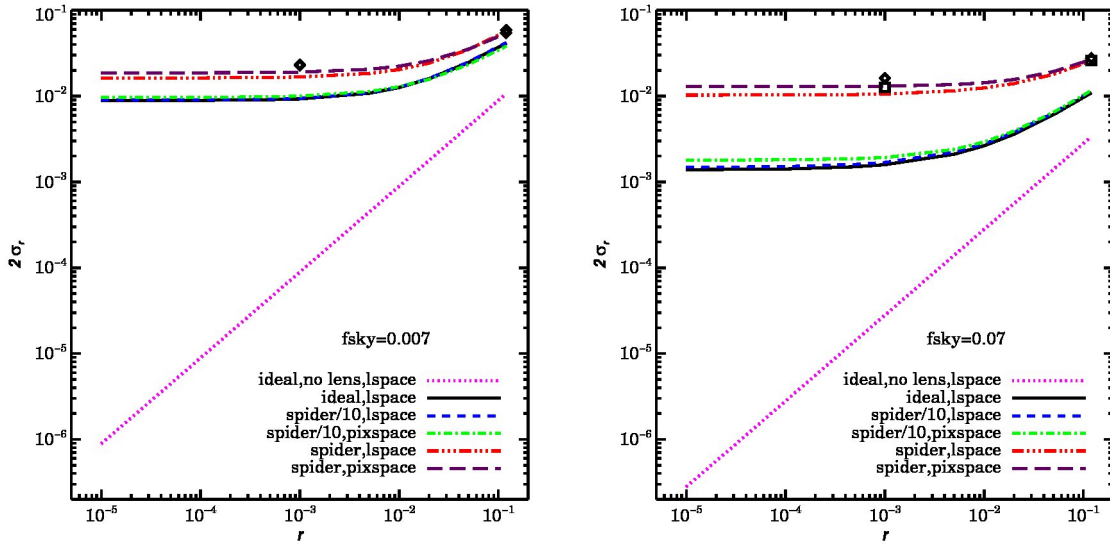


Figure 2.7: The curves show $2\sigma_r$ as a function of r_{fid} obtained from the Fisher matrix in ℓ and pixel-space for $f_{\text{sky}} = 0.007$ (top) and 0.07 (bottom). The choices for the curves are meant to unravel the impact of the cosmic variance, lensing, instrument noise and mode mixing on σ_r . The symbols show errors from the full likelihood calculated on a gridded 2D parameter space, and agree nicely for both pixel-space (squares) and ℓ -space (diamonds).

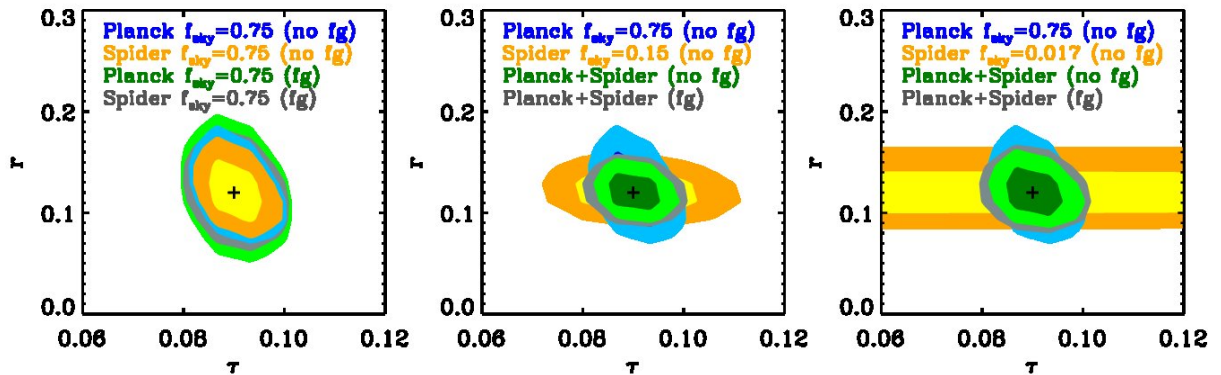


Figure 2.8: 1σ and 2σ r - τ contours with and without foregrounds for a Spider-like experiment with different sky cuts and for a Planck-like Galaxy-masked experiment with effective $f_{\text{sky}} \sim 0.75$. In the two right panels the contours for the combined Spider-like and Planck-like experiments are also plotted. The black plus signs denote the input $r_{\text{fid}} = 0.12$ and $\tau_{\text{fid}} = 0.09$. Expanding Spider-like observing time on large sky coverage would not improve much the Planck forecasted τ error, but would decrease the combined r error, suggesting the deep small-sky option is better.

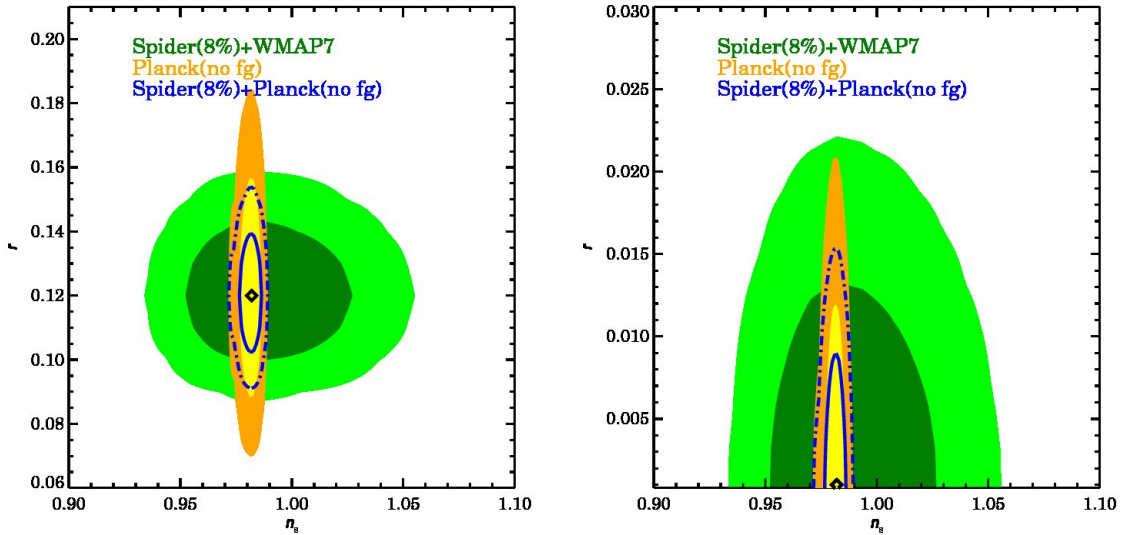


Figure 2.9: r - n_s contours for a Spider-like ($f_{\text{sky}} \sim 0.08$)+WMAP7 experiment, contrasted with a Planck-like (Galaxy-masked $f_{\text{sky}} \sim 0.75$) experiment, assuming no foreground contamination, compared to the results for the combination of the two (the solid and dot-dashed blue curves). The $r - n_s$ correlation has been ignored, as discussed in § 2.5.3. We also explicitly verified this for the specific case of the Planck-like survey from post-processing the CosmoMC chains. The r constraints are calculated by the numerical methods used throughout the paper. For the case of Spider+WMAP7, we assumed an asymmetric Gaussian likelihood for n_s with the widths coming from the lower and upper $1\sigma_{n_s}$ as measured by WMAP7 (http://lambda.gsfc.nasa.gov/product/map/dr4/params/lcdm_sz_lens_tens_wmap7.cfm). For the n_s likelihood from the Planck-like case, CosmoMC chains (<http://cosmologist.info/cosmomc/>) were used to properly take into account the correlations of n_s with other cosmic parameters, which, unlike r , are non-negligible. Top has $r_{\text{fid}} = 0.12$ and bottom has $r_{\text{fid}} = 0.001$; both have $n_{s,\text{fid}} = 0.98$. The plots indicate a possibly very rosy picture for constraining these two critical inflation parameters.

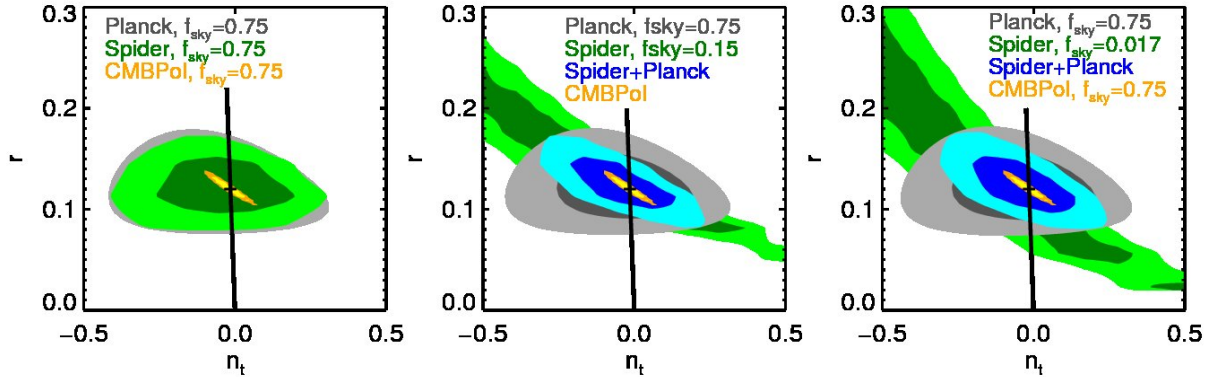


Figure 2.10: 1σ and 2σ r - n_t contours for a Spider-like experiment with different sky cuts and for a Planck-like Galaxy-masked $f_{\text{sky}}=0.75$ experiment. The contours for a CMBPol-like experiment as well as those for the combined Planck-like and Spider-like experiments are plotted for comparison. The black line is the inflation consistency line and the black plus sign is the fiducial input, $r = 0.12$ and $n_t = -0.015$. Even with this CMBPol, inflation consistency is not that well tested.

full sky.

Extending to the full Galaxy-masked sky improves the upper limit on r since the window function captures the low- ℓ bump. The ℓ -space and pixel-space calculations disagree slightly, but when the Galaxy mask is removed, the estimates agree.

At small f_{sky} , $2\sigma_r$ increases due to lensing which dominates the total BB spectrum at small scales. The competition between avoiding contamination by lensing and avoiding the $\ell \approx 12$ valley produces a weak minimum in σ_r at $f_{\text{sky}} \approx 0.15$ for $r = 0.12$, when a detection is expected, and at $f_{\text{sky}} \approx 0.03$ for $r = 0.001$, when an upper limit is expected. The full sky is weakly optimal for setting an upper limit in the absence of foregrounds.

The Planck-like measurements in the lower plots of Figures 2.5 and 2.6 show a rise in $2\sigma_r$ as f_{sky} drops. In this case, the information on the large scales are lost while the pixel noise stays unchanged. The dashed lines in these plots show the approximate $2\sigma_r$ for a full-sky Galaxy-masked Planck-like experiment if the large-scale modes are filtered, e.g., by time-domain filtering or due to high foreground contamination and thus the observed region is considered to be a combination of smaller patches (adding up to the full sky in total observed area).

Not surprisingly, we see that foregrounds mostly affect experiments with larger f_{sky} , and for fiducial models with smaller r . We also see that deep observations of quite small patches seem to do as well as larger patches (observed less deeply) and even much better if r is small (for which the sample variance is very small and instrument noise plays the dominant role).

Figure 2.7 shows how different components contribute to the error on r calculated using the Fisher matrix for various r_{fid} and $f_{\text{sky}} = 0.007$ and 0.07 . As before the mode mixing is ignored in the ℓ -space calculation. If there were no lensing and no mode-mixing, in the limit of no instrument noise, the only source of error would be the sample variance, which is, as expected, proportional to r . The solid black lines show the minimum irreducible errors due to sample variance and lensing. We contrast this with calculations in both pixel and ℓ -space of two Spider-like experiments. One has 10 times less noise than the fiducial Spider case. This noise level can be seen to give almost no contribution to the errors for these sky cuts since lensing noise is dominant. The other has our standard Spider-like noise, which can be seen to significantly add to the error. The impact of neglecting mode-mixing in determining σ_r vanishes as r increases, since sample variance dominates the error, as a comparison of the curves from the pixel-space and ℓ -space analyses shows. The over-plotted symbols represent the errors from measuring the likelihood curve in a gridded 2D parameter space (as explained earlier). The $2\sigma_r$'s from the full method and the Fisher matrix approximation are close. The small difference is because the r -likelihood curve is not a perfect Gaussian.

Figure 2.8 shows the 2D r - τ contours for 3 different values of sky coverage for a Spider-like experiment compared to a full-sky Planck-like experiment (with Galaxy mask cut), with and without foreground contamination. As expected, τ is unconstrained as f_{sky} decreases for the Spider-like experiment since τ -constraints come from the largest angular scales: what is optimal for r detection is awful for τ determination, for which all-sky is best.

2.5.5 Results in r - n_s Space

In Figure 2.9, we have plotted the r - n_s contours for an $f_{\text{sky}} = 0.08$ Spider-like experiment and for a full-sky Planck-like survey, with and without foregrounds, using the model discussed in § 2.5.4. This shows almost no correlation between the two parameters for these experimental cases, as expected from the discussion in § 2.5.3. It also shows the remarkable set of inflation constraints that may arise from Planck and Spider-like experiments.

2.5.6 Results in r - n_t Space

Although detecting r would provide an invaluable measure of the mean acceleration parameter (and energy scale) of inflation, we want more, the shape of the tensor power embodied in the tensor tilt n_t . We explore this here in a 2D space by fixing τ, n_s and the other cosmic parameters. Figure 2.10 shows the 2D contours for r - n_t with $r_{\text{fid}} = 0.12$, and fiducial tensor tilt $n_{t,\text{fid}} = -0.0150$ satisfying the inflation consistency condition (eq. 2.2.1). Alas, we see that n_t is hardly constrained by Spider-like and Planck-like experiments, no matter how large

f_{sky} is. To see whether a post-Planck deep all-sky experiment could modify this conclusion, we ran our analysis using the specification of a putative mid-cost CMBPol mission outlined in Baumann et al. (2009), using the frequency channels described in Table 2.5.1. There is of course improvement, and the COrE and PIXIE post-Planck missions would do better, but the relatively short $\Delta\ell \sim 150$ baseline precludes even an ideal experiment from providing a powerful test of inflation consistency.

2.5.7 Breaking r up into $r_{X\beta}$ -Shape Parameters: A Tensor Consistency Check

Because r is essentially a linear parameter (for given A_s), we are effectively determining a single (very) broad bandpower amplitude multiplying a collection of fiducial X -template shapes $\mathcal{C}_{X\ell}^{(g)}$ given by the gravitational wave powers. It is natural to test this locked-in monolithic parameterization by introducing a collection of parameters $r_{X\beta}$ multiplying individual X and ℓ -band templates, i.e.,

$$\begin{aligned}\mathcal{C}_{EE\ell} &= \mathcal{C}_{EE\ell}^{(s)} + r_{EE\beta}\chi_{\beta}(\ell)\mathcal{C}_{EE\ell}^{(g)} \\ \mathcal{C}_{BB\ell} &= \mathcal{C}_{BB\ell}^{(\text{lens})} + r_{BB\beta}\chi_{\beta}(\ell)\mathcal{C}_{BB\ell}^{(g)}.\end{aligned}\tag{2.8}$$

Here $\mathcal{C}_{EE\ell}^{(s)}$ is the scalar part of $\mathcal{C}_{EE\ell}$, including lensing, and $\mathcal{C}_{BB\ell}^{(\text{lens})}$ is the lensed BB power. The overall normalization is arranged so that $r_{X\beta} = r$ is the tensor consistency condition. The $\chi_{\beta}(\ell)$'s are the β -windows. These have often been taken to be top-hats satisfying a saturation property $\sum_{\beta}\chi_{\beta}(\ell) = 1$ and an orthogonality property $\chi_{\beta}(\ell)\chi_{\beta'}(\ell) = \delta_{\beta\beta'}$ in bandpower work. However, the modes could also be quite overlapping as long as saturation and the $r_{X\beta} = r$ normalization are satisfied.

This is a reasonable path to finding the tensor bandpowers for BB and EE but, given the § 2.5.6 result on n_t , we will content ourselves with a 2D example using one ℓ -band β and two X parameters, r_{EE} and r_{BB} . For this study, we keep A_s fixed (cf. § 2.5.4 and 2.5.6). The contours in Figure 2.11 show the degree to which the tensor consistency encoded in the $r_{EE} = r_{BB}$ line, can be checked. The contours confirm the expectation that the B -modes are the most influential source of information about primordial tensor perturbations, since the large scalar contribution to EE swamps the tiny tensor signal and inflates the error bars. Using checks like these for showing consistency have had a long history. In the first EE polarization detection papers, the EE amplitude was shown to be consistent with the amplitude expected from TT parameters (Kovac et al., 2002; Sievers, 2004). In the first lensing detections in the TT power spectra, the deviations from lens-free results were shown to be consistent with expectations from the parameters determined from the primary TT data (Reichardt et al., 2009b; Dunkley et al., 2011).

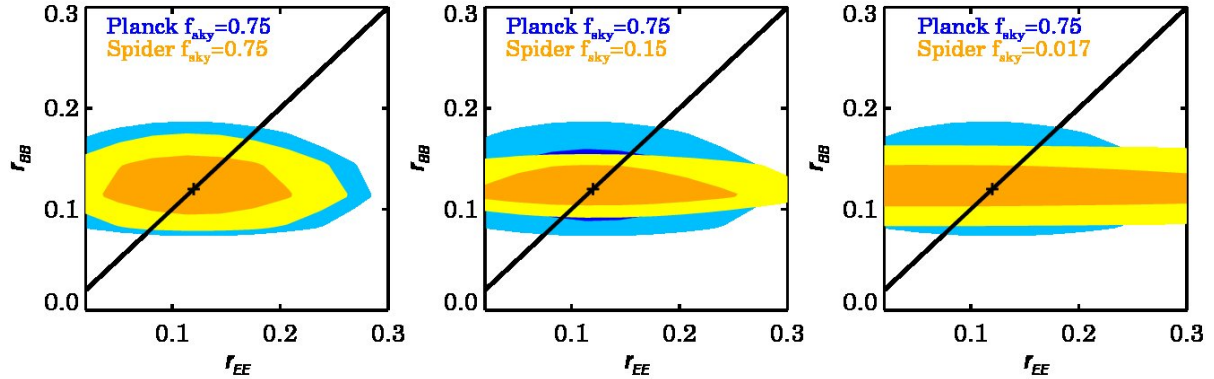


Figure 2.11: 1σ and 2σ contours in the r_{EE} - r_{BB} plane for a Spider-like experiment with different sky cuts and for a Planck-like experiment with $f_{\text{sky}}=0.75$. The black solid lines show the *tensor consistency* curves $r_{EE} = r_{BB}$ and the plus signs show the fiducial $r_{EE} = r_{BB} = 0.12$ input model. As expected, r_{BB} is better determined than r_{EE} and this tensor consistency is not well tested.

2.5.8 Breaking f_{sky} into Many Fields

Using multiple (foreground-minimized) fields to make up a total f_{sky} is an approach that has been advocated for ground-based strategies (e.g., for ABS¹¹). In Figure 2.12 we show the impact of splitting f_{sky} into four patches, while keeping the total integration time and the instrument noise constant. One does not lose that much as long as the total probe is a few percent of the sky, a consequence of the broad single-patch $\sigma_r(f_{\text{sky}})$ minimum. The number of polarization-foreground-clean patches is of course still to be determined. We also varied the patch geometry; e.g., for an $f_{\text{sky}} \sim 0.08$ rectangular region with $r_{\text{fid}} = 0.12$, we get $2\sigma_r = 0.048$ without foregrounds, in good agreement with the cap result $2\sigma_r = 0.050$.

2.6 Summary and Conclusions

In this paper, we applied a full map-based likelihood analysis to multifrequency Q - U polarization maps and T -maps of forecasted data to determine the posterior probability distribution of r .

2.6.1 Leakage Levels and Leakage Avoidance

This method avoids the explicit linear E - B decomposition of the polarization maps before doing the likelihood analysis and gives the best possible determination of r , provided that systematic

¹¹<http://www.princeton.edu/physics/research/cosmology-experiment/abs-experiment/>

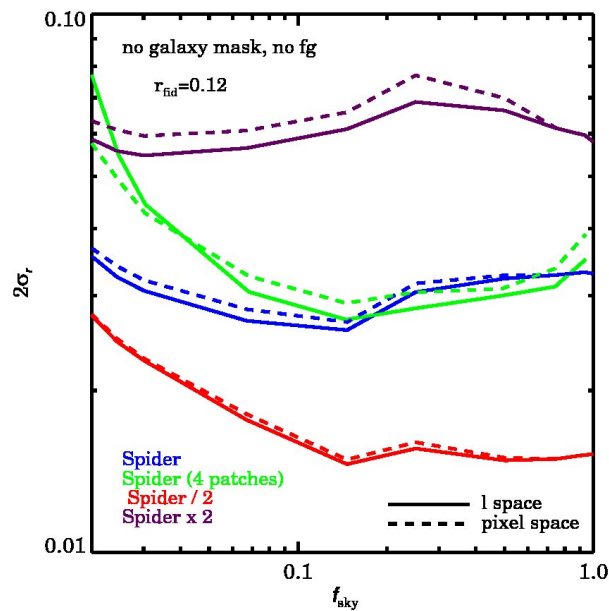


Figure 2.12: When one patch covering f_{sky} is broken up into four $f_{\text{sky}}/4$ cap-patches, but the noise and observing time remain constant, the (τ -marginalized) r -errors remain similar except at very small f_{sky} . We also show that factors of two changes in the noise swamp this effect. The calculations were done with $r_{\text{fid}} = 0.12$ in the pixel-space except for the highest sky coverages where the pixel and ℓ -space analysis are in excellent agreement. The effect of foreground contamination and Galaxy cut has not been taken into account here.

errors are correctly modelled. For realistic cut-sky observations, we measured the level of BB contamination from the inevitable mode-mixing from the much larger EE power. In addition, there is leakage from instrumental effects, in particular with T seeping into Q and U , which has to be included in any approach. We have left the investigation of this issue to future work.

2.6.2 Computational Feasibility of Exact Likelihoods

It is often the case in CMB cosmology that the sheer number of pixels precludes a direct full map-based likelihood procedure and necessitates an intermediate power spectrum determination before parameter estimation. However, for Spider and similar ground and balloon experiments targeting r , relatively low resolution and restricted sky coverage are all that is really needed for detection. The result is a total pixel number that allows computationally feasible inverse and determinant calculations of the large signal-plus-noise correlation matrices $\mathbf{C}_t = \mathbf{C}_n + \mathbf{C}_s(q)$ – with contributions from both the parameter-dependant signal covariance $\mathbf{C}_s(q)$ and the generalized noise \mathbf{C}_n , which includes uncertainties from the foreground subtraction as well as from instrumental and systematic noise in the maps

Map-based methods have had a long history, dating from the earliest CMB data sets (e.g., Bond & Crittenden, 2001). For example, they were used for COBE, Saskatoon, Boomerang, and CBI analyses. Often compression was used, e.g., to signal-to-noise eigenmodes (Bond, 1995; Bond & Crittenden, 2001) or by coarse-grained gridding (Myers et al., 2003), to make the matrix manipulations tractable. With Boomerang, an important aspect was to make sure all issues regarding data-filtering, inhomogeneous and aspherical beams, transfer functions, striping, etc. were properly included. Invariably, a Monte Carlo simulator of each experiment has been built, in which simulated timestreams have as many effects from systematic and data processing as one can think of included.

2.6.3 Matrix Estimation from Monte Carlo Noise and Signal Simulations and Relation to Master/XFaster

The Master/XFaster approach encodes this in isotropized ℓ -space filters and rotationally symmetrized masks which allow one to relate the underlying all-sky $\mathbf{C}_{s,cX\ell}$ to the filtered cut sky. Similarly an isotropized noise $\mathbf{C}_{n,cX\ell}$ is also determined by taking processed noise timestreams, creating maps with them, $Y_{\ell m}$ transforming them, then forming a quadratic average over noise samples J_s , $\mathbf{C}_{n,cX\ell} = \sum_{J_s, m} |a_{nJ_s, cX\ell m}|^2 / [(2\ell + 1)N_s]$.

When one has a large number of detectors, using only cross-correlations and no auto-correlations has an advantage, namely that the cross-noise is small, from systematic effects in the arrays and instrument as a whole. Precise modelling of the auto-noise is not easy. How-

ever, any operation that can be done for Master or X Faster can also be done to estimate the noise matrices, using noise sample sums. (Getting convergence of small off-diagonal components may require many samples.) Matrices have the advantage that they naturally allow for anisotropic and inhomogeneous components, in the noise maps - including striping effects - and in the beam maps and in the foreground maps. There are issues about optimal estimation of the generalized pixel-pixel matrices that one would like to tune, but there are no fundamental obstacles to making the \mathbf{C}_n and \mathbf{C}_s matrices highly accurate for parameter estimation.

WMAP used a map-based likelihood for low ℓ , connected to an isotropized ℓ -space likelihood covering the high ℓ 's. Planck is doing the same. We expect such a hybridized likelihood code will also be used for Spider-like experiments for routine parameter estimation, even though we think one can get away with a full map-based likelihood code.

If simulated timestreams are used for \mathbf{C}_n and \mathbf{C}_s estimation, generalized pixels may prove preferable to the usual spatial pixels. The Cosmic Background Imager CBI (Myers et al., 2003; Sievers, 2004) used the reciprocal space pixels for the primary construction, rather natural for an interferometry experiment where the timestream analog is a set of visibilities. ACT and QUaD also have done their power spectrum estimation in the Fourier transform space of spatial maps.

2.6.4 The CBIPol Approach as a Guide for Small Deep-sky Analyses

The use of map-based likelihood codes does not mean that E and B maps will not be constructed, just that parameters would not be extracted from them. The CBI example of how such E and B maps were made and used, and why bandpower and parameter estimations did not use E and B maps serves as a paradigm for how things could proceed for Spider-like data. The CBI data were compressed (via a GRIDR code) onto a discrete (reciprocal) lattice of wavenumbers by projecting measured interferometer visibilities onto a gridded 2D \mathbf{K} -space. A direct unitary transformation takes such a basis of “momentum” modes into a basis of spatial modes in real space where Q - U is a more appropriate representation. An important point is that the polarization map estimators evaluated on the discrete wavenumbers of the lattice are linear combinations of the continuous wavenumbers, the mode-coupling of finite maps which also leads to an E - B mixing.

In the lattice representation, the resulting size of the correlation matrices for CBI was quite tractable for direct inversion and the full likelihood was evaluated (via an mLikely code) to determine bandpowers for TT , EE , BB and TE , without separation of the Fourier maps into E and B .

An optimal linear map reconstruction of E and B was done for visualization purposes, with real-space and momentum-space maps showing the CBI E and B Wiener-filtered means,

accompanied by a few maps showing typical fluctuation maps about the mean maps. These were contour maps, since the usual headless vector polarization plots are of the length of polarization degree, $\sqrt{Q^2 + U^2}$, tilted at an angle $\arctan(U/Q)/2$.

For Spider-like bolometer-based experiments for which the raw data are bolometer time-streams from which Q - U maps are constructed, the compression step leads to tractable matrices as in the CBIpol case, although in the first instance the pixelization choice may be in real space rather than in wavenumber space or in a generalized-pixel space. Just as with CBIpol, parameters and bandpowers would be determined with direct likelihood calculations, yet Wiener-filtered E and B maps would still be made for visualization.

2.6.5 Exact 2D Likelihood Computation

Given the matrix construction method, we determined the posterior probabilities on reduced 2D-grids consisting of r and one other cosmic parameter, in many cases the Thomson scattering depth to reionization, τ . The grid could be extended to higher dimensions, as they were in early CMB analyses of COBE, Boomerang, CBI and ACBAR. More efficiently, MCMC chains could be used to explore the posterior probability surface. Since, as we have shown, r is relatively weakly correlated with the other standard cosmic parameters, our use of a reduced dimensionality is accurate. We targeted τ for a second parameter because of its importance for the reionization bump in BB which is picked by large f_{sky} experiments such as Planck. However, it too is weakly correlated for Spider-like experiments probing modest f_{sky} . We showed that as long as the input value r_{fid} is reasonably larger than the error σ_r , e.g., ~ 0.1 , r_{fid} can be well-recovered by our methods.

2.6.6 The Inflation and Tensor Consistency Checks

We have used r and n_t for our reduced 2D parameter space to see how well the inflation consistency condition, $n_t \approx -r/8$, can be tested. For example, with $r_{\text{fid}} = 0.12$ and the consistency value $n_{t,\text{fid}} = -0.015$, we obtain $2\sigma_r \approx 0.036$ and $2\sigma_{n_t} \approx 0.28$. The large 1-sigma error on n_t is what one might have expected given the relatively small ℓ -baseline (reminiscent of the ± 0.2 limit on n_s from the even smaller baseline COBE DMR data). Thus, although breaking up r into bands will be useful, the n_t slope that follows will not be powerful enough to test consistency. With CMBPol and at $N_{\text{side}} = 512$, the errors are $2\sigma_r \approx 0.014$ and $2\sigma_{n_t} \approx 0.07$, still too large. A more prosaic internal consistency check was done to show that what one thinks is r from the total BB agrees with what one gets from the less-tensor-sensitive total EE .

2.6.7 Relation to Planck

We based our Planck-like case on the Blue Book detector specifications. The actual in-flight performance is quite similar (Planck HFI Core Team et al., 2011; Mennella et al., 2011). What will emerge from the actual Planck polarization analysis may be quite different from the simplified foreground-free $2\sigma_r(f_{\text{sky}} = 0.75) \sim 0.015$ forecast of white experimental noise and with no systematics. This relies on the BB reionization bump being picked up, but the required low ℓ 's are especially susceptible to the foreground-subtraction residuals ($2\sigma_r(f_{\text{sky}} = 0.75) \sim 0.05$ for a model of well-subtracted foregrounds of known residual) and systematic effects. Some of the issues are described in Efstathiou et al. (2009). Irrespective of how well Planck wrestles with the low ℓ issues, it will be able to analyze many patches within the 75% of the sky, rank-ordered by degree of foreground contamination. Although such a procedure would lose the reionization bump, robustness to foreground threshold variation of any r -detection could be well demonstrated. Apart from its many other virtues, Planck should be very good for this.

2.6.8 Relation to Spider

The same strategy of using many fields with the lowest foregrounds to make up the total f_{sky} may also prove useful for Spider-like experiments (such as the ground-based ABS). We showed that splitting f_{sky} into four patches with fixed integration time and the instrument noise results in only a small loss in r -sensitivity because $\sigma_r(f_{\text{sky}})$ has a relatively wide single-patch minimum. How many polarization-foreground-clean patches there are is still to be determined.

Although the specifications we chose for “Spider-like” was motivated by a bolometer array experiment feasible with current technology, our forecasts should not be taken as realistic mocks of the true Spider which is under development, and for which a number of campaigns are envisaged (see the footnote under Spider-like in Table 2.5.1). The techniques used here have, however, already been applied in Spider forecast papers using more realistic statistically inhomogeneous noise, scanning strategies and observational durations, e.g., in Filippini et al. (2010) and Fraisse et al. (2011). On $f_{\text{sky}} \sim 0.1$, $r_{\text{fid}} = 0.01$ simulations, we compared the Fraisse et al. (2011) non-uniform noise modulated spatially by the scanning strategy’s number-of-hits-per-pixel with uniform white noise with the same integrated noise power. Although the deviation in the standard deviation of the noise rms was about a factor of two times the mean noise rms , with largest impact near the scanning boundaries, we found very similar results for the posterior, showing this paper’s conclusions are insensitive to our use of uniform white noise. (Of course the foreground noise radically alters the whiteness, and this of course has been included by us, but only in a statistically isotropic way — the Galactic latitude dependence breaks this isotropy just as the pixel hits do.) In § 2.5.4, we showed that in the absence of

foregrounds our Spider-like case could achieve $2\sigma_r \approx 0.02$ over a broad range of f_{sky} .

We presented Figure 2.1 in the introduction as a summary of the current and future r -posteriors. The forecasted likelihood curves were made with the numerical codes described here, for the Spider-like case (the default experiment of this paper), for the Spider experiment labeled as “Spider” in the plot (Fraisse et al., 2011), and for a more ambitious campaign of Spider, labeled as SCIP. We see that the performance of the experiment with Spider-like specifications used in this paper is very close to the actual Spider. A different foreground model used in Fraisse et al. (2011) for $f_{\text{sky}} \sim 0.1$ led to a similar $\sim 50\%$ error degradation.

2.6.9 History and Forecasts of r Constraints

When the large angle CMB anisotropies were first detected with COBE DMR, the broad-band TT power amplitude ($\ell \lesssim 20$), with wavenumbers $k^{-1} \gtrsim 1000$ Mpc, was related to the linear density power spectrum amplitude at the radically different $k^{-1} \sim 6$ Mpc scale, assuming a nearly scale-invariant primordial spectrum: $\sigma_8 \approx 0.85e^{-(\tau-0.1)}/\sqrt{1+0.6r} \times 1_{-0.6}^{0.7}$ for typical Λ CDM parameters popular in mid nineties, $\Omega_\Lambda \sim 2/3, h \sim 0.7$ (Bond, 1996a), rather similar to the values now. Requiring $\sigma_8 > 0.7$ to get reasonable cluster abundances at zero redshift – a venerable cosmological requirement from the 80s – gives a rough constraint on r from the COBE data in conjunction with large scale structure (LSS) data: $2\sigma_r < 1$ for current τ values – but τ only had an upper limit until WMAP1, with a more accurate determination waiting until WMAP3.

The first 2003 WMAP constraint on r from TT and TE CMB-only data (with weak priors) was $2\sigma_r < 0.81$, reducing to $2\sigma_r < 0.64$ with the WMAP3 TT, TE and EE data, and other TT CMB data available in 2005. It decreased to 0.31 with the LSS data of the time (MacTavish et al., 2006). The most recent r -constraint from the low ℓ amplitude and shape of the TT and EE spectra from WMAP9+ACT+SPT (Hinshaw et al., 2012) is the upper limit $2\sigma_r \sim 0.17$, reducing to 0.12 when LSS is added (Figure 2.1).

To make a further leap awaits an effective B -mode constraint. The current best constraint on r from the measurements of the B -mode amplitude comes from the QUIET experiment with $2\sigma_r < 2.8$ (QUIET Collaboration et al., 2012). As we have seen, Planck can give 0.015-0.05, Spider 0.014-0.02. The COre satellite proposal (The COre Collaboration, 2011) suggests better than a 3-sigma detection could be made for r_{fid} above 0.001 with bolometer arrays in space. The PIXIE satellite proposal (Kogut et al., 2011) claims $2\sigma_r \approx 4 \times 10^{-4}$ is achievable with Fourier Transform Spectrometry. We apply our methods to CMBPol specifications (Baumann et al., 2009). The two cases in Figure 2.1 show what a (very small) detection with $r_{\text{fid}} = 0.001$ ($2\sigma_r \approx 4 \times 10^{-4}$) and a non-detection with $r_{\text{fid}} = 0.0001$ ($2\sigma_r \approx 1.2 \times 10^{-4}$) would look like. If r_{fid} is as large as 0.12, as in the simple $m^2\phi^2$ chaotic inflation, we get $2\sigma_r \approx 0.015$ (and $2\sigma_{n_t} \approx 0.07$

encompassing the consistency input of $n_t = -0.015$). For a noiseless all-sky experiment, hence with errors from cosmic variance only, we get $2\sigma_r \approx 10^{-4}$ for $N_{\text{side}} = 128$ for tiny r_{fid} . It is unclear at this time how much inexact foreground subtraction and lensing noise will limit r determinations in these ideal cases.

2.6.10 The 1D Shannon Entropy of r

We have described another way to cast the improvements expected in r -estimation as experiments attain higher and higher sensitivity, the marginalized 1D Shannon entropy for r , $\Delta S_{\text{1f}}(r)$. This measures the (phase-space) volume of r -space that the measurement allows. It is obtained by direct integration over the normalized 1D likelihood for r , with all non-Gaussian features in the likelihood properly included. We have found in practice that $\Delta S_{\text{1f}}(r) \approx \Delta \ln[\sigma_r \sqrt{2\pi}]$, with σ_r determined by the forced Gaussianization described in the paper, works quite well, so in a way we are just restating the error improvements in the information theoretic language of bits.

We use the current WMAP9+ACT+SPT TT, TE and $EE + \text{LSS}$ $2\sigma_r \sim 0.12$ constraint (Hinshaw et al., 2012) for our baseline. The first WMAP constraint in 2003 (Spergel et al., 2003), with $\Delta S_{\text{1f}}(r) = 2.7$ bits had, of course, higher information entropy. Here, as in the abstract, we have translated from nats to bits. The asymptotic perfect noiseless all-sky experiment gives (the somewhat r -dependent) $\Delta S_{\text{1f}}(r) \approx -10$ bits, the limit on obtainable knowledge from the CMB. The proposed post-Planck COre, PIXIE and CMBPol-like experiments claim about -8 bits. For the Spider-like experiments forecasted here, the foreground-free decrease is -3.1 bits (and -2.6 bits with a 95% effective component separation). Thus balloon-borne and ground-based experiments with large arrays making deep surveys focussing on a relatively clean few-percent of the sky yield tensor information at least comparable to shallow and wide surveys and are a powerful step towards a near-perfect deep and wide satellite future.

We would like to thank our many Spider, ABS and Planck collaborators for many stimulating discussions about the experimental assault on CMB tensor mode detection. We would like to thank William C. Jones for his helpful comments on the text. We thank Marc Antoine Miville Deschênes for advice and aid on foregrounds. Support from NSERC, the Canadian Institute for Advanced Research, and the Canadian Space Agency (for PlanckHFI and Spider work) is gratefully acknowledged. Part of the research described in this paper was carried out at the Jet Propulsion Laboratory, California Institute of Technology, under a contract with the National Aeronautics and Space Administration. The large matrix computations were performed using the SciNET facility at the University of Toronto. Some of the results in this paper have been derived using the HEALPix package (Górski et al., 2005), <http://healpix.jpl.nasa.gov>.

Chapter 3

Semi-blind Eigen-analyses of Recombination Histories Using CMB Data

A version of this chapter has been published in the Astrophysical Journal as “Semi-blind Eigen Analyses of Recombination Histories Using Cosmic Microwave Background Data”, Farhang, M.; Bond, J. R.; Chluba, J. , Volume 752, Issue 2, article id. 88, 26 pp. (2012).

3.1 Chapter Overview

Cosmological parameter measurements from CMB experiments such as Planck, ACTPol, SPT-Pol and other high resolution follow-ons fundamentally rely on the accuracy of the assumed recombination model, or one with well prescribed uncertainties. Deviations from the standard recombination history might suggest new particle physics or modified atomic physics. Here we treat possible perturbative fluctuations in the free electron fraction, $X_e(z)$, by a semi-blind expansion in densely-packed modes in redshift. From these we construct parameter eigenmodes, which we rank order so that the lowest modes provide the most power to probe $X_e(z)$ with CMB measurements. Since the eigenmodes are effectively weighed by the fiducial X_e history, they are localized around the differential visibility peak, allowing for an excellent probe of hydrogen recombination, but a weaker probe of the higher redshift helium recombination and the lower redshift highly neutral freeze-out tail. We use an information-based criterion to truncate the mode hierarchy, and show that with even a few modes the method goes a long way from the fiducial recombination model computed with RECFast, $X_{e,i}(z)$, towards the precise underlying history given by the new and improved recombination calculations of COSMOREC or HYREC, $X_{e,f}(z)$, in the hydrogen recombination regime, though not well in the helium regime. Without

such a correction, the derived cosmic parameters are biased. We discuss an iterative approach for updating the eigenmodes to further hone in on $X_{e,f}(z)$ if large deviations are indeed found. We also introduce control parameters that downweight the attention on the visibility peak structure, e.g., focusing the eigenmode probes more strongly on the $X_e(z)$ freeze-out tail, as would be appropriate when looking for the X_e signature of annihilating or decaying elementary particles.

3.2 Introduction

The PLANCK Surveyor¹ is now well into its mission, observing the temperature and polarization anisotropies of the cosmic microwave background (CMB) with unprecedented accuracy (Planck HFI Core Team et al., 2011; Mennella et al., 2011). Both ACT (e.g., see Hajian et al., 2011; Dunkley et al., 2011; Das et al., 2011) and SPT (Lueker et al., 2010; Vanderlinde et al., 2010) are pushing the frontier of TT CMB power spectra at small scales, and in the near future SPTPOL² (Austermann et al., 2012) and ACTPOL³ (Niemark et al., 2010) will provide additional small scale E -mode polarization data, complementing the polarization power spectra obtained with PLANCK and further increasing the significance of TT power spectra.

Using these datasets, cosmologists will be able to determine the key cosmological parameters with high precision (The Planck Collaboration, 2006; Tauber et al., 2010), making it possible to distinguish between various models of *inflation* (e.g. see Komatsu et al., 2011, for recent constraints from WMAP) by measuring the precise value of the spectral index of scalar perturbations, n_s , and constraining its possible running, n_{run} , as well as the tensor-to-scalar ratio, r . In addition many non-standard extensions of the minimal inflationary model are under discussion, and the observability of these possibilities with PLANCK (The Planck Collaboration, 2006) and future CMB experiment is being considered.

These encouraging observational prospects have motivated various independent groups (e.g. see Dubrovich & Grachev, 2005; Chluba & Sunyaev, 2006b; Kholupenko & Ivanchik, 2006; Switzer & Hirata, 2008; Wong & Scott, 2007; Rubiño-Martín et al., 2008; Karshenboim & Ivanov, 2008; Hirata, 2008; Chluba & Sunyaev, 2008; Jentschura, 2009; Labzowsky et al., 2009; Grin & Hirata, 2010; Ali-Haïmoud & Hirata, 2010) to assess how uncertainties in the theoretical treatment of the cosmological recombination process could affect the science return of PLANCK and future CMB experiments. The precise evolution of the free electron fraction, X_e , with time influences the shape and position of the peak of the Thomson visibility function, which

¹<http://www.rssd.esa.int/Planck>

²<http://pole.uchicago.edu/>

³<http://www.physics.princeton.edu/act/>

defines the last scattering surface (Sunyaev & Zeldovich, 1970; Peebles & Yu, 1970), and hence controls how photons and baryons decouple as electrons recombine to form neutral helium and hydrogen atoms. Consequently, the ionization history changes the acoustic oscillations in the photon-baryon fluid during recombination and therefore directly affects the CMB temperature and polarization power spectra. For the analysis of future CMB data this implies that in particular close to $z \sim 1100$ the ionization history better be understood at the $\sim 0.1\%$ level.

Probing the ionization history in time is equivalent to probing it in space with the light cone relating the two. Thus what we try to do in this paper, namely to come up with optimized probing functions for the recombination history, is quite akin to creating probes of the spatial structure of the boundary between HII and neutral hydrogen regions. Here of course we look from neutral to ionized, the cosmological recombination problem being an inside-out HII region, except in a predominantly electron scattering regime with a very large photon to baryon ratio which lowers the transition temperature between ionized and neutral.

The old recombination standard was set by RECFAST (Seager et al., 1999, 2000), but its reliability for the precision cosmology was brought into question, e.g., by Seljak et al. (2003). For the standard six parameter cosmology in particular our ability to measure the precise value of n_s and the baryon content of our Universe may be compromised if modifications to the recombination model of RECFAST are neglected (Rubiño-Martín et al., 2010; Shaw & Chluba, 2011), introducing biases of a few σ for PLANCK.

Currently it appears that *all* important corrections to the *standard* recombination scenario (SRS hereafter) have been identified (e.g., see Fendt et al., 2009; Rubiño-Martín et al., 2010, for an overview). The new recombination codes, COSMOREC (Chluba & Thomas, 2011) and HYREC (Ali-Haïmoud & Hirata, 2011) both account for these modifications to the SRS, superseding the physical model of RECFAST and allowing fast and accurate computation of the ionization history on a model-by-model basis. COSMOREC and HYREC presently agree at a level of $\sim 0.1\% - 0.2\%$ during hydrogen recombination, so that from standard recombination physics little room for big surprises seems to be left.

However, *what if something non-standard happened? What if something was overlooked in the standard recombination scenario?* From the scientific point of view the ionization history is a theoretical ingredient to the cosmological model, which usually is assumed to be precisely known and not subject to direct measurement. Clearly, it is important to estimate the possible level of uncertainty in the recombination model and to confront our understanding of the recombination problem with direct observational evidence. Here we describe how well future cosmological data alone are able to constrain possible deviations from the SRS.

In the past, several non-standard extensions of the recombination scenario have been considered. These include models of *delayed recombination*, in which hypothetical sources of ex-

tra photons that can lead to ionizations or excitations of atoms are introduced using simple parametrizations (Peebles et al., 2000). In particular, models of *decaying* (e.g., see Chen & Kamionkowski, 2004; Zhang et al., 2007) and *annihilating particles* (e.g., see Padmanabhan & Finkbeiner, 2005; Zhang et al., 2006; Galli et al., 2009a; Hütsi et al., 2009; Slatyer et al., 2009; Hütsi et al., 2011; Galli et al., 2011) were discussed. In addition to extra photons, *varying fundamental constants* (e.g., see Kaplinghat et al., 1999; Scóccola et al., 2009; Galli et al., 2009b) could affect the recombination dynamics in subtle ways.

All these ideas rely on a specific model for the (physical) process under consideration, with the derived constraints depending on the chosen parametrization. This minimizes the number of additional parameters, but does not allow us to answer questions about more general perturbations around the SRS and how well they can actually be constrained.

Here we approach this problem in a different way. We introduce perturbations to the SRS over a wide range of redshifts around hydrogen ($z \sim 1100$) and helium ($z \sim 1800$) recombination, using different basis functions. We then compute the corresponding signals in the CMB power spectra and perform a principal component decomposition to obtain eigenmode functions, ordered with respect to the level at which they can be constrained by the data. We study in detail how the eigenmodes depend on the chosen parametrization for the recombination perturbations as well as the fiducial model and different experimental settings.

Our method is similar to the one used by Mortonson & Hu (2008), where the eigenmodes for different reionization scenarios ($6 \lesssim z \lesssim 30$) were constructed. However, here we explicitly construct the mode functions at redshifts $z \gtrsim 200$, with particular attention to the dependence of the eigenmodes on different assumptions. We investigate how to use our prior knowledge of possible perturbations of the ionization history to choose the parametrization which is more preferred by the data. We also carry out a careful convergence study and show the equivalence of different basis functions (e.g., triangles, Gaussian bumps, Fourier series and Chebyshev polynomials). We particularly focus on the helium recombination problem, showing that in the absence of very tight constraints on the hydrogen recombination, we are unable to unravel well remaining uncertainties in helium recombination with CMB data. Similarly, small changes in the freeze-out tail of recombination are only weakly constrained, if possible ambiguities during hydrogen recombination are included.

Details of the general methodology to construct the eigenmodes for perturbations to ionization history are given in § 4.3 and Appendices 3.7.1, 3.7.2 and 3.7.3. In § 3.4 we compute different eigenmodes over a rather wide redshift range ($z \in [200, 3000]$) and investigate their properties. In § 3.4.6 we develop a criterion which allows us to truncate the hierarchy of the eigenmodes based on their information content. In § 3.5 the modes are applied to two specific examples of ionization scenarios, illustrating how the method should be used with real CMB

data. At the end of that section, we also discuss how the approach should be iterated if hints toward a considerable difference between the assumed and true model of recombination are indicated by the data. We close the paper by a brief discussion.

3.3 Methodology

In this section we introduce the approach and parametrization used to construct the principal components, or the eigenmodes, which is later used to describe possible corrections to the recombination scenario. Our method is mainly driven by the assumption of *small relative* perturbations around the fiducial model computed with the RECFAST code (Seager et al. (1999); see Wong et al. (2008) for recent updates). As an example we have in mind the recombination corrections obtained with refined recombination models (Chluba & Thomas, 2011; Ali-Haïmoud & Hirata, 2011). However we also briefly discuss the possibility to constrain significant changes in the freeze-out tail of recombination and modes that mainly focus on helium recombination.

Throughout this paper the cosmic parameters, referred to as the standard (cosmological) parameters, are $(\Omega_b h^2, \Omega_{\text{dm}} h^2, H_0, \tau, n_s, A_s)$ as measured by WMAP7⁴, unless stated otherwise. In several cases we also vary Y_p as a seventh parameter. Lensing is included in all simulations if not explicitly stated otherwise.

3.3.1 The standard recombination scenario

The cosmological recombination history is one of the major theoretical inputs for computations of the CMB anisotropies. Consequently, high precision unbiased cosmic parameter measurements from current and future CMB experiments require a sufficiently accurate model for hydrogen and helium recombination.

The ionization fraction for the SRS is shown in the left panel of Fig. 3.1. It was calculated using RECFAST v1.4.2, which accounts for some of the modification to helium recombination (Kholupenko et al., 2007; Switzer & Hirata, 2008; Rubiño-Martín et al., 2008; Chluba & Sunyaev, 2010) using fudge parameters, but neglects detailed radiative transfer corrections (see Chluba & Thomas, 2011; Ali-Haïmoud & Hirata, 2011, and references therein) around $z \sim 1100$. The solid curve corresponds to an ionization fraction with the measured temperature of the CMB radiation, $T_{\text{CMB}} \sim 2.726\text{K}$ (Fixsen, 2009). For comparison and to illustrate the temperature dependence of the ionization history, the ionization fraction corresponding to $T_{\text{CMB}} = 3\text{K}$ is also plotted (dashed curve). A larger value of T_{CMB} means more photons in the

⁴http://lambda.gsfc.nasa.gov/product/map/dr4/params/lcdm.sz.lens_wmap7.cfm

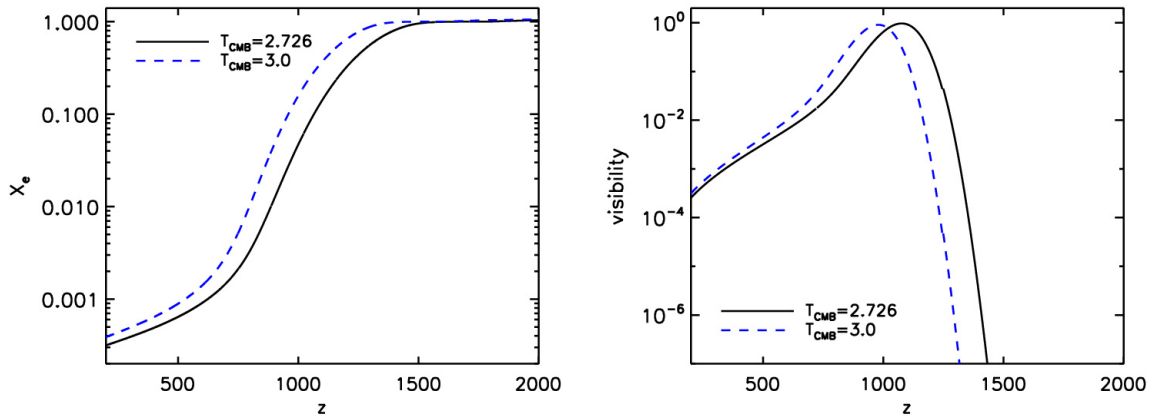


Figure 3.1: The cosmological ionization history (left), $X_e \equiv N_e/[N_p + N_{\text{HI}}]$, and differential visibility function (right) for the standard recombination scenario with $T_{\text{CMB}} = 2.726\text{K}$ (Fixsen, 2009) contrasted to a case with $T_{\text{CMB}} = 3\text{K}$. Here N_p and N_{HI} represent the number density of ionized and neutral hydrogen, while N_e denotes the number density of free electrons. The visibility function has been plotted in units of maximum visibility.

Wien tail of the CMB blackbody, so that the matter is kept ionized until lower redshift.

On the right the corresponding differential visibility functions (or visibility functions for short) are plotted:

$$g(z) \equiv \frac{de^{-\tau(z)}}{d\eta},$$

where η is the conformal time and τ is the Thomson scattering optical depth from redshift z to now.

The visibility function describes the probability that a photon we observe today last scattered off free electrons at a certain position along the line of sight. The CMB anisotropies formed mainly during the epoch of hydrogen recombination defined by the peak of the visibility function located at redshift $z \sim 1100$. They are thus most sensitive to changes around the maximum of visibility. For example, an increase in the width of the visibility bump corresponds to a more extended or slower recombination process, leading to more Thomson scatterings of photons off free electrons. These scatterings lead to the cancellation of the CMB anisotropies along the line of sight on scales comparable and smaller than the recombination width, while enhancing the polarization signal on larger scales. The location of the maximum of the visibility function for an assumed cosmological model, on the other hand, determines the distance to the last scattering surface. This in turn affects the positions of the peaks of the CMB power spectra. Similarly, any change in the ionization history, through affecting the visibility, leads

to (possibly measurable) changes in the CMB power spectra.

As the right panel of Fig. 3.1 indicates, at high redshifts $z \gtrsim 1400$ the visibility function falls off very quickly. At those times the number of free electrons is still so large that scatterings occur very frequently and the mean free path is very short. Consequently, the part of the ionization history which is connected to helium recombination mainly affects the damping tail of the CMB anisotropies, but even there the effect is rather moderate, as in the redshift range⁵ $1400 \lesssim z \lesssim 3000$ helium can at most alter the number of electrons by $\sim 8\%$.

3.3.2 Choice of perturbation parametrization

There are different ways to parametrize possible deviations from the assumed fiducial ionization history in a (semi-)model-independent way. For example, to study how well the low redshift ionization history ($6 \leq z \leq 30$) can be constrained by future CMB data, Hu & Holder (2003) and Mortonson & Hu (2008) introduced changes in the ionization fraction in different redshift bins with $\delta X_e(z) = \text{const}$ to parametrize the uncertainties. This is a valid choice for the low redshift region, because our ignorance of the underlying model of reionization does not suggest any preferred non-uniform weighting of the perturbations at different redshifts. In this regime $\delta X_e(z)$ probes the ionization fraction itself and not perturbations guided by a fiducial model. The results from this choice of parametrization are shown to be fiducial model-independent which is expected due to the weak signal from the reionization process.

In contrast to this, at high redshifts ($z \sim 1100$) there is strong theoretical support for the exhaustively studied model of recombination in the realm of standard atomic physics and radiative processes. Also, the current generation of CMB data is sensitive to changes in X_e at the level of a few percent. Therefore the main assumption in this paper is that the *fiducial* model for the ionization history, $X_e^{\text{fid}}(z)$, is close to the true underlying history, $X_e(z)$, which we are looking for. We call this method *semi-blind* emphasizing our belief in the SRS as the framework of recombination, with the search for deviations being limited to small perturbations around this reference model. The goal is to detect or place upper limits on possible small deviations. Clearly, if data point toward significant deviations from the SRS, an iterative approach should be adopted, as discussed in § 3.5.4.

With small deviations in mind we can write:

$$X_e(z) = X_e^{\text{fid}}(z) + \delta X_e(z),$$

with $|\delta X_e|/X_e^{\text{fid}} \ll 1$. A natural parameter to describe the perturbation is then the relative

⁵The recombination of doubly ionized helium ends around redshift $z \sim 5000$.

deviation in the ionization fraction:

$$\delta u(z) \equiv \delta X_e(z)/X_e^{\text{fid}}(z) \quad \text{with} \quad |\delta u(z)| \ll 1. \quad (3.1)$$

This parametrization has the advantage of always satisfying the necessary condition $X_e \geq 0$. It is also straightforward to fulfill $X_e \leq X_{e,\text{max}}$ in the simulations, where $X_{e,\text{max}}$ is determined by Y_p , the primordial helium mass abundance, through $X_{e,\text{max}} \simeq 1 + Y_p/2(1 - Y_p)$. The parametrization in Eq. (3.1) weights possible perturbations at different redshifts by the fiducial ionization fraction. This implies that for $\delta u(z) = \text{const}$ the absolute change in the ionization fraction $|\delta X_e|$ is down-weighted in the freeze-out tail of X_e ($z \lesssim 800$; see Fig. 3.1), compared to perturbations around maximum visibility ($z \sim 1100$) where X_e rapidly approaches unity. Throughout this paper $\delta u(z)$ as defined in Eq. (3.1) is our main choice of parametrization.

A more general parameter which includes the above parametrization as a special case is given by:

$$\delta u(z) \equiv \delta X_e(z)/[X_e^{\text{fid}}(z) + \sigma(z)], \quad (3.2)$$

where $\sigma(z) \geq 0$ can be a constant or otherwise convenient function of redshift allowing to focus on different redshift ranges of interest. In particular, when considering possible modifications to the ionization history introduced by *energy injection*, e.g. because of annihilating dark matter, or decaying relic particles (Chen & Kamionkowski, 2004; Padmanabhan & Finkbeiner, 2005; Zhang et al., 2006, 2007; Hütsi et al., 2009; Slatyer et al., 2009; Galli et al., 2009a; Hütsi et al., 2011; Galli et al., 2011), where the freeze-out tail of recombination is disturbed, a value of $\sigma \gg X_e^{\text{fid}}$ might be a good choice, giving higher weight to the perturbations in the lower redshift part (see § 3.4.1 and Fig. 3.12). In the limit of a high value of σ relative to the fiducial X_e the parameters approach $\delta u(z) = \delta X_e(z)$ which uniformly weights perturbations at different redshifts. This, as already discussed, is a good choice for regions where there is no strong *a priori* belief in the underlying model or if the redshifts of interest have comparatively low X_e where $\delta u(z)$ with $\sigma = 0$ does not lead to strong enough signals to probe. In principle, a conveniently chosen redshift dependent $\sigma(z)$ is a tool to effectively incorporate our prior knowledge of the ionization history in the parametrization of its perturbations. For example, with $\delta u(z)$ defined by Eq. (3.2) one can smoothly interpolate between relative and absolute perturbations to X_e , at high and low redshifts respectively. Also it is clear that one can focus on different parts of the recombination history by limiting the redshift range over which the eigenmodes are constructed, e.g., just on reionization ($0 \lesssim z \lesssim 30$) or helium recombination ($1400 \lesssim z \lesssim 3000$).

Alternative parametrizations

We comment that instead of directly perturbing the ionization fraction, as we chose here, it is plausible to parametrize possible changes in the physical *sources* of perturbation to the

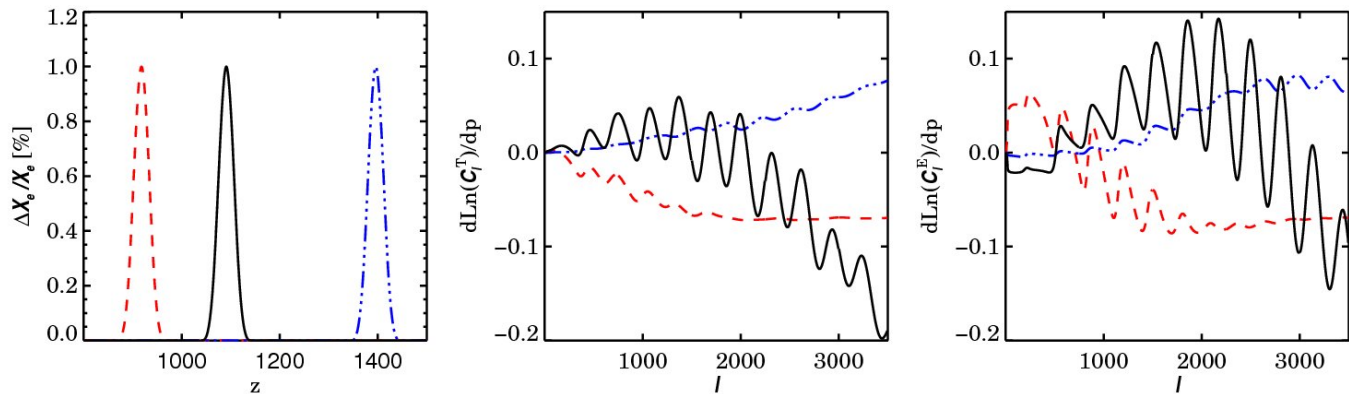


Figure 3.2: Localized perturbations in the X_e history, in the form of M_4 splines (left) and the derivatives of the C_ℓ 's with respect to the amplitude of each perturbation (TT power spectrum in the center, EE on the right).

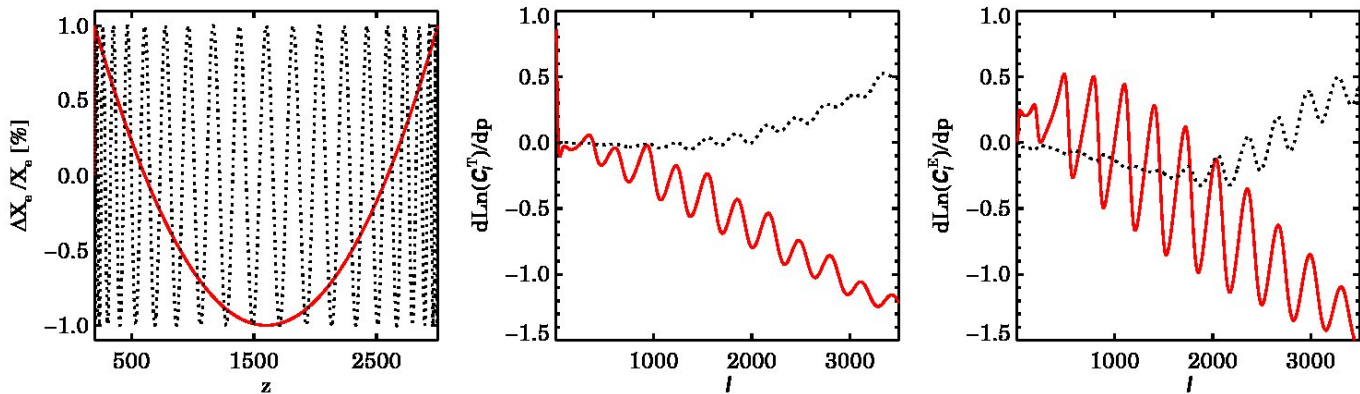


Figure 3.3: Similar to Fig. 3.2 but for non-localized perturbations in the form of Chebyshev polynomials.

ionization history, such as energy injection in the medium which leads to excitation or ionization of atoms, or the Ly α escape probability during recombination (see introduction). For example Mitra et al. (2011) chose the number of photons in the IGM per baryon in collapsed objects as the parameter to study the low redshift ionization history. Alternatively, one could modify the fudge factors or functions in RECFAST, or alter the expansion rate given by the Hubble factor, $H(z)$.

Each of these possibilities implies different priors on the regions that can be altered and, e.g., in the case of $H(z)$, other aspects of the cosmological model are also affected. They also cover, in general, only a limited class of changes to the recombination history. When interested in perturbations to the ionization history, X_e is the physical quantity which, via the visibility function and the optical depth, most directly enters the Boltzmann equations describing the evolution of radiation anisotropies routinely solved using the Boltzmann codes such as CAMB (Lewis et al., 2000) or CMBFAST (Seljak & Zaldarriaga, 1996).

The ionization fraction has the additional advantage, over the visibility and the optical depth, of being straightforward to limit to physically allowed values. The nearly direct mathematical encounter of X_e with CMB anisotropies guarantees that any perturbation in the plasma that would lead to changes in the radiation anisotropies should go through and thus be reflected in X_e . Therefore the relative changes in X_e constitute our preferred physical parameters.

We close by mentioning that, it is also theoretically possible to consider different variables for time such as (conformal) time, optical depth and scale factor. However, for our purpose we choose to work with redshift to describe temporal dependence. In principle different parametrizations, if they cover the same range of physical perturbations, can be transformed to one another with the proper change of the *a priori* distribution of parameters. Here, in the absence of physically motivated constraints, a uniform prior is assumed for perturbations at different redshifts regardless of parametrization (here, e.g., for various values of σ in Eq. (3.2)). If the perturbation is strongly constrained by data, the choice of the prior does not play a major role.

3.3.3 Basis functions and their different characteristics

Having chosen the parametrization, we now expand the perturbations in a discrete set of mode (or basis) functions, $\varphi_i(z)$:

$$\delta u(z) = \sum_{i=1}^N y_i \varphi_i(z) + r(z) \quad z_{\min} \leq z \leq z_{\max} \quad (3.3)$$

and $\delta u(z) = 0$ elsewhere. Here $r(z)$ is the residual and y_i 's are the parameters defining the strength of the mode $\varphi_i(z)$. Often we take $\varphi_i(z)$ to be localized in z about a *knot* value z_i , but

this is not necessary. We can, for example, choose the $\varphi_i(z)$ to form a complete orthonormal set in which case $N \rightarrow \infty$ and the residual r approaches zero. Below we discuss different possibilities for the mode functions. We modified the publicly available code CAMB⁶ to simulate CMB power spectra for a more general recombination scenario that includes perturbations on top of the SRS. Introducing narrow features into the ionization history also required an increase in the redshift sampling of X_e . We checked the numerical convergence and stability of the results by using high accuracy settings.

Localized basis functions. We first investigated three sets of localized basis functions: Gaussian and triangular bumps, which can be considered as approximations to the Dirac δ -function, and M_4 splines, a commonly used kernel in Smoothed-Particle Hydrodynamics. For a detailed description of these functions and how their properties compare, see Appendix 3.7.1. As examples for localized perturbations, Fig. 3.2 shows three perturbation functions $\delta u(z) = \delta \ln(X_e)$ using M_4 splines (left panel) and the corresponding C_ℓ response in TT and EE . The perturbations are located at different redshifts and have equal widths. We see that the amplitude of the response typically increases at smaller scales indicating a change in the duration of the recombination epoch (i.e., the effective width of the visibility function). The C_ℓ response also has an oscillatory component similar to a change of the position of the visibility peak. These oscillations are most noticeable for the perturbations close to the visibility peak ($z \sim 1100$).

Non-localized basis functions. We also expanded the perturbations in terms of two non-localized basis functions, namely a *Fourier series* and *Chebyshev polynomials*. For more details see Appendix 3.7.2. The non-local basis functions are very different in nature from the localized ones discussed above. Therefore the response of the observables (here the C_ℓ 's) to the perturbation $\delta u(z)$ in the form of these functions is also expected to be rather different. Figure 3.3 shows the C_ℓ responses when perturbing the ionization history using Chebyshev polynomials with different frequencies. We see that perturbations with low frequencies, covering a large redshift range, lead to C_ℓ responses with much larger mean amplitudes when compared to the perturbations in the form of local bumps (Fig. 3.2). However, as the frequency of the oscillations of the basis function increases, the response becomes weaker and its oscillations damp away. That is because neighbouring oscillations lead to similar responses in the C_ℓ 's with opposite signs and can partially cancel each other. In other words, the CMB power spectra are less sensitive to high frequency perturbations in the ionization history.

In principle, in the limit of large mode number, all bases work well (see §3.4.1). However, we found that for the recombination history, although non-localized basis sets have their virtues, the z -localized bases are better, especially if we are trying to describe narrow features in redshift.

⁶<http://camb.info/>

We return to this point in § 3.4.1.

3.3.4 Constructing the eigenmodes

So far we introduced our choice of parametrization for characterizing possible perturbations to X_e and illustrated how different set of basis functions affect the CMB power spectra. In principle all the amplitudes y_i defined in Eq. (3.3) are needed for a (nearly) complete reconstruction of a general perturbation $\delta u(z)$. However, in practice data cannot constrain the perturbations in detail in many cases. As we saw in Fig. 3.3, very high frequency perturbations are expected to lead to much smaller signals.

To avoid dealing with many correlated (and possibly weakly constrained) parameters (i.e., the y_i 's), we construct a set of their linear combinations which are uncorrelated with each other and only keep those combinations that are most constrained by data. This procedure provides a hierarchy of mode functions and their corresponding signals in the CMB temperature and polarization power spectra. Exclusion of the weakly constrained eigenmodes does not affect the measurement of the rest of parameters since the eigenmodes describing the recombination perturbations are by construction uncorrelated. The standard well-developed procedure of using an orthogonal transformation to replace the parameters of the problem with a set of uncorrelated variables is called *principal component analysis* or PCA for short. The parameter eigenmodes were used for CMB in Bond (1996a) and subsequently in Bond et al. (1997) and many subsequent papers.

In the process of eigenmode construction for the perturbations, assuming the standard parameters are known with high precision (see discussion in § 3.4.3), one only needs to deal with the perturbations in a fixed background cosmology. We call these modes X_e eigenmodes, or XeMs for short. However, for cases where the cosmic parameters are also measured simultaneously with the perturbations, these XeMs are no longer the optimal perturbation patterns. They do not stay uncorrelated and the uncertainty in their measurement increases, as we see in § 3.5.1. In such cases, the effect of the correlation of the cosmic parameters with the perturbations needs to be taken into account while constructing the eigenmodes. In other words, the modes should be marginalized over the standard cosmic parameters. We call these eigenmodes the *extended* X_e eigenmodes or eXeMs. The eXeMs stay uncorrelated to each other (but not necessarily to the standard parameters) even in the presence of varying background cosmology. A detailed discussion of the PCA for both fixed and varying background cosmology is presented in Appendix 3.7.3.

In general, the PCA needs to be applied to the whole ionization history simultaneously (as well as the standard cosmic parameters), since we do not know *a priori* how the ambiguity in one epoch affects the measurements of perturbations in other epochs. However, if it turns

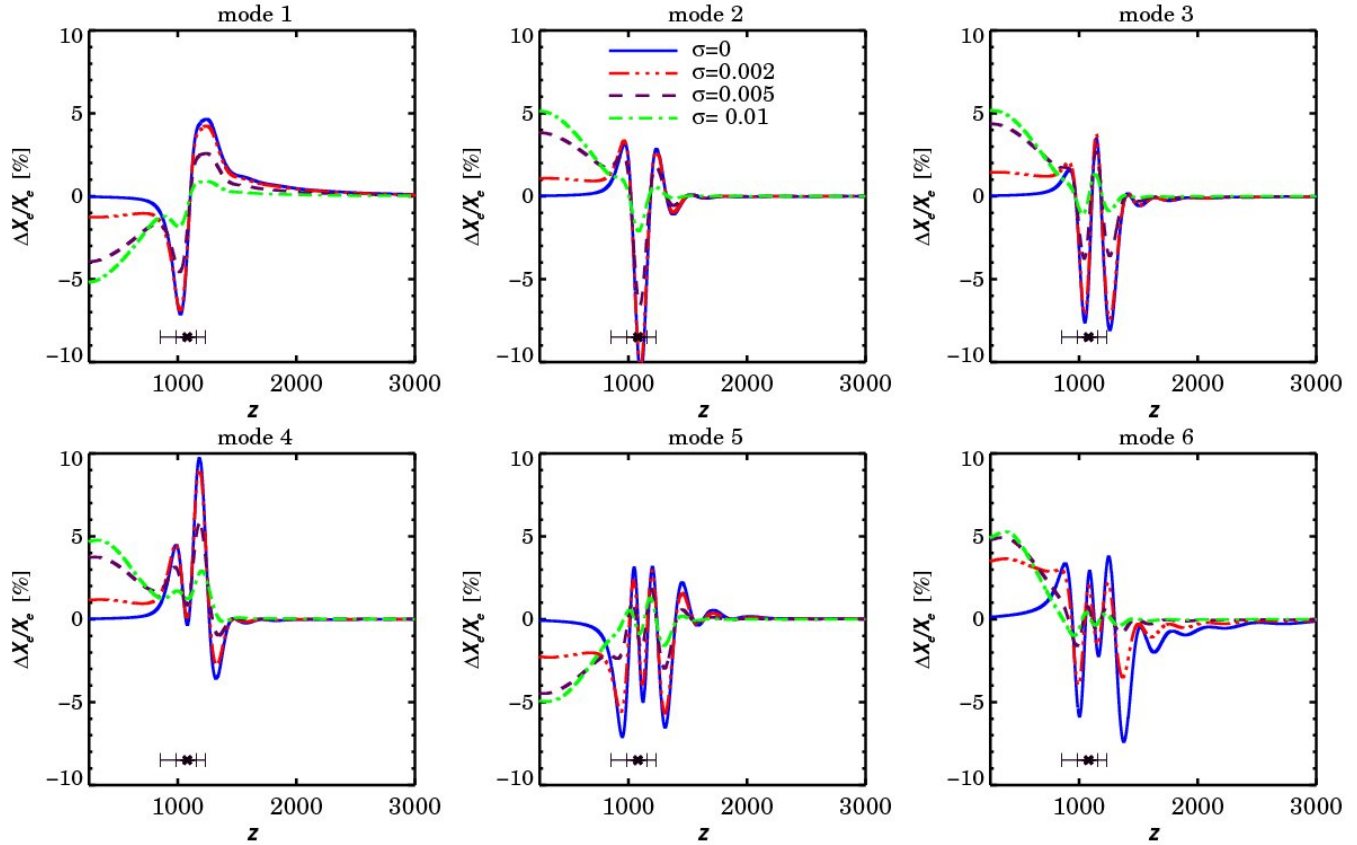


Figure 3.4: The six most constrained XEMs with $\delta u(z) = \delta \ln(X_e + \sigma)$ as the parameter, having four different values for σ , and with Gaussian bumps as the basis functions. The maximum and width (at 68% and 95% levels) of the Thomson visibility function have been marked in all figures.

out that a particular period of X_e history could be relatively well constrained, e.g. by other cosmological probes, one could leave that epoch out of perturbations. Moreover, choosing a suitable parametrization, potentially changing over time to properly take into account the different physics at different epochs, is a necessary but not straightforward task. In this work, the focus is on the epoch of recombination since that is where the main CMB signal is coming from. A more complete analysis for the whole ionization history or where different parts of it are considered simultaneously is for future work.

We mention that in the process of eigenmode construction it is also possible to treat the standard parameters depending on the way they affect the power spectra. Among the standard parameters, Y_p has this unique property of influencing C_ℓ 's *only* through its impact on X_e . In other words, if we find the X_e template in X_e parameter space corresponding to Y_p , i.e., dX_e/dY_p , small changes in Y_p can be mimicked by properly changing the amplitude of this

template while Y_p is left unchanged. Note that changes in other standard parameters either directly lead to changes in the CMB with no influence on X_e (such as n_s and A_s), or have both direct and indirect (i.e., through X_e) impacts on the CMB (such as Ω_b). Therefore, when including a Y_p -like parameter in the analysis, we can restrict our search for the perturbation eigenmodes to the part of X_e space which is uncorrelated to the X_e template corresponding to this parameter as described above. In this way if perturbations to X_e are initially described by N parameters, in the end we have the Y_p -like parameter or its associated template as one parameter and $N - 1$ eigenmodes which are uncorrelated to the Y_p -like parameter. These $N - 1$ eigenmodes together with the Y_p -like parameter fully describe the original N -dimensional space of the perturbations. However, for the purpose of this work we did not further explore this possibility.

3.4 Perturbation eigenmodes for Recombination

In this section we follow the procedure of § 3.3.4 (and Appendix 3.7.3) to find the eigenmodes for perturbations in the ionization fraction at high redshifts. We choose the redshift range of $[200, 3000]$ which covers hydrogen and singly ionized helium recombination ($z \sim 1100$ and $z \sim 1800$ respectively) as well as part of the dark ages while leaving reionization ($z \lesssim 30$) unaltered. We assume the fiducial recombination history is given by the SRS, as explained in § 3.3.1, unless otherwise stated.

In the following (and in Appendix 3.7.4) we compare the eigenmodes generated by using various bases and several different parametrizations and study some of the aspects associated with them, such as their convergence and fiducial model dependence. Special attention is given to perturbation to helium recombination. We also study how including the standard cosmic parameters in the analysis changes the eigenmodes. We propose an information-based criterion for truncating the eigenmode hierarchy to be used in the data analysis. Finally, in two examples, we show how these eigenmodes help reconstruct some physically motivated perturbations.

3.4.1 XeM construction

In this section we use the perturbation parametrization $\delta u(z) = \delta \ln(X_e + \sigma)$ with various values of σ , including $\sigma = 0$. For each σ we calculate the $N \times N$ Fisher information matrix as explained in the Appendix 3.7.3 where the N parameters are the amplitudes of the perturbations in the form of the basis functions (e.g., Gaussians), i.e., y_i 's introduced in Eq. (3.3). The standard cosmic parameters are fixed to their fiducial values. For the *data* we simulate the TT , TE and EE spectra up to $\ell = 3500$ for a full-sky, cosmic variance-limited (hereafter CVL) CMB experiment, unless otherwise stated. We then construct the Fisher matrix (Eq. (3.8)) and from

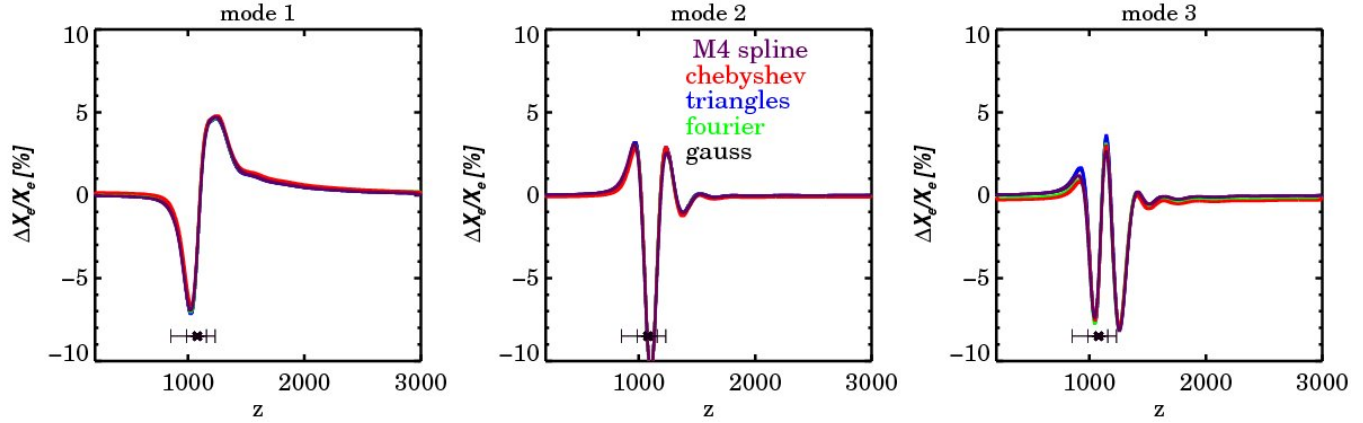


Figure 3.5: The three most constrained XEMs for five different basis functions (with 160 parameters).

Table 3.1: The forecasted standard deviations of the first six XEMs ($\sigma = 0$) from the Fisher analysis for different observational cases.

XeM	1	2	3	4	5	6
CVL($\ell_{\max} = 3500$)	0.003	0.009	0.013	0.016	0.022	0.047
CVL($\ell_{\max} = 2000$)	0.011	0.019	0.024	0.041	0.094	0.190
CVL($\ell_{\max} = 3500$, T only)	0.004	0.021	0.064	0.103	0.208	0.275
Planck-ACTPol($\ell_{\max} = 3500$)	0.015	0.047	0.068	0.13	0.22	0.31

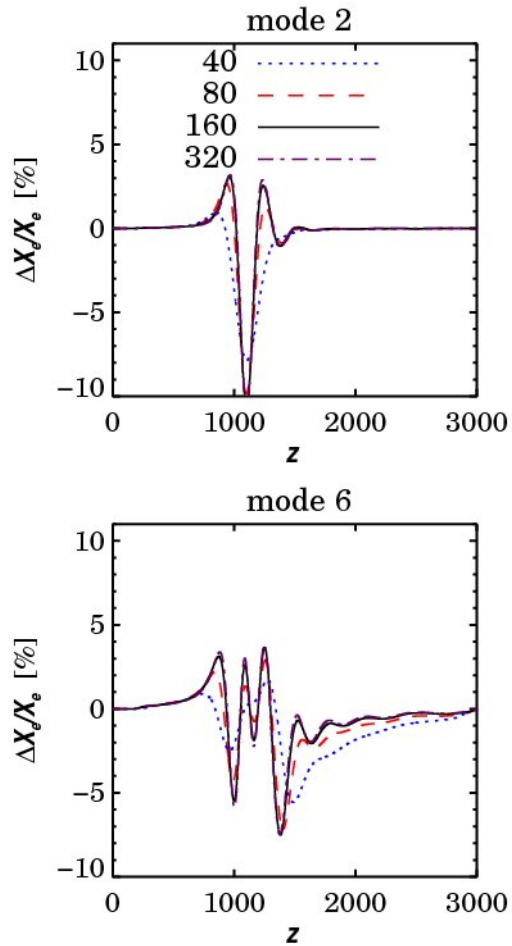


Figure 3.6: Testing the convergence of the eigenmodes. As examples, the second and the sixth most constrained XeMs are shown for cases with different number of parameters (40, 80, 160 and 320) and with M_4 splines as the basis functions. We see that the modes for 160 and 320 parameters are basically the same, indicating that these modes have already converged with 160 parameters.

it the N XeMs (Eq. (3.10)). The first six XeMs for $N = 160$ and for four values of σ are shown in Fig. 3.4. The first row in Table 3.4 shows the forecasted errors of these XeMs for $\sigma = 0$, obtained from the eigenvalues of the Fisher matrix. Note that including standard parameters in the analysis, e.g. in Markov-Chain Monte-Carlo (MCMC) simulations, increases the error bars, as we discuss in § 3.5.

We see that the first six XeMs – which are the most constrained modes – all have the strongest variations close to the maximum of Thomson visibility function and the freeze-out tail is not perturbed significantly, especially for lower values of σ 's. As σ increases, however, the amplitude of the XeMs in the freeze-out tail increases. This is because choosing $\sigma > 0$ results in over-weighting the signal from perturbations at low z (with low X_e) compared to a case with $\sigma = 0$ for the same value of $\delta u(z)$. It is illustrated in § 3.4.7 that a relatively high value for σ is the preferred choice for studying perturbations that most significantly alter the freeze-out tail.

The oscillations around helium recombination ($z \sim 1800$) have also much smaller amplitude than those at $z \sim 1100$. This is expected since the CMB anisotropies are most sensitive to perturbations during maximum visibility and features at low and high redshift are not weighing as much in the CMB power spectra, if uncertainties close to $z \sim 1100$ are admitted. This in turn implies that only once the ionization history during hydrogen recombination is known well can small modifications at higher redshift or in the freeze-out tail be constrained.

In Fig. 3.4, we can observe another aspect of the XeMs: the larger the expected error bar the more high frequency oscillations the modes have and the further away from the visibility peak they probe. This is again understandable, since neighbouring ups and downs in the mode functions lead to partial cancelation of the effect on the C_ℓ 's. Once several oscillations are occurring close to $z \sim 1100$, signals produced farther away from maximum visibility can start competing with those from $z \sim 1100$, and hence become constrainable by the data.

One also expects the XeMs to be independent of the choice of the basis functions. We demonstrate this by trying the five different sets of basis functions of § 3.3.3 (see also Appendix 3.7.1 and 3.7.2): Chebyshev polynomials and Fourier series as orthogonal non-local functions of redshift, and M_4 splines, triangular and Gaussian bumps as localized basis functions. We find that the first few XeMs are practically the same independent of the chosen expansion basis (three sample XeMs are shown in Fig. 3.5), although individual perturbations in different bases lead to totally different C_ℓ responses (cf. Figs. 3.2 and 3.3).

The eigenmodes are also converged and do not change by including a larger number of parameters. We tested this by trying $N = 40, 80, 160$ and 320 in different bases and found that by $N = 160$ the first few modes are converged (cf. Fig. 3.6). For the case of M_4 spline functions the robustness of the results should also be checked against increasing the width of

the kernel. By comparing the (first six) XeMs with $h = 1.5\delta z$ (as defined in Appendix 3.7.1) to those with $h = 3\delta z$, we conclude that the modes have already converged for $h = 1.5\delta z$ which we adopt for the rest of this paper.

However, as we go to modes with higher uncertainty (not shown and used here), the XeMs from different bases start to slightly differ from each other. A larger number of basis functions are required to make these higher XeMs agree as well. Moreover, we found that the higher (poorly constrained) XeMs, in particular from the extended basis expansions such as Fourier, become dominated by numerical noise. The reason is that for weakly constrained modes where the higher frequencies start to play a more important role, the impact of adjacent ups and downs from the high frequency perturbations (e.g. sine functions) may not be well resolvable in the C_ℓ 's, resulting in their net effect being dominated by numerical noise. For the localized basis functions, as long as the individual bumps are numerically resolvable, we do not find this issue, because each perturbation has just one bump with no destructive neighbour.

For more precise computations of the higher XeMs improvements of the numerical treatment in CAMB would become necessary. We tried several obvious modifications, as well as different settings for the accuracy level, but were unable to stabilize the results for very high frequency modes. However, since in the analysis we are hardly using more than a few XeMs, for the purpose of this work this was sufficient.

In Appendix 3.7.4 we also studied how the eigenmodes respond to changes in the fiducial model and simulated CMB dataset used for their construction.

3.4.2 eXeM construction

The XeMs discussed so far were constructed with non-varying standard parameters and therefore can be considered as the limiting case of zero errors on the standard parameters. However, as mentioned in § 3.3.4, the eigenmodes become correlated when they are simultaneously being measured with the standard parameters, due to their degeneracy with standard parameters. The strength of the impact of these correlations on the XeM estimation depends on the (prior) constraints on the standard parameters. It is therefore worthwhile to see how the modes and their rank ordering change if the standard parameters are allowed to vary as well.

Fig. 3.7 illustrates the first three eXeMs constructed after marginalization over the main six and seven (including Y_p) standard parameters. For all cases considered in this section we set $\sigma = 0$. The eXeMs have stronger high redshift features compared to the XeMs. This implies that the degeneracy between the standard parameters and some features in the perturbations of the ionization fraction has pushed back some patterns of high significance to lower levels opening up the room for some high redshift or higher frequency patterns which only had the chance to show up at lower significance XeMs.

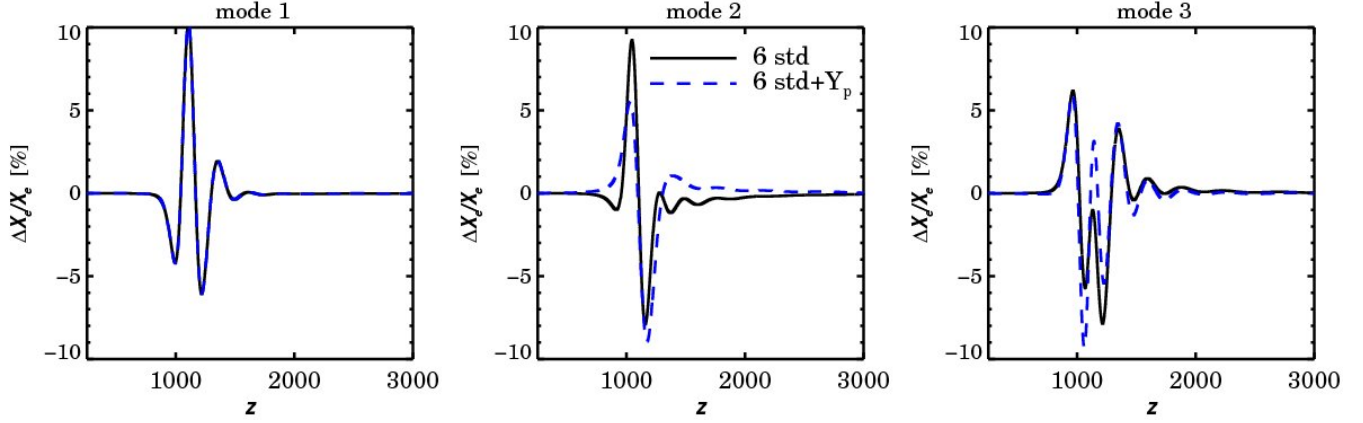


Figure 3.7: The three most constrained eXeMs. The solid blue lines correspond to modes constructed after marginalization over six standard parameters while for the dashed red curves Y_p is marginalized over in addition.

Table 3.2: The forecasted standard deviations of the first six eXeMs from the Fisher analysis constructed by marginalization over different number of standard cosmic parameters and for different observational cases. In all cases, $\ell_{\max} = 3500$.

eXeM	1	2	3	4	5	6
CVL, marg: six std	0.011	0.012	0.029	0.052	0.059	0.064
CVL, marg: six std + Y_p	0.011	0.027	0.029	0.052	0.059	0.071
Planck-ACTPol, marg: six std	0.058	0.074	0.189	0.308	0.439	0.532
CVL, marg: n_s, A_s	0.009	0.011	0.016	0.018	0.033	0.059

Table 3.3: The coefficients of projection of the six most constrained eXeMs on the first eight XeMs.

	XeM 1	XeM 2	XeM 3	XeM 4	XeM 5	XeM 6	XeM 7	XeM 8
eXeM 1	-0.00	-0.90	0.21	-0.29	-0.12	0.02	0.02	0.01
eXeM 2	-0.76	-0.05	-0.48	-0.35	0.16	-0.02	-0.02	-0.01
eXeM 3	-0.31	0.34	0.42	-0.38	-0.54	-0.41	0.02	-0.11
eXeM 4	-0.35	0.13	-0.48	-0.31	-0.50	0.27	-0.28	0.37
eXeM 5	0.24	-0.01	-0.15	-0.20	0.06	-0.48	0.63	0.49
eXeM 6	-0.19	-0.22	-0.07	0.41	0.00	-0.41	-0.55	0.49

The modes in the shown two cases (i.e., marginalized over six and seven standard parameters) differ only slightly. That is because Y_p is rather weakly constrained using CMB data alone and in the presence of other standard parameters its role in shaping the eigenmodes is only secondary. If, on the other hand, we hold the six standard parameters fixed and only let Y_p vary, the eigenmodes are more significantly affected (see Fig 3.8). The reason is that Y_p is comparable in significance to small changes in the ionization fraction and marginalizing over it, without the dominance of the standard parameters, leads to marked changes in the eigenmodes. The forecasted errors on the first six eXeMs with and without Y_p included are compared in Table 3.4.2. We see that the errors are mostly the same, again implying the subdominant role of Y_p . In terms of the errors the most affected modes are eXeM 2 and 6.

It is instructive to see how the eXeMs can be constructed from the XeMs. Table 3.4.2 shows the coefficients of the projection of the first six eXeMs on the best eight XeMs. Note that the most constrained eXeMs have their strongest projections along these first few XeMs and the contribution from all other modes, i.e., higher than the eighth mode, is at most about a percent for these first six eXeMs. This means that allowing the standard parameters to vary mixes and rearranges the first few XeMs with negligible leakage from higher neglected XeMs. This implies that using similar number of XeMs and eXeMs in an analysis of possible recombination perturbations should give similar results for the reconstructed modification in the ionization history, at least for the CVL case where relatively large number of eigenmodes are included. However, it also turns out that the eXeMs perform better than the XeMs in the simulated analysis of PLANCK data, where only 1-3 modes seem to be constrainable. The main advantage of the eXeMs is that one can obtain more realistic estimates for the error bars directly after the construction of these modes.

3.4.3 From eXeMs to XeMs

The two sets of ionization perturbation eigenmodes introduced and constructed so far, i.e., the XeMs and the eXeMs, allow us to best describe and measure the uncertainties in the ionization fraction in the two extreme ends of our knowledge of the standard cosmic parameters. The eXeMs present a case where the tightest constraints on the standard (six) parameters are from CMB data alone. Therefore a simultaneous measurement of the standard parameters and the uncertainties in the ionization fraction, using the CMB dataset at hand, is required. The construction of the XeMs, on the other hand, assumes the standard cosmic parameters are measured with high accuracy from other cosmological probes and the CMB data are only used for the direct measurement of the ionization history. In other words, the XeMs, by ignoring the uncertainties in the standard parameters, extract the maximal amount of information that the CMB data would ever have to offer about the ionization fraction.

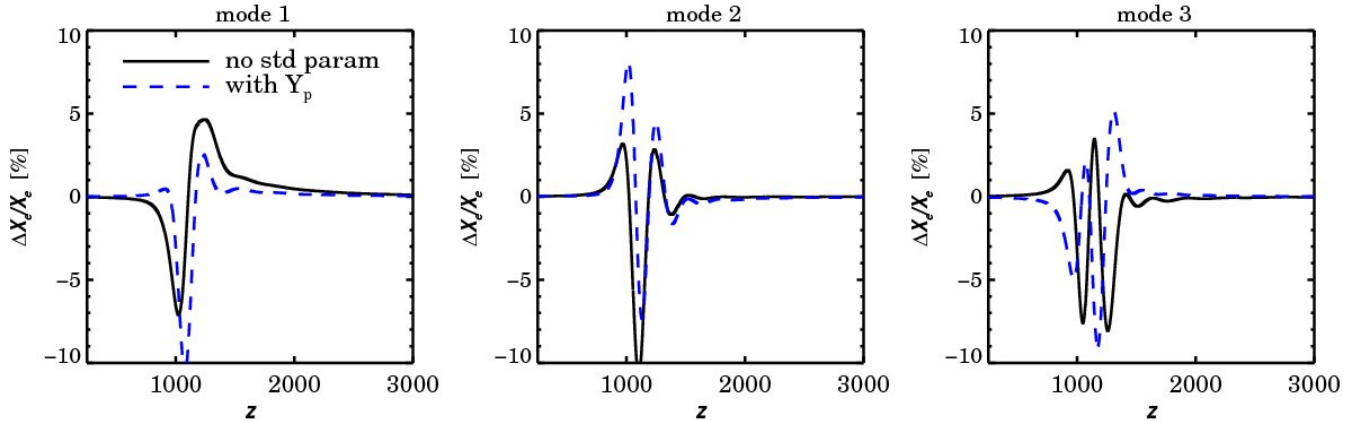


Figure 3.8: The first three eXeMs with only Y_p being marginalized over (dashed blue curves). For comparison, the first three XeMs are also plotted (solid black curves).

Between these two limiting cases, there is a *gray* region where, depending on the dataset at hand, tight priors from non-CMB surveys can be imposed on some of the standard parameters while the rest are marginalized over when constructing the eigenmodes. For example, if all standard parameters, but the inflationary ones A_s and n_s , are measured to very high precision by other probes, such as large scale structure, baryonic oscillation, lensing and supernova surveys (e.g. LSST⁷, Pan-STARRS⁸, BigBOSS, WFIRST⁹, EUCLID¹⁰), the corresponding eigenmodes would be constructed after marginalization only over these inflationary parameters.

Fig 3.9 compares the first three XeMs with eigenmodes only marginalized over A_s and n_s . The forecasted errors on these eigenmodes (from the Fisher analysis) are presented in the last row of Table 3.4.2. Not surprisingly, these modes have smaller errors compared to the eXeMs which have been made after marginalization over six standard parameters, and have larger errors compared to XeMs (with no standard parameter varying). These modes and similar ones after marginalization over different sets of standard parameters smoothly bridge the gap between the XeMs and the eXeMs. Depending on the datasets available at the time of real data analysis, the proper eigenmodes marginalized over the appropriate standard parameters must be constructed. With the current (and very near future) surveys, the most realistic choice are the eXeMs, constructed according to the experiment under consideration, which should be quite similar to the Planck-ACTPol-like case studied here.

⁷<http://www.lsst.org/lsst/>

⁸<http://pan-starrs.ifa.hawaii.edu/public/home.html>

⁹<http://wfirst.gsfc.nasa.gov/>

¹⁰<http://sci.esa.int/science-e/www/object/index.cfm?fobjectid=42266>

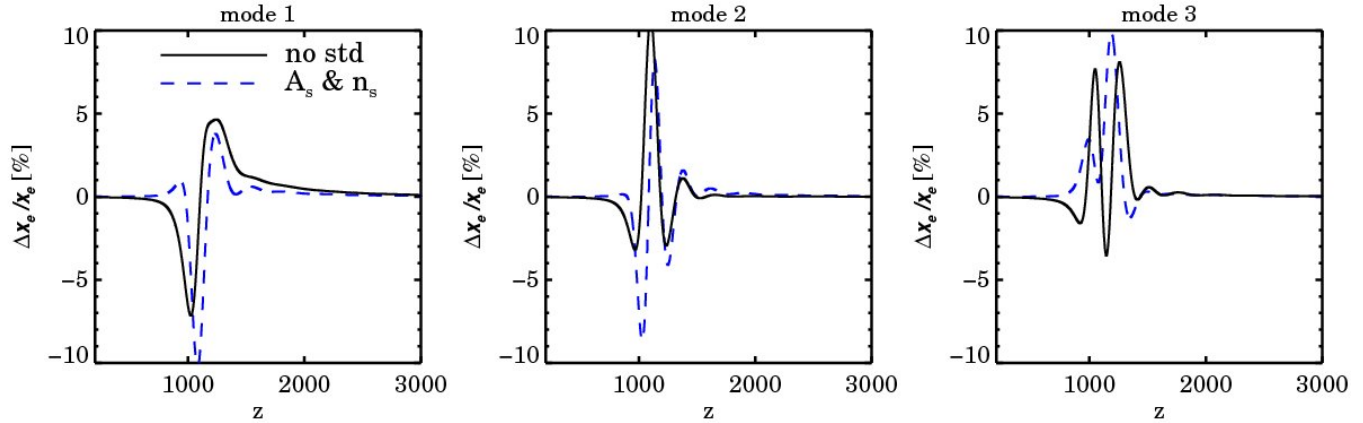


Figure 3.9: The best three eXeMs with the two inflationary parameters A_s and n_s being marginalized over, compared to the XeMs, where all standard cosmic parameters are held fixed in the construction process of perturbation eigenmodes.

3.4.4 Perturbations to helium recombination

As mentioned early in this section, the redshift range chosen in our analysis of perturbations to ionization fraction includes the recombination of singly ionized helium. Some of the most constrained XeMs we found also extend up to $z \sim 1600$. These, therefore imply some impact from the helium recombination epoch on the XeMs.

One way to confirm this statement is to limit the redshift range of perturbations to mainly include singly ionized helium recombination, e.g., $[1500, 3000]$, while the total X_e (from both hydrogen and helium) is perturbed. We observe that the XeMs constructed this way have comparably large values at the lower redshift boundary ($z = 1500$) and would steeply go to zero if enforced by the imposed boundary conditions, e.g., by prior knowledge that only this specific redshift range of helium recombination is uncertain and the perturbations outside this range are enforced to be zero. This indicates that despite being restricted to the helium recombination epoch, the XeMs are still most sensitive to changes in the signal from the hydrogen recombination and changes in X_e due to helium recombination are hardly constrainable, unless a properly chosen non-uniform prior on δX_e is imposed.

As already emphasized, the parameters $\delta u(z)$ only characterize relative changes in X_e and the full description of the ionization fraction depends also on the standard cosmic parameters as well as the relevant theoretical assumptions about the physics of recombination. Among the standard parameters, Y_p has a distinct role in describing an aspect of the ionization fraction complementary to $\delta u(z)$ by determining the maximum total number of electrons available at each redshift: $N_{e,\max} = N_{e,\max}^H + N_{e,\max}^{\text{He}} \approx (1 - Y_p/2)N_b$, where N_b is the baryon number density.

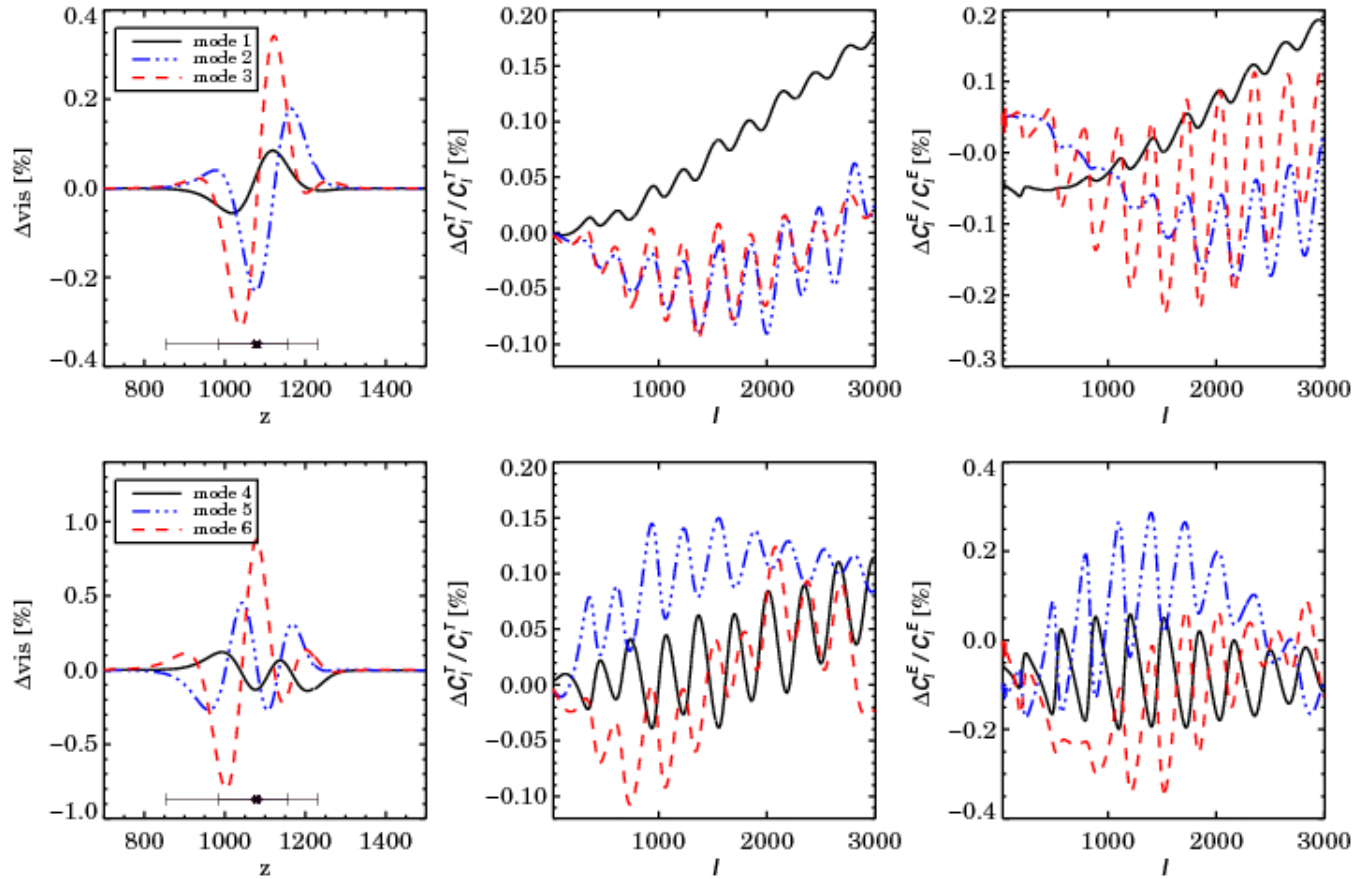


Figure 3.10: The $\delta \text{vis} = (\text{vis} - \text{vis}_{\text{fid}})$, normalized to the maximum of the fiducial visibility, (left) and the relative changes in the TT and EE power spectra (middle and right) for the six most constrainable XeMs.

Therefore, although Y_p , in the first instance, requires to be marginalized over when constructing the eXeMs, due to its intimate relation with the ionization fraction it is also legitimate to treat recombination perturbations and the maximum number of electrons available at each redshift separately.

In § 3.5.1 we use MCMC to measure constraints on Y_p alongside the six standard parameters and the first few XeMs using (simulated) CMB data. Also in the next section, we explore in more detail how the eigenmodes change if they are marginalized over Y_p .

3.4.5 Impact of the eigenmodes on differential visibility and CMB power spectra

It is worthwhile to see how the eigenmodes affect the visibility function and the CMB power spectra. The left panel of Fig. 3.10 shows the change in the visibility function (normalized to the maximum of the fiducial visibility) for the first six XeMs. The central and right panels illustrate the relative changes in the CMB temperature and E -mode polarization power spectra due to these first six XeMs. The amplitudes of XeMs are chosen proportional to their corresponding 1σ values. Thus, we expect the perturbations to lead to comparable changes in the C_ℓ 's. It is remarkable that such tiny relative changes in X_e (and correspondingly in the visibility) lead to potentially measurable effects (\sim tenth of a percent) in the CMB power spectra. This confirms the high sensitivity of the C_ℓ 's to tiny changes in the visibility.

From Fig. 3.10 we see that the most constrained mode, XeM 1, has an effect on the CMB power spectra consistent with changes in the width of the visibility function and a slight shift of its peak position. For this XeM, due to its narrower visibility width compared to the fiducial model, the high ℓ damping in the temperature and polarization anisotropies is smaller. At the same time, because of fewer scattering opportunities for the photons, this mode leads to less polarization (negative δC_ℓ^E at low ℓ 's). Higher XeMs lead to less trivial changes in the width and position of the visibility function. However, the mainly oscillatory impact of these modes on the C_ℓ 's suggests an effective shift in the position of the visibility function. But, e.g., for mode XeM 4 the tail of the power spectrum is also less strongly damped, corresponding to a change in the effective width of the visibility.

3.4.6 Criteria for truncating the eigenmode hierarchy

For the full reconstruction of perturbations to the ionization fraction, all eigenmodes are in principle needed since they form a complete basis set. In practice, sequentially adding modes rank ordered in the (possibly renormalized) eigenvalues $f_k^{-1} = \sigma_k^2$ of \mathbf{F}^{-1} (or the eigenvalues of $(\mathbf{F}^{-1})_{pp}$ in the more general case where the background cosmology also changes) from low to high gives a rapidly diminishing return once one goes beyond a dozen or so. And often we can learn much from using just the first few. As more modes are added, the width covered by the allowed X_e trajectories increases, as Figs. 3.19 to 3.23 in § 3.5.3 show. The errors in those standard cosmic parameters which are correlated with the X_e eigen-parameters also increase. On both counts, it behooves us to develop criteria for selecting which modes to keep, bearing in mind Occam's Razor for minimizing the number of new parameters to be added. Thus we show in § 3.5 what happens when one mode, a few modes and a handful of modes are added. To be more quantitative, we explore an additional criterion based on not allowing the Shannon

entropy to increase too much as the next eigenmodes in the hierarchy are added.

The information action is defined in terms of the *a posteriori* probability of the variables p_f and the evidence \mathcal{E} as $\mathcal{S}_{I,f}(\mathbf{q}) \equiv \ln p_f^{-1} - \ln \mathcal{E}$. As explained in Appendix 3.3.4, the *a posteriori* probability $p_f \equiv p(\mathbf{q}|d, \mathcal{T})$ of variables $\mathbf{q} = (q_1, \dots, q_N)$ given the theory space \mathcal{T} and the datasets d is related to the *a priori* probability $p_i \equiv p(\mathbf{q}|\mathcal{T})$, the likelihood $\mathcal{L}(\mathbf{q}|d, \mathcal{T}) \equiv p(d|\mathbf{q}, \mathcal{T})$ and the evidence $\mathcal{E} \equiv p(d|\mathcal{T})$ through Bayes theorem: $p_f = \mathcal{L}(\mathbf{q}|d, \mathcal{T})p_i/\mathcal{E}$. The information action can then be written in terms of p_i and \mathcal{L} :

$$\mathcal{S}_{I,f}(\mathbf{q}) = \ln p_i^{-1} + \ln \mathcal{L}^{-1}.$$

For basic information theoretic and Bayesian notions and notations see, e.g., the MacKay (2003) textbook. The framework given here was used in a CMB context by Farhang et al. (2011). For us the q_k 's are the amplitudes of the ordered eigenmodes for XEMs or eXeMs. Generally the fluctuations in the standard cosmic parameters from their maximum likelihood values are included along with these eigen-parameters. We shall assume the prior distribution of the parameters to be uniform in the q_k . The expansion of $\mathcal{S}_{I,f}$ to quadratic order is the basic perturbative approach used throughout this paper, leading to a Gaussian p_f : $\mathcal{S}_{I,f}(\mathbf{q}) \approx \mathcal{S}_{I,m} + \mathbf{q}^\dagger \mathbf{F} \mathbf{q}/2$ in terms of the Fisher matrix and the information action minimum $\mathcal{S}_{I,m} = -\ln(p_i \mathcal{L}_{\max})$.

The posterior Shannon entropy is related to the final-state ensemble-average of the information action and the evidence:

$$S_f \equiv \langle \ln p_f^{-1} \rangle_f = \langle \mathcal{S}_{I,f}(\mathbf{q}) \rangle_f + \ln \mathcal{E}.$$

For the quadratic order expansion it is

$$\begin{aligned} S_f &\approx \frac{1}{2} \text{Tr} \ln \mathbf{F}^{-1} + \frac{N}{2} \ln(2\pi) + \frac{1}{2} \text{Tr} \left(\langle \mathbf{q} \mathbf{q}^\dagger \rangle \mathbf{F} \right) \\ &= \frac{1}{2} \text{Tr} \ln \mathbf{F}^{-1} + \frac{N}{2} (\ln(2\pi) + 1). \end{aligned}$$

The second line follows from the first since the correlation matrix of the \mathbf{q} is $\langle \mathbf{q} \mathbf{q}^\dagger \rangle = \mathbf{F}^{-1}$. The associated evidence involves the information action minimum, $\ln \mathcal{E} \approx S_f - \mathcal{S}_{I,m} - \frac{N}{2}$.

The entropy associated with mode n is

$$S_n \equiv -\frac{1}{2} \ln f_n + (1 + \ln 2\pi)/2 = S(\leq n) - S(\leq n-1).$$

It is a finite difference of the total entropy of the first n modes in the eigen-hierarchy,

$$S(\leq n) = \frac{n}{2} (1 + \ln 2\pi) - \frac{1}{2} \sum_{k=1}^n \ln f_k$$

and

$$\langle s \rangle_n \equiv S(\leq n)/n$$

is the associated mean entropy-per-mode. Fig. 3.11 shows how the relative entropy $S_n - S_1$ and the mean entropy $\langle s \rangle_n - S_1 = S(\leq n)/n - S_1$ grow with n for the modes derived from the localized Gaussian expansion. We also plot two versions of "white-noise" entropy.

$$\begin{aligned} S(\text{wn}, \leq n)(\sigma^2) &\equiv n(\ln \sigma + (1 + \ln 2\pi)/2), \\ \text{mean - variance } \sigma^2 &= \sum_{k \leq n} f_k^{-2}/n, \\ \text{mean - weight } \sigma^2 &= [\sum_{k \leq n} f_k^2/n]^{-1}. \end{aligned}$$

These are entropies maximized subject to the constraint that we only have knowledge of the integrated σ^2 , whereas $S(\leq n)$ is the maximized entropy given knowledge of the full spectrum $\{f_k^{-1}\}$. The mean-variance white noise lies above $S(\leq n)$ and the mean-weight white noise lies below. The mean-weight behaviour is dominated by a $\ln(n)$ rise, since the total weight of modes below n , $\ln \sum_{k \leq n} f_k^2$, quickly approaches a constant, reflecting the dominance of the high-weight eigenmodes in the sum.

We first discuss why we do not use the traditional evidence ratio often used in Bayesian theory to decide if a new parameter q_n should be added. The log-evidence difference for the addition of q_n is

$$\begin{aligned} \Delta \ln \mathcal{E}_n &\equiv \ln \mathcal{E}(\leq n) - \ln \mathcal{E}(\leq n - 1) \\ &= S_n - 1/2 - \Delta S_{\text{I,m}}. \end{aligned}$$

This requires evaluation of the change in the information minimum. It also has the usual disadvantage of depending upon the f_k measure. Although using eigen-parameters ensures the same dimensionality for the different f_k , it does not fully remove this re-parameterization ambiguity since there can be a k -dependent scaling. (In fact, we have usually renormalized our f_k so that the associated eigenmodes $E_k(z)$ have unit norm upon z -integration.)

Our preferred approach for hierarchy truncation is to use suitably-defined entropy differences. In particular we wish to set a threshold control on the injection entropy,

$$\delta S_{\text{inj},n} = S_n - \langle s \rangle_n,$$

the entropy from adding mode n relative to the mean-entropy from all $\leq n$ modes. It is related to the relative increase in phase space volume $V(\leq n) = \exp(S(\leq n) - n/2) = \exp(n(\langle s \rangle_n - 1/2))$ associated with mode additions:

$$\ln \left[V(\leq n + 1)/V(\leq n)^{(n+1)/n} \right] = S_{n+1} - \langle s \rangle_n.$$

We chose $S_{\text{inj},n}$ instead because it is zeroed out for mode one, but $S_{\text{inj},n}$ quickly approaches $S_{n+1} - \langle s \rangle_n$. For example, if we impose a $\Delta S_t \sim 1/2$ threshold in Fig. 3.11 on the CVL XeM

case, we would use only one mode, whereas $\Delta S_t \sim 1$ picks up about 5, $\sim 3/2$ harvests about 10, and 2 gives about a dozen. Similar tales can be told for the eXeM CVL case and for both Planck+ACTpol forecasts.

Another more erratic measure is relative injection jumps, which is nearly $S_{n+1} - S_n$. In Fig. 3.11, the negative of this is plotted for clarity of presentation. Either reading off from the figure, or using the lists of errors in Tables 3.4 and 3.4.2, the sample threshold $\Delta S_t = 1/2$ again yields only a mode or two.

The fluctuating nature of $S_{n+1} - S_n$ implies we can use it to split the modes into groups of similar information content which arise by thresholding it. Thus, for a chosen threshold value all the modes between two successive boundaries, where ΔS exceeds a certain value, are considered as one *mode-group*. If a mode is selected to be included in the analysis by, say, sharp-thresholding the injection entropy, it is logical that all of its co-modes be included, which is akin to softening the threshold. The groupings found with $\Delta S_t = 1/2$ imposed upon $S_{n+1} - S_n$ creates boundaries at one mode, five modes, and so on. These are, not surprisingly, similar to mode numbers obtained as we move the threshold on injection up, hence that criterion can be used instead to define mode groups.

Although these entropy difference criteria imply that relatively little additional information is gained by including more than a handful of higher modes, in real data analysis the situation is subtler, with other criteria important to consider. For example, depending on how close the assumed model is to the true underlying history, our measurements of standard cosmic parameters might be biased. In that case one would like to add enough modes to remove the bias, sequentially checking if the recovered values of the standard parameters are robust against introduction of the next eigenmode. A reasonable strategy is to add one *mode-group* at a time to the analysis until the biases are removed. In the next section, we show how varying the mode number cutoff affects our results, roughly following this grouping procedure.

3.4.7 Perturbation reconstruction: eigenmodes as a complete basis

Any function $X_e(z)$ (in the redshift range under consideration) can be expanded in terms of these XeMs unless it has highly localized features compared to the highest frequency present in the basis functions or to the width of the bumps in the case of localized modes. That is because the XeMs are just linear combinations of the original basis functions, and thus cannot have frequencies higher than the maximum frequency present in the basis functions. On the other hand, as is clear from Fig. 3.5, strongly localized features in possible perturbations to recombination history are not constrained with CMB datasets. Therefore the lost features of an ionization model via expansion by these eigenmodes are not measurable even if modes with higher frequencies are included in the analysis. In other words, the XeMs serve as a

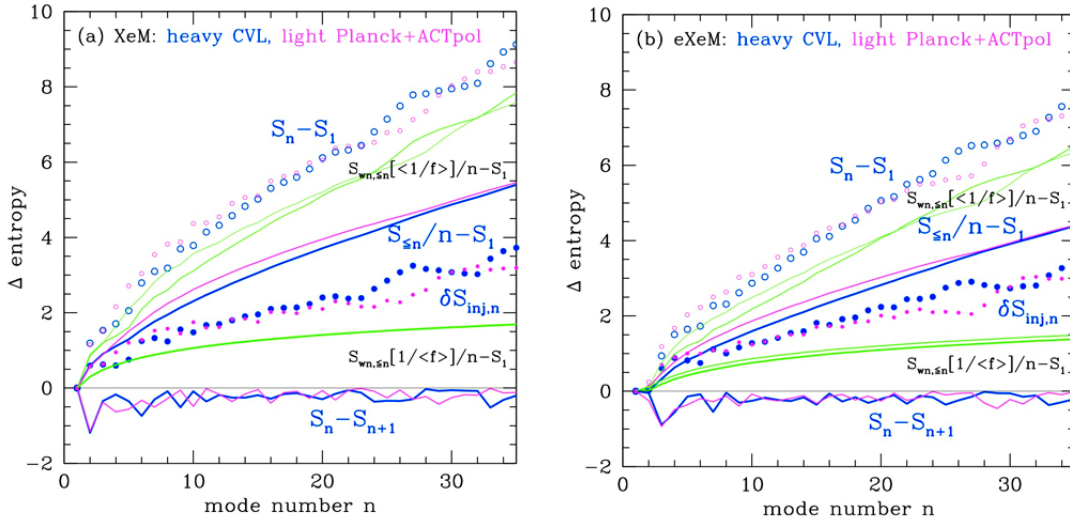


Figure 3.11: Various measures of entropy differences defined in the text are plotted against increasing eigenmode number, for (a) the XeM case and (b) the eXeM case. The Cosmic Variance Limited mode results have heavy lines or points, the Planck+ACTpol forecast has lighter lines and points, as indicated. They look quite similar. For this figure, the modes are determined by the densely-packed Gaussian bump expansion, but the triangular and spline expansions look similar, differences becoming notable only at higher n . The basic information on growing entropy is given by $S_n - S_1$, and the mean difference $S_{\leq n}/n - S_1$, with the latter bracketed by the two white-noise entropies. The criteria for threshold selection discussed in the text involve the injection entropy, $S_n - S_{\leq n}/n$ and $S_{n+1} - S_n$ (plotted with opposite sign for clarity). Thresholding at $\Delta S_t \sim 1/2$ selects the first mode or two, but mode-groups are also evident, suggesting modes should be added in blocks rather than singly as we eliminate bias, check convergence and demonstrate robustness.

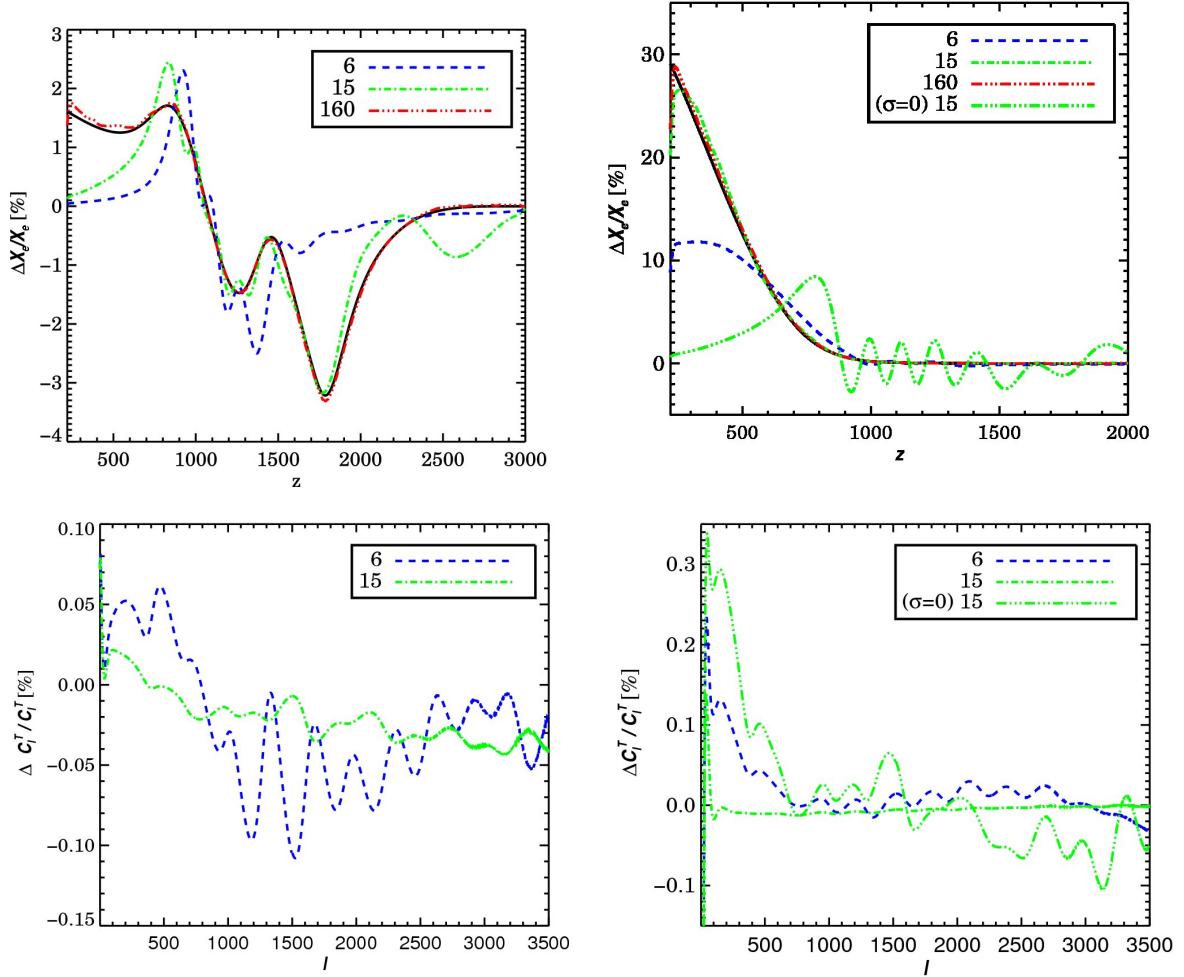


Figure 3.12: The reconstruction of two physically motivated X_e perturbation scenarios on (different number of) X_e Ms generated with Gaussian bumps (top) and the relative difference in the temperature power spectrum between the reconstructed perturbations and the full corrections (bottom). Right: The perturbations come from deviation from physical corrections to the recombination process (CT2011). Here the perturbation parameter is $\delta \ln(X_e)$. Left: The perturbations are due to a model of dark matter annihilation. As the perturbation parameter we used $\delta \ln(X_e + 0.01)$ to better accommodate for the freeze-out perturbation. A case with $\delta u(z) = \delta \ln(X_e)$, i.e., $\sigma = 0$, is shown for comparison.

complete basis for the expansion of *constrainable* features in the possible perturbations in the recombination history.

To demonstrate the reconstruction of perturbations using the XeMs we choose two physically motivated ionization perturbations, one associated with physical corrections to the recombination process (Chluba & Thomas (2011), hereafter CT2011) and the other due to energy injection coming from a model of dark matter annihilation (using the description of Chluba, 2010).

Standard recombination corrections

The modification to X_e corresponding to CT2011 is shown in the top left panel of Fig. 3.12 (black solid line). This correction should be added to the X_e from the original version of RECFAST (or the X_e from RECFAST v1.4.2 setting $\text{He}_{\text{Switch}} = 0$). At high redshifts one can see the effect of accelerated helium recombination caused by absorption of photons in the Lyman continuum of hydrogen. During hydrogen recombination the corrections are caused by detailed radiative transfer effects as well as two-photon and Raman scattering events. The freeze-out tail is slightly higher than obtained with RECFAST because of deviations from statistical equilibrium in the angular momentum sub-states. We note that with RECFAST v1.5 a large part of all these corrections can be accounted for, however, these corrections are not explicitly modelled using a physical description but have been fudged to reproduce the results obtained with detailed recombination codes.

We project this $\delta \ln(X_e)$ on the 160 XeMs constructed from perturbations in the recombination history in the form of Gaussian bumps and with the perturbation parameter being $\delta u(z) = \delta \ln(X_e)$ for the CVL case with $\ell_{\text{max}} = 3500$, as described in § 3.4.1. Figure 3.12 compares the reconstructed perturbation for three cases with different number of XeMs included. First note that by including all 160 XeMs the original perturbation is practically fully recovered. If only the 15 most constrained modes are included, the helium correction ($z \sim 1800$) and also hydrogen correction around $z \sim 1100$ are well restored while for lower z regions higher modes are required. The reconstruction by six XeMs, however, is most sensitive to variations around $z \sim 1100$ and cannot tell much about the helium correction. The projection coefficients for the first six XeMs are shown in Table 3.4.7. For this particular model of corrections to the perturbation scenario we see that the XeM 1, 3 and 6 are strongly dominant among the first six modes.

The lower left panel in Fig. 3.12 illustrates the relative difference between the temperature power spectrum for the reconstructed perturbations and the original full corrections. We see that with only six modes the error in the recovered C_ℓ 's is less than 0.1% although the difference with respect to the SRS is $\sim 4\%$ at high ℓ 's. Remembering that the changes in the C_ℓ 's due to the full corrections are about a few percent, this shows that the main corrections to the CMB

Table 3.4: The projection of the modifications to recombination history on the first six XeMs. Note the different values of σ used for the two cases.

XeM	1	2	3	4	5	6
CT2011 ($\sigma = 0$)	-0.32	0.08	0.16	0.02	-0.09	0.25
DM annihilation ($\sigma = 0.01$)	-0.31	-0.30	0.46	-0.14	0.33	0.88

power spectra can be captured by just introducing a small number of modes. The CMB data indeed are not very sensitive to all the details in the freeze-out tail of recombination and during helium recombination, unless prior knowledge renders uncertainties at $z \sim 1100$ very small. As we see below, part of the corrections from higher modes are compensated for by biasing the XeMs included in the analysis.

Dark matter annihilation scenario

As the second example we chose the perturbations arising from a model of dark matter annihilation. It was computed using the description of Chluba (2010) with an annihilation efficiency $f_{\text{DM}} \sim 2 \times 10^{-24}$ eV/s. The difference with respect to RECFast is shown in the right panel of Fig. 3.12. In contrast to the previous case, the perturbations here are not concentrated around the maximum of differential visibility but are most significant at lower redshifts. Therefore, for the decomposition of the DM perturbations we choose $\delta u(z) = \delta \ln(X_e + 0.01)$ (see § 3.4.1 and Fig. 3.4) to allow a better recovery of the relatively large perturbations in the freeze-out tail without the need to include too many modes. This procedure can be interpreted as placing a strong prior on (physically) expected changes in the freeze-out tail.

The top right panel of Fig 3.12 shows the reconstructed perturbation including three different number of XeMs. Here the recovered curve becomes very close to the original perturbation by including the first 15 XeMs, while six XeMs have a poor recovery of the low- z part. Note that the plots are illustrating $\delta \ln(X_e(z))$ although the XeMs and thus the decomposition of the perturbation are all performed with $\delta \ln(X_e + 0.01)$.

For comparison the reconstruction of the perturbation with $\delta u(z) = \delta \ln(X_e)$, i.e., with $\sigma = 0$, and with 15 XeMs taken into account is also shown. As expected, this reconstruction is much poorer compared to the previous case with $\delta u(z) = \delta \ln(X_e + 0.01)$ due to its lack of coverage of corrections in the freeze-out tail. This demonstrates that when there is prior knowledge in favour of the freeze-out tail of recombination being affected, a parametrization with $\sigma > 0$ should be used in the analysis. However, it is still correct that the main signal is produced by the modifications close to $z \sim 1100$, even if the freeze-out tail apparently has the largest deviation from the SRS. This is why the first few mode functions for $\sigma = 0$ do not have

any strong low redshift tails. The eigenvectors naturally order the perturbations in the strength of the associated change in the CMB power spectra, as explained in § 3.4.1. This point is visible from the lower right panel where the C_ℓ difference is plotted for reconstructed perturbations with different number of modes included compared to the full perturbations. Similar to the previous case, these differences are several times smaller than the changes in the C_ℓ 's caused by this model of DM annihilation, again meaning that these few modes can well capture the constrainable features of the perturbations.

Also if we look at the decomposition of the recombination correction into the first six XeMs (see Table 3.4.7) we see that they all have comparable contributions. This seems reasonable if we remember that the mode functions, despite being weighted toward the low redshift part, still have a significant component at high redshift which need to be cancelled out to recover this pattern of perturbation with its low redshift modification. Therefore the neighbouring modes have the same order of amplitude to properly cancel out the high redshift perturbations. This implies that the distribution of the mode amplitudes can in principle hint to the type of perturbation involved. However, a detailed analysis of this kind requires a model selection study. E.g., in the data analysis, one could treat σ as a hyper-parameter and estimate its best fit value at the same time as the corresponding perturbation eigenmodes and the standard cosmic parameters. This allows us to choose the most preferred model among the class of all models parametrized by σ .

3.5 Measuring the amplitudes of perturbation eigenmodes for simulated data

Having constructed the eigenmodes, their amplitudes can now be considered as additional parameters to be plugged into COSMOMC, "a Fortran 90 Markov-Chain Monte-Carlo (MCMC) engine for exploring cosmological parameter space"¹¹. In this section we investigate how well the most constrained XeMs and eXeMs can be measured by simulated data. To study the impact of these new variables on the standard parameter estimation, we first consider the case in which the data are both simulated and analyzed using the SRS (§ 3.3.1). We then study the case for which the effects of physical corrections to the recombination history (CT2011, see § 3.4.7) are included in the constructions of the mock data, but are neglected in the fiducial recombination model used in the analysis. Here the question is how well the eigenmodes compensate for the deviations from the fiducial model and how much the data are telling us about the amplitudes of the modes. We also briefly discuss how the eigenmodes should be used in a more general

¹¹ <http://cosmologist.info/cosmomc/>

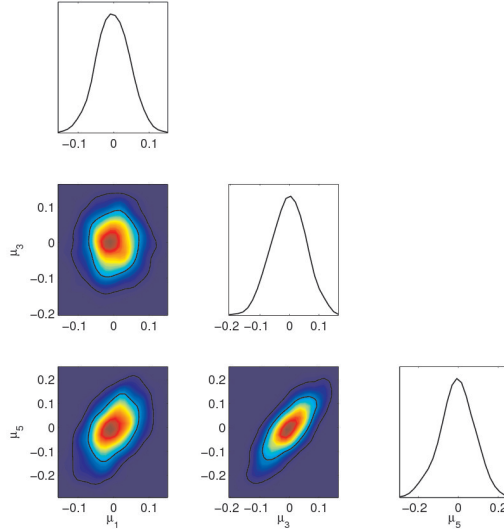


Figure 3.13: 2D contours for the amplitudes of some of the best five XeMs, chosen as examples, as measured by a CVL experiment and with the standard recombination history. Here the six standard cosmic parameters were also allowed to vary. That is why the measured eigenmodes are correlated. The solid black lines mark the 1σ and 2σ contour levels.

Table 3.5: The standard deviations of the first five XeMs from chains produced by CosmoMC, marginalized over the main six standard parameters (for the CVL case with $\ell_{\max} = 3500$).

XeM	1	2	3	4	5
1σ	0.046	0.030	0.057	0.088	0.086

case where little prior knowledge about the recombination perturbations is available.

3.5.1 Case 1: The standard recombination scenario

As the first example we choose the fiducial recombination model (here the SRS) to be identical to the ionization history used in the simulation of the data. We ran COSMOMC to estimate the best-fit values and errors of the six standard parameters together with those for the perturbation eigenmodes. We tried the two sets of eigenmodes described before: the first five XeMs and the first six eXeMs. The number of modes in each case was chosen in rough agreement with the mode cutoffs described in § 3.4.6 (more precisely with $\Delta S_t = S_{n+1} - S_n = \frac{1}{2}$). The simulations were carried out for a CVL experiment.

One expects no detection of eigenmodes since the fiducial model for X_e and the underlying model used to simulate data are the same, as verified by Figs. 3.13 and 3.14. Also, by construction there is almost no visible correlation between the measured parameters for the

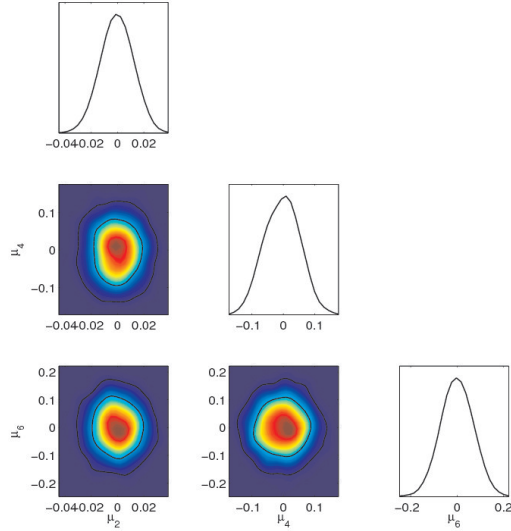


Figure 3.14: 2D contours for the amplitudes of some of the best six eXeMs, chosen as examples, as measured by a CVL experiment and with the standard recombination history. The six standard cosmic parameters were also allowed to vary in the simulations.

eXeMs, at least sufficiently close to the best-fit model where the assumptions of the Gaussianity for the likelihood surface approximately holds. However, Fig. 3.13 indicates that the XeMs become partially correlated with each other, although by construction these were initially uncorrelated¹². The reason is that the standard parameters were held fixed during the process of XeM construction, but now that they are allowed to vary, their degeneracy with the XeMs induces correlations. These new correlations lead to larger errors than those deduced from the simple Fisher analysis (Table 3.4 cf. Table 3.5.1) and can also change the rank ordering of the modes, e.g., the error on XeM 2 is smaller than XeM 1 (Table 3.5.1).

The standard parameters remain unbiased, as the model used for simulating data and the theoretical model used in the analysis were the same. This is no longer true once recombination corrections to the SRS are added (see Fig. 3.17). However, the correlations of the eigenmodes with some of the standard parameters increase the errors of the standard parameters.¹³ From Fig. 3.15 we see that among the standard parameters, $\Omega_b h^2$, n_s and A_s are the ones most affected by the introduction of the eigenmodes into the analysis. This can be understood by noting the relatively high degeneracy between these parameters and some of the eigenmodes. The most evident one is the correlation of n_s with the first XeM which by changing the width of the visibility function leads to a tilt in the power spectra (compare Figs 3.16 and 3.10).

¹²We confirmed this statement by running MCMC with non-varying standard parameters.

¹³It should also be noted that the correlations between the standard parameters themselves also change when the eigenmodes are introduced.

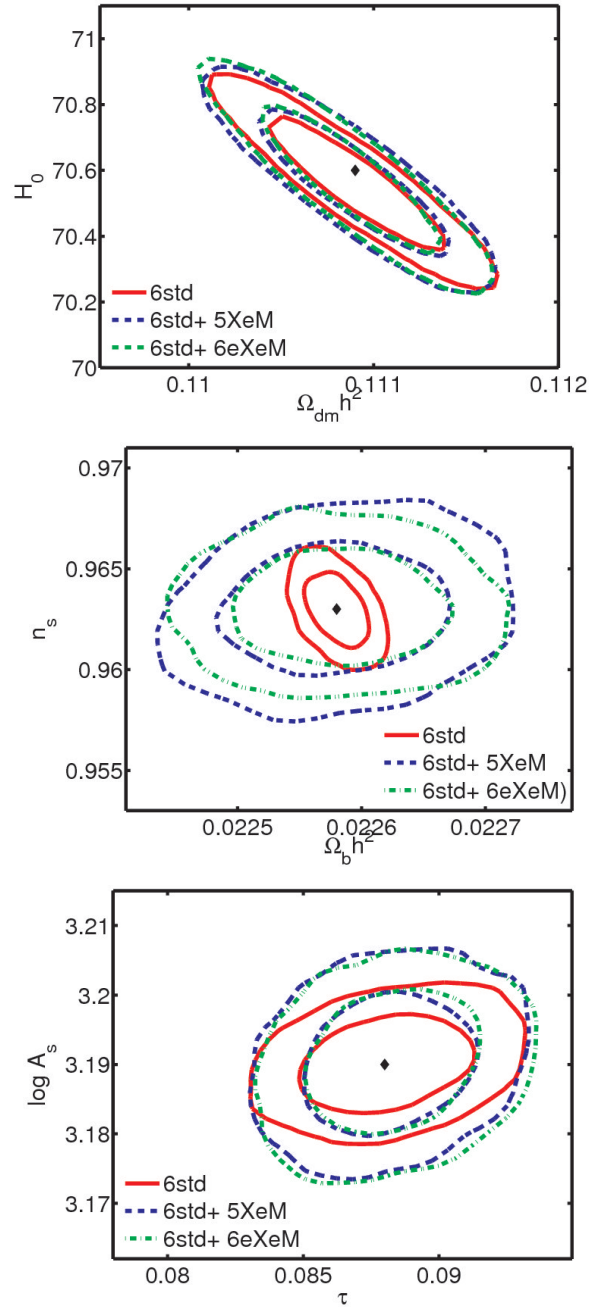


Figure 3.15: The contours at 1σ and 2σ levels for the standard parameters as measured by an ideal experiment in the presence of five (six) XeMs (eXeMs) compared to the case with no eigenmodes included. The input value of the parameters is shown by the black diamond.

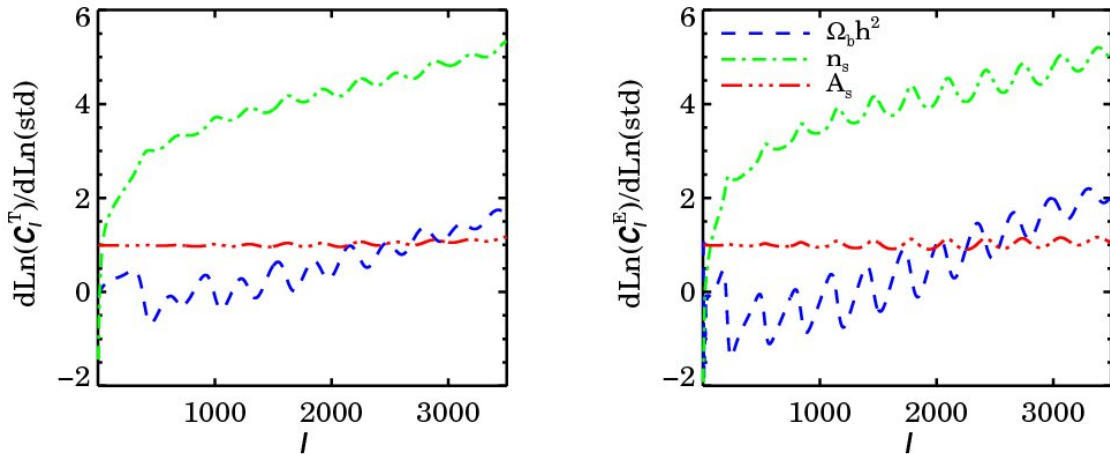


Figure 3.16: The derivatives of the $C_\ell^{T,E}$'s with respect to some of the standard parameters.

table:yp

Table 3.6: Y_p and its measured error from simulations for a CVL and a Planck-ACTPol-like experiment (abbreviated as Pl-APol), with XeMs and eXeMs taken into account as perturbation eigenmodes, compared to the case with no eigenmodes.

	CVL(std)	Pl-APol(std)	CVL(+5XeMs)	CVL(+6eXeMs)	Pl-APol (+3XeMs)
Y_p	0.240 ± 0.0016	0.240 ± 0.006	0.239 ± 0.005	0.240 ± 0.004	0.238 ± 0.017

For the case of $\Omega_b h^2$ and A_s it is harder to give a visual interpretation. $\Omega_b h^2$, leading to both tilt changes and oscillations in the C_ℓ 's, correlates with most of the first five XeMs (the highest being with XeM 1), while A_s , being an amplitude multiplier, mainly correlates with XeM 1. These correlations between the standard parameters and the eigenmodes emphasize the fact that uncertainties in the recombination scenario in particular undermine our ability to measure the precise values of n_s and $\Omega_b h^2$ (see e.g., Shaw & Chluba, 2011). Also note that the changes in the error bars of the standard parameters are actually practically independent of which set of eigenmodes are used (Fig. 3.15). This suggests that in terms of the standard parameter estimation, the use of XeMs or eXeMs should not lead to vastly different results in the parameter estimation. However, the perturbations are measured to higher accuracy with the eXeMs (Table 3.4.2) than XeMs (Table 3.5.1) especially if only a few modes are included in the analysis. Therefore, as long as only CMB data are used, the eXeMs are the more appropriate choice of eigenmodes.

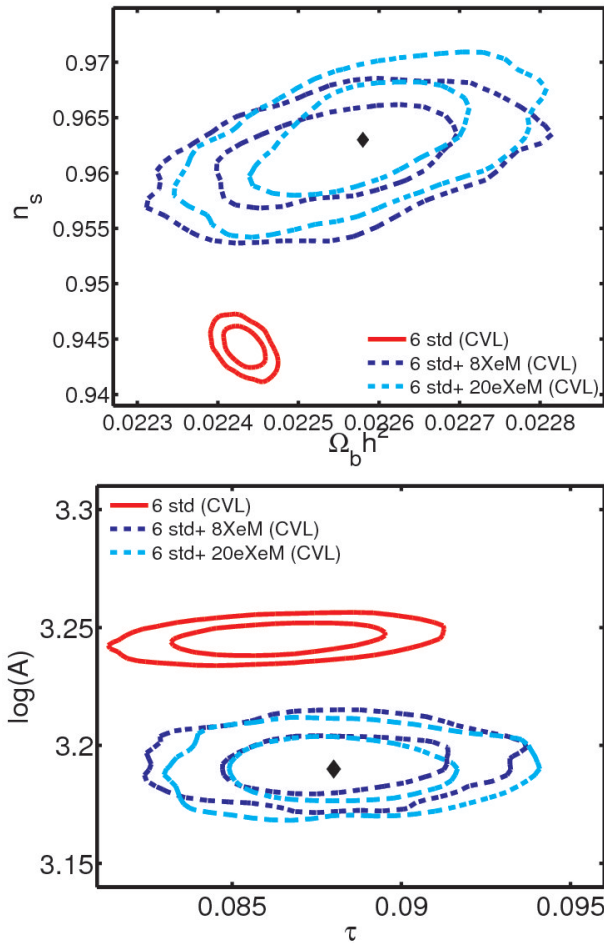


Figure 3.17: Contours of some of standard parameters for CT2011 case, with eight XeMs in one case and 20 eXeMs in the other case included in the analysis, compared to a case where no perturbation eigenmodes (of any kind) has been included (the solid red curves). The simulations are performed for a CVL experiment. The input value of the parameters is shown by the black diamond.

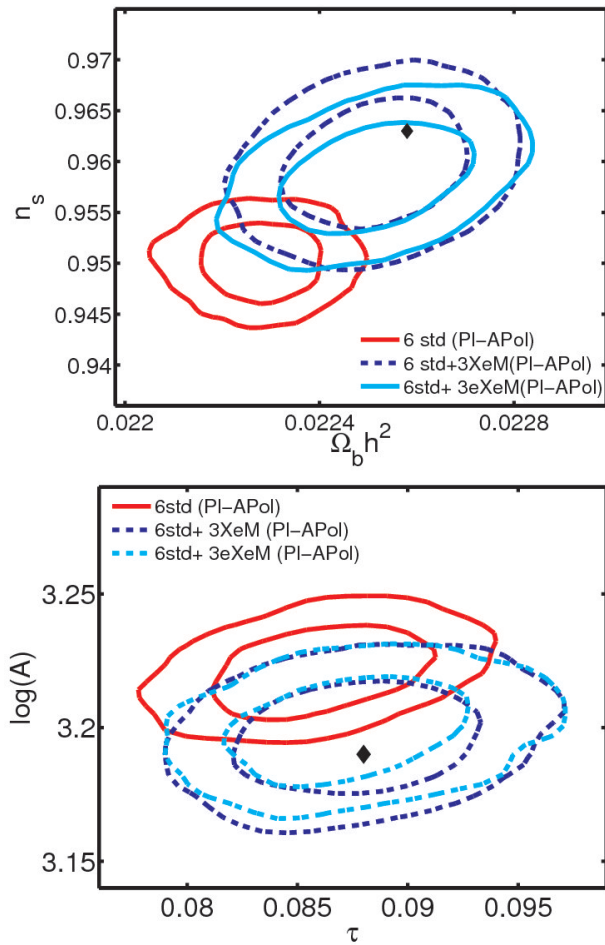


Figure 3.18: Similar to Fig. 3.17 but for a Planck-ACTPol-like experiment. Here three eigenmodes were added for both the XeM and eXeM case.

Finally, we studied how much the presence of perturbations to recombination could affect our ability to determine the precise value of Y_p . The abundance of helium affects the CMB anisotropies mainly because more helium implies fewer free electrons during hydrogen recombination. Consequently, Y_p should also couple significantly to the perturbation eigenmodes. We therefore performed simulations in which Y_p was also allowed to vary. The analysis was performed with three and five XeMs in the Planck-ACTPol-like and CVL case, and with six eXeMs for the simulated CVL data. Table ?? compares the 1σ error bars on Y_p in these cases. We see that for the CVL case similar number of XeMs and eXeMs used as the eigenmodes lead to similar constraints on helium abundance. However, a Planck-ACTPol-like observation gives a few times larger error due to lack of very high sensitivity to very small scales, although fewer XeMs compared to the CVL case have been used.

3.5.2 Case 2: A perturbed recombination scenario

As the second example of parameter estimation and perturbation reconstruction, we simulate *data* assuming the recombination calculation of CT2011 (Fig. 3.12), while we take the fiducial model to be as of RECFAST v1.4.1 or older (equivalent to SRS with $\text{He}_{\text{switch}} = 0$, to remove the helium correction which has been assumed as part of the *perturbations* in the data). The purpose here is to find out how well the biases in the standard parameters due to this *lack* of knowledge about the physical corrections can be removed by including the perturbation eigenmodes, and whether or not, *data* can reconstruct part of the true recombination history.

Constructed from COSMOMC chains for a CVL experiment, Fig. 3.17 illustrates the 2D-contours of some of the standard parameters. The large biases in the estimated values of the parameters when only the six standard parameters are measured is due to the mismatch between the ionization history in the theoretical model and the *data*. Here only contours for parameters with the largest biases are shown. See also Shaw & Chluba (2011). To compensate for this mismatch we separately add to the parameters the two different sets of the eigenmodes, the XeMs and eXeMs, as the new parameters.

As Fig. 3.17 demonstrates, without the eigenmodes the bias in, e.g., $\Omega_b h^2$ and n_s is about 5σ and 7σ , while adding the eigenmodes eliminates the bias at the cost of increased error bars (the difference in measured uncertainty of τ with and without the eigenmodes is rather small). Our computations also indicate that with the XeMs as the eigenmodes and for a CVL observation, the minimum number of modes required to remove the bias from these standard parameters is six. However, we included eight modes in the analysis to take into account the mode-selection criterion of § 3.4.6 (determined by the relative injection jumps).

We also observe that the recovered values for the amplitude of the XeMs are biased (compared to the theoretically expected values from direct projection on the XeMs, Table 3.4.7), and

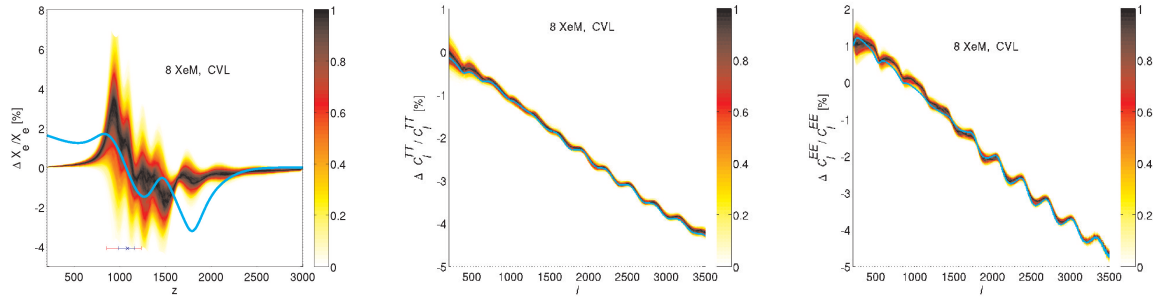


Figure 3.19: Left: The $\delta X_e/X_e$ as measured by a CVL experiment by including eight XeMs (and six standard parameters) in the analysis. The colors show the density of trajectories going through each point in the z - $\delta X_e/X_e$ space, normalized to one at each z . The maximum and 1 and 2σ widths of the Thomson visibility function have been marked at the bottom of the plot. As this plot and the next ones indicate, the main recovery of X_e is the slope of the curve around this visibility peak. Middle and right: similar to the left figure, but for $\delta C_\ell^{TT,EE}/C_\ell^{TT,EE}$ trajectories.

change by varying the number of modes included in the analysis. That is due to the correlation of the XeMs in the presence of the standard parameters, and the fact that not all XeMs are included into the parameter estimation. As a result, parts of the perturbation that project on the neglected higher XeMs leak into the lower XeMs. The bias in the measured XeM amplitudes is similar to the bias in the standard parameters when there are no eigenmodes in the analysis, but with a much lower significance.

For the same reason, the errors on the XeMs also change when the number of modes included in the analysis changes. However, as mentioned before, due to the low significance of the perturbation detection for most of the XeMs this is not as important as for the main cosmic parameters. For the CVL simulations with six and eight XeMs included, we see that the most significant contribution comes from the first mode (respectively $\mu_1 = -0.23 \pm 0.05$, $\mu_1 = -0.18 \pm 0.04$) while the other modes are consistent with zero. This is also true for a Planck-CTPol-like case, which we come to shortly, where the first XeM is measured to be $\mu_1 = -0.22 \pm 0.06$ $\mu_1 = -0.24 \pm 0.12$ for one and three XeM measurements.

If instead eXeMs are used as the perturbation eigenmodes, our computations show that at least ten modes should be added to get rid of the bias for a CVL case. However, as a test case, we tried including the best 20 eXeMs (see Fig. 3.17).

We also found that although the errors on the standard parameters keep increasing by adding more eXeMs to the analysis up to around the tenth mode (which is required to remove the bias) it stays more or less the same afterwards. This suggests that in terms of the constraints

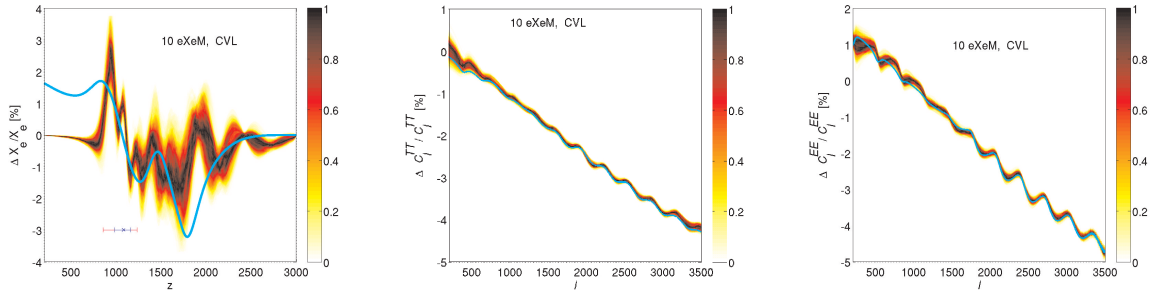


Figure 3.20: Similar to Fig. 3.19 but with the first ten eXeMs.

on the standard parameters, we do not lose much by increasing the number of eXeMs. Besides, including more eXeMs does not affect the measurement of the previously included eigenmodes, as they are by construction uncorrelated (in the presence of standard parameters). Including more eXeMs, on the other hand, makes the reconstructed perturbations closer to the input model of perturbations (as in Fig. 3.12). However, as the errors of modes increase by going to higher orders, the error on the reconstructed curve increases. We address this point in the next section.

Among the first 20 eXeMs for a CVL experiment, the modes with the most significant contributions (i.e., with at least 1σ detection) are $\mu_2 = 0.11 \pm 0.02$, $\mu_3 = 0.10 \pm 0.03$, $\mu_9 = -0.31 \pm 0.16$ and $\mu_{11} = -0.36 \pm 0.24$ (compare to their theoretical prediction from direct projection of the perturbations on the eXeMs: $\mu_2 = 0.14$, $\mu_3 = 0.10$, $\mu_9 = -0.33$ and $\mu_{11} = -0.39$). The reason that the recovered value, though close, is not exactly the same as the forecast is that the assumption of the Gaussianity of the distributions of the eXeMs and the standard parameters is only approximate. Also the eigenmodes have been slightly smoothed in the construction process which may cause numerical inaccuracy and induce slight correlation between the smoothed modes. By comparing the theoretical values of projection of the perturbation on the eXeMs and their forecast errors (from Fisher analysis) we do not expect any perturbation detection after eXeM 11.

Fig. 3.18 shows similar contours but for a simulated Planck-CTPol-like observation. For the analysis we used the eigenmodes (both eXeMs and XeMs) constructed with the Planck-CTPol simulated noise. The results from the two sets of eigenmodes are very similar. For both XeMs and eXeMs, one mode was sufficient to remove the bias ($\mu_1 = -0.22 \pm 0.06$ and $\mu_1 = -0.20 \pm 0.06$ respectively). This happens to be in agreement with the cutoff mode for the XeMs while with the eXeMs the second mode should also be included. The lower number of modes required for the Planck-CTPol-like case compared to the ideal experiment is expected due to higher sensitivity of the data in the latter to deviations from the underlying X_e history.

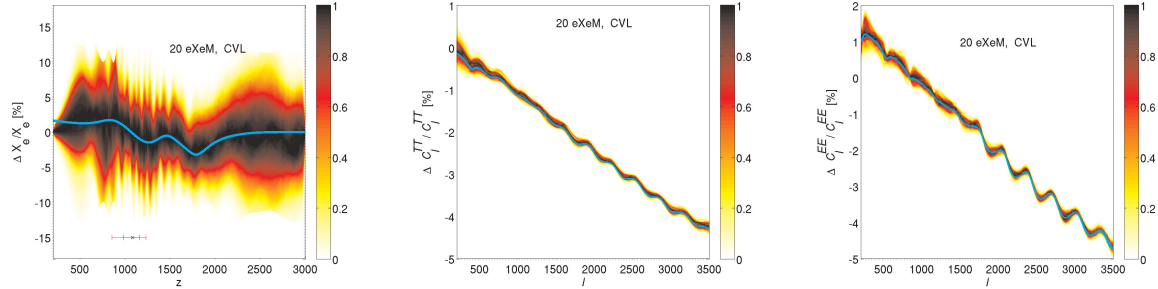


Figure 3.21: Similar to Fig. 3.19 but with the first twenty eXeMs. As this figure demonstrates, including a higher number of modes does not necessarily lead to better X_e recovery. Here the recovered X_e becomes noisier compared to the case with only ten modes included, while the C_ℓ trajectories do not change significantly except for the diminished oscillations around the input model, as discussed in the text.

We also tried three modes, with no significant detection of the new modes, while the error on the XeM 1 increases by a factor of 2.

3.5.3 Trajectories

In this section we investigate the reconstruction of the X_e -perturbations using the simulated data to illustrate the corresponding uncertainty at different redshifts. The left plot in Fig. 3.19 shows the redshift interval covered by 500 $\delta \ln X_e$ -trajectories corresponding to an ideal observational case with eight XeM included, for the CT2011 model. The color indicates the number of trajectories passing through each $(z, \delta X_e/X_e)$ bin, normalized to one at each redshift snapshot. The trajectories clearly show deviations from the SRS, slowly morphing into the correction obtained by CT2011 (the cyan curve). However, the recovery is not perfect, as the model of CT2011 has non-zero (and relatively significant) projection on higher XeMs which are not well constrained by data, and therefore were not included into the analysis. Most obviously, corrections to helium recombination are not captured well when using only the first few XeMs. These trajectories do not recover the analytical projection of the CT2011 corrections on the first eight XeMs very well either. The reason, as discussed before, is that the correlation of the XeMs induced by the standard parameters draws some contribution from the higher absent modes which biases the measurement of the first few XeMs included in the measurement.

To test this impact of higher, excluded modes on the recovered (low XeM) trajectories, we ran simulations with the data that only accounted for the contributions from these low modes. As expected, in the absence of higher modes in the data, the measured XeMs were non-biased and thus the highest probability region of the trajectories covered the $\delta \ln X_e$ curve of the input

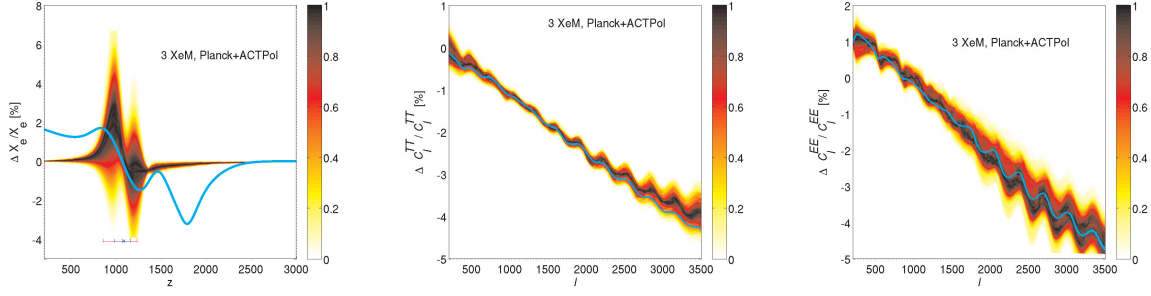


Figure 3.22: Similar to Fig. 3.19 but for a Planck-ACTPol-like experiment and with only three XeMs taken into account.

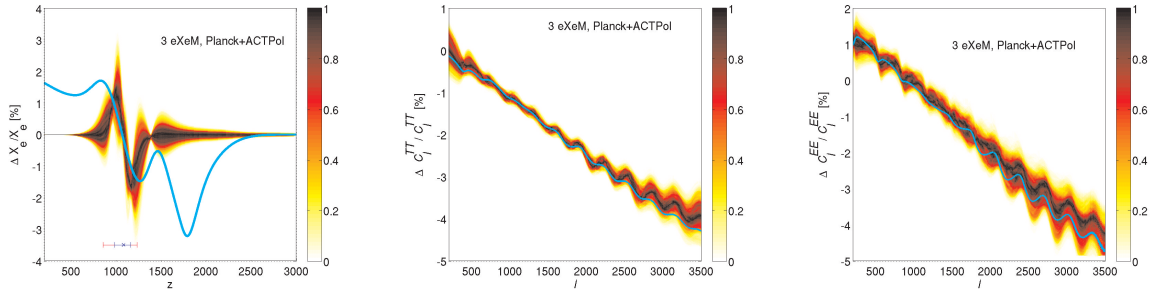


Figure 3.23: Similar to Fig. 3.20 but for a Planck-ACTPol-like experiment and with only three eXeMs taken into account.

model.

Although our basic target is X_e -recovery, the relevant space for determining how well we have done is that of the CMB data, reduced to the power spectra, C_ℓ^{TT} and C_ℓ^{EE} . The central and right panels of Fig. 3.19 show the $\delta C_\ell^{TT} / C_\ell^{TT}$ and $\delta C_\ell^{EE} / C_\ell^{EE}$ trajectories, where $\delta C_\ell^X / C_\ell^X = (C_\ell^X - C_\ell^{X,\text{fid}}) / C_\ell^{X,\text{fid}}$ and C_ℓ^{fid} is the fiducial power spectrum without any perturbations. The transformation from X_e trajectories to C_ℓ trajectories shows a much tighter band around the input signal. This is a visual confirmation of the point that some features in the $\delta \ln X_e$ which make the X_e trajectories thick do not leave a measurable imprint on the C_ℓ 's. Notice there are small residual oscillations, i.e., in the difference between the recovered trajectory and the input power spectrum. They coincide with the peaks and troughs of the C_ℓ curves for both TT and EE (which is out of phase with TT). One source for the oscillations seems to be the eigenmode truncation, as we will see later. Using only a limited number of the modes in the analysis causes the non- X_e cosmic parameters to try to match the injected X_e perturbations. There is also an issue of accuracy of the C_ℓ code for some of the distortions.

Fig. 3.20 similarly shows the 2D histograms of trajectories for the case with the first ten

eXeMs included. Around the maximum of the Thomson visibility function the X_e reconstruction is slightly stronger and less fuzzy than in Fig. 3.19, with part of the helium recombination correction being recovered. The improvement in the reconstruction is because for the computation of these eigenmodes their correlation with the standard parameters have been optimally taken care of. In contrast, the XeMs used in the previous case are non-optimal if no strong additional priors can be placed on the standard parameters, leading to confusion in the errors and the rank-ordering of the modes. Fig. 3.21, constructed with 20 eXeMs included, shows that the oscillation effect mentioned above around the input C_ℓ signal is diminished (and also partially swamped by the slightly higher dispersion around the input curve) for the 20-mode compared to the ten-mode case. We also see that including a higher number of modes does not necessarily lead to better X_e recovery.

Similar trajectories for a Planck-ACTPol-like experiment are shown in Figs. 3.22 and 3.23, with three XeMs and three eXeMs as the eigenmodes respectively. The trajectories for the XeMs are more widely spread and blurred due to experimental noise. The eXeMs perform slightly better. However, the overall reconstruction is clearly lacking detailed agreement with the full recombination correction of CT2011. In particular, most of the modification during helium recombination is not captured, as the corresponding signals can only be picked up with higher modes, which in the considered case are not constrainable at a significant level. In the $\delta C_\ell/C_\ell$ plots of these Planck-ACTPol-like cases, there is a small disagreement at high multipoles between the theoretical curve and the highest probability region of the chains. That is mainly due to mode truncation at a relatively low mode number, i.e., three. We tested this by including eight modes and as expected, observed a wider spread around the input signal with the disagreement diminished.

Although we do not plot the equivalent $\delta C_\ell/C_\ell$ for the DM case discussed in § 3.4.7, very similar plots result, namely good recovery of the power spectra with a dispersion around the input perturbation signal.

3.5.4 Beyond small perturbations

In this paper it was explicitly assumed that the model best explaining the ionization fraction (or the true model underlying the ionization history) is only slightly different from our fiducial model, justifying our choice of parameter $\delta \ln X_e$. Therefore, the eigenmodes constructed for the *fiducial* model are also very close to the eigenmodes for the perturbations to the *true* X_e , the corrections to the eigenmodes arising from the difference between the fiducial and true X_e model being only of second order. Under this assumption, a one step search for the best-fit parameters suffices to extract the available relevant information from the data, provided that the minimum required number of modes are included in the analysis. Finding the minimum

number of required modes can by itself involve several parameter estimation steps in parameter spaces with different dimensions, the criterion being that the best fit values for the standard parameters stop changing. That is what was done in the examples in this work (§ 3.5.2), to illustrate how the method works.

However, if the fiducial model is *very* far from the true X_e history, such that the eigenmodes are expected to be affected at a significant level, an iterative approach toward finding the best modes with their associated amplitudes and errors is required: starting with our best guess for the fiducial model, we estimate its deviation from the true ionization history using the dataset available and the eigenmodes constructed based on this fiducial model. We then update the model by adding to it the measured deviations in the eigenmodes (and the standard parameters, if required). This process is repeated until the convergence of the model and its eigenmodes.

However, current constraints seem to indicate that such an iterative procedure is not necessary within the standard picture. For example, as shown by Shaw & Chluba (2011), the recombination corrections of CT2011 are readily incorporated using one calibrated redshift dependent correction function relative to the original recombination model of Seager et al. (1999). Even for CVL errors a second update of the correction functions leads to minor effects. Nevertheless, if something more surprising occurred during recombination, an iterative approach might be required.

3.6 conclusion and discussion

CMB data today are becoming so precise that small modifications in standard ionization history are important. This impressive progress not only implies that measurements of the main cosmological parameters are becoming increasingly accurate, but also means that remaining uncertainties in the recombination dynamics, e.g., caused by neglected standard or non-standard physical processes, should be quantified. In this work we discuss a novel approach to constrain this remaining ambiguity with future CMB data. We performed a principal component analysis to find parameter eigenmodes that can be used to describe uncertainties in the ionization fraction. We constructed X_e eigenmodes over the redshift range of $[200, 3000]$, performing several consistency checks to prove the correctness of our method. This approach automatically delivers a hierarchy of mode functions that can be selected according to their error and then are added to the standard cosmological parameters when analyzing CMB data.

Due to the strong CMB signal imprinted by hydrogen recombination, the most constrained modes are mainly localized around $z \sim 1100$, with some extensions to lower and higher redshift regions (see Fig. 3.5 and 3.7). This emphasizes that CMB data are very sensitive to small changes during hydrogen recombination, while details of helium recombination or small

changes in the freeze-out tail are hard to constrain, unless strong priors on the reliability of the hydrogen recombination model are imposed. With the method described here it is possible to construct mode functions for different experimental situations, also folding in prior knowledge on the recombination history using appropriate weight functions and fiducial X_e models. For example, if there are physically motivated and experimentally supported hints toward (significant) changes in the freeze-out tail of recombination, e.g., due to energy injection from dark matter annihilation, we propose a parametrization which weights the low redshift part more strongly (see Fig. 3.4).

After we completed this work, we received a preprint (Finkbeiner et al., 2012) which investigated the use of CMB data to constrain details of energy injection scenarios related to decaying or annihilating particles. They also used parameter eigenmodes, but these were constructed based on an energy release history which is in our language akin to the imposition of a strong prior on the recombination dynamics around $z \sim 1100$ and a focus on the freeze-out tail of the recombination.

We applied the method to different simulated datasets with the aim to assess how well future CMB experiments will be able to constrain modifications to the standard recombination scenario. (Current WMAP plus ACT and SPT data will provide only relatively weak constraints, but Planck plus ACTPol and SPTPol will considerably improve the situation.) As a working example we used the refined recombination calculations of COSMOREC. For simulated CMB datasets corresponding to Planck-ACTPol-like experiments we found that the first 3 eigenmodes can be rather well constrained. The addition of these modes allows us to compensate for the measurable differences between the fiducial old X_e model as given by RECFAST to the new recombination history computed with COSMOREC, and thus partially reconstruct the true X_e history, without actually directly using the recombination corrections in the analysis. However, because the first few mode functions are strongly localized around $z \sim 1100$ details during helium recombination and in the freeze-out tail are not captured (Fig. 3.23). The addition of the first 3 eigenmodes is sufficient to remove the biases in the standard parameters, however, at the cost of increased error bars. We also show that for CVL limited experiments up to $l \sim 3500$ up to 10 modes might be constrainable, in this case allowing us to pick up part of the details during helium recombination (Fig. 3.20).

The significance of the detection of any perturbation obviously depends on the underlying ionization history of the real data. In the specific COSMOREC example for Planck-ACTPol-like experiments, all three modes but the first one are consistent with zero. A significant source for large errors on the eigenmodes is their correlation with the standard parameters. If tight constraints are imposed on the standard parameters by non-CMB experiments such as BAO or SN data, the errors on the eigenmodes will be correspondingly reduced. Comparing the first

rows of Table 3.4 (where all standard parameters are held fixed) and Table 3.4.2 (where all standard parameters are being marginalized over) illustrates the effect of this correlation in the extremes.

This also shows how important one’s knowledge in how well elements of recombination are known, expressed through prior probabilities, will be. If the uncertainty in the ionization history during hydrogen recombination can be reliably reduced by other methods then the sensitivity to small perturbations at higher or lower redshifts is enhanced. We note that measurements of the cosmological recombination radiation (e.g., see Chluba & Sunyaev, 2006a; Sunyaev & Chluba, 2009) could in principle provide an alternative way of constraining the recombination dynamics in the future. In particular, the recombination radiation could exhibit significant features if something more unexpected occurred during different cosmological epochs (e.g., see Chluba & Sunyaev, 2009; Chluba, 2010).

In principle, for a complete study of ionization history, late reionization should also be included in the analysis. Ambiguities in the low redshift part of the ionization history may affect the measurements of high redshift perturbations and vice versa. However, the main signal from the reionization epoch is measurable from the very large scale CMB polarization, and the high redshift perturbations of X_e affect anisotropies with smaller angular scales. Therefore the signals from these two regions are rather uncorrelated. A more complete analysis for the whole ionization history or where different parts of it are considered simultaneously is for future work.

An aspect requiring decision when analyzing real data is the choice of parametrization. For most of this work we weighted the perturbations in X_e by the fiducial history. If, for example, the recovered perturbations point towards modifications in the freeze-out tail of recombination, or if there is strong belief that no sign of significant deviations around the maximum of visibility are present, an alternative parametrization which allows better reconstruction of the tail can be constructed, using appropriate weight functions that quantify our belief in the underlying fiducial model.

As discussed in § 3.5.4, our semi-blind XeMs are designed to only probe small perturbations about the fiducial model X_e^{fid} . When it comes to real CMB data analysis, iterations of X_e^{fid} may be required to ensure no leftover bias remains. We look forward to the application of iteratively-improved eigenmodes to the coming high resolution CMB data from Planck, ACTPol and SPTPol.

We thank Doug Finkbeiner, Tongyan Lin and Olivier Doré for useful discussions and Eric Switzer for his comments on the text. Support from NSERC and the Canadian Institute for Advanced Research is gratefully acknowledged.

3.7 Appendix

3.7.1 Localized basis functions

To expand perturbations to the ionization scenario, three sets of localized mode functions have been considered in this paper: Gaussian and triangular bumps and M_4 -splines. For the Gaussian and triangular bumps, we define the i th basis function centered at redshift z_i and having width σ_i by

$$\varphi_i(z) \propto \exp\left(-\frac{[z - z_i]^2}{2\sigma_i^2}\right) \quad (3.4)$$

for the Gaussian case and by

$$\varphi_i(z) \propto \begin{cases} 1 - \frac{|z - z_i|}{\sigma_i} & |z - z_i| < \sigma_i, \\ 0 & \text{otherwise,} \end{cases} \quad (3.5)$$

for the triangles. The widths of the bumps σ_i 's can in general be redshift dependent, enabling us to differently sample different intervals. However, throughout this work, we have taken them to be constant. Triangular bumps were used earlier in the principal component analysis of different reionization scenarios (Hu & Holder, 2003; Mortonson & Hu, 2008). In some circumstances, the sharp edges in the triangles could cause numerical problems. Smoothed localized functions such as Gaussians and the M_4 splines introduced below have therefore numerical advantage.

Instead of Gaussian and triangular bumps, one can also adopt an approach similar to that used in Smoothed-Particle Hydrodynamics (SPH), and think of the basis functions as window functions (or kernels) used to interpolate the properties of particles to any point in the medium. For us, the *particles* would be the spline *knots* (e.g. see De Boor, 2001) at the specific z_i with the associated magnitude y_i . There is a smoothing length h associated with the kernel over which the properties of the particles are smoothed. Another commonly used kernel (other than the Gaussian considered above) is the *cubic M_4 spline* (e.g. Monaghan, 2005), defined by:

$$\begin{aligned} \varphi_i(z) &\propto M_4(|z - z_i|) \\ &= \begin{cases} \frac{1}{6}[(2 - q)^3 - 4(1 - q)^3] & 0 \leq q \leq 1; \\ \frac{1}{6}(2 - q)^3 & 1 \leq q \leq 2; \\ 0 & q > 2; \end{cases} \end{aligned} \quad (3.6)$$

where $q = |z - z_i|/h$. Whereas the Gaussian kernel has non-zero contributions from every redshift (though the range is usually truncated beyond about 3σ), the cubic spline is compact, reaching zero for particles beyond $2h$.

As mentioned above, in this work the width of the bumps of these mode functions is chosen to be independent of redshift. We choose $\sigma_i = \delta z/2$ for Gaussian and triangular bumps (Eqs. (3.4) and (3.5)) and $h = 1.5\delta z$ for M_4 splines (Eq. (3.6)). In all cases, $\delta z = \Delta z/(N + 1)$ is the spacing

between the centers of adjacent bumps, where Δz is the redshift range of interest and N is the number of basis functions used.

As basis functions, it is more convenient if the set of φ_i 's is an orthogonal set. For this, there should be no overlap between different bumps. On the other hand, there is no way to cover the whole redshift range – a necessary condition for completeness – with a finite number of non-overlapping bumps. However, depending on the problem of interest, the width and separation of the (overlapping) bumps can be properly chosen to ensure all points in the redshift interval have been covered, while at the same time the orthogonality is not strongly violated.

3.7.2 Non-localized basis function

The most commonly used set of non-localized basis functions is the *Fourier series*:

$$u_i(z) \propto \cos(i\pi y) \quad i = 0, 1, 2, \dots \quad (3.7a)$$

$$u_i(z) \propto \sin(i\pi y) \quad i = 1, 2, \dots \quad (3.7b)$$

$$y = \frac{z - z_{\text{mid}}}{\Delta z/2} \quad (3.7c)$$

where Δz and z_{mid} are the width and central point in the redshift range of interest. Thus we have $|y| \leq 1$ as is required for Fourier expansion.

Alternatively, we can use *Chebyshev polynomials* of the first kind, T_i , to form the basis. These modes are constructed using the recursion formula:

$$T_{i+1}(y) = 2yT_i(y) - T_{i-1}(y)$$

with initial conditions $T_0(y) = 1$ and $T_1(y) = y$, and y is given by Eq. (3.7c). Chebyshev polynomials of the first kind are orthogonal with respect to the weight function $w(y) = 1/\sqrt{1-y^2}$.

These non-localized mode functions, unlike the localized case (with finite number of basis functions), do not suffer from non-orthogonality. However, both localized and non-localized sets of basis functions can in practice be considered complete if sufficiently many functions are taken into account.

3.7.3 Eigenmodes with fixed and varying background cosmology

For a model described by N possibly correlated parameters, there is in general an orthogonal transformation which linearly maps these parameters into a set of N uncorrelated ones. These parameters are determined by the eigenmodes of the ($N \times N$) Fisher information matrix:

$$F_{ij} \equiv - \left\langle \frac{\partial^2 \ln p_f}{\partial q_i \partial q_j} \right\rangle, \quad 1 \leq i, j \leq N$$

where in the language of Bayesian analysis, $p_f \equiv p(\mathbf{q}|d, \mathcal{T})$ (with $\mathbf{q} = (q_1, \dots, q_N)$) describes the posterior probability of the parameters q_i 's for the given data d in the theory space \mathcal{T} . I.e., $p_f = \mathcal{L}(\mathbf{q}|d, \mathcal{T})p_i/\mathcal{E}$ is an update from the prior probability distribution of the parameters, $p_i = p(\mathbf{q}|\mathcal{T})$ driven by the likelihood $\mathcal{L}(\mathbf{q}|d, \mathcal{T}) \equiv p(d|\mathbf{q}, \mathcal{T})$. Here the evidence $\mathcal{E} \equiv p(d|\mathcal{T})$ is a normalization factor. We include \mathcal{T} in the notation only if there is ambiguity in the theory space under consideration. The derivatives are calculated at the fiducial values of the parameters. The ensemble average $\langle \dots \rangle$ is over realizations of the CMB sky and instrument noise.

Under the assumption of uniform priors for the q_i 's, the Fisher matrix reduces to:

$$F_{ij} = - \left\langle \frac{\partial^2 \ln \mathcal{L}}{\partial q_i \partial q_j} \right\rangle.$$

In the standard CMB analysis with Gaussian signal and noise, we have $\mathcal{L} = \exp(-\Delta^\dagger \mathbf{C}^{-1} \Delta/2)/\sqrt{2\pi|\mathbf{C}|}$. Here Δ represents the temperature and polarization maps including CMB signal as well as instrumental noise and $\mathbf{C} = \langle \Delta \Delta^\dagger \rangle$ is the theoretical pixel-pixel covariance matrix. With this likelihood function, the Fisher matrix simplifies to:

$$F_{ij} = \frac{1}{2} \text{Tr} \left(\mathbf{C}^{-1} \frac{\partial \mathbf{C}}{\partial q_i} \mathbf{C}^{-1} \frac{\partial \mathbf{C}}{\partial q_j} \right).$$

In the limit of full sky observation, or in cut-sky cases where coupling between modes of different scales can be ignored, \mathbf{F} can be written as:

$$F_{ij} = f_{\text{sky}} \sum_{\ell=2}^{\ell_{\text{max}}} \frac{2\ell+1}{2} \frac{\partial \mathbf{C}_\ell}{\partial q_i} \mathbf{C}_\ell^{-1} \frac{\partial \mathbf{C}_\ell}{\partial q_j} \mathbf{C}_\ell^{-1} \quad (3.8)$$

with

$$\mathbf{C}_\ell = \begin{pmatrix} C_\ell^{TT} e^{-\ell^2 \sigma^2} + N_\ell^T & C_\ell^{TE} e^{-\ell^2 \sigma^2} \\ C_\ell^{TE} e^{-\ell^2 \sigma^2} & C_\ell^{EE} e^{-\ell^2 \sigma^2} + N_\ell^E \end{pmatrix},$$

where we have included CMB temperature T , E -mode polarization and their cross correlation TE . Here $N_\ell^{T,E}$ stands for instrumental noise contribution to the power spectra and σ is the width of the Gaussian beam. The effect of incomplete sky coverage has been naively taken into account by the f_{sky} multiplier which reduces the effective number of observed modes.

Our goal here is to find the uncorrelated set of parameters that describe possible perturbations to the ionization history. For this purpose we need to eigendecompose the block of the inverse of the Fisher matrix which corresponds to the perturbation parameters. In the most general case with the background cosmology also being varied, the Fisher matrix has the following general form

$$\mathbf{F} = \begin{pmatrix} F_{ss} & F_{sp} \\ F_{ps} & F_{pp} \end{pmatrix}, \quad (3.9)$$

where we have $\mathbf{F}_{ss} = -\left\langle \frac{\partial^2 \ln \mathcal{L}}{\partial s \partial s} \right\rangle$, $\mathbf{F}_{sp} = \mathbf{F}_{ps} = -\left\langle \frac{\partial^2 \ln \mathcal{L}}{\partial s \partial p} \right\rangle$ and $\mathbf{F}_{pp} = -\left\langle \frac{\partial^2 \ln \mathcal{L}}{\partial p \partial p} \right\rangle$, with s and p symbolically representing the standard and perturbation parameters.

To find the eigenmodes for perturbations after marginalization over the standard parameters, under the assumption of ellipsoidal parameter contours, we need to eigendecompose $(\mathbf{F}^{-1})_{pp}$ and find the eigenvectors. However, the inversion of the Fisher matrix is numerically problematic as it is ill-conditioned due the non-constrainable parameters which exist in the parameter space under study.

In the case of fixed standard parameters, the Fisher matrix reduces to the perturbation block only, and since the eigenvectors of a symmetric matrix and its inverse are the same (with inverse eigenvalues), there is no need to invert the Fisher matrix before its eigendecomposition. Similarly to get the eXeM, i.e., the eigenvectors of $(\mathbf{F}^{-1})_{pp}$ with \mathbf{F} as in Eq. (3.9), we avoid the direct full inversion of \mathbf{F} by noting that

$$(\mathbf{F}^{-1})_{pp} = (\mathbf{F}_{pp} - \mathbf{F}_{ps} \mathbf{F}_{ss}^{-1} \mathbf{F}_{sp})^{-1}.$$

The eigendecomposition of $\mathbf{F}_{pp} - \mathbf{F}_{ps} \mathbf{F}_{ss}^{-1} \mathbf{F}_{sp}$ then only requires the inversion of the well-behaved standard parameter block. It is straightforward to directly check that $(\mathbf{F}^{-1})_{pp}$ properly describes the marginal likelihood of the perturbation parameters:

$$\begin{aligned} \mathcal{L}(\mathbf{p}|d) &\propto e^{-\mathbf{p}^T \mathbf{F}_{pp} \mathbf{p} / 2} \int e^{-\mathbf{s}^T \mathbf{F}_{ss} \mathbf{s} / 2} e^{-\mathbf{p}^T \mathbf{F}_{ps} \mathbf{s}} d\mathbf{s} \\ &\propto e^{-\mathbf{p}^T (\mathbf{F}_{pp} - \mathbf{F}_{ps} \mathbf{F}_{ss}^{-1} \mathbf{F}_{sp}) \mathbf{p} / 2}. \end{aligned}$$

Here \mathbf{p} and \mathbf{s} are the arrays of the perturbation and standard parameters.

The eigenmodes we are looking for can now be constructed using the eigenvectors of the inverse of the pp block of the Fisher matrix $(\mathbf{F}_{pp})^{-1} = \mathbf{S} \mathbf{f}^{-1} \mathbf{S}^T$ where the columns of \mathbf{S} are the eigenvectors of $(\mathbf{F}_{pp})^{-1}$ with their corresponding (non-negative) eigenvalues on the diagonal of the real diagonal matrix \mathbf{f}^{-1} . The eigenmodes we are looking for can now be constructed using these eigenvectors of the Fisher matrix and the basis functions we started with:

$$E_k(z) = \sum_{i=1}^N S_{ik} \varphi_i(z). \quad (3.10)$$

If the φ_i 's happen to be orthonormal, then we have:

$$\int_{z_{\min}}^{z_{\max}} E_k(z) E_{k'}(z) w(z) dz = \delta_{kk'}. \quad (3.11)$$

Here $w(z)$ is the weight function with respect to which φ_i 's are orthonormal. Since Eq. (3.11) is not necessarily fulfilled, we enforce the $E_k(z)$'s to be normalized to unity (as a matter of convenience), which is equivalent to a renormalization of the eigenvectors of \mathbf{F} . Although in

general this could change the rank ordering of the modes, in our case a reordering was not required for the modes included in the analysis. Now, instead of the original φ_i 's, the set of the eigenmodes can serve as basis functions for the expansion of perturbations (compare with Eq. (3.3)):

$$\delta u(z) = \sum_{k=1}^N \mu_k E_k(z) + r(z).$$

In § 3.4.7 we discuss two examples of perturbation reconstruction with different numbers of eigenmodes taken into account (Fig. 3.12). We demonstrate how well these eigenmodes serve as basis functions and also which features of the original perturbations are restored (or lost) if only a subset of the eigenmodes are used in the reconstruction process.

The square root of the eigenvalues of the inverse of the Fisher matrix can be used to forecast the error bars of the eigenmodes, i.e., $f_{ij} = \sigma_i^{-2} \delta_{ij}$, assuming the probability distribution of the parameters is multivariate Gaussian close to the maximum. For non-Gaussian likelihoods, the σ_i 's give the lower bound for the errors. In the rest of this paper we use the term *error* for the σ_i 's, as the Gaussianity of the likelihood function close to its maximum is usually a good assumption. If the modes are sorted in descending order of eigenvalues, the first few (with smallest σ_i 's) are the most constrainable. Thus, the constrainable part of the perturbations to the ionization history can be described by the eigenmodes which have reasonably small uncertainties (i.e., high eigenvalues), while the rest is practically unconstrainable by the dataset under consideration.

3.7.4 Fiducial model and dataset dependence

The eigenmodes are by construction fiducial model dependent. In principle, the observables (such as C_ℓ 's) for different fiducial models respond differently to the same perturbations depending on the strength of the signals, at different redshifts, from the unperturbed fiducial model.

As an example, in Fig. 3.24 we compare the eigenmodes for three fiducial X_e histories. Two of the models have different CMB temperatures and in the third one lensing has not been included. In the first two, the different T_{CMB} 's lead to different fiducial X_e 's. Here, the main difference in the eigenmodes is their shift towards lower z 's for the case with higher CMB temperature. This is consistent with the delayed recombination shown in Fig. 3.1, remembering that XeMs are primarily localized around the maximum of visibility where the C_ℓ 's are most sensitive to. For the latter case with no lensing, although X_e and the physics around recombination have not changed, there are still slight changes in some of the XeMs as seen in Fig. 3.24.

We also checked the robustness of the eigenmodes against changes in the fiducial value of

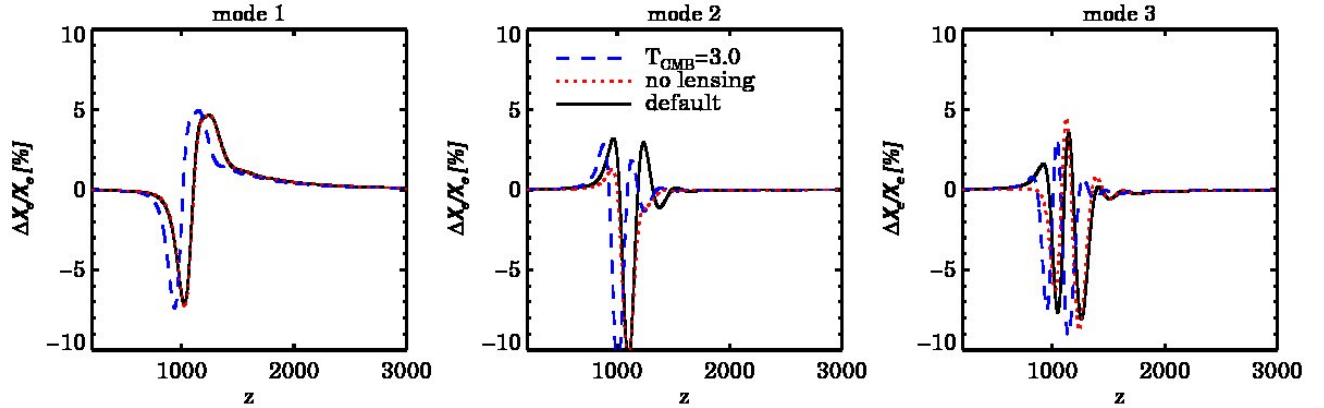


Figure 3.24: The three most constrained XEMs for three different fiducial models. The default model corresponds to the SRS and the effect of gravitational lensing on the CMB anisotropies has been included. One model corresponds to a recombination history with a different CMB temperature and in the other model lensing is not included. For the case of the two different CMB temperatures, the major difference is the shift in the eigenmodes associated to the shift in the fiducial X_e and visibility functions (see Fig. 3.1).

other parameters and the assumed reionization scenario. We tried a different value for Ω_b , as the parameter most strongly affecting the ionization fraction, 1σ away from its fiducial value. For the late reionization we tried an extended reionization scenario (i.e., $X_e = 1$ for $z \leq 6$; $X_e = 0.5$ for $6 < z \leq 30$ and $X_e = 0$ elsewhere) radically different from our sharp fiducial reionization model (the default in CAMB). For both of these tests the first six eigenmodes were found to be the same as our main eigenmodes (Fig 3.5) with tiny differences in the fifth and sixth modes for the latter case.

This implies that, although the eigenmodes are fiducial model dependent, the constrainable ones are not practically sensitive to changes in the fiducial model or its parameters in the limits currently allowed by the data for the standard model of cosmology. That is because small changes in the fiducial parameters and the corresponding small changes in the ionization history only affect the XEMs at second order. Here by small we mean changes that lead to (smaller than or) the same order of magnitude signal in the simulated data as the (few best) XEMs. The higher XEMs with larger uncertainties are more affected by the same changes in the fiducial parameters, as these changes are no longer considered small relative to these poorly constrained XEMs. This non-sensitivity of the best modes to the fiducial values of parameters does not contradict their significant correlation once the standard parameters are also allowed to vary, as we see in § 3.5.1.

We also studied the dependence of the XEMs on some properties of the simulated CMB

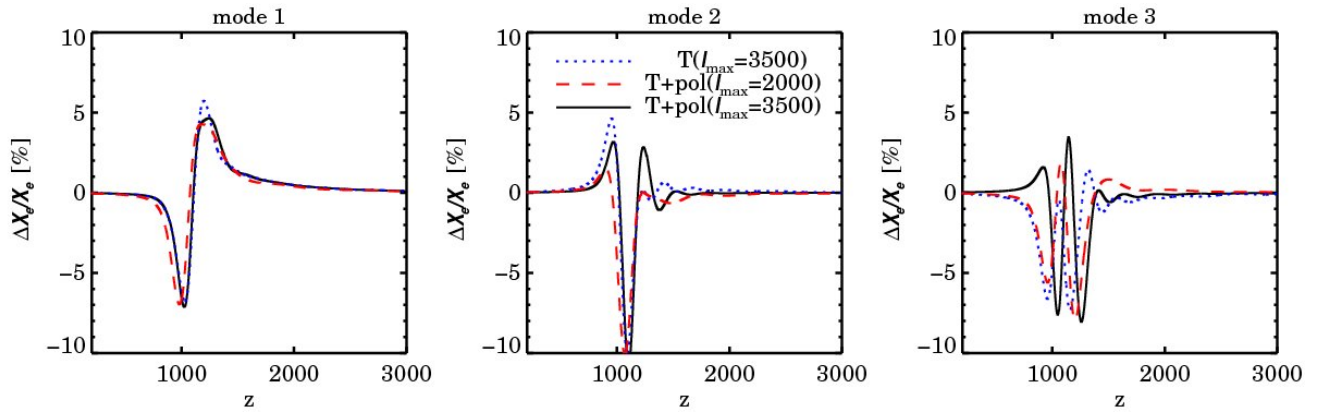


Figure 3.25: The three most constrained XEMs with and without polarization and with $\ell_{\max} = 2000$ and 3500.

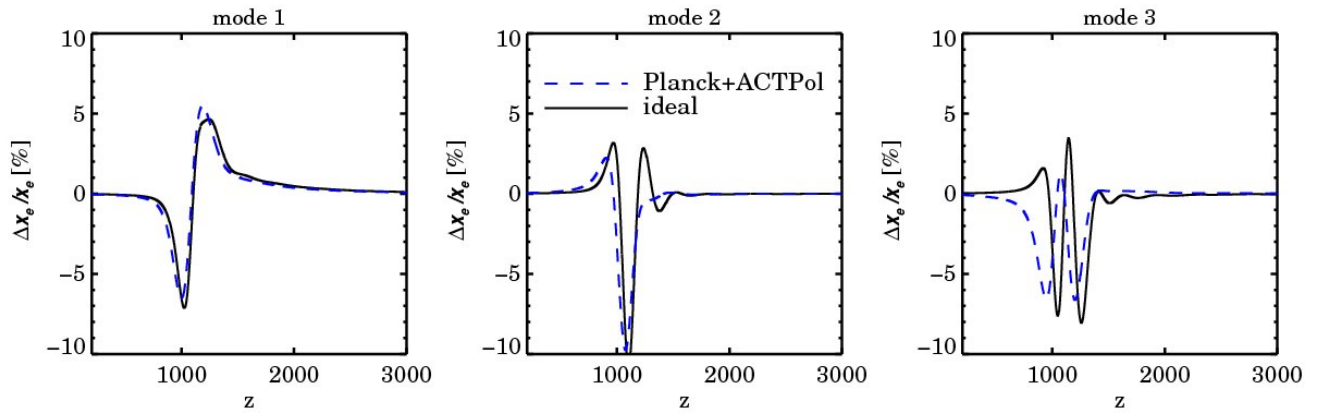


Figure 3.26: The three most constrained XEMs for a Planck-ACTPol-like experiment compared to a CVL experiment.

datasets used for their construction, such as different ℓ_{\max} corresponding to the smallest scale information present in the data, and different experimental noise levels. The results for a CVL experiment up to $\ell = 2000$ in temperature and polarization and also a CVL experiment only sensitive to temperature (up to $\ell = 3500$) are shown in Fig. 3.25. As a more experimentally motivated case, we calculated the XeMs for simulated Planck-like data¹⁴ (using 100, 143 and 217 GHz channels, with effective galaxy-cut sky coverage of 75%) and ACTPol-like data, including both wide and deep surveys (Niemack et al., 2010). As shown in Fig. 3.26, there is a tiny shift in the first mode relative to the mode for an ideal experiment and the changes grow as we proceed to higher modes.

More significant than the small changes in the XeMs constructed with different assumptions about data, are the forecasted error bars in different cases (see Table 3.4). By removing the temperature at high ℓ 's or the polarization spectrum, the constraints on the amplitudes of the modes, determined from the eigenvalues of the Fisher matrix, become considerably larger. All these errors are calculated with the standard parameters fixed. However, the considered cases illustrate the general behaviour of the method. Taking into account the correlation between the perturbations and the standard cosmic parameters leads to relatively higher error bars, depending on the dataset used (Table 3.4.2).

¹⁴http://www.rssd.esa.int/SA/PLANCK/docs/Bluebook-ESA-SCI282005291_V2.pdf

Chapter 4

Constraints on perturbations to the recombination history from measurements of the CMB damping tail

A version of this chapter is published in the Astrophysical Journal as “Constraints on perturbations to the recombination history from measurements of the CMB damping tail”, Farhang, M.; Bond, J. R.; Chluba, J.; Switzer, E. R.

4.1 Chapter Overview

The primordial CMB at small angular scales is sensitive to the ionization and expansion history of the universe around the time of recombination. This dependence has been exploited to constrain the helium abundance and the effective number of relativistic species. Here we focus on allowed ionization fraction trajectories, $X_e(z)$, by constraining low-order principal components of perturbations to the standard recombination scenario (X_e -eigenmodes) in the circa 2011 SPT, ACT and WMAP7 data. Although the trajectories are statistically consistent with the standard recombination, we find that there is a tension similar to that found by varying the helium fraction. As this paper was in press, final SPT and ACT datasets were released and we applied our framework to them: we find the tension continues, with slightly higher significance, in the new 2012 SPT data, but find no tension with the standard model of recombination in the new 2012 ACT data. We find that the prior probabilities on the eigenamplitudes are substantially influenced by the requirement that X_e trajectories conserve electron number. We propose requiring

a sufficient entropy decrease between posterior and prior marginalized distributions be used as an X_e -mode selection criterion. We find that in the case of the 2011 SPT/ACT+WMAP7 data only two modes are constrainable, but upcoming ACTPol, Planck and SPTPol data will be able to test more modes and more precisely address the current tension.

4.2 Introduction

A primary goal of CMB experiments after the discovery of the acoustic features in the angular power spectrum was to measure the damping tail. This was achieved by the CBI (Sievers et al., 2003, 2007a) and ACBAR (Goldstein et al., 2003; Reichardt et al., 2009a) experiments, and spectacularly verified by the Atacama Cosmology Telescope (ACT, e.g., Dunkley et al., 2011) and the South Pole Telescope (SPT, e.g., Keisler et al., 2011). There is even higher precision data on its way from ACT, SPT and Planck. Initially the goal was simply to confirm that the damping tail agreed with theoretical predictions based on cosmological parameters determined from the first set of peaks and troughs. Contemporary high-precision data opens the opportunity for new constraints of cosmological parameters that specifically influence the damping tail and have little influence on larger scales. The parameters wagged the tail, and now the tail can wag the parameters. Examples of these parameters are the primordial helium abundance Y_p and the effective number of relativistic species, N_{eff} . Both experiments have hinted at a deficit of power in the damping tail through the Y_p and N_{eff} probes (Keisler et al., 2011; Dunkley et al., 2011; Hou et al., 2011). Other physical possibilities have also been investigated to explain this damping tail tension; these include dark radiation (Smith et al., 2012; Eggers Bjaelde et al., 2012), the annihilation or decay of dark matter particles (Giesen et al., 2012), cosmic strings (Lizarraga et al., 2012) or a high-frequency cosmic gravitational wave background (Sendra & Smith, 2012).

CMB anisotropies are suppressed on small scales by shear viscosity and thermal diffusion when the photons and electrons are tightly coupled, and by higher order transport effects as the photons break out from their random-walk Thomson scatterings by electrons to approach free-streaming. The physics of Silk damping (Silk, 1968) has been heavily explored, as reviewed in Bond (1996b); Hu & White (1997); Sievers et al. (2003), and is very accurately computed numerically in CMB transport codes (Seljak & Zaldarriaga, 1996; Lewis et al., 2000). One can associate a characteristic damping wavenumber $k_D(z)$ with the processes, determined by the steep variation in the mean free path $(n_e(z)\sigma_T)^{-1}$ with redshift, where $n_e(z)$ is the free-electron number density at redshift z and σ_T is the Thomson scattering cross section. The overall effect on the CMB power spectrum C_ℓ can be approximately characterized by an exponentially damped envelope suppressing the baryon acoustic oscillations, encoded in an associated angular

multipole damping scale $\ell_D \sim k_D(z_{\text{dec}})\chi(z_{\text{dec}}) \sim 1350$, where $\chi(z_{\text{dec}})$ is the comoving distance to the last scattering redshift $z_{\text{dec}} \sim 1088$.

Our focus here is how the damping tail is impacted by perturbations of the free-electron fraction, $X_e(z) = n_e/(n_p + n_{\text{HI}})$, where n_p and n_{HI} are the number density of ionized and neutral hydrogen atoms, during cosmological recombination in a model-independent way. This complements model-independent studies of $H(z)$ variations (Samsing et al., 2012). Opening the constraint to the functional form of $X_e(z)$ broadens the range of non-standard physics that can be tested, such as energy injection from decaying particles or dark matter annihilation (Chen & Kamionkowski, 2004; Padmanabhan & Finkbeiner, 2005), which cause a delay of recombination (Peebles et al., 2000).

The present data are only suggestive of a damping deficit, so discrimination between physical causes is not yet possible, but we develop a framework for considering general modifications and the impact of physical requirements on the posterior distributions. The recombination history is a central quantity in the interpretation of CMB data, and it has evolved significantly over time as more and more effects have been included (Zeldovich et al., 1968; Peebles, 1968; Seager et al., 1999), and, with extensive recent work, it may now have nearly converged (Chluba & Thomas, 2011; Ali-Haïmoud & Hirata, 2011). It is important, however, to test directly whether tensions may exist which suggest that there are missing elements to the recombination story. For example, residual uncertainties in $X_e(z)$ directly affect our ability to distinguish between different inflationary scenarios (Hu et al., 1995; Lewis et al., 2006; Rubiño-Martín et al., 2010; Shaw & Chluba, 2011).

In this paper we follow the approach of Farhang et al. (2012a) to generate eigenmodes for perturbations to the high redshift ionization history focussing on the epoch of recombination. The method is applied to the seven-year WMAP data combined with the 2011 SPT, ACT data and their recent updates, using a Fisher matrix eigenanalysis (Section 4.3) of finely binned redshift-localized X_e -modes. In Farhang et al. (2012a) the eigenanalysis was performed for simulated datasets consisting of CMB maps (or their spherical harmonic amplitudes $a_{\ell m}$). Here, the modes are defined from the measured CMB bandpower errors, which leads to a different structure for the Fisher matrix. Further extending Farhang et al. 2012, we jointly treat the foreground nuisance parameters of the ACT, SPT, and WMAP7 experimental data. We use these data to constrain the amplitude of deviations from the standard recombination scenario in Section 4.4. In Section 4.5, we investigate the impact of imposing electron number conservation (through $X_e(z)$) on the initial and final probability distributions of the parameters and quantify its effect relative to the information delivered by the data. We conclude with a brief discussion in Section 4.6.

4.3 Eigenmodes for Perturbations to the High- z Ionization History

4.3.1 Eigenmode construction

The functional form of deviations from the standard recombination history can be decomposed into a set of uncorrelated functions ranked by their significance in the data, here the increasing order of their forecasted errors. We construct these functions from the inverse of the Fisher information matrix \mathbf{F} for the given combination of data used,

$$\mathbf{F}_{ij} = \sum_{b,b'} \frac{\partial C_b}{\partial q_i} \text{Cov}_{bb'}^{-1} \frac{\partial C_{b'}}{\partial q_j}, \quad (4.1)$$

where the C_b 's are the simulated bandpower measurements for a fiducial set of cosmic parameters and for a given experiment, and $\text{Cov}_{bb'}$ is the bandpower covariance matrix for that experiment. The parameters q_i include recombination perturbation parameters as well as the standard cosmological parameters and the various nuisance parameters for the experiments and for secondary effects. This form for \mathbf{F}_{ij} assumes uniform prior distributions for the parameters, Gaussian likelihoods for the bandpower data points and that information on the parameters mainly comes from the mean of the bandpowers, C_b , rather than their covariance, Cov . The latter can be verified for the high multipoles of interest by comparing the contributions to the Fisher matrix from the mean and the covariance of data (see, e.g., Tegmark et al., 1997). Gaussianity is a reasonable approximation again for the high multipoles which are of interest in this work (see, e.g., Verde et al. (2003)). Further, it is the assumption adopted in the released likelihood codes for SPT and ACT.

We use $\delta \ln(X_e(z))$ as the perturbation parameter. X_e is the parameter of direct relevance to probe the atomic physics involved at recombination. It is also straightforward to limit its variations within physical ranges. However, it does not affect the CMB anisotropies as closely as, e.g., n_e and τ do. Using n_e would also decrease possible degeneracies with baryonic matter density. Using the log in the expansion balances the low and high z -regimes, but the data define the region of dominant impact, namely around decoupling, rather solidly in the hydrogen recombination regime. These perturbations can be represented interchangeably by any basis that represents their degrees of freedom and does not produce numerical errors (see Farhang et al., 2012a, for a discussion on other parametrizations as well as various extended and localized basis functions). Here we have used the cubic M_4 spline (see e.g. Monaghan, 2005) representation, and confirmed convergence against an increasing number of basis functions, for the explicit Fisher form, eq. 4.1, for these experiments.

As mentioned above, the Fisher matrix considered here includes the $X_e(z)$ amplitudes, the instrument-dependent nuisance parameters and the six primary cosmological parameters

$(\Omega_b h^2, \Omega_{\text{dm}} h^2, \theta_s, \tau, n_s, \Delta_{\mathcal{R}}^2)$, respectively describing the physical baryon density, physical dark matter density, the angular size of sound horizon at the last scattering surface, the reionization optical depth, the scalar spectral index, and the curvature fluctuation amplitude. In taking the full Fisher inverse and focussing on sub-blocks of it, we are in effect marginalizing over the parameter directions not in the block in the approximation of a Gaussian posterior.

To analyze multiple experiments with different sets of nuisance parameters, their individual Fisher matrices should be constructed and marginalized to give effective matrices containing only standard cosmological and X_e perturbation parameters which are common between all experiments. The effective Fisher matrices, now with the same dimension, are added to get the total Fisher matrix $\tilde{\mathbf{F}}$. The X_e perturbation eigenmodes are the eigenvectors of the perturbation block of $\tilde{\mathbf{F}}^{-1}$ with their uncertainties estimated from the roots of the corresponding eigenvalues, assuming a Gaussian distribution for the mode amplitudes in the vicinity of their maximum likelihoods. Henceforth, the X_e eigenmodes are unambiguously referred to as the eigenmodes or simply the *modes*. Details on the Fisher eigenanalysis for multiple experiments with different nuisance parameters are discussed in Appendix 4.7. To generate the bandpowers required in the Fisher matrix construction we modified the publicly available code CAMB¹(Lewis et al., 2000) to include the more general ionization histories required for this work.

4.3.2 Datasets and their eigenmodes

Throughout this work, the SPT (Keisler et al., 2011) and ACT (Dunkley et al., 2011) measurements of the CMB temperature and the seven-year WMAP measurement of CMB temperature and polarization (Larson et al., 2011) are used to study perturbations around the ionization history of the universe during recombination.² The SPT and ACT data consist of observation of 790 and 296 deg² of the sky, at 150 and 148 GHz, during 2008- 2009 and 2008 seasons, respectively. For simplicity, we neglect non-CMB cosmological constraints.

The left plot in Figure 4.1 shows the first two ionization eigenmodes generated for the combined SPT+WMAP7 dataset. The right and middle plots show the impact of these modes (with an amplitude equal to their 1σ error bars) on the CMB temperature power spectrum and on the Thomson differential visibility $g(z) = n_e \sigma_T c(1+z)^{-1} e^{-\tau}$, where the Thomson depth to redshift z is $\tau(z) = \int n_e \sigma_T / H d \ln(1+z)$. The first two ACT+WMAP7 modes look very similar, so for definiteness, unless stated otherwise, *modes* refer to these and lower significance SPT+WMAP7 eigenmodes in this paper. Indeed, it turns out that the first two X_e perturbation modes for Planck+ACTPol data and for a high resolution cosmic variance limited experiment

¹<http://camb.info/>

²The small overlap of the observed regions of SPT and ACT telescopes with WMAP has been neglected in this work.

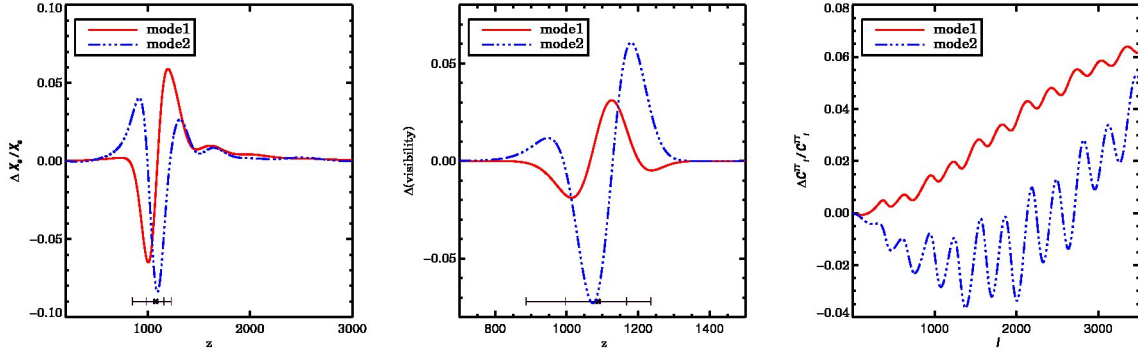


Figure 4.1: The first two modes (constructed for SPT+WMAP7 data), normalized to have unit norm (left), the corresponding changes in the visibility functions (middle), and the resulting differential changes in the temperature power spectrum C_ℓ (right). The middle and right plots corresponds to perturbations with SNR=1. The visibility function is defined as $g(z) = de^{-\tau}/d\eta$, where η is the conformal time and τ is the optical depth to the last scattering surface. The visibility functions have been normalized to the maximum of the fiducial model’s visibility, which occurs at $z_{\text{dec}} = 1088$. The width (at 68% and 95% levels) of the visibility function has been marked as error bars about z_{dec} in the figures.

also have similar shapes (Farhang et al., 2012a), with their order reversed in some cases. We now show that the physical significance of the dominant first mode is, not surprisingly, intimately related to basic perturbative features in the differential visibility.

4.3.3 The Damping Physics of the Low Order Recombination Modes

Since the rank-ordered eigenmodes are direct probes of the map from X_e -trajectories to C_ℓ , the data-sensitive top-ranked modes should reflect the most basic C_ℓ -sensitive recombination effects, namely through the damping tail, which is intimately related to the sharply-peaked differential visibility. We find the first two SPT+WMAP7 modes confirm this: they largely describe shifts in the decoupling redshift (defined as the peak of $g(z)$, $z_{\text{dec}} \approx 1088$) and shifts in the decoupling width, $\sigma_{z,\text{dec}}$, the “1-sigma” spread in g . We find that a $+1\sigma$ amplitude for the first mode changes the visibility by $\sim -1.4\%$ in the width and by $\sim 0.4\%$ in the position of the peak; for the second mode, the width increases by $\sim 6.2\%$ and the peak by $\sim 0.8\%$.

The physical processes that define the structure of the damping tail have been well understood for a long time (for a review see Bond, 1996b; Hu & White, 1997, and references therein), and were discussed in relation to the experimental unveiling of the damping tail, first by CBI (Sievers et al., 2003) and then by ACBAR (Goldstein et al., 2003). Not surpris-

ingly, the tail is controlled by the Compton scattering rate, $n_e\sigma_T c$, and the way it runs as the baryon density n_b drops, characterized by the local power law index, $p_e = 3d\ln(n_e/n_b)/d\ln n_b = d\ln X_e/d\ln(1+z)$ (Bond, 1996b). The basic recombination quantities can be related to p_e , which is zero at low and high z , has a maximum of about 12 and is about 9 at z_{dec} for ΛCDM . The peak of the differential visibility $g(z)$ occurs when $n_e\sigma_T/H(z) = p_e + 2$, and the ‘‘Gaussian’’ width of decoupling in $\ln(1+z)/\ln(1+z_{\text{dec}})$ is $\sigma_{z,\text{dec}} \sim (p_e + 2)^{-1}$. Thus for ΛCDM , the Compton time is about 1/20 of the horizon size at z_{dec} , about 1/5 of the sound crossing time, and the relative width is about 0.09.

Earlier than decoupling, the photons and baryons are so tightly coupled by Thomson scattering that they can be treated as a single fluid with sound speed $c_s = (1+R)^{-1/2}c/\sqrt{3}$, lowered by the extra inertia of the baryons, $R \equiv \frac{3\bar{\rho}_b}{4\bar{\rho}_\gamma}$, a photon+baryon kinematic shear viscosity $(4/5)c_s^2(n_e\sigma_T c)^{-1}$ (in a full treatment of Thomson scattering including angular anisotropy and polarization effects), zero bulk viscosity, and thermal conductivity $\kappa_\gamma = n_b s_\gamma (n_e\sigma_T c)^{-1}$, where $s_\gamma \sim 10^{9.8}$ is the photon entropy per baryon. In this tightly coupled regime, a WKB treatment of the perturbed photon density shows the baryon acoustic oscillations are exponentially damped, $\propto \exp(-\int \Gamma/H d\ln a)$, where the sound wave damping rate relative to the Hubble expansion rate is (see section C.3.1 in Bond, 1996b; Kaiser, 1983)

$$\begin{aligned} \Gamma/H &= \frac{1}{2}(kc_s/Ha)^2 \frac{H}{n_e\sigma_T c} \frac{16}{15} \left[1 + \frac{\Gamma_{\text{diff}}}{\Gamma_{\text{visc}}} \right], \\ \frac{\Gamma_{\text{diff}}}{\Gamma_{\text{visc}}} &= \frac{15R^2}{16(1+R)}. \end{aligned} \quad (4.2)$$

Here $a = (1+z)^{-1}$. kc_s/Ha multiplies the comoving wavenumber k of the acoustic oscillations by (approximately) the comoving distance sound travels in a Hubble time, $c_s(Ha)^{-1}$. The contribution of thermal diffusion relative to that of shear viscosity is $\Gamma_{\text{diff}}/\Gamma_{\text{visc}} \approx 0.22$.

To relate this to a WKB damping envelope acting on C_ℓ , we replace k by ℓ/χ_{dec} , where χ_{dec} is the comoving distance from us to decoupling, and integrate up to $\ln a_{\text{dec}}$. The damping scale obtained is

$$\begin{aligned} \ell_D &\approx 1.7(p_e + 2)(1 + z_{\text{dec}})^{1/2}(c/c_{s,\text{dec}}) \\ &\times [1 + \Gamma_{\text{diff}}/\Gamma_{\text{visc}}]^{-1/2}(1 + a_{\text{eq}}/a_{\text{dec}})^{1/2} \\ &\times (c_{s,\text{dec}}/\bar{c}_{s,\text{dec}}) \sqrt{1 + \frac{1/2}{p_e + 2}}. \end{aligned} \quad (4.3)$$

The dominant first line gives the main dependences, $(1 + z_{\text{dec}})^{1/2}(p_e + 2)(1 + R)^{1/2}$. With $p_{e,\text{dec}} \approx 9$ and $z_{\text{dec}} \approx 1088$, $c_{s,\text{dec}} \approx 0.79c/\sqrt{3}$ at decoupling, the first line gives $\ell_D \sim 1360$. The terms in the second and third line are subdominant. The first adds the thermal diffusion contribution to the viscous one, giving a $\sim 10\%$ decrease; the second from the relativistic matter

contribution to H gives a $\sim 14\%$ rise. With these two, $\ell_D \sim 1410$. The fourth correction accounts for the decoupling sound speed being about 10% lower than the speed averaged over the $z > z_{\text{dec}}$ range; and the last 2.4% correction occurs if we use a sharp integration down to z_{dec} , then stop. The third line terms change ℓ_D to 1290, but are not there if we just replace $\int \Gamma/H d \ln a$ by $\Gamma/H \sigma_{z,\text{dec}}$.

Of course a full transport treatment taking into account multipoles beyond the three which enter tight coupling (density, velocity and anisotropic stress) is required to get an accurate damping rate. The phenomenology adopted by Hu & White (1997) estimated damping envelope functions multiplying “undamped” acoustic C_ℓ ’s from numerical C_ℓ -results, fitting them to a form $\exp[-(\ell/\ell_D)^{m_D}]$, similar to the WKB approximation but with a floating slope to allow for a slower falloff reflecting complexities beyond WKB physics (such as the less severe damping associated with fuzziness of last scattering reflected in the $g(z)$ structure cf. the stronger viscous damping; the break-out into higher temperature multipoles in the Thomson-thick to Thomson-thin transition). For Λ CDM parameters, we get $\ell_D \approx 1345$ and $m_D \approx 1.26$, in better-than-expected accord with the WKB estimate.

Apart from the residual memory of the acoustic oscillations, the rise in $\delta \ln C_\ell$ of the first mode seen in Fig. 4.1(c) conforms to the $(\ell/\ell_D)^{m_D}$ form. The fluctuations in C_ℓ are dominated by those in ℓ_D , with less sensitivity to m_D . These are related to the fluctuations in the peak position and width (which is in turn related to $p_{e,\text{dec}}$) by eq. 4.3,

$$\begin{aligned} \delta C_\ell / C_{f\ell} &\sim (\ell/\ell_{fD})^{m_D} m_D \delta \ell_D / \ell_{fD} \\ \delta \ell_D / \ell_{fD} &\sim -\frac{\delta \sigma_{z,\text{dec}}}{\sigma_{fz,\text{dec}}} + \frac{1}{2} \frac{\delta z_{\text{dec}}}{(1+z_{f,\text{dec}})}, \end{aligned}$$

with respect to the fiducial values with subscript f. So we can interpret the first, most significant, mode as primarily due to ℓ_D variations. Similarly we can understand the sign change in Δg for the first mode as being in response to δz_{dec} .

If we use the same approach for the influence of helium abundance fluctuations, the effect would be the smaller number of hydrogen nuclei near decoupling, suggesting a $\delta C_\ell / C_{f\ell} \sim -(\ell/\ell_{fD})^{m_D} m_D \delta Y_p / (1 - Y_p)$ form, in accord with what we see in Fig. 4.4.

4.4 Constraints from circa 2011 ACT, SPT and WMAP7 data

To search for perturbations in the standard recombination history (RECFAST (Seager et al., 1999) with recent recombination corrections included (Chluba & Thomas, 2011; Ali-Haïmoud & Hirata, 2011), we use the amplitude of the modes introduced in Section 4.3.2 as a set of new parameters, and estimate them jointly with the six primary and three nuisance parameters. The nuisance parameters follow Keisler et al. (2011) and Dunkley et al. (2011) and are the amplitudes

of the Poisson and clustered power from point sources, and a template for the total thermal and kinetic SZ power. The shapes of the associated C_ℓ templates do not look like our X_e -modes, and the data can differentiate what is nuisance from what may be standard recombination deviation, albeit with correlations that are fully taken into account in the statistics. This statement holds even though we restricted ourselves to single effective frequency analyses for SPT and ACT. The priors used for the nuisance parameters are taken from multi-band data particular to the flux cut for point source removal. Unless stated otherwise, throughout the analysis, Y_p and N_{eff} are fixed to $Y_p = 0.2478$ (from SPT data for the Λ CDM model and standard BBN, Keisler et al., 2011) and $N_{\text{eff}} = 3.046$ (from the standard model of particle physics, Beringer et al., 2012).

For parameter estimation we use the publicly available code, COSMOMC³, and modify it to include estimation of the mode amplitudes. We use the versions of COSMOMC adapted for SPT⁴ and ACT⁵ dataset likelihood functions. We checked that when the mode amplitudes are fixed to zero, the modified COSMOMC recovers the reported SPT and ACT parameter measurements (Keisler et al., 2011; Dunkley et al., 2011). Lensing of the C_ℓ 's has been included throughout this work.

Tables 4.4 and 4.4 summarize the results when one and two modes are used in the analysis, for SPT+WMAP7 and ACT+WMAP7 respectively, and compares them to the standard six-parameter model. Both experiments find a non-zero (but different) amplitude for the first mode, but they are only of 1.7σ significance and so do not correspond to a detection; they have $\Delta\chi^2 \sim 2$. ACT+WMAP7 also has a non-zero mean for the second mode, but only at 1.3σ . When the second mode is added to the ACT+WMAP7 analysis, the shift and uncertainty of the first mode change slightly.

While this paper was in press, improved measurements of the damping tail were released by SPT (Hou et al., 2012, referred to as SPT12) and ACT (Dunkley et al., 2013; Sievers et al., 2013, referred to as ACT13). We present our new results using these recent datasets for the SPT11+WMAP7 modes in Table 2. We verified our SPT12 and ACT12 implementations in COSMOMC by checking we reproduce the Hou et al. (2012) and Sievers et al. (2013) determinations for the standard six cosmological case and also for the cases including Y_p or N_{eff} variation. The table shows that the mode amplitudes for SPT12 are highly consistent with those of SPT11, with a slight error decrease, with a mean for the first mode amplitude now 1.9σ away from zero. As our discussion of the similarity of the first mode δC_ℓ shape and the perturbed Helium abundance shape illustrates, this is as expected from the new Hou et al.

³<http://cosmologist.info/cosmomc/>

⁴http://lambda.gsfc.nasa.gov/product/spt/spt_spectra.2011_get.cfm

⁵http://lambda.gsfc.nasa.gov/product/act/act_likelihood_get.cfm

Table 4.1: The constraints on cosmological parameters with different sets of parameters used, as measured by SPT+WMAP7. μ_1 and μ_2 refer to the amplitudes of the first and second modes.

parameters	SPT+WMAP7		
	6s	+ mode 1	+ mode 2
$100\Omega_b h^2$	2.221 ± 0.042	2.253 ± 0.046	2.249 ± 0.047
$\Omega_c h^2$	0.1110 ± 0.0048	0.1123 ± 0.0049	0.1118 ± 0.0052
$100\theta_s$	1.041 ± 0.002	1.041 ± 0.002	1.040 ± 0.003
τ	0.086 ± 0.015	0.089 ± 0.015	0.089 ± 0.015
n_s	0.964 ± 0.011	0.977 ± 0.013	0.975 ± 0.016
$10^9 \Delta_{\mathcal{R}}^2$	2.43 ± 0.10	2.40 ± 0.10	2.40 ± 0.10
μ_1^a	(0)	-0.77 ± 0.46	-0.76 ± 0.47
μ_2	(0)	(0)	-0.39 ± 1.09
$\sigma_8(\text{derived})$	0.807 ± 0.024	0.825 ± 0.027	0.818 ± 0.032
$\delta z_{\text{dec}}/z_{\text{dec}}^b$	–	-0.6%	-0.7%
$\delta\sigma_{z,\text{dec}}/\sigma_{z,\text{dec}}^c$	–	1.5%	-0.5%
$(\delta X_e /X_e)_{\text{max}}^d$	–	5% ($z \sim 1196$)	5% ($z \sim 1039$)
$\Delta\chi^2$	–	2.5	2.5

^a The mode amplitudes and errors in this table (and throughout the paper) should be interpreted with respect to the normalized version of the modes as plotted in Figure 4.1. So, e.g., perturbations with $\mu_1 = 1$ correspond to X_e changes in the form of mode 1 and with an amplitude exactly as plotted in Figure 4.1.

^b relative change in the redshift of maximum visibility where $z_{\text{dec}} = 1088$ is the fiducial maximum visibility point.

^c relative change in the width of the visibility function.

^d maximum relative change in the ionization fraction. The redshift corresponding to this maximum change is also included.

Table 4.2: The constraints on cosmological parameters with different sets of parameters used, as measured by ACT+WMAP7. μ_1 and μ_2 refer to the amplitudes of the first and second modes.

parameters	ACT+WMAP7		
	6s	+ mode 1	+ mode 2
$100\Omega_b h^2$	2.219 ± 0.051	2.240 ± 0.050	2.236 ± 0.053
$\Omega_c h^2$	0.1121 ± 0.0052	0.1155 ± 0.0056	0.1121 ± 0.0061
$100\theta_s$	1.039 ± 0.002	1.039 ± 0.002	1.035 ± 0.004
τ	0.086 ± 0.015	0.089 ± 0.015	0.0875 ± 0.015
n_s	0.963 ± 0.013	0.976 ± 0.015	0.960 ± 0.019
$10^9 \Delta_{\mathcal{R}}^2$	2.45 ± 0.11	2.43 ± 0.11	2.45 ± 0.11
μ_1	(0)	-1.27 ± 0.74	-1.67 ± 0.86
μ_2	(0)	(0)	-3.5 ± 2.7
σ_8 (derived)	0.814 ± 0.028	0.841 ± 0.031	0.802 ± 0.040
$\delta z_{\text{dec}}/z_{\text{dec}}$	–	-1.0%	-1.7%
$\delta\sigma_{z,\text{dec}}/\sigma_{z,\text{dec}}$	–	2.6%	-14.0%
$(\delta X_e /X_e)_{\text{max}}^a$	–	8% ($z \sim 1006$)	31% ($z \sim 1076$)
$\Delta\chi^2$	–	2.1	2.5

^a This large deviation, though looking curious, is not statistically significant. This point is understandable given the relatively large estimated values for μ_1 and μ_2 and their uncertainties.

Table 4.3: The constraints on the first two modes (μ_1 and μ_2), as measured by SPT12+WMAP7 and ACT12+WMAP7.

parameters	SPT12+WMAP7		ACT12+WMAP7	
	+ mode 1	+ mode 2	+ mode 1	+ mode 2
μ_1	-0.73 ± 0.38	-0.68 ± 0.39	0.30 ± 0.47	-0.06 ± 0.55
μ_2	(0)	-1.04 ± 0.83	(0)	1.3 ± 1.1

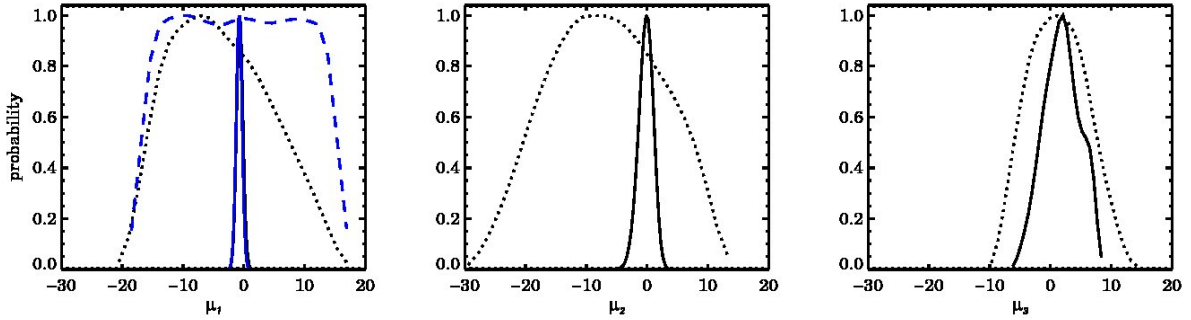


Figure 4.2: Black lines: marginalized 1D-prior (dotted lines) and posterior probabilities (solid lines) with SPT+WMAP7 data for the first three modes, in an analysis where six standard parameters, three nuisance parameters and the first three X_e perturbation modes were used. Blue lines, left plot: the prior (dashed line) and posterior (solid line) distributions for μ_1 , similar to black lines, but with only one mode included in the analysis. Note that the solid black and blue curves coincide in the left plot.

(2012) SPT measurement of $Y_p = 0.300 \pm 0.025$ (and $N_{\text{eff}} = 3.62 \pm 0.48$). ACT12 reported values of these parameters that were consistent with the unperturbed values of the basic-six parameter case, and as expected we see consistency with zero for the ACT12 mode amplitudes. Updated measurements of the amplitude of the first mode with WMAP9 are quite close to their WMAP7 values, -0.80 ± 0.37 for WMAP9+SPT and 0.14 ± 0.45 for WMAP9+ACT, and again indicate a mild tension for SPT and none for ACT; the combined SPT+ACT+WMAP9, -0.44 ± 0.33 , lessens the tension to about 1σ .

4.5 The impact of electron number conservation on the posterior

Our perturbed ionization history is required to satisfy electron conservation through

$$0 \leq X_e(z) \leq x_e^{\text{max}}$$

where $x_e^{\text{max}} = 1 + \frac{2Y_p}{3.97(1-Y_p)}$ is the maximum total electron fraction, using $m_{\text{He}}/m_{\text{H}} \approx 3.97$, obtained when helium and hydrogen are fully ionized. When the mode amplitudes are poorly determined by data, the reconstructed $X_e(z)$ could break through this bound, which of course we do not allow. Thus, although our starting prior may have been uniform with a wide possible spread in the amplitudes, the true prior distribution can only be determined with a full suite of Monte Carlo calculations restricting the allowed range. The Fisher analysis does not catch this

because the amplitudes are supposed to be tiny. They are not in our case for which the data do not have strong discriminatory power so allowed variations in the ionization history can be very broad. Intuitively, if the volume spanned by the prior space is comparable to or smaller than the volume of the likelihood space (at a given significance level), the posterior will be influenced by the physical constraint, and the Fisher matrix analysis will be a poor approximation to the full analysis. Experiments with higher sensitivities will provide information about a larger number of modes before running into this condition, (see simulations for Planck+ACTPol-like observations in Farhang et al., 2012a).

Figure 4.2 shows the marginalized 1D-distributions of the amplitudes of the first three modes, μ_1 to μ_3 , in an analysis with three modes included, and for two experimental setups: the posterior distributions of the SPT+WMAP7 case (solid black lines) and the prior-only simulations (dotted black lines) by ignoring the likelihood, i.e., assuming infinite errors in the data. The overplotted blue lines (in the left plot only) correspond to a case with only one mode being included in the analysis. Note that the prior distributions of the first and second modes are skewed toward negative values for the case with three modes in the analysis (black lines). However, the prior distribution for the first-mode-only case (the quite symmetric blue dashed curve) shows that the μ_1 measurement is not prior-driven.

The very narrow posterior distributions of μ_1 and μ_2 relative to their priors illustrate the power of the ACT/SPT data in constraining these parameters, although they are not found to be significantly different from zero. For μ_3 , on the other hand, the comparable widths of the prior and posterior distributions imply that the dataset under consideration hardly contains more information about this parameter than the limits set by electron conservation. The measured errors on the fourth and higher modes differ significantly from their Fisher forecasts, not even keeping their ranking. The insensitivity of the data to higher modes explains why we have limited our study to the first two modes.

We can quantify the impact of the prior by measuring the Shannon entropy decrease in the measurement of n -parameters, $\mathbf{q} = \{q_i\}$, associated with the transition from the prior distribution p_i to the posterior distribution p_f when data are added,

$$R(n) \equiv S_i(n) - S_f(n) \equiv \langle \ln p_f \rangle_f - \langle \ln p_i \rangle_i. \quad (4.4)$$

For us the relevant q_i 's are the amplitudes of the first n modes.

Although the full calculation can be made, we have found that a Gaussian approximation works reasonably well, and does not have the numerical challenges associated with an accurate full calculation. The posterior p_f is closer to Gaussian than is the prior p_i . With an n D-Gaussian distribution with zero mean and covariance matrices \mathbf{C} , $S = 1/2 \ln \det(\mathbf{C}) + n \ln(2\pi)/2 + 1/2 \langle \mathbf{q}^T \mathbf{C}^{-1} \mathbf{q} \rangle$. The last term is $1/2$ of the mean χ^2 associated with the measurement, hence is

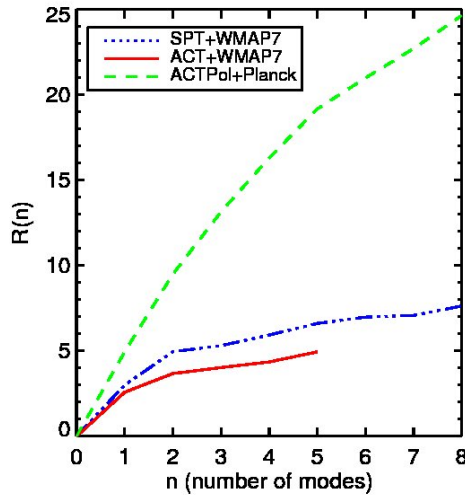


Figure 4.3: Increase in the information content of the measured modes delivered by data relative to the volume of parameter space allowed by electron conservation, for different number of modes included in the analysis and various experimental cases. The modes in each case are constructed for the corresponding dataset.

$n/2$ since $\langle \mathbf{q}^T \mathbf{C}^{-1} \mathbf{q} \rangle = n$. The entropy difference is then the ratio of mean log-volumes of the parameter space in question, namely

$$R(n) = \frac{1}{2} \ln(\det(\mathbf{C}_i)/\det(\mathbf{C}_f)), \quad (4.5)$$

where $\mathbf{C}_{i,f}$ are the prior and posterior parameter covariance matrices. We checked the Gaussian approximation by comparing eq. 4.5 with estimates of the integral form eq. 4.4 of the entropies. The integral was calculated from the nearest neighbor entropy estimate (Singh et al., 2003). This non-parametric entropy estimation method is based on the distribution of the nearest neighbor distance of the samples, here the MCMC chain outputs, and is used for parameter spaces with more than one dimension. We found that the results from Gaussian approximation agree well with those from full integration, and are less noisy as the dimensionality of the parameter space increases. Using the determinant ratio to measure the level of improvement with improved data is familiar as a figure-of-merit (see, e.g., Mortonson et al., 2010). Although we have found for our application for deciding which modes to include that eq. 4.5 is adequate, eq. 4.4 is the better expression for a more accurate figure-of-merit (Farhang et al., 2011).

As n increases, the data add less information about the parameters relative to the prior. Thus, the difference between successive R 's gradually decreases. By adding new parameters, the volumes of the posterior and prior spaces change by a similar prior-dominated factor. In the limit of very large n , $R(n) \rightarrow \text{constant}$. This is shown in Figure 4.3 where we compare $R(n)$ for

different datasets and various numbers of modes included, n . For this plot, the modes of each curve are the eigenmodes constructed for the corresponding experiment. For ACT+WMAP7 and SPT+WMAP7, the difference between one and two parameters is greater than the difference between other subsequent modes. This shows that these datasets are much more informative about the second mode than the higher modes, which are entering the prior-dominated regime. This difference between the first two modes and the higher ones is also evident from Figure 4.2. With higher precision datasets, we expect the transition from likelihood to prior-dominance to happen at a higher mode number. This prior-likelihood dominance transition hints to a natural criterion for mode-hierarchy truncation. However, one should note that choosing a quantitative mode selection criterion can be rather subjective and not necessarily applicable to all datasets.

The mode-selection criterion introduced here is much stronger than the Occam’s razor argument developed in Farhang et al. (2012a), where the truncation of the mode hierarchy was based on the change in the information content as more ordered modes were added. Here, we have used the posterior information that the modes have in excess of the prior, a change of perspective motivated by the weak constraints from current datasets. The analysis enters a prior-dominated regime beyond just one or two modes and there is no need to consider the more sophisticated Farhang et al. (2012a) criteria.

4.6 Discussion

In this work we studied how allowing for some freedom in the recombination history gives a better fit to the damping tail of the CMB power spectrum as measured by SPT and ACT, compared to the primary six-parameter model. The red solid line in Figure 4.4 shows the relatively small shift between the best-fit SPT+WMAP7 C_ℓ ’s, one with the basic six parameters fixed at their best-fit values with the X_e -perturbations on, and the other with the basic six parameters fixed at their unperturbed values. That is because the non-zero μ_1 is accompanied by compensation in the values of the standard parameters, most significantly shifting n_s and $\Omega_b h^2$ (see Figure 4.5) to give a small net ΔC_ℓ . (Although the modes are marginalized over standard parameters, they are generally correlated with them.) When the basic six parameters are set to their X_e -unperturbed values, and only μ_1 varies, the red dashed line is obtained. Apart from the oscillation difference, the shape and value look rather like that for Y_p variation, for the reasons discussed in Section 4.3.3.

The goodness of fit with μ_1 added to the analysis is comparable to cases where the recombination history is assumed to be perfectly known (see Chluba & Thomas, 2011; Ali-Haïmoud & Hirata, 2011, for the most recent calculations) and instead either Y_p or N_{eff} are allowed to vary (Keisler et al., 2011; Dunkley et al., 2011). (The corresponding best-fit C_ℓ difference between

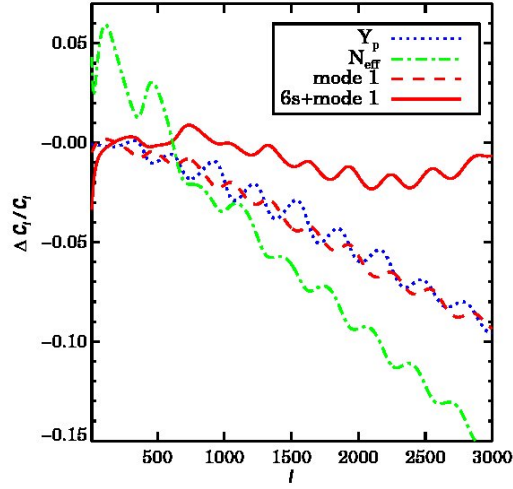


Figure 4.4: The solid red line corresponds to the difference between the best-fit C_ℓ 's for the standard case and the case with the first mode included, measured by SPT+WMAP7. That is, the two cases have different background cosmology (as measured by data) as well as different values for μ_1 ($\mu_1 = 0$ and $\mu_1 = -0.77$). The dashed and dotted curves show the response to changes in Y_p , N_{eff} and the first mode. In these cases, the six standard parameters are fixed for all models, while $Y_p = 0.296$, $N_{\text{eff}} = 3.898$ and $\mu_1 = -0.77$ have been chosen for their corresponding curves.

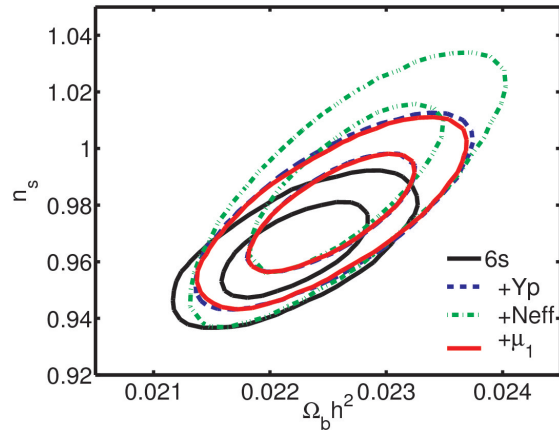


Figure 4.5: The marginalized 68% and 95% n_s - $\Omega_b h^2$ contours for various sets of parameters being included in the analysis. The 6s contours represent the standard model with six parameters. Other cases each have one extra parameter, being Y_p , N_{eff} and μ_1 . Note that these extended models favor a slightly higher value of n_s compared to the standard case.

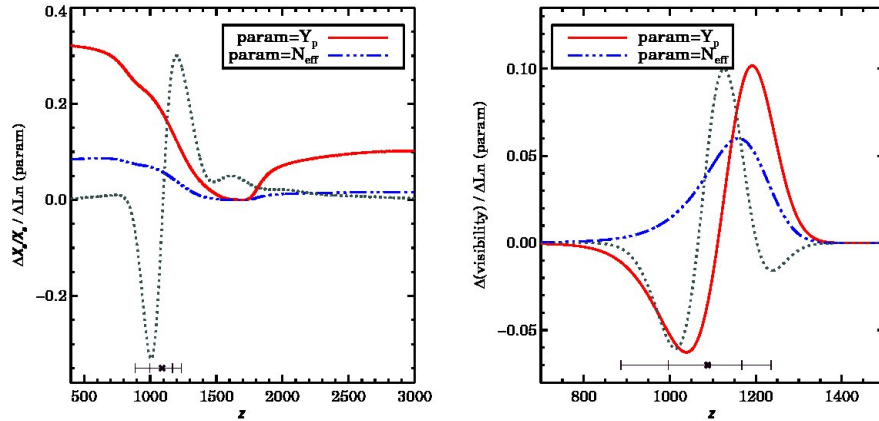


Figure 4.6: The relative X_e and differential visibility changes due to relative infinitesimal changes in Y_p and N_{eff} (with other parameters fixed). The first mode has been added in the background (the gray dotted lines) to aid visual comparison. It has been normalized to be comparable to Y_p changes.

these two cases with the standard six parameter case is not shown here but is similar to the red solid line for the μ_1 case.) As mentioned, including Y_p has a similar impact on the standard parameter measurements to that of μ_1 , as illustrated in Figure 4.5, where n_s and $\Omega_b h^2$ have the most significant shifts. N_{eff} , on the other hand, behaves differently, with a different C_ℓ -shape, and it also has a large impact on $\Omega_{\text{dm}} h^2$ and H_0 (see Keisler et al., 2011; Dunkley et al., 2011).

It is also noteworthy that the measurements of σ_8 (the amplitude of linear matter fluctuations at $z = 0$ on scales of $8h^{-1}\text{Mpc}$) for the model with N_{eff} for ACT data ($\sigma_8 = 0.906 \pm 0.059$, Dunkley et al., 2011) and for SPT data ($\sigma_8 = 0.859 \pm 0.043$, Keisler et al., 2011) are currently slightly disfavored by σ_8 inferred from clusters ($\sigma_8(\Omega_m/0.25)^{0.47} = 0.813 \pm 0.013 \pm 0.024$; here the second set of errors is systematic and due to the uncertainty in cluster masses, Vikhlinin et al., 2009). Including μ_1 and especially μ_2 in the analysis, with fixed $N_{\text{eff}} = 3.046$, brings σ_8 towards lower values (see Tables 4.4 and 4.4), consistent with external datasets.

The first principal component X_e -mode, Y_p , and N_{eff} are strongly correlated due to their similar effects on the damping tail of the power spectrum as illustrated in Figure 4.4. The correlation coefficients of μ_1 with the other two are $\text{corr}(\mu_1, Y_p) = 0.95$ and $\text{corr}(\mu_1, N_{\text{eff}}) = 0.72$, based on results from COSMOMC for SPT+WMAP7 bandpower data. Due to this partial degeneracy, varying more than one of these parameters simultaneously would significantly increase their uncertainties. The improvement in errors forecasted for near-future data and the addition of polarization information will modestly reduce the degeneracy of μ_1 with Y_p and N_{eff} . For example, for a Planck+ACTPol-like scenario the correlation coefficients for an ℓ -by- ℓ

analysis from COSMOMC are forecasted to be $\text{corr}(\mu_1, Y_p) = 0.77$ and $\text{corr}(\mu_1, N_{\text{eff}}) = 0.60$. (An ℓ -by- ℓ analysis is more sensitive to acoustic oscillation phase information than data with wide bandpowers.)

The perturbative $X_e(z)$ -eigenmodes are, by definition, those that are most constrained by the CMB. The perturbations in $X_e(z)$ induced by varying Y_p and N_{eff} , are shown in Fig. 4.6. They look very different than our most significant mode. What is interesting is the response in differential visibility. The first mode and the Y_p -induced perturbations look somewhat similar, although the differences are important. In C_ℓ the dominant damping tail behaviour of ΔC_ℓ is even closer, although the details of the peak-trough oscillations about it differ. The full Y_p -induced perturbation involves a coherent sum over many eigenmodes, but the data are mostly trying to constrain its component in the first mode, as Figure 4.4 shows. The low order mode amplitudes are therefore a way to efficiently transfer information from the CMB into constraints on ionization perturbations. Alternative high- z ionization history models due to specific physical effects (and priors they may impose) could then be differentiated in e.g. the $\mu_1 - \mu_2$ plane.

There are several alternative effects that can cause modifications to the CMB power spectrum in the damping tail. These include possible modifications to the physics of recombination, dark radiation (e.g., Archidiacono et al., 2011, and references therein), changes in the fine structure constant α (Kaplinghat et al., 1999; Battye et al., 2001; Scóccola et al., 2008), high-frequency cosmic gravitational wave background (Smith et al., 2006), dark matter annihilation and particle decay (Chen & Kamionkowski, 2004; Padmanabhan & Finkbeiner, 2005; Zhang et al., 2006, 2007; Hütsi et al., 2009; Galli et al., 2009a; Hütsi et al., 2011; Galli et al., 2011; Giesen et al., 2012). Deviations from standard recombination may be differentiated or corroborated by non-CMB measurements. Apart from invoking additional physical processes to explain damping tail measurements, it is important to note that the tail is sensitive to experimental issues, such as the instrumental beam, point sources in the maps, and detector time constants.

As shown in table 4.4, we have now found the damping tail tension in the SPT11 and ACT11 data of table 4.4 persists in the full 2500 deg² SPT data reported in Story et al. (2012) and Hou et al. (2012), but not in the three-season ACT12 data. The combined SPT12-ACT12-WMAP9 data are also consistent with the standard recombination scenario (Calabrese et al., 2013). The Planck data, with its much larger sky coverage, should be able to address whether tension exists or not. Our forecasts for Planck 2.5 year data show that the current SPT11 best-fit amplitude of the first mode, $\mu_1 = -0.77$ (which is only 1.7σ now), could be detected at more than 10σ .

If such a deviation were found, it would be well beyond the levels of the standard recombination corrections which have been discussed extensively over the past several years (see Dubrovich & Grachev, 2005; Chluba & Sunyaev, 2006b; Kholupenko & Ivanchik, 2006; Switzer

& Hirata, 2008; Hirata, 2008; Grin & Hirata, 2010; Ali-Haïmoud & Hirata, 2010, and additional references) and would have to indicate a new and possibly non-standard process at work. These physical mechanisms, with their high level of nuance and theoretical concordance, result in a modification to recombination which is 3.5 times smaller than the 1σ errors found here (Dunkley et al., 2011). In the far future, measurements of the cosmological recombination radiation from hydrogen and helium (see Sunyaev & Chluba, 2009, for an overview) may provide another way to investigate this question and break some of the expected degeneracies.

If a detection of deviation is made with high significance, further explorations could be done with the same sort of analysis as that given here, but with modes weighted towards different redshift regimes. Indeed, although we have focussed here on just the recombination epoch, viewing recombination and reionization as a connected X_e -trajectory has appeal, since CMB data (though at large rather than small angular scales) inform the latter. In these extended studies one needs to explore other possible variables to linearly expand in rather than $\delta \ln(X_e(z))$, as discussed in Farhang et al. (2012a). The merit of $X_e(z)$ expansions is that one can weight them to concentrate on specific recombination regions, e.g., at higher z where helium recombines, or at lower z as X_e -freeze-out is approached. Ultimately showing in a model-independent way that the allowed X_e -trajectories do not compromise our determination of cosmological parameters would further increase our confidence in conclusions drawn from CMB datasets.

This work was accomplished by support from NSERC and the Canadian Institute for Advanced Research.

4.7 Appendix: Fisher Analysis

The goal of this work is to search for deviations from the standard ionization scenario at high redshifts, around the epoch of recombination. For this purpose, we search for the perturbation patterns in X_e best constrained by data (see Farhang et al., 2012a, for more details). The most constrained perturbation parameters are the eigenvectors of the X_e -perturbation block of the inverse of Fisher information matrix. The Fisher matrix for each dataset under consideration is

$$\mathbf{F}_{ij} = \sum_{b,b'} \frac{\partial C_b^T}{\partial q_i} \text{Cov}_{bb'}^{-1} \frac{\partial C_{b'}}{\partial q_j}$$

where the q 's represent any of the standard, the X_e -perturbation, the secondary or experimental nuisance parameters. The bandpowers C_b are

$$C_b = \sum W_{b\ell} \tilde{C}_\ell, \quad \tilde{C}_\ell = \frac{\ell(\ell+1)}{2\pi} C_\ell$$

where the window functions, W_{bl} 's, are specific to the experiment and $\text{Cov}_{bb'} = \langle \delta C_b \delta C_{b'} \rangle$ is their covariance matrix. The derivatives are calculated at the fiducial q_i 's. If multiple experiments are used, the total Fisher matrix is the sum of the individual Fisher matrices constructed for each experiment — if they are statistically independent — and marginalized over their nuisance, experiment-dependent parameters. To make this marginalized Fisher matrix, we divide \mathbf{F} into blocks of nuisance parameters (represented by n) and the cosmologically interesting parameters, represented by y . We then have

$$\mathbf{F} = \begin{pmatrix} \mathbf{F}_{yy} & \mathbf{F}_{yn} \\ \mathbf{F}_{ny} & \mathbf{F}_{nn} \end{pmatrix}, \quad \mathbf{F}|_m = \mathbf{F}_{yy} - \mathbf{F}_{yn} \mathbf{F}_{nn}^{-1} \mathbf{F}_{ny}$$

where $\mathbf{F}|_m$ is the Fisher matrix (including only cosmologically interesting parameters) marginalized over nuisance parameters. The individual $\mathbf{F}|_m$'s should be added to get the total Fisher matrix. The X_e perturbation eigenmodes are the eigenvectors of the perturbation block of the total Fisher matrix after it has been marginalized over the standard parameters, similar to the above marginalization.

Another approach is to calculate Fisher matrices that include all nuisance parameters. Then, for those experiments that provide no constraint on a set of nuisance parameters, set those matrix entries to zero, sum the matrices over experiments and marginalize over nuisance and standard cosmic parameters.

Chapter 5

Outlook

In this work the two important cosmic epochs of inflation and recombination were investigated through their imprints on the cosmic background radiation. The results, challenges and future prospects are discussed at the end of the relevant chapter in details. Here is a summary of the main points.

5.1 Summary

- Chapter 2
 - A map-based maximum likelihood estimator was developed for optimal measurement of the amplitude of inflationary gravity waves from CMB polarization. This direct map-to-parameter estimator, by construction, bypasses E - B mixing which, in cut-sky observations, is a possible source of contamination to the tiny gravity wave signal.
 - Due to large matrix manipulations, the method is computationally costly relative to suboptimal fast parameter estimators, yet feasible and accurate thanks to current computation power. We find that, with current experiment characterizations, the correlation of r with other standard parameters is relatively small. Thus, one could safely limit the analysis to the 1D parameter space of r , for which a direct map-based approach is feasible.
 - The method was used for investigation of sky coverage optimization of B -mode surveys for various observational cases. For Spider specifications we found that with $f_{\text{sky}} \sim 0.02 - 0.2$, the 95% confidence limits on r are ~ 0.014 for a foreground-free sky and ~ 0.02 with a modest treatment of ℓ -dependent foreground residual. Similarly, we find that for a Planck-like experiment with a Galaxy-masked sky the

95% confidence limit on r is 0.015 for a foreground clean sky, rising to 0.05 with the foreground residual.

- We also explored the 2D parameter space of $r - n_t$ and found that a powerful test of the inflation consistency relation $n_t \approx -r/8$ will evade our measurements even with a post-Planck deep full-sky experiment.

- Chapters 3 and 4

- The goal in these chapters was to study the details of the recombination history by investigating perturbative fluctuations in the free electron fraction X_e . Using a model-independent approach, the rank-ordered parameter eigen-modes with the highest power to probe X_e were constructed. The modes were shown to be converged, against increasing the number of basis functions, and expansion-basis independent. Also, various properties of the modes were studied, such as their fiducial model dependence, their response to different X_e parametrizations and their sensitivity to marginalization over different cosmic parameters. As a sanity check, we showed that they serve as a full basis for decomposing various physically motivated X_e perturbations if enough modes are included in the expansion. We found that the most constrained modes are localized around $z \sim 1100$, where the CMB signal mainly comes from, with some extensions to higher and lower redshifts. The details of helium recombination and the freeze-out tail are hard to recover, unless strong priors are imposed on the X_e history around $z \sim 1100$.
- An information-based criterion for the truncation of eigen-mode hierarchy was developed. The criterion uses the added amount of information when a new mode is included in the analysis and compares it to the previous steps (chapter 3). A slightly different criterion was suggested for cases when available data are not highly informative about the modes compared to the limits set on the parameters by enforcing physical requirements (chapter 4). This criterion uses the difference in the information content of the prior and posterior distributions as more modes are added. It then suggests keeping the modes for which this difference is not too small relative to the previous step. These criteria can be adapted for other similar hierarchical model selections as well.
- The method was applied to simulations of Planck+ACTPol and a cosmic variance limited survey with differing simulated recombination histories (chapter 3). We studied how ignoring possible fluctuations around the recombination history can lead to biased measurement of standard parameters. Also, X_e trajectories for the simulated

perturbations were constructed for different number of modes. The trajectories, being tightest around the recombination epoch, hardly recovered any information about helium recombination and low- z perturbations. This result is to be expected from the patterns of the best constrainable modes.

- The method was also applied to the available CMB data at 2012, i.e., WMAP7+2010 ACT/SPT, and updated to the recent 2012 ACT/SPT and WMAP9. We also did the joint WMAP9-SPT-ACT analysis (chapter 4). The first constructed eigen-mode turns out to be a direct measure of the CMB damping envelope. It is highly degenerate with variations in Y_p and to a smaller degree with N_{eff} . However, it has the advantage of not being a priori associated to any physical processes, although prejudices are unavoidable in X_e parametrization. Its measurement by SPT slightly indicates a damping tail anomaly while the recent ACT as well as the joint ACT-SPT data are consistent with a standard recombination scenario. Future high resolution data will address this issue. If the currently observed deviation by SPT is real, our simulations show that it should be detectable with more than 10σ by Planck.

5.2 Future Prospects

The natural follow-up of this work is to adapt the developed tools, already used for forecasts of future and the analysis of current CMB data, to the high precision data of the coming experiments.

The map-based maximum likelihood estimator discussed in chapter 2 is the optimal method for measuring r with Planck and other CMB polarization experiments. The estimator should be hybridized with ℓ -space methods if simultaneous high- ℓ analysis is required. This is similar to what was done for WMAP analysis and is done for Planck.

The estimator also needs to be extended for a more sophisticated treatment of foreground contamination and to deal with experiment-dependent analysis issues and complex noise characteristics, not taken care of in the simulations of this work.

Planck and SPTPol/ACTPol, combined with non-CMB data to break parameter degeneracies, will provide excellent opportunities to test our assumptions about the physics at high redshifts. In this work, the focus was on the recombination epoch, a legitimate choice for the precision level of current CMB data. To properly deal with the coming high precision data, however, requires searching for deviations around the standard scenario at other redshift intervals as well. This could be achieved through using different parametrizations focusing on different epochs. One way could be expanding the $\delta \ln(X_e)$ used in this work to $\delta \ln(X_e + \sigma)$, with σ a positive free parameter, to adjust the weight toward lower redshifts. In the search for

the maximum likelihood point, σ can be treated as a hyper parameter with the parameter space extended to include σ as well. In other words, including the floating σ in the analysis allows us to select between models with different parametrizations. If there are hints of fluctuations in the data, an iterative approach needs to be taken toward a full reconstruction of X_e history. This search will either put stringent constraints on the standard X_e history, or open a window to the beyond-standard physics relevant at high redshifts. Possible detection of fluctuations would motivate the search for new techniques to discriminate between different possible cosmological sources of the observed phenomenon.

With Planck, EBEX, Keck, Spider, QUIET, BiCEP, ABS, ACTPol, SPTPol, etc. CMB research is going through a very thrilling period in anticipation of great discoveries, and who knows, the future may bring new space-based experiments, such as LiteBIRD, PIXIE or COrE.

Bibliography

Ali-Haïmoud, Y. & Hirata, C. M. 2010, *Phys. Rev. D*, 82, 063521

—. 2011, *Phys. Rev. D*, 83, 043513

Archidiacono, M., Calabrese, E., & Melchiorri, A. 2011, *Phys. Rev. D*, 84, 123008

Austermann, J. E., Aird, K. A., Beall, J. A., Becker, D., Bender, A., Benson, B. A., Bleem, L. E., Britton, J., Carlstrom, J. E., Chang, C. L., Chiang, H. C., Cho, H.-M., Crawford, T. M., Crites, A. T., Datesman, A., de Haan, T., Dobbs, M. A., George, E. M., Halverson, N. W., Harrington, N., Henning, J. W., Hilton, G. C., Holder, G. P., Holzappel, W. L., Hoover, S., Huang, N., Hubmayr, J., Irwin, K. D., Keisler, R., Kennedy, J., Knox, L., Lee, A. T., Leitch, E., Li, D., Lueker, M., Marrone, D. P., McMahon, J. J., Mehl, J., Meyer, S. S., Montroy, T. E., Natoli, T., Nibarger, J. P., Niemack, M. D., Novosad, V., Padin, S., Pryke, C., Reichardt, C. L., Ruhl, J. E., Saliwanchik, B. R., Sayre, J. T., Schaffer, K. K., Shirokoff, E., Stark, A. A., Story, K., Vanderlinde, K., Vieira, J. D., Wang, G., Williamson, R., Yefremenko, V., Yoon, K. W., & Zahn, O. 2012, in *Society of Photo-Optical Instrumentation Engineers (SPIE) Conference Series*, Vol. 8452, Society of Photo-Optical Instrumentation Engineers (SPIE) Conference Series

Barkats, D., Bischoff, C., Farese, P., Fitzpatrick, L., Gaier, T., Gundersen, J. O., Hedman, M. M., Hyatt, L., McMahon, J. J., Samtleben, D., Staggs, S. T., Vanderlinde, K., & Winstein, B. 2005, *ApJ*, 619, L127

Battye, R. A., Crittenden, R., & Weller, J. 2001, *Phys. Rev. D*, 63, 043505

Baumann, D., Jackson, M. G., Adshead, P., Amblard, A., Ashoorioon, A., Bartolo, N., Bean, R., Beltrán, M., de Bernardis, F., Bird, S., Chen, X., Chung, D. J. H., Colombo, L., Cooray, A., Creminelli, P., Dodelson, S., Dunkley, J., Dvorkin, C., Easther, R., Finelli, F., Flauger, R., Hertzberg, M. P., Jones-Smith, K., Kachru, S., Kadota, K., Khoury, J., Kinney, W. H., Komatsu, E., Krauss, L. M., Lesgourgues, J., Liddle, A., Liguori, M., Lim, E., Linde, A., Matarrese, S., Mathur, H., McAllister, L., Melchiorri, A., Nicolis, A., Pagano, L., Peiris,

- H. V., Peloso, M., Pogosian, L., Pierpaoli, E., Riotto, A., Seljak, U., Senatore, L., Shandera, S., Silverstein, E., Smith, T., Vaudrevange, P., Verde, L., Wandelt, B., Wands, D., Watson, S., Wyman, M., Yadav, A., Valkenburg, W., & Zaldarriaga, M. 2009, in *American Institute of Physics Conference Series*, Vol. 1141, American Institute of Physics Conference Series, ed. S. Dodelson, D. Baumann, A. Cooray, J. Dunkley, A. Fraisse, M. G. Jackson, A. Kogut, L. Krauss, M. Zaldarriaga, & K. Smith, 10–120
- Beringer, J., Arguin, J. F., Barnett, R. M., Copic, K., Dahl, O., Groom, D. E., Lin, C. J., Lys, J., Murayama, H., Wohl, C. G., Yao, W. M., Zyla, P. A., Amsler, C., Antonelli, M., Asner, D. M., Baer, H., Band, H. R., Basaglia, T., Bauer, C. W., Beatty, J. J., Belousov, V. I., Bergren, E., Bernardi, G., Bertl, W., Bethke, S., Bichsel, H., Biebel, O., Blucher, E., Blusk, S., Brooijmans, G., Buchmueller, O., Cahn, R. N., Carena, M., Ceccucci, A., Chakraborty, D., Chen, M. C., Chivukula, R. S., Cowan, G., D'Ambrosio, G., Damour, T., de Florian, D., de Gouvêa, A., DeGrand, T., de Jong, P., Dissertori, G., Dobrescu, B., Doser, M., Drees, M., Edwards, D. A., Eidelman, S., Erler, J., Ezhela, V. V., Fetscher, W., Fields, B. D., Foster, B., Gaiser, T. K., Garren, L., Gerber, H. J., Gerbier, G., Gherghetta, T., Golwala, S., Goodman, M., Grab, C., Gritsan, A. V., Grivaz, J. F., Grünewald, M., Gurtu, A., Gutsche, T., Haber, H. E., Hagiwara, K., Hagmann, C., Hanhart, C., Hashimoto, S., Hayes, K. G., Heffner, M., Heltsley, B., Hernández-Rey, J. J., Hikasa, K., Höcker, A., Holder, J., Holtkamp, A., Huston, J., Jackson, J. D., Johnson, K. F., Junk, T., Karlen, D., Kirkby, D., Klein, S. R., Klempt, E., Kowalewski, R. V., Krauss, F., Kreps, M., Krusche, B., Kuyanov, Y. V., Kwon, Y., Lahav, O., Laiho, J., Langacker, P., Liddle, A., Ligeti, Z., Liss, T. M., Littenberg, L., Lugovsky, K. S., Lugovsky, S. B., Mannel, T., Manohar, A. V., Marciano, W. J., Martin, A. D., Masoni, A., Matthews, J., Milstead, D., Miquel, R., Mönig, K., Moortgat, F., Nakamura, K., Narain, M., Nason, P., Navas, S., Neubert, M., Nevski, P., Nir, Y., Olive, K. A., Pape, L., Parsons, J., Patrignani, C., Peacock, J. A., Petcov, S. T., Piepke, A., Pomarol, A., Punzi, G., Quadt, A., Raby, S., Raffelt, G., Ratcliff, B. N., Richardson, P., Roesler, S., Rolli, S., Romaniouk, A., Rosenberg, L. J., Rosner, J. L., Sachrajda, C. T., Sakai, Y., Salam, G. P., Sarkar, S., Sauli, F., Schneider, O., Scholberg, K., Scott, D., Seligman, W. G., Shaevitz, M. H., Sharpe, S. R., Silari, M., Sjöstrand, T., Skands, P., Smith, J. G., Smoot, G. F., Spanier, S., Spieler, H., Stahl, A., Stanev, T., Stone, S. L., Sumiyoshi, T., Syphers, M. J., Takahashi, F., Tanabashi, M., Terning, J., Titov, M., Tkachenko, N. P., Törnqvist, N. A., Tovey, D., Valencia, G., van Bibber, K., Venanzoni, G., Vincter, M. G., Vogel, P., Vogt, A., Walkowiak, W., Walter, C. W., Ward, D. R., Watari, T., Weiglein, G., Weinberg, E. J., Wiencke, L. R., Wolfenstein, L., Womersley, J., Woody, C. L., Workman, R. L., Yamamoto, A., Zeller, G. P., Zenin, O. V., Zhang, J., Zhu, R. Y., Harper, G., Lugovsky, V. S., & Schaffner, P. 2012, *Phys. Rev. D*, 86,

010001

Bond, J. R. 1995, *Physical Review Letters*, 74, 4369

Bond, J. R. 1996a, in *Cosmology and Large Scale Structure*, ed. R. Schaeffer, J. Silk, M. Spiro, & J. Zinn-Justin, 469–+

Bond, J. R. 1996b, in *Cosmology and Large Scale Structure*, ed. R. Schaeffer, J. Silk, M. Spiro, & J. Zinn-Justin, 469–+

Bond, J. R. & Crittenden, R. 2001, in *NATO ASIC Proc. 565: Structure Formation in the Universe*, ed. R. G. Crittenden & N. G. Turok, 241–+

Bond, J. R., Efstathiou, G., & Tegmark, M. 1997, *MNRAS*, 291, L33

Bond, J. R., Jaffe, A. H., & Knox, L. 1998, *Phys. Rev. D*, 57, 2117

Bunn, E. F. 2011, *Phys. Rev. D*, 83, 083003

Bunn, E. F., Zaldarriaga, M., Tegmark, M., & de Oliveira-Costa, A. 2003, *Phys. Rev. D*, 67, 023501

Calabrese, E., Hlozek, R. A., Battaglia, N., Battistelli, E. S., Bond, J. R., Chluba, J., Crichton, D., Das, S., Devlin, M. J., Dunkley, J., Dünner, R., Farhang, M., Gralla, M. B., Hajian, A., Halpern, M., Hasselfield, M., Hincks, A. D., Irwin, K. D., Kosowsky, A., Louis, T., Marriage, T. A., Moodley, K., Newburgh, L., Niemack, M. D., Nolta, M. R., Page, L. A., Sehgal, N., Sherwin, B. D., Sievers, J. L., Sifón, C., Spergel, D. N., Staggs, S. T., Switzer, E. R., & Wollack, E. 2013, *ArXiv e-prints*

Challinor, A. & Chon, G. 2005, *MNRAS*, 360, 509

Chen, X. & Kamionkowski, M. 2004, *Phys. Rev. D*, 70, 043502

Chiang, H. C., Ade, P. A. R., Barkats, D., Battle, J. O., Bierman, E. M., Bock, J. J., Dowell, C. D., Duband, L., Hivon, E. F., Holzappel, W. L., Hristov, V. V., Jones, W. C., Keating, B. G., Kovac, J. M., Kuo, C. L., Lange, A. E., Leitch, E. M., Mason, P. V., Matsumura, T., Nguyen, H. T., Ponthieu, N., Pryke, C., Richter, S., Rocha, G., Sheehy, C., Takahashi, Y. D., Tolan, J. E., & Yoon, K. W. 2010, *ApJ*, 711, 1123

Chluba, J. 2010, *MNRAS*, 402, 1195

Chluba, J. & Sunyaev, R. A. 2006a, *A&A*, 458, L29

—. 2006b, *A&A*, 446, 39

—. 2008, *A&A*, 480, 629

—. 2009, *A&A*, 501, 29

—. 2010, *MNRAS*, 402, 1221

Chluba, J. & Thomas, R. M. 2011, *MNRAS*, 412, 748

Chon, G., Challinor, A., Prunet, S., Hivon, E., & Szapudi, I. 2004, *MNRAS*, 350, 914

Chuss, D. T., Ade, P. A. R., Benford, D. J., Bennett, C. L., Dotson, J. L., Eimer, J. R., Fixsen, D. J., Halpern, M., Hilton, G., Hinderks, J., Hinshaw, G., Irwin, K., Jackson, M. L., Jah, M. A., Jethava, N., Jhabvala, C., Kogut, A. J., Lowe, L., McCullagh, N., Miller, T., Mirel, P., Moseley, S. H., Rodriguez, S., Rostem, K., Sharp, E., Staguhn, J. G., Tucker, C. E., Voellmer, G. M., Wollack, E. J., & Zeng, L. 2010, in *Society of Photo-Optical Instrumentation Engineers (SPIE) Conference Series*, Vol. 7741, *Society of Photo-Optical Instrumentation Engineers (SPIE) Conference Series*

Contaldi, C. R., Rocha, G., Contaldi, C. R., Bond, J. R., Gorski, K. M., R., C., Rocha, G., Contaldi, C. R., Bond, J. R., Gorski, K. M., R., C., Rocha, G., Contaldi, C. R., Bond, J. R., & Gorski, K. M. 2010, in prep.

Das, S., Marriage, T. A., Ade, P. A. R., Aguirre, P., Amiri, M., Appel, J. W., Barrientos, L. F., Battistelli, E. S., Bond, J. R., Brown, B., Burger, B., Chervenak, J., Devlin, M. J., Dicker, S. R., Bertrand Doriese, W., Dunkley, J., Dünner, R., Essinger-Hileman, T., Fisher, R. P., Fowler, J. W., Hajian, A., Halpern, M., Hasselfield, M., Hernández-Monteaquedo, C., Hilton, G. C., Hilton, M., Hincks, A. D., Hlozek, R., Huffenberger, K. M., Hughes, D. H., Hughes, J. P., Infante, L., Irwin, K. D., Baptiste Juin, J., Kaul, M., Klein, J., Kosowsky, A., Lau, J. M., Limon, M., Lin, Y., Lupton, R. H., Marsden, D., Martocci, K., Mauskopf, P., Menanteau, F., Moodley, K., Moseley, H., Netterfield, C. B., Niemack, M. D., Nolte, M. R., Page, L. A., Parker, L., Partridge, B., Reid, B., Sehgal, N., Sherwin, B. D., Sievers, J., Spergel, D. N., Staggs, S. T., Swetz, D. S., Switzer, E. R., Thornton, R., Trac, H., Tucker, C., Warne, R., Wollack, E., & Zhao, Y. 2011, *ApJ*, 729, 62

de Bernardis, P., Ade, P. A. R., Bock, J. J., Bond, J. R., Borrill, J., Boscaleri, A., Coble, K., Crill, B. P., De Gasperis, G., Farese, P. C., Ferreira, P. G., Ganga, K., Giacometti, M., Hivon, E., Hristov, V. V., Iacoangeli, A., Jaffe, A. H., Lange, A. E., Martinis, L., Masi, S., Mason, P. V., Mauskopf, P. D., Melchiorri, A., Miglio, L., Montroy, T., Netterfield, C. B., Pascale, E., Piacentini, F., Pogosyan, D., Prunet, S., Rao, S., Romeo, G., Ruhl, J. E., Scaramuzzi, F., Sforna, D., & Vittorio, N. 2000a, *Nature*, 404, 955

—. 2000b, *Nature*, 404, 955

De Boor, C. 2001, *A Practical Guide to Splines* (Springer-Verlag)

Delabrouille, J., Betoule, M., Melin, J.-B., Miville-Deschênes, M.-A., Gonzalez-Nuevo, J., Le Jeune, M., Castex, G., de Zotti, G., Basak, S., Ashdown, M., Aumont, J., Baccigalupi, C., Banday, A., Bernard, J.-P., Bouchet, F. R., Clements, D. L., da Silva, A., Dickinson, C., Dodu, F., Dolag, K., Elsner, F., Fauvet, L., Faÿ, G., Giardino, G., Leach, S., Lesgourgues, J., Liguori, M., Macias-Perez, J. F., Massardi, M., Matarrese, S., Mazzotta, P., Montier, L., Mottet, S., Paladini, R., Partridge, B., Piffaretti, R., Prezeau, G., Prunet, S., Ricciardi, S., Roman, M., Schaefer, B., & Toffolatti, L. 2012, ArXiv e-prints

Dubrovich, V. K. & Grachev, S. I. 2005, *Astronomy Letters*, 31, 359

Dunkley, J., Calabrese, E., Sievers, J., Addison, G. E., Battaglia, N., Battistelli, E. S., Bond, J. R., Das, S., Devlin, M. J., Dunner, R., Fowler, J. W., Gralla, M., Hajian, A., Halpern, M., Hasselfield, M., Hincks, A. D., Hlozek, R., Hughes, J. P., Irwin, K. D., Kosowsky, A., Louis, T., Marriage, T. A., Marsden, D., Menanteau, F., Moodley, K., Niemack, M., Nolta, M. R., Page, L. A., Partridge, B., Sehgal, N., Spergel, D. N., Staggs, S. T., Switzer, E. R., Trac, H., & Wollack, E. 2013, ArXiv e-prints

Dunkley, J., Hlozek, R., Sievers, J., Acquaviva, V., Ade, P. A. R., Aguirre, P., Amiri, M., Appel, J. W., Barrientos, L. F., Battistelli, E. S., Bond, J. R., Brown, B., Burger, B., Chervenak, J., Das, S., Devlin, M. J., Dicker, S. R., Bertrand Doriese, W., Dünner, R., Essinger-Hileman, T., Fisher, R. P., Fowler, J. W., Hajian, A., Halpern, M., Hasselfield, M., Hernández-Monteagudo, C., Hilton, G. C., Hilton, M., Hincks, A. D., Huffenberger, K. M., Hughes, D. H., Hughes, J. P., Infante, L., Irwin, K. D., Juin, J. B., Kaul, M., Klein, J., Kosowsky, A., Lau, J. M., Limon, M., Lin, Y.-T., Lupton, R. H., Marriage, T. A., Marsden, D., Mauskopf, P., Menanteau, F., Moodley, K., Moseley, H., Netterfield, C. B., Niemack, M. D., Nolta, M. R., Page, L. A., Parker, L., Partridge, B., Reid, B., Sehgal, N., Sherwin, B., Spergel, D. N., Staggs, S. T., Swetz, D. S., Switzer, E. R., Thornton, R., Trac, H., Tucker, C., Warne, R., Wollack, E., & Zhao, Y. 2011, *ApJ*, 739, 52

Efstathiou, G., Gratton, S., & Paci, F. 2009, *MNRAS*, 397, 1355

Eggers Bjaelde, O., Das, S., & Moss, A. 2012, ArXiv:1205.0553

Essinger-Hileman, T., Appel, J. W., Beall, J. A., Cho, H. M., Fowler, J., Halpern, M., Hasselfield, M., Irwin, K. D., Marriage, T. A., Niemack, M. D., Page, L., Parker, L. P., Pufu, S., Staggs, S. T., Stryzak, O., Visnjic, C., Yoon, K. W., & Zhao, Y. 2010, ArXiv e-prints

- Farhang, M., Bond, J. R., & Chluba, J. 2012a, *ApJ*, 752, 88
- Farhang, M., Bond, J. R., Chluba, J., & Switzer, E. R. 2012b, *ArXiv e-prints*
- Farhang, M., Bond, J. R., Doré, O., & Barth Netterfield, C. 2011, *ArXiv e-prints*
- Fendt, W. A., Chluba, J., Rubiño-Martín, J. A., & Wandelt, B. D. 2009, *ApJS*, 181, 627
- Filippini, J. P., Ade, P. A. R., Amiri, M., Benton, S. J., Bihary, R., Bock, J. J., Bond, J. R., Bonetti, J. A., Bryan, S. A., Burger, B., Chiang, H. C., Contaldi, C. R., Crill, B. P., Doré, O., Farhang, M., Fissel, L. M., Gandilo, N. N., Golwala, S. R., Gudmundsson, J. E., Halpern, M., Hasselfield, M., Hilton, G., Holmes, W., Hristov, V. V., Irwin, K. D., Jones, W. C., Kuo, C. L., MacTavish, C. J., Mason, P. V., Montroy, T. E., Morford, T. A., Netterfield, C. B., O’Dea, D. T., Rahlin, A. S., Reintsema, C. D., Ruhl, J. E., Runyan, M. C., Schenker, M. A., Shariff, J. A., Soler, J. D., Trangsrud, A., Tucker, C., Tucker, R. S., & Turner, A. D. 2010, in *Society of Photo-Optical Instrumentation Engineers (SPIE) Conference Series*, Vol. 7741, *Society of Photo-Optical Instrumentation Engineers (SPIE) Conference Series*
- Finkbeiner, D. P., Galli, S., Lin, T., & Slatyer, T. R. 2012, *Phys. Rev. D*, 85, 043522
- Fixsen, D. J. 2009, *ApJ*, 707, 916
- Fraisse, A. A., Ade, P. A. R., Amiri, M., Benton, S. J., Bock, J. J., Bond, J. R., Bonetti, J. A., Bryan, S., Burger, B., Chiang, H. C., Clark, C. N., Contaldi, C. R., Crill, B. P., Davis, G., Doré, O., Farhang, M., Filippini, J. P., Fissel, L. M., Gandilo, N. N., Golwala, S., Gudmundsson, J. E., Hasselfield, M., Hilton, G., Holmes, W., Hristov, V. V., Irwin, K., Jones, W. C., Kuo, C. L., MacTavish, C. J., Mason, P. V., Montroy, T. E., Morford, T. A., Netterfield, C. B., O’Dea, D. T., Rahlin, A. S., Reintsema, C., Ruhl, J. E., Runyan, M. C., Schenker, M. A., Shariff, J. A., Soler, J. D., Trangsrud, A., Tucker, C., Tucker, R. S., Turner, A. D., & Wiebe, D. 2011, *ArXiv e-prints*
- Galli, S., Iocco, F., Bertone, G., & Melchiorri, A. 2009a, *Phys. Rev. D*, 80, 023505
- . 2011, *Phys. Rev. D*, 84, 027302
- Galli, S., Melchiorri, A., Smoot, G. F., & Zahn, O. 2009b, *Phys. Rev. D*, 80, 023508
- Giesen, G., Lesgourgues, J., Audren, B., & Ali-Haïmoud, Y. 2012, *ArXiv:1209.0247*
- Goldstein, J. H., Ade, P. A. R., Bock, J. J., Bond, J. R., Cantalupo, C., Contaldi, C. R., Daub, M. D., Holzzapfel, W. L., Kuo, C., Lange, A. E., Lueker, M., Newcomb, M., Peterson, J. B., Pogosyan, D., Ruhl, J. E., Runyan, M. C., & Torbet, E. 2003, *ApJ*, 599, 773

- Górski, K. M., Hivon, E., Banday, A. J., Wandelt, B. D., Hansen, F. K., Reinecke, M., & Bartelmann, M. 2005, *ApJ*, 622, 759
- Grain, J., Tristram, M., & Stompor, R. 2009, *Phys. Rev. D*, 79, 123515
- Grin, D. & Hirata, C. M. 2010, *Phys. Rev. D*, 81, 083005
- Hajian, A., Acquaviva, V., Ade, P. A. R., Aguirre, P., Amiri, M., Appel, J. W., Barrientos, L. F., Battistelli, E. S., Bond, J. R., Brown, B., Burger, B., Chervenak, J., Das, S., Devlin, M. J., Dicker, S. R., Bertrand Doriese, W., Dunkley, J., Dünner, R., Essinger-Hileman, T., Fisher, R. P., Fowler, J. W., Halpern, M., Hasselfield, M., Hernández-Monteagudo, C., Hilton, G. C., Hilton, M., Hincks, A. D., Hlozek, R., Huffenberger, K. M., Hughes, D. H., Hughes, J. P., Infante, L., Irwin, K. D., Baptiste Juin, J., Kaul, M., Klein, J., Kosowsky, A., Lau, J. M., Limon, M., Lin, Y.-T., Lupton, R. H., Marriage, T. A., Marsden, D., Mauskopf, P., Menanteau, F., Moodley, K., Moseley, H., Netterfield, C. B., Niemack, M. D., Nolta, M. R., Page, L. A., Parker, L., Partridge, B., Reid, B., Sehgal, N., Sherwin, B. D., Sievers, J., Spergel, D. N., Staggs, S. T., Swetz, D. S., Switzer, E. R., Thornton, R., Trac, H., Tucker, C., Warne, R., Wollack, E., & Zhao, Y. 2011, *ApJ*, 740, 86
- Halverson, N. W., Leitch, E. M., Pryke, C., Kovac, J., Carlstrom, J. E., Holzapfel, W. L., Dragovan, M., Cartwright, J. K., Mason, B. S., Padin, S., Pearson, T. J., Readhead, A. C. S., & Shepherd, M. C. 2002, *ApJ*, 568, 38
- Hanany, S., Ade, P., Balbi, A., Bock, J., Borrill, J., Boscaleri, A., de Bernardis, P., Ferreira, P. G., Hristov, V. V., Jaffe, A. H., Lange, A. E., Lee, A. T., Mauskopf, P. D., Netterfield, C. B., Oh, S., Pascale, E., Rabii, B., Richards, P. L., Smoot, G. F., Stompor, R., Winant, C. D., & Wu, J. H. P. 2000, *ApJ*, 545, L5
- Hansen, F. K. & Górski, K. M. 2003, *MNRAS*, 343, 559
- Hinshaw, G., Larson, D., Komatsu, E., Spergel, D. N., Bennett, C. L., Dunkley, J., Nolta, M. R., Halpern, M., Hill, R. S., Odegard, N., Page, L., Smith, K. M., Weiland, J. L., Gold, B., Jarosik, N., Kogut, A., Limon, M., Meyer, S. S., Tucker, G. S., Wollack, E., & Wright, E. L. 2012, *ArXiv e-prints*
- Hirata, C. M. 2008, *Phys. Rev. D*, 78, 023001
- Hivon, E., Górski, K. M., Netterfield, C. B., Crill, B. P., Prunet, S., & Hansen, F. 2002, *ApJ*, 567, 2
- Hou, Z., Keisler, R., Knox, L., Millea, M., & Reichardt, C. 2011, *ArXiv e-prints*

- Hou, Z., Reichardt, C. L., Story, K. T., Follin, B., Keisler, R., Aird, K. A., Benson, B. A., Bleem, L. E., Carlstrom, J. E., Chang, C. L., Cho, H., Crawford, T. M., Crites, A. T., de Haan, T., de Putter, R., Dobbs, M. A., Dodelson, S., Dudley, J., George, E. M., Halverson, N. W., Holder, G. P., Holzappel, W. L., Hoover, S., Hrubes, J. D., Joy, M., Knox, L., Lee, A. T., Leitch, E. M., Lueker, M., Luong-Van, D., McMahon, J. J., Mehl, J., Meyer, S. S., Millea, M., Mohr, J. J., Montroy, T. E., Padin, S., Plagge, T., Pryke, C., Ruhl, J. E., Sayre, J. T., Schaffer, K. K., Shaw, L., Shirokoff, E., Spieler, H. G., Staniszewski, Z., Stark, A. A., van Engelen, A., Vanderlinde, K., Vieira, J. D., Williamson, R., & Zahn, O. 2012, ArXiv e-prints
- Hu, W. & Holder, G. P. 2003, *Phys. Rev. D*, 68, 023001
- Hu, W., Scott, D., Sugiyama, N., & White, M. 1995, *Phys. Rev. D*, 52, 5498
- Hu, W. & White, M. 1997, *ApJ*, 479, 568
- Hütsi, G., Chluba, J., Hektor, A., & Raidal, M. 2011, *A&A*, 535, A26
- Hütsi, G., Hektor, A., & Raidal, M. 2009, *A&A*, 505, 999
- Jentschura, U. D. 2009, *Phys. Rev. A*, 79, 022510
- Kaiser, N. 1983, *MNRAS*, 202, 1169
- Kallosh, R. & Linde, A. 2010, *Journal of Cosmology and Astroparticle Physics*, 11, 11
- Kamionkowski, M., Kosowsky, A., & Stebbins, A. 1997, *Phys. Rev. D*, 55, 7368
- Kaplinghat, M., Scherrer, R. J., & Turner, M. S. 1999, *Phys. Rev. D*, 60, 023516
- Karshenboim, S. G. & Ivanov, V. G. 2008, *Astronomy Letters*, 34, 289
- Keisler, R., Reichardt, C. L., Aird, K. A., Benson, B. A., Bleem, L. E., Carlstrom, J. E., Chang, C. L., Cho, H. M., Crawford, T. M., Crites, A. T., de Haan, T., Dobbs, M. A., Dudley, J., George, E. M., Halverson, N. W., Holder, G. P., Holzappel, W. L., Hoover, S., Hou, Z., Hrubes, J. D., Joy, M., Knox, L., Lee, A. T., Leitch, E. M., Lueker, M., Luong-Van, D., McMahon, J. J., Mehl, J., Meyer, S. S., Millea, M., Mohr, J. J., Montroy, T. E., Natoli, T., Padin, S., Plagge, T., Pryke, C., Ruhl, J. E., Schaffer, K. K., Shaw, L., Shirokoff, E., Spieler, H. G., Staniszewski, Z., Stark, A. A., Story, K., van Engelen, A., Vanderlinde, K., Vieira, J. D., Williamson, R., & Zahn, O. 2011, *ApJ*, 743, 28
- Kholupenko, E. E. & Ivanchik, A. V. 2006, *Astronomy Letters*, 32, 795

- Kholupenko, E. E., Ivanchik, A. V., & Varshalovich, D. A. 2007, *MNRAS*, 378, L39
- Kogut, A., Fixsen, D. J., Chuss, D. T., Dotson, J., Dwek, E., Halpern, M., Hinshaw, G. F., Meyer, S. M., Moseley, S. H., Seiffert, M. D., Spergel, D. N., & Wollack, E. J. 2011, *Journal of Cosmology and Astroparticle Physics*, 7, 25
- Komatsu, E., Smith, K. M., Dunkley, J., Bennett, C. L., Gold, B., Hinshaw, G., Jarosik, N., Larson, D., Nolta, M. R., Page, L., Spergel, D. N., Halpern, M., Hill, R. S., Kogut, A., Limon, M., Meyer, S. S., Odegard, N., Tucker, G. S., Weiland, J. L., Wollack, E., & Wright, E. L. 2011, *ApJS*, 192, 18
- Kovac, J. M., Leitch, E. M., Pryke, C., Carlstrom, J. E., Halverson, N. W., & Holzappel, W. L. 2002, *Nature*, 420, 772
- Labzowsky, L., Solovyev, D., & Plunien, G. 2009, *Phys. Rev. A*, 80, 062514
- Lange, A. E., Ade, P. A., Bock, J. J., Bond, J. R., Borrill, J., Boscaleri, A., Coble, K., Crill, B. P., de Bernardis, P., Farese, P., Ferreira, P., Ganga, K., Giacometti, M., Hivon, E., Hristov, V. V., Iacoangeli, A., Jaffe, A. H., Martinis, L., Masi, S., Mauskopf, P. D., Melchiorri, A., Montroy, T., Netterfield, C. B., Pascale, E., Piacentini, F., Pogosyan, D., Prunet, S., Rao, S., Romeo, G., Ruhl, J. E., Scaramuzzi, F., & Sforna, D. 2001, *Phys. Rev. D*, 63, 042001
- Larson, D., Dunkley, J., Hinshaw, G., Komatsu, E., Nolta, M. R., Bennett, C. L., Gold, B., Halpern, M., Hill, R. S., Jarosik, N., Kogut, A., Limon, M., Meyer, S. S., Odegard, N., Page, L., Smith, K. M., Spergel, D. N., Tucker, G. S., Weiland, J. L., Wollack, E., & Wright, E. L. 2011, *ApJS*, 192, 16
- Leach, S. M., Cardoso, J.-F., Baccigalupi, C., Barreiro, R. B., Betoule, M., Bobin, J., Bonaldi, A., Delabrouille, J., de Zotti, G., Dickinson, C., Eriksen, H. K., González-Nuevo, J., Hansen, F. K., Herranz, D., Le Jeune, M., López-Caniego, M., Martínez-González, E., Massardi, M., Melin, J.-B., Miville-Deschênes, M.-A., Patanchon, G., Prunet, S., Ricciardi, S., Salerno, E., Sanz, J. L., Starck, J.-L., Stivoli, F., Stolyarov, V., Stompor, R., & Vielva, P. 2008, *A&A*, 491, 597
- Lewis, A., Challinor, A., & Lasenby, A. 2000, *ApJ*, 538, 473
- Lewis, A., Challinor, A., & Turok, N. 2002, *Phys. Rev. D*, 65, 023505
- Lewis, A., Weller, J., & Battye, R. 2006, *MNRAS*, 373, 561
- Lizarraga, J., Sendra, I., & Urrestilla, J. 2012, *Phys. Rev. D*, 86, 123014

- Lueker, M., Reichardt, C. L., Schaffer, K. K., Zahn, O., Ade, P. A. R., Aird, K. A., Benson, B. A., Bleem, L. E., Carlstrom, J. E., Chang, C. L., Cho, H., Crawford, T. M., Crites, A. T., de Haan, T., Dobbs, M. A., George, E. M., Hall, N. R., Halverson, N. W., Holder, G. P., Holzzapfel, W. L., Hrubes, J. D., Joy, M., Keisler, R., Knox, L., Lee, A. T., Leitch, E. M., McMahon, J. J., Mehl, J., Meyer, S. S., Mohr, J. J., Montroy, T. E., Padin, S., Plagge, T., Pryke, C., Ruhl, J. E., Shaw, L., Shirokoff, E., Spieler, H. G., Stalder, B., Staniszewski, Z., Stark, A. A., Vanderlinde, K., Vieira, J. D., & Williamson, R. 2010, *ApJ*, 719, 1045
- Lyth, D. H. 1997, *Physical Review Letters*, 78, 1861
- MacKay, D. J. 2003, *Information Theory, Inference, and Learning Algorithms*, 1st edn. (Cambridge: Cambridge University Press)
- MacTavish, C. J., Ade, P. A. R., Bock, J. J., Bond, J. R., Borrill, J., Boscaleri, A., Cabella, P., Contaldi, C. R., Crill, B. P., de Bernardis, P., De Gasperis, G., de Oliveira-Costa, A., De Troia, G., di Stefano, G., Hivon, E., Jaffe, A. H., Jones, W. C., Kisner, T. S., Lange, A. E., Lewis, A. M., Masi, S., Mauskopf, P. D., Melchiorri, A., Montroy, T. E., Natoli, P., Netterfield, C. B., Pascale, E., Piacentini, F., Pogosyan, D., Polenta, G., Prunet, S., Ricciardi, S., Romeo, G., Ruhl, J. E., Santini, P., Tegmark, M., Veneziani, M., & Vittorio, N. 2006, *ApJ*, 647, 799
- McAllister, L., Silverstein, E., & Westphal, A. 2010, *Phys. Rev. D*, 82, 046003
- Mennella, A., Butler, R. C., Curto, A., Cuttaia, F., Davis, R. J., Dick, J., Frailis, M., Galeotta, S., Gregorio, A., Kurki-Suonio, H., Lawrence, C. R., Leach, S., Leahy, J. P., Lowe, S., Maino, D., Mandolesi, N., Maris, M., Martínez-González, E., Meinhold, P. R., Morgante, G., Pearson, D., Perrotta, F., Polenta, G., Poutanen, T., Sandri, M., Seiffert, M. D., Suur-Uski, A.-S., Tavagnacco, D., Terenzi, L., Tomasi, M., Valiviita, J., Villa, F., Watson, R., Wilkinson, A., Zacchei, A., Zonca, A., Aja, B., Artal, E., Baccigalupi, C., Banday, A. J., Barreiro, R. B., Bartlett, J. G., Bartolo, N., Battaglia, P., Bennett, K., Bonaldi, A., Bonavera, L., Borrill, J., Bouchet, F. R., Burigana, C., Cabella, P., Cappellini, B., Chen, X., Colombo, L., Cruz, M., Danese, L., D’Arcangelo, O., Davies, R. D., de Gasperis, G., de Rosa, A., de Zotti, G., Dickinson, C., Diego, J. M., Donzelli, S., Efstathiou, G., Enßlin, T. A., Eriksen, H. K., Falvella, M. C., Finelli, F., Foley, S., Franceschet, C., Franceschi, E., Gaier, T. C., Génova-Santos, R. T., George, D., Gómez, F., González-Nuevo, J., Górski, K. M., Gruppuso, A., Hansen, F. K., Herranz, D., Herreros, J. M., Hoyland, R. J., Hughes, N., Jewell, J., Jukkala, P., Juvela, M., Kangaslahti, P., Keihänen, E., Keskitalo, R., Kilpia, V.-H., Kisner, T. S., Knoche, J., Knox, L., Laaninen, M., Lähteenmäki, A., Lamarre, J.-M., Leonardi, R., León-Tavares, J., Leutenegger, P., Lilje, P. B., López-Caniego, M., Lubin, P. M., Malaspina, M.,

- Marinucci, D., Massardi, M., Matarrese, S., Matthai, F., Melchiorri, A., Mendes, L., Miccolis, M., Migliaccio, M., Mitra, S., Moss, A., Natoli, P., Nesti, R., Nørgaard-Nielsen, H. U., Pagano, L., Paladini, R., Paoletti, D., Partridge, B., Pasian, F., Pettorino, V., Pietrobon, D., Pospieszalski, M., Prézeau, G., Prina, M., Procopio, P., Puget, J.-L., Quercellini, C., Rachen, J. P., Rebolo, R., Reinecke, M., Ricciardi, S., Robbers, G., Rocha, G., Roddis, N., Rubino-Martín, J. A., Savelainen, M., Scott, D., Silvestri, R., Simonetto, A., Sjomán, P., Smoot, G. F., Sozzi, C., Stringhetti, L., Tauber, J. A., Tofani, G., Toffolatti, L., Tuovinen, J., Türler, M., Umana, G., Valenziano, L., Varis, J., Vielva, P., Vittorio, N., Wade, L. A., Watson, C., White, S. D. M., & Winder, F. 2011, *A&A*, 536, A3
- Mitra, S., Choudhury, T. R., & Ferrara, A. 2011, *MNRAS*, 413, 1569
- Monaghan, J. J. 2005, *Reports on Progress in Physics*, 68, 1703
- Montroy, T. E., Ade, P. A. R., Bock, J. J., Bond, J. R., Borrill, J., Boscaleri, A., Cabella, P., Contaldi, C. R., Crill, B. P., de Bernardis, P., De Gasperis, G., de Oliveira-Costa, A., De Troia, G., di Stefano, G., Hivon, E., Jaffe, A. H., Kisner, T. S., Jones, W. C., Lange, A. E., Masi, S., Mauskopf, P. D., MacTavish, C. J., Melchiorri, A., Natoli, P., Netterfield, C. B., Pascale, E., Piacentini, F., Pogosyan, D., Polenta, G., Prunet, S., Ricciardi, S., Romeo, G., Ruhl, J. E., Santini, P., Tegmark, M., Veneziani, M., & Vittorio, N. 2006, *ApJ*, 647, 813
- Mortonson, M. J. & Hu, W. 2008, *ApJ*, 672, 737
- Mortonson, M. J., Huterer, D., & Hu, W. 2010, *Phys. Rev. D*, 82, 063004
- Myers, S. T., Contaldi, C. R., Bond, J. R., Pen, U.-L., Pogosyan, D., Prunet, S., Sievers, J. L., Mason, B. S., Pearson, T. J., Readhead, A. C. S., & Shepherd, M. C. 2003, *ApJ*, 591, 575
- Netterfield, C. B. 1995, PhD thesis, PRINCETON UNIVERSITY.
- Niemack, M. D., Ade, P. A. R., Aguirre, J., Barrientos, F., Beall, J. A., Bond, J. R., Britton, J., Cho, H. M., Das, S., Devlin, M. J., Dicker, S., Dunkley, J., Dünner, R., Fowler, J. W., Hajian, A., Halpern, M., Hasselfield, M., Hilton, G. C., Hilton, M., Hubmayr, J., Hughes, J. P., Infante, L., Irwin, K. D., Jarosik, N., Klein, J., Kosowsky, A., Marriage, T. A., McMahon, J., Menanteau, F., Moodley, K., Nibarger, J. P., Nolte, M. R., Page, L. A., Partridge, B., Reese, E. D., Sievers, J., Spergel, D. N., Staggs, S. T., Thornton, R., Tucker, C., Wollack, E., & Yoon, K. W. 2010, in *Society of Photo-Optical Instrumentation Engineers (SPIE) Conference Series*, Vol. 7741, *Society of Photo-Optical Instrumentation Engineers (SPIE) Conference Series*

- Nolta, M. R., Devlin, M. J., Dorwart, W. B., Miller, A. D., Page, L. A., Puchalla, J., Torbet, E., & Tran, H. T. 2003, *ApJ*, 598, 97
- O'Dea, D. T., Ade, P. A. R., Amiri, M., Benton, S. J., Bock, J. J., Bond, J. R., Bonetti, J. A., Bryan, S., Burger, B., Chiang, H. C., Clark, C. N., Contaldi, C. R., Crill, B. P., Davis, G., Doré, O., Farhang, M., Filippini, J. P., Fissel, L. M., Fraisse, A. A., Gandilo, N. N., Golwala, S., Gudmundsson, J. E., Hasselfield, M., Hilton, G., Holmes, W., Hristov, V. V., Irwin, K., Jones, W. C., Kuo, C. L., MacTavish, C. J., Mason, P. V., Montroy, T. E., Morford, T. A., Netterfield, C. B., Rahlin, A. S., Reintsema, C., Ruhl, J. E., Runyan, M. C., Schenker, M. A., Shariff, J. A., Soler, J. D., Trangsrud, A., Tucker, C., Tucker, R. S., Turner, A. D., & Wiebe, D. 2011, *ApJ*, 738, 63
- O'Dea, D. T., Clark, C. N., Contaldi, C. R., & MacTavish, C. J. 2012, *MNRAS*, 419, 1795
- Padmanabhan, N. & Finkbeiner, D. P. 2005, *Phys. Rev. D*, 72, 023508
- Page, L., Hinshaw, G., Komatsu, E., Nolta, M. R., Spergel, D. N., Bennett, C. L., Barnes, C., Bean, R., Doré, O., Dunkley, J., Halpern, M., Hill, R. S., Jarosik, N., Kogut, A., Limon, M., Meyer, S. S., Odegard, N., Peiris, H. V., Tucker, G. S., Verde, L., Weiland, J. L., Wollack, E., & Wright, E. L. 2007, *ApJS*, 170, 335
- Peebles, P. J. E. 1968, *ApJ*, 153, 1
- Peebles, P. J. E., Seager, S., & Hu, W. 2000, *ApJ*, 539, L1
- Peebles, P. J. E. & Yu, J. T. 1970, *ApJ*, 162, 815
- Piacentini, F., Ade, P. A. R., Bock, J. J., Bond, J. R., Borrill, J., Boscaleri, A., Cabella, P., Contaldi, C. R., Crill, B. P., de Bernardis, P., De Gasperis, G., de Oliveira-Costa, A., De Troia, G., di Stefano, G., Hivon, E., Jaffe, A. H., Kisner, T. S., Jones, W. C., Lange, A. E., Masi, S., Mauskopf, P. D., MacTavish, C. J., Melchiorri, A., Montroy, T. E., Natoli, P., Netterfield, C. B., Pascale, E., Pogosyan, D., Polenta, G., Prunet, S., Ricciardi, S., Romeo, G., Ruhl, J. E., Santini, P., Tegmark, M., Veneziani, M., & Vittorio, N. 2006, *ApJ*, 647, 833
- Planck HFI Core Team, Ade, P. A. R., Aghanim, N., Ansari, R., Arnaud, M., Ashdown, M., Aumont, J., Banday, A. J., Bartelmann, M., Bartlett, J. G., Battaner, E., Benabed, K., Benoît, A., Bernard, J.-P., Bersanelli, M., Bhatia, R., Bock, J. J., Bond, J. R., Borrill, J., Bouchet, F. R., Boulanger, F., Bradshaw, T., Bréelle, E., Bucher, M., Camus, P., Cardoso, J.-F., Catalano, A., Challinor, A., Chamballu, A., Charra, J., Charra, M., Chary, R.-R., Chiang, C., Church, S., Clements, D. L., Colombi, S., Couchot, F., Coulais, A., Cressiot, C., Crill, B. P., Crook, M., de Bernardis, P., Delabrouille, J., Delouis, J.-M., Désert, F.-X., Dolag, K.,

- Dole, H., Doré, O., Douspis, M., Efstathiou, G., Eng, P., Filliard, C., Forni, O., Fosalba, P., Fourmond, J.-J., Ganga, K., Giard, M., Girard, D., Giraud-Héraud, Y., Gispert, R., Górski, K. M., Gratton, S., Griffin, M., Guyot, G., Haissinski, J., Harrison, D., Helou, G., Henrot-Versillé, S., Hernández-Monteagudo, C., Hildebrandt, S. R., Hills, R., Hivon, E., Hobson, M., Holmes, W. A., Huffenberger, K. M., Jaffe, A. H., Jones, W. C., Kaplan, J., Kneissl, R., Knox, L., Lagache, G., Lamarre, J.-M., Lami, P., Lange, A. E., Lasenby, A., Lavabre, A., Lawrence, C. R., Leriche, B., Leroy, C., Longval, Y., Macías-Pérez, J. F., Maciaszek, T., MacTavish, C. J., Maffei, B., Mandolesi, N., Mann, R., Mansoux, B., Masi, S., Matsumura, T., McGehee, P., Melin, J.-B., Mercier, C., Miville-Deschênes, M.-A., Moneti, A., Montier, L., Mortlock, D., Murphy, A., Nati, F., Netterfield, C. B., Nørgaard-Nielsen, H. U., North, C., Noviello, F., Novikov, D., Osborne, S., Paine, C., Pajot, F., Patanchon, G., Peacocke, T., Pearson, T. J., Perdureau, O., Perotto, L., Piacentini, F., Piat, M., Plaszczynski, S., Pointecouteau, E., Pons, R., Ponthieu, N., Prézeau, G., Prunet, S., Puget, J.-L., Reach, W. T., Renault, C., Ristorcelli, I., Rocha, G., Rosset, C., Roudier, G., Rowan-Robinson, M., Rusholme, B., Santos, D., Savini, G., Schaefer, B. M., Shellard, P., Spencer, L., Starck, J.-L., Stassi, P., Stolyarov, V., Stompor, R., Sudiwala, R., Sunyaev, R., Sygnet, J.-F., Tauber, J. A., Thum, C., Torre, J.-P., Touze, F., Tristram, M., van Leeuwen, F., Vibert, L., Vibert, D., Wade, L. A., Wandelt, B. D., White, S. D. M., Wiesemeyer, H., Woodcraft, A., Yurchenko, V., Yvon, D., & Zacchei, A. 2011, *A&A*, 536, A4
- QUIET Collaboration, Araujo, D., Bischoff, C., Brizius, A., Buder, I., Chinone, Y., Cleary, K., Dumoulin, R. N., Kusaka, A., Monsalve, R., Næss, S. K., Newburgh, L. B., Reeves, R., Wehus, I. K., Zwart, J. T. L., Bronfman, L., Bustos, R., Church, S. E., Dickinson, C., Eriksen, H. K., Gaier, T., Gundersen, J. O., Hasegawa, M., Hazumi, M., Huffenberger, K. M., Ishidoshiro, K., Jones, M. E., Kangaslahti, P., Kapner, D. J., Kubik, D., Lawrence, C. R., Limon, M., McMahan, J. J., Miller, A. D., Nagai, M., Nguyen, H., Nixon, G., Pearson, T. J., Piccirillo, L., Radford, S. J. E., Readhead, A. C. S., Richards, J. L., Samtleben, D., Seiffert, M., Shepherd, M. C., Smith, K. M., Staggs, S. T., Tajima, O., Thompson, K. L., Vanderlinde, K., & Williamson, R. 2012, *ApJ*, 760, 145
- QUIET Collaboration, Bischoff, C., Brizius, A., Buder, I., Chinone, Y., Cleary, K., Dumoulin, R. N., Kusaka, A., Monsalve, R., Næss, S. K., Newburgh, L. B., Reeves, R., Smith, K. M., Wehus, I. K., Zuntz, J. A., Zwart, J. T. L., Bronfman, L., Bustos, R., Church, S. E., Dickinson, C., Eriksen, H. K., Ferreira, P. G., Gaier, T., Gundersen, J. O., Hasegawa, M., Hazumi, M., Huffenberger, K. M., Jones, M. E., Kangaslahti, P., Kapner, D. J., Lawrence, C. R., Limon, M., May, J., McMahan, J. J., Miller, A. D., Nguyen, H., Nixon, G. W., Pearson, T. J., Piccirillo, L., Radford, S. J. E., Readhead, A. C. S., Richards, J. L., Samtleben, D.,

- Seiffert, M., Shepherd, M. C., Staggs, S. T., Tajima, O., Thompson, K. L., Vanderlinde, K., Williamson, R., & Winstein, B. 2010, ArXiv e-prints
- Reichardt, C. L., Ade, P. A. R., Bock, J. J., Bond, J. R., Brevik, J. A., Contaldi, C. R., Daub, M. D., Dempsey, J. T., Goldstein, J. H., Holzappel, W. L., Kuo, C. L., Lange, A. E., Lueker, M., Newcomb, M., Peterson, J. B., Ruhl, J., Runyan, M. C., & Staniszewski, Z. 2009a, *ApJ*, 694, 1200
- . 2009b, *ApJ*, 694, 1200
- Reichborn-Kjennerud, B., Aboobaker, A. M., Ade, P., Aubin, F., Baccigalupi, C., Bao, C., Borrill, J., Cantalupo, C., Chapman, D., Didier, J., Dobbs, M., Grain, J., Grainger, W., Hanany, S., Hillbrand, S., Hubmayr, J., Jaffe, A., Johnson, B., Jones, T., Kisner, T., Klein, J., Korotkov, A., Leach, S., Lee, A., Levinson, L., Limon, M., MacDermid, K., Matsumura, T., Meng, X., Miller, A., Milligan, M., Pascale, E., Polsgrove, D., Ponthieu, N., Raach, K., Sagiv, I., Smecher, G., Stivoli, F., Stompor, R., Tran, H., Tristram, M., Tucker, G. S., Vinokurov, Y., Yadav, A., Zaldarriaga, M., & Zilic, K. 2010, in *Society of Photo-Optical Instrumentation Engineers (SPIE) Conference Series*, Vol. 7741, Society of Photo-Optical Instrumentation Engineers (SPIE) Conference Series
- Rocha, G., Contaldi, C. R., Bond, J. R., & Górski, K. M. 2011, *MNRAS*, 414, 823
- Rocha, G., Contaldi, C. R., Colombo, L. P. L., Bond, J. R., Gorski, K. M., & Lawrence, C. R. 2010, ArXiv e-prints
- Rubiño-Martín, J. A., Chluba, J., Fendt, W. A., & Wandelt, B. D. 2010, *MNRAS*, 403, 439
- Rubiño-Martín, J. A., Chluba, J., & Sunyaev, R. A. 2008, *A&A*, 485, 377
- Ruhl, J. E., Ade, P. A. R., Bock, J. J., Bond, J. R., Borrill, J., Boscaleri, A., Contaldi, C. R., Crill, B. P., de Bernardis, P., De Troia, G., Ganga, K., Giacometti, M., Hivon, E., Hristov, V. V., Iacoangeli, A., Jaffe, A. H., Jones, W. C., Lange, A. E., Masi, S., Mason, P., Mauskopf, P. D., Melchiorri, A., Montroy, T., Netterfield, C. B., Pascale, E., Piacentini, F., Pogosyan, D., Polenta, G., Prunet, S., & Romeo, G. 2003, *ApJ*, 599, 786
- Samsing, J., Linder, E. V., & Smith, T. L. 2012, ArXiv:1208.4845
- Scóccola, C. G., Landau, S. J., & Vucetich, H. 2008, *Physics Letters B*, 669, 212
- . 2009, *Memorie della Societ Astronomica Italiana*, 80, 814
- Seager, S., Sasselov, D. D., & Scott, D. 1999, *ApJ*, 523, L1

—. 2000, *ApJS*, 128, 407

Seljak, U., Sugiyama, N., White, M., & Zaldarriaga, M. 2003, *Phys. Rev. D*, 68, 083507

Seljak, U. & Zaldarriaga, M. 1996, *ApJ*, 469, 437

Sendra, I. & Smith, T. L. 2012, *Phys. Rev. D*, 85, 123002

Shaw, J. R. & Chluba, J. 2011, *MNRAS*, 415, 1343

Sheehy, C. D., Ade, P. A. R., Aikin, R. W., Amiri, M., Benton, S., Bischoff, C., Bock, J. J., Bonetti, J. A., Brevik, J. A., Burger, B., Dowell, C. D., Duband, L., Filippini, J. P., Golwala, S. R., Halpern, M., Hasselfield, M., Hilton, G., Hristov, V. V., Irwin, K., Kaufman, J. P., Keating, B. G., Kovac, J. M., Kuo, C. L., Lange, A. E., Leitch, E. M., Lueker, M., Netterfield, C. B., Nguyen, H. T., Ogburn, IV, R. W., Orlando, A., Pryke, C. L., Reintsema, C., Richter, S., Ruhl, J. E., Runyan, M. C., Staniszewski, Z., Stokes, S., Sudiwala, R., Teply, G., Thompson, K. L., Tolan, J. E., Turner, A. D., Wilson, P., & Wong, C. L. 2010, in *Society of Photo-Optical Instrumentation Engineers (SPIE) Conference Series*, Vol. 7741, Society of Photo-Optical Instrumentation Engineers (SPIE) Conference Series

Sievers, J. L. 2004, PhD thesis, California Institute of Technology, California, USA

Sievers, J. L., Achermann, C., Bond, J. R., Bronfman, L., Bustos, R., Contaldi, C. R., Dickinson, C., Ferreira, P. G., Jones, M. E., Lewis, A. M., Mason, B. S., May, J., Myers, S. T., Oyarce, N., Padin, S., Pearson, T. J., Pospieszalski, M., Readhead, A. C. S., Reeves, R., Taylor, A. C., & Torres, S. 2007a, *ApJ*, 660, 976

—. 2007b, *ApJ*, 660, 976

Sievers, J. L., Bond, J. R., Cartwright, J. K., Contaldi, C. R., Mason, B. S., Myers, S. T., Padin, S., Pearson, T. J., Pen, U.-L., Pogosyan, D., Prunet, S., Readhead, A. C. S., Shepherd, M. C., Udomprasert, P. S., Bronfman, L., Holzappel, W. L., & May, J. 2003, *ApJ*, 591, 599

Sievers, J. L., Hlozek, R. A., Nolta, M. R., Acquaviva, V., Addison, G. E., Ade, P. A. R., Aguirre, P., Amiri, M., Appel, J. W., Barrientos, L. F., Battistelli, E. S., Battaglia, N., Bond, J. R., Brown, B., Burger, B., Calabrese, E., Chervenak, J., Crichton, D., Das, S., Devlin, M. J., Dicker, S. R., Bertrand Doriese, W., Dunkley, J., Dünner, R., Essinger-Hileman, T., Faber, D., Fisher, R. P., Fowler, J. W., Gallardo, P., Gordon, M. S., Gralla, M. B., Hajian, A., Halpern, M., Hasselfield, M., Hernández-Monteagudo, C., Hill, J. C., Hilton, G. C., Hilton, M., Hincks, A. D., Holtz, D., Huffenberger, K. M., Hughes, D. H., Hughes, J. P., Infante, L., Irwin, K. D., Jacobson, D. R., Johnstone, B., Baptiste Juin, J.,

- Kaul, M., Klein, J., Kosowsky, A., Lau, J. M., Limon, M., Lin, Y.-T., Louis, T., Lupton, R. H., Marriage, T. A., Marsden, D., Martocci, K., Mauskopf, P., McLaren, M., Menanteau, F., Moodley, K., Moseley, H., Netterfield, C. B., Niemack, M. D., Page, L. A., Page, W. A., Parker, L., Partridge, B., Plimpton, R., Quintana, H., Reese, E. D., Reid, B., Rojas, F., Sehgal, N., Sherwin, B. D., Schmitt, B. L., Spergel, D. N., Staggs, S. T., Stryzak, O., Swetz, D. S., Switzer, E. R., Thornton, R., Trac, H., Tucker, C., Uehara, M., Visnjic, K., Warne, R., Wilson, G., Wollack, E., Zhao, Y., & Zuncke, C. 2013, ArXiv e-prints
- Silk, J. 1968, ApJ, 151, 459
- Singh, H., Misra, N., Misra, N., Hnizdo, V., Fedorowicz, A., & Demchuk, E. 2003, American Journal of Mathematical and Management Sciences, 23, 301
- Slatyer, T. R., Padmanabhan, N., & Finkbeiner, D. P. 2009, Phys. Rev. D, 80, 043526
- Smith, K. M. 2006, Phys. Rev. D, 74, 083002
- Smith, K. M., Cooray, A., Das, S., Doré, O., Hanson, D., Hirata, C., Kaplinghat, M., Keating, B., LoVerde, M., Miller, N., Rocha, G., Shimon, M., & Zahn, O. 2008, ArXiv e-prints
- Smith, K. M. & Zaldarriaga, M. 2007, Phys. Rev. D, 76, 043001
- Smith, T. L., Das, S., & Zahn, O. 2012, Phys. Rev. D, 85, 023001
- Smith, T. L., Pierpaoli, E., & Kamionkowski, M. 2006, Physical Review Letters, 97, 021301
- Smoot, G. F., Bennett, C. L., Kogut, A., Wright, E. L., Aymon, J., Boggess, N. W., Cheng, E. S., de Amici, G., Gulkis, S., Hauser, M. G., Hinshaw, G., Jackson, P. D., Janssen, M., Kaita, E., Kelsall, T., Keegstra, P., Lineweaver, C., Loewenstein, K., Lubin, P., Mather, J., Meyer, S. S., Moseley, S. H., Murdock, T., Rokke, L., Silverberg, R. F., Tenorio, L., Weiss, R., & Wilkinson, D. T. 1992, ApJ, 396, L1
- Spergel, D. N., Verde, L., Peiris, H. V., Komatsu, E., Nolta, M. R., Bennett, C. L., Halpern, M., Hinshaw, G., Jarosik, N., Kogut, A., Limon, M., Meyer, S. S., Page, L., Tucker, G. S., Weiland, J. L., Wollack, E., & Wright, E. L. 2003, ApJS, 148, 175
- Story, K. T., Reichardt, C. L., Hou, Z., Keisler, R., Aird, K. A., Benson, B. A., Bleem, L. E., Carlstrom, J. E., Chang, C. L., Cho, H., Crawford, T. M., Crites, A. T., de Haan, T., Dobbs, M. A., Dudley, J., Follin, B., George, E. M., Halverson, N. W., Holder, G. P., Holzzapfel, W. L., Hoover, S., Hrubes, J. D., Joy, M., Knox, L., Lee, A. T., Leitch, E. M., Lueker, M., Luong-Van, D., McMahon, J. J., Mehl, J., Meyer, S. S., Millea, M., Mohr, J. J., Montroy, T. E., Padin, S., Plagge, T., Pryke, C., Ruhl, J. E., Sayre, J. T., Schaffer, K. K., Shaw, L.,

- Shirokoff, E., Spieler, H. G., Staniszewski, Z., Stark, A. A., van Engelen, A., Vanderlinde, K., Vieira, J. D., Williamson, R., & Zahn, O. 2012, ArXiv e-prints
- Sunyaev, R. A. & Chluba, J. 2009, *Astronomische Nachrichten*, 330, 657
- Sunyaev, R. A. & Zeldovich, Y. B. 1970, *Astrophysics and Space Science*, 7, 3
- Switzer, E. R. & Hirata, C. M. 2008, *Phys. Rev. D*, 77, 083006
- Szapudi, I., Prunet, S., & Colombi, S. 2001, ArXiv Astrophysics e-prints
- Tauber, J. A., Mandolesi, N., Puget, J., Banos, T., Bersanelli, M., Bouchet, F. R., Butler, R. C., Charra, J., Crone, G., Dodsworth, J., & et al. 2010, *A&A*, 520, A1+
- Tegmark, M. & de Oliveira-Costa, A. 2001, *Phys. Rev. D*, 64, 063001
- Tegmark, M., Taylor, A. N., & Heavens, A. F. 1997, *ApJ*, 480, 22
- The CORe Collaboration. 2011, ArXiv e-prints
- The Planck Collaboration. 2006, astro-ph/0604069
- The Polarbear Collaboration, Errard, J., Ade, P. A. R., Anthony, A., Arnold, K., Aubin, F., Boettger, D., Borrill, J., Cantalupo, C., Dobbs, M. A., Flanigan, D., Ghribi, A., Halverson, N., Hazumi, M., Holzzapfel, W. L., Howard, J., Hyland, P., Jaffe, A., Keating, B., Kisner, T., Kermish, Z., Lee, A. T., Linder, E., Lungu, M., Matsumura, T., Miller, N., Meng, X., Myers, M., Nishino, H., O'Brien, R., O'Dea, D., Reichardt, C., Schanning, I., Shimizu, A., Shimmin, C., Shimon, M., Spieler, H., Steinbach, B., Stompor, R., Suzuki, A., Tomaru, T., Tran, H. T., Tucker, C., Quealy, E., Richards, P. L., & Zahn, O. 2010, ArXiv e-prints
- Vanderlinde, K., Crawford, T. M., de Haan, T., Dudley, J. P., Shaw, L., Ade, P. A. R., Aird, K. A., Benson, B. A., Bleem, L. E., Brodwin, M., Carlstrom, J. E., Chang, C. L., Crites, A. T., Desai, S., Dobbs, M. A., Foley, R. J., George, E. M., Gladders, M. D., Hall, N. R., Halverson, N. W., High, F. W., Holder, G. P., Holzzapfel, W. L., Hrubes, J. D., Joy, M., Keisler, R., Knox, L., Lee, A. T., Leitch, E. M., Loehr, A., Lueker, M., Marrone, D. P., McMahon, J. J., Mehl, J., Meyer, S. S., Mohr, J. J., Montroy, T. E., Ngeow, C., Padin, S., Plagge, T., Pryke, C., Reichardt, C. L., Rest, A., Ruel, J., Ruhl, J. E., Schaffer, K. K., Shirokoff, E., Song, J., Spieler, H. G., Stalder, B., Staniszewski, Z., Stark, A. A., Stubbs, C. W., van Engelen, A., Vieira, J. D., Williamson, R., Yang, Y., Zahn, O., & Zenteno, A. 2010, *ApJ*, 722, 1180

- Verde, L., Peiris, H. V., Spergel, D. N., Nolta, M. R., Bennett, C. L., Halpern, M., Hinshaw, G., Jarosik, N., Kogut, A., Limon, M., Meyer, S. S., Page, L., Tucker, G. S., Wollack, E., & Wright, E. L. 2003, *ApJS*, 148, 195
- Vikhlinin, A., Kravtsov, A. V., Burenin, R. A., Ebeling, H., Forman, W. R., Hornstrup, A., Jones, C., Murray, S. S., Nagai, D., Quintana, H., & Voevodkin, A. 2009, *ApJ*, 692, 1060
- Wong, W. Y., Moss, A., & Scott, D. 2008, *MNRAS*, 386, 1023
- Wong, W. Y. & Scott, D. 2007, *MNRAS*, 375, 1441
- Wraith, D., Kilbinger, M., Benabed, K., Cappé, O., Cardoso, J., Fort, G., Prunet, S., & Robert, C. P. 2009, *Phys. Rev. D*, 80, 023507
- Zaldarriaga, M. & Seljak, U. 1997, *Phys. Rev. D*, 55, 1830
- Zeldovich, Y. B., Kurt, V. G., & Syunyaev, R. A. 1968, *Zhurnal Eksperimental noi i Teoreticheskoi Fiziki*, 55, 278
- Zhang, L., Chen, X., Kamionkowski, M., Si, Z., & Zheng, Z. 2007, *Phys. Rev. D*, 76, 061301
- Zhang, L., Chen, X., Lei, Y., & Si, Z. 2006, *Phys. Rev. D*, 74, 103519